

# **Developing A Broadly Applicable and Facile $^{18}\text{F}$ -Labelling Method for PET Imaging**

by

Zhibo Liu

B.Sc. Nanjing University, 2010

A THESIS SUBMITTED IN PARTIAL FULFILMENT OF  
THE REQUIREMENTS FOR THE DEGREE OF

DOCTOR OF PHILOSOPHY

in

The Faculty of Graduate and Postdoctoral Studies

(Chemistry)

The University Of British Columbia

(Vancouver)

July 2014

©Zhibo Liu, 2014

## Abstract

Positron emission tomography (PET) is on the forefront of cancer diagnosis, clinical drug evaluation, and patient management. Among the numbers of  $\beta^+$ -emitting nuclides,  $^{18}\text{F}$  ( $t_{1/2}=109.8$  min) is a mainstay isotope for PET imaging owing to its excellent nuclear properties and on-demand production at Curie levels. Despite the success of PET and increasing interests of  $^{18}\text{F}$ -radiochemistry, a facile  $^{18}\text{F}$ -labeling method that can be broadly applied to biomolecules has been a long-standing challenge. Most known  $^{18}\text{F}$ -labeling methods are relatively onerous and lengthy processes, which is a particularly serious problem given the short half-life of  $^{18}\text{F}$ . This thesis describes the design, synthesis and *in vivo* evaluation of novel  $^{18}\text{F}$ -radioprosthetics based on  $\text{B-}^{18}\text{F}$  formation, and aims at developing a facile and broadly applicable  $^{18}\text{F}$ -labeling method for PET imaging. Previously, the Perrin group has established  $^{18}\text{F}$ -aryltrifluoroborates as a promising radiosynthon to radiolabel bioligands. In light of this success, this thesis has dedicated to expand  $\text{B-}^{18}\text{F}$  labeling method from a scientific design to a generic clinical-friendly tool for developing new PET tracers. The first highlight of this thesis is to create new labeling methods (Chapter 4 and Chapter 5) to increase the specific activity of  $^{18}\text{F}$ -radiotracers to  $15\text{ Ci}/\mu\text{mol}$ , which is about a magnitude higher than normal maximum. The second highlight is to discover a heretofore-unknown linear correlation between the solvolytic stability for a given organotrifluoroborate and the  $\text{pK}_a$  of the corresponding carboxylic acids (Chapter 3). This discovery has fundamental interests for Suzuki-Miyaura coupling and also leads me to find a novel  $\text{B-}^{18}\text{F}$  radiosynthon that combines high *in vivo* stability and “kit-like”  $^{18}\text{F}$ -labelling technology, which is the third highlight and also the core of this body of work (Chapter 6). Along with this, numbers of bioligands have been biologically evaluated, and some of them demonstrate excellent *in vivo* performance. Particularly, TATE- $\text{AMBF}_3$ , which is an octreotate derivative, showing the best performance of any ligands for imaging somatostatin receptors in several decades (Chapter 7). In addition, for seamless bench-to-bed translation, a dual-modal strategy of synthesizing fluorescent PET tracer is presented (Chapter 8).

# Preface

Chapter 1 is the introduction of this dissertation.

Chapter 2 is an adaption of published work, and is reproduced in part with permission from Liu Z., Hundal N., Wong M., Yapp D., Lin K.-S., Benard F., Perrin D. M., A new  $^{18}\text{F}$ -heteroaryltrifluoroborate with greatly enhanced stability that is labelled by  $^{18}\text{F}$ - $^{19}\text{F}$  isotope exchange in good yield at high specific activity, *Med. Chem. Commun.*, **2014**, *5*, 171–179. Synthesis and radiolabelling was performed by Zhibo Liu at TRIUMF and at BC Cancer. Specific activity measurement, stability binding assay and data fitting were performed by Zhibo Liu. Animal experiments were contracted to BC Cancer Agency, and the protocol used in these animal studies was approved by the Institutional Animal Care Committee (IACC) of University of British Columbia (protocol #A11-0060) and was performed by May Wong and Navjit Hundal. This project was supervised by Dr. David M. Perrin. The manuscript was written by Zhibo Liu, with input and editing from Dr. David M. Perrin.

Chapter 3 is an adaption of a manuscript in preparation for publication. Liu Z., Chao D., Li Y., Cojocaru D., Perrin D. M., Organotrifluoroborate Solvolysis: a Linear Free Energy Relationship with Implications for Suzuki-Miyaura Coupling Reactions and the Design of *in vivo* Stable PET Tracers. Expected submission date April-May 2014. Zhibo Liu performed the synthesis and  $^{19}\text{F}$ -NMR study, with some assistance from Daniel Chao who is an undergraduate volunteering student in our lab. Data fitting was performed by Zhibo Liu. This project was supervised by Dr. David M. Perrin. The manuscript was written by Zhibo Liu, with input and editing from Dr. David M. Perrin.

Chapter 4 is an adaption of published work, and is reproduced in part with permission from Liu Z., Li Y., Lozada J., Schaffer P., Adam M. J., Ruth T. J., Perrin D. M., Stoichiometric Leverage: Rapid  $^{18}\text{F}$ -Aryltrifluoroborate Radiosynthesis at Exceptionally High Specific Activity For Click Conjugation, *Angew. Chem. Int. Ed.* **2013**, *52*, 2303-2307. Zhibo Liu performed the synthesis, with some assistance from Dr. Ying Li who was a PhD student in our lab. Radiochemistry was performed by Zhibo Liu at TRIUMF

with the assistance from Dr. Hua Yang, Dr. Ying Li, Dr. Qing Miao and Dr. Paul Schaffer. Specific activity measurement and data fitting were performed by Zhibo Liu, with some assistance from Jerome Lozada, who is a master student in our lab. This project was supervised by Dr. David M. Perrin. The manuscript was written by Zhibo Liu and Dr. David M. Perrin.

Chapter 5 is an adaption of published work, and is reproduced in part with permission from Liu Z., Li Y., Lozada J., Pan J., Lin K.-S., Schaffer P., Perrin D. M., Rapid One-Step  $^{18}\text{F}$ -Labeling of Aryltrifluoroborate Conjugates by Isotope Exchange at High Specific Activity, *Journal of labelled compounds and radiopharmaceuticals* **2012**, 55 491–496 and Liu Z., Li Y., Lozada J., Wong M. Q., Greene J., Lin K.-S., Yapp D., Perrin D. M., Kit-like  $^{18}\text{F}$ -labeling of RGD- $^{19}\text{F}$ -Aryltrifluoroborate in High Yield and at Extraordinarily High Specific Activity with Preliminary *in vivo* Tumor Imaging, *Nuclear Medicine and Biology* **2013**, 40, 841-849. Zhibo Liu performed the synthesis, with some assistance from Ying Li who was a PhD student in our lab. Radiochemistry was performed by Zhibo Liu at TRIUMF with the assistance from Dr. Hua Yang and Dr. Qing Miao, and at BC Cancer Agency with the assistance of Jennifer Green, Dr. Jinhe Pan and Dr. Kuo-Shyan Lin. Specific activity measurement, stability binding assay and data fitting were performed by Zhibo Liu. Animal experiments were contracted to BC Cancer Agency, and the protocol used in these animal studies was approved by the Institutional Animal Care Committee (IACC) of University of British Columbia (protocol #A11-0060) and was performed by May Wong and Navjit Hundal. This project was supervised by Dr. David M. Perrin. The manuscript was written by Zhibo Liu, with input and editing from Dr. David M. Perrin.

Chapter 6 is an adaption of a manuscript in preparation for publication. Liu Z., Pourghiasian M., Dias G., Lau J., Amouroux G., Lin K.-S., Benard F. Perrin D. M., A facile and broadly applicable  $^{18}\text{F}$ -fluoridation method for PET imaging. Expected submission date April-May 2014. Zhibo Liu performed the synthesis, with some assistance from Dr. Jinhe Pan and Dr. Zhengxin Zhang who work at BC Cancer Agency. Radiochemistry was performed by Zhibo Liu at TRIUMF and at BC Cancer Agency with the assistance of Dr. Kuo-Shyan Lin. Specific activity measurement, stability binding

assay and data fitting were performed by Zhibo Liu. Animal experiments were contracted to BC Cancer Agency, and the protocol used in these animal studies was approved by the Institutional Animal Care Committee (IACC) of University of British Columbia (protocol #A11-0060) and was performed by Joseph Lau, Gemma Dias, Maral Pourghiasian, Donald Yapp and Navjit Hundal. This project was supervised by Dr. David M. Perrin. The manuscript was written by Zhibo Liu, with input and editing from Dr. David M. Perrin.

Chapter 7 is an adaption of work accepted for publication. Liu Z., Pourghiasian M., Benard F., Pan J., Lin K.S., Perrin D. M., Preclinical evaluation of a high affinity  $^{18}\text{F}$ -trifluoroborate octreotate derivative for somatostatin receptor imaging, *Journal of Nuclear Medicine*, **2014**. Synthesis was performed by Zhibo Liu, and radiochemistry was performed by Zhibo Liu at BC Cancer Agency with the assistance of Dr. Kuo-Shyan Lin. Specific activity measurement, stability binding assay and data fitting were performed by Zhibo Liu. Binding affinity assay and biological evaluation were performed by Maral Pourghiasian. Animal experiments were contracted to BC Cancer Agency, and the protocol used in these animal studies was approved by the Institutional Animal Care Committee (IACC) of University of British Columbia (protocol #A11-0060) and was performed by Maral Pourghiasian and Navjit Hundal. This project was supervised by Dr. Francois Benard and Dr. David M. Perrin. The manuscript was written by Zhibo Liu, with input and editing from Maral Pourghiasian, Dr. Francois Benard and Dr. David M. Perrin.

Chapter 8 is an adaption of a manuscript in preparation for publication. Liu Z., Radtke M. A., Wong M., Lau J., Lin K.-S., Yapp D., and Perrin D. M., Dual Mode Fluorescent PET Tracers: Efficient modular synthesis of [cRGD]<sub>2</sub>-Rhodamine-Alkyl- $^{18}\text{F}$ -Trifluoroborate, Rapid  $^{18}\text{F}$ -radiolabeling at very high specific activity, *in vivo* PET Imaging and *ex vivo* fluorescence. Expected submission date April-May 2014. Zhibo Liu performed the synthesis, with some assistance from Mark Alex Radtke who worked in our lab as a 449 student (undergraduate thesis). Radiochemistry was performed by Zhibo Liu at BC Cancer Agency with the assistance of Dr. Kuo-Shyan Lin. Specific activity measurement, stability binding assay and data fitting were performed by Zhibo Liu. Animal

experiments were contracted to BC Cancer Agency, and the protocol used in these animal studies was approved by the Institutional Animal Care Committee (IACC) of University of British Columbia (protocol #A11-0060) and was performed by May Wong, Donald Yapp and Navjit Hundal. This project was supervised by Dr. David M. Perrin. The manuscript was written by Zhibo Liu, with input and editing from Dr. David M. Perrin.

# Table of contents

<b>Abstract .....</b>	<b>ii</b>
<b>Preface .....</b>	<b>iii</b>
<b>Table of contents .....</b>	<b>vii</b>
<b>List of tables .....</b>	<b>xvi</b>
<b>List of figures .....</b>	<b>xvii</b>
<b>List of schemes .....</b>	<b>xxvii</b>
<b>List of abbreviations and symbols.....</b>	<b>xxviii</b>
<b>Acknowledgement.....</b>	<b>xxxii</b>
<b>Dedication.....</b>	<b>xxxiii</b>
<b>Chapter 1: Introduction.....</b>	<b>1</b>
<b>1.1 Molecular imaging .....</b>	<b>1</b>
<b>1.2 PET imaging .....</b>	<b>5</b>
<b>1.3 Radionuclides for PET imaging.....</b>	<b>6</b>
<b>1.3 <sup>18</sup>F-based radiopharmaceutical designs .....</b>	<b>8</b>
<b>1.4 Key-properties of <sup>18</sup>F-radioprosthesis .....</b>	<b>10</b>
1.4.1 <i>In vivo</i> stability of <sup>18</sup> F-radioprosthesis.....	10
1.4.2 Specific activity .....	10
1.4.3 Operational simplicity of <sup>18</sup> F-radiolabelling.....	11

1.5 Mini-review of B- <sup>18</sup> F labeling.....	11
1.5 The goal of this dissertation .....	15
<b>Chapter 2: Synthesis and Evaluation of Kinetically Stable Aryl/Alkyltrifluoroborates.....</b>	<b>16</b>
2.1 Introduction.....	16
2.2 Results .....	20
2.2.1 Assessing the hydrolytic stability of organotrifluoroborates.....	20
2.2.2 <i>In vitro</i> stability evaluation .....	22
2.2.2.1 Fluorescent TLC analysis .....	22
2.2.2.2 Radioactive HPLC analysis .....	25
2.2.3 <i>In vivo</i> stability assay .....	27
2.3 Discussion.....	29
2.4 Conclusion .....	30
2.5 Materials and synthesis .....	30
2.5.1 General information.....	30
2.5.2 HPLC methods.....	30
2.5.3 Preparation and synthesis.....	31
2.5.4 Animal protocol .....	37
<b>Chapter 3: Organotrifluoroborate Hydrolysis: Implications for Suzuki-Miyaura Coupling and The Design of <i>In Vivo</i> Stable PET Tracers .....</b>	<b>38</b>

<b>3.1 Introduction</b> .....	<b>38</b>
<b>3.2 Results</b> .....	<b>42</b>
<b>3.3 Discussion</b> .....	<b>46</b>
<b>3.4 Conclusion</b> .....	<b>48</b>
<b>3.5 Experimental</b> .....	<b>49</b>
3.5.1 Synthesis .....	49
3.5.2 <sup>19</sup> F-NMR analysis of the solvolysis of organotrifluoroborates.....	53
3.5.2.1 Butyltrifluoroborate (3.1).....	53
3.5.2.2 Vinyltrifluoroborate (3.2) .....	54
3.5.2.3 Bromomethyltrifluoroborate (3.4) .....	55
3.5.2.4 Sulfoniummethyltrifluoroborate (3.5).....	56
3.5.2.5 Ammoniomethyltrifluoroborate (3.6) .....	57
3.5.2.6 Phenacylmethyltrifluoroborate (3.8).....	58
3.5.2.7 Benzoylmethyltrifluoroborate (3.9) .....	59
3.5.2.8 Pyridiniummethyltrifluoroborate (3.10) .....	60
3.5.2.9 Ammoniomethyltrifluoroborate (3.11) .....	61
3.5.2.10 Dichloromethyltrifluoroborate (3.12) .....	62
3.5.2.11 Imidazolymethyltrifluoroborate (3.13) .....	63
3.5.2.12 Ammoniomethyltrifluoroborate (3.14) .....	64
3.5.2.13 Ammoniomethyltrifluoroborate (3.15) .....	65

<b>Chapter 4: Direct <math>^{18}\text{F}</math>-Fluoridation With No-Carrier-Added (NCA) <math>^{18}\text{F}</math>-Fluoride .....</b>	<b>66</b>
<b>4.1 Introduction.....</b>	<b>66</b>
<b>4.2 Results and discussion .....</b>	<b>70</b>
4.2.1 Optimization for fluoridation of arylboronates with fluorescent TLC analysis .....	70
4.2.1.1 pH optimization .....	70
4.2.1.2 Buffer selection.....	72
4.2.1.3 Reaction time and reaction temperature optimization .....	74
4.2.1.4 Development of an <i>in vacuo</i> method for NCA radiofluoridaiton .....	75
4.2.3 NCA $^{18}\text{F}$ -fluoridation of a fluorescent $\text{ArBF}_3^-$ .....	76
<b>4.3 Special discussion: stoichiometric leverage of specific activity.....</b>	<b>79</b>
4.3.1 Mathematic explanation regarding the tripling of specific activity .....	80
4.3.2 Specific activity of NCA $^{18}\text{F}$ -fluoride.....	81
4.3.3 Specific activity of $\text{ArBF}_3^-$ (4.16) .....	83
4.3.3.1 Calculation of specific activity from HPLC trace in UV-Vis mode.....	83
4.3.3.2 Measurement of specific activity by Fluorescence.....	83
4.3.4 Summary .....	85
<b>4.4 Conclusion .....</b>	<b>86</b>
<b>4.5 Experimental information.....</b>	<b>86</b>

4.5.1 General information .....	86
4.5.2 Synthesis .....	87
4.5.3 Radiosynthesis of 4.15 and Radiolabeling of 4.16 .....	93
4.5.4 HPLC analysis and specific activity measurement .....	95
4.5.5 Specific activity measurement .....	96
<b>Chapter 5: Developing An <math>^{18}\text{F}</math>-<math>^{19}\text{F}</math> Isotope Exchange (IEX) Reaction to Achieve High Specific Activity with An <math>\text{ArBF}_3^-</math> Bioconjugate.....</b>	<b>97</b>
<b>5.1 Introduction.....</b>	<b>97</b>
<b>5.2 Results .....</b>	<b>100</b>
5.2.1 $^{18}\text{F}$ - $^{19}\text{F}$ IEX with a fluorescent $\text{ArBF}_3^-$ .....	100
5.2.2 Specific activity measurement of $^{18}\text{F}$ -Rhodamine- $\text{ArBF}_3^-$ .....	102
5.2.3 Towards a kit-like radiosynthesis of $\text{RGD-}^{18}\text{F-ArBF}_3^-$ by IEX.....	102
5.2.4 Specific activity measurement of $^{18}\text{F}$ -RGD- $\text{ArBF}_3^-$ .....	105
5.2.5 Biological evaluation of $^{18}\text{F}$ -RGD- $\text{ArBF}_3^-$ (5.2) at high specific activity .....	106
<b>5.3 Discussion.....</b>	<b>107</b>
<b>5.5 Conclusion .....</b>	<b>111</b>
<b>5.5 Experimental section .....</b>	<b>112</b>
5.5.1 General information.....	112
5.5.1 HPLC methods.....	112
5.5.3 Synthesis .....	113

5.5.4 Preparation of $^{18}\text{F}$ -fluoride.....	114
5.5.5 Radiosynthesis of $^{18}\text{F}$ -5.2 by IEX .....	114
5.5.6 Animal imaging and <i>in vivo</i> biodistribution .....	116
<b>Chapter 6: A Broadly Applicable and Facile <math>^{18}\text{F}</math>-labeling Method for PET Imaging .....</b>	<b>117</b>
<b>6.1 Introduction.....</b>	<b>117</b>
<b>6.2 Results and discussion .....</b>	<b>119</b>
6.2.1 Hydrolytic stability .....	119
6.2.2 Kit-like radiolabeling.....	121
6.2.3 <i>In vivo</i> stability.....	122
6.2.4 <i>In vivo</i> tumor targeting.....	124
<b>6.3 Conclusion .....</b>	<b>128</b>
<b>6.4 Materials and methods .....</b>	<b>129</b>
6.4.1 General information.....	129
6.4.2 HPLC gradient .....	129
6.4.3 Synthesis .....	130
6.4.4 <i>In vitro</i> binding assays .....	138
6.4.5 Radiolabeling.....	138
6.4.6 <i>In vitro</i> stability.....	139
6.4.7 Animal model and biodistribution studies .....	139

6.4.8 PET/CT imaging .....	139
<b>Chapter 7: Preclinical Evaluation of a Novel <sup>18</sup>F-Labeled Somatostatin Receptor-Binding Peptide.....</b>	<b>141</b>
<b>7.1 Introduction.....</b>	<b>141</b>
<b>7.2 Results .....</b>	<b>143</b>
7.2.1 Radiochemistry .....	143
7.2.2 <i>In vitro</i> affinity.....	144
7.2.3 PET/CT .....	145
7.2.4 Time activity curve (TAC) analysis.....	147
7.2.5 Biodistribution studies .....	147
<b>7.3 Discussion.....</b>	<b>148</b>
<b>7.4 Conclusion .....</b>	<b>152</b>
<b>7.5 Materials and methods .....</b>	<b>152</b>
7.5.1 General information.....	152
7.5.1 Synthesis .....	152
7.5.2 <i>In vitro</i> binding assay.....	154
7.5.3 Radiolabeling.....	155
7.5.4 <i>In vitro</i> stability.....	156
7.5.5 Animal model and biodistribution studies .....	157
7.5.6 PET/CT imaging .....	157

7.5.7 Specific activity measurement .....	158
<b>Chapter 8: A Dual Modal Fluorescent PET Tracer .....</b>	<b>160</b>
<b>8.1 Introduction .....</b>	<b>160</b>
<b>8.2 Results .....</b>	<b>163</b>
8.2.1 Modular synthesis .....	163
8.2.2 Radiosynthes .....	164
8.2.3 Specific activity measurement .....	166
8.2.4 <i>In vitro</i> fluorescent binding assay .....	167
8.2.5 <i>In vivo</i> imaging .....	168
<b>8.3 Discussion.....</b>	<b>169</b>
8.3.1 Modular synthesis .....	169
8.3.2 Dual modal imaging: low/high specific activity .....	170
<b>8.4 Conclusion .....</b>	<b>172</b>
<b>8.5 Experimental .....</b>	<b>173</b>
8.5.1 General information .....	173
8.5.2 Synthesis .....	173
8.5.2 Cell based assay .....	177
8.5.3 Serum stability assay.....	178
8.5.4 Animal care and <i>in vivo</i> image acquisition .....	178
<b>Chapter 9: Conclusion and Future Work .....</b>	<b>182</b>

<b>9.1 Summary</b> .....	<b>182</b>
<b>References</b> .....	<b>185</b>

## List of tables

<b>Table 1.1</b> Summary of imaging modalities. <sup>3,4,20-22,24,33</sup> .....	4
<b>Table 1.2</b> Some positron-emitting radionuclides for PET imaging. <sup>2,34,38,39</sup> .....	7
<b>Table 2.1</b> Summary of solvolytic stability of all the new organotrifluoroborates.....	22
<b>Table 3.1</b> Summary of hydrolysis rate constant of organotrifluoroborates and the pKa of the corresponding carboxylic acid. ....	44
<b>Table 4.1</b> Experiment design of pH effect on $\text{ArBF}_3^-$ formation.....	71
<b>Table 4.2</b> List of the buffers for the fluoridation of arylborates. ....	72
<b>Table 4.3</b> Selection of buffers for the fluoridation of arylborates. ....	73
<b>Table 4.4</b> Experiment design of temperature effect on $\text{ArBF}_3^-$ formation. ....	75
<b>Table 4.5</b> Designed experiments to discover to new radiolabeling method. Experiment A: radiosynthesis $^{18}\text{F-ArBF}_3^-$ with previous method. Experiment B: radiosynthesis of the same $^{18}\text{F-ArBF}_3^-$ with “dry down” method. BOS: Beginning of the synthesis... ..	76
<b>Table 4.6</b> Summary of specific activity measurement.....	85
<b>Table 5.1</b> Summary of measured specific activity based on standard curve analysis. ....	105
<b>Table 7.2</b> The comparison of the most representative radiolabeled TATE derivatives. In spite of the facile radiosynthesis, TATE- $^{18}\text{F-AMBF}_3$ demonstrated one of the highest binding affinities to the ssrt2 receptors, and also one of the best tumor uptake. <sup>162,163,190,191,197-199,205,215,217-221</sup> .....	149
<b>Table 7.1:</b> Summary of specific activity measurement of TATE- $^{18}\text{F-AMBF}_3$ . ....	159
<b>Table 8.1</b> Summary of specific activity measurement of $^{18}\text{F-8.6}$ . ....	167
<b>Table 8.2</b> Fluorescent radiotracer assessments at high/low specific activity. ....	172

## List of figures

<b>Figure 1.1</b> An illustration of PET acquisition process.....	6
<b>Figure 1.2</b> Representative $^{18}\text{F}$ -radiolabeling methods. <sup>54-61</sup> .....	9
<b>Figure 1.3</b> Hypothetical mechanism for the hydrolysis of an $\text{ArBF}_3^-$ .....	13
<b>Figure 1.4</b> Chemical structure of marimastat- $\text{ArBF}_3^-$ .....	14
<b>Figure 1.5</b> <i>In vivo</i> PET imaging of MMPs in murine breast carcinomas with $^{18}\text{F}$ -labeled Marimastat. Both of the mice were directly injected with 100 $\mu\text{Ci}$ $^{18}\text{F}$ -labeled Marimastat at 0.39 $\text{Ci}/\mu\text{mol}$ , but the right mice was pre-blocked with 100 $\mu\text{g}$ unlabeled Marimastat to validate the binding specificity of the radiotracer. In this experiment, $^{18}\text{F}$ -labeled Marimastat demonstrated visible tumor uptake (blue circled) with specificity.....	14
<b>Figure 2.1</b> Plot of relative integration of the $^{19}\text{F}$ -PyrBF <sub>3</sub> as a fraction of ( $^{19}\text{F}$ -fluoride) vs. time. The solvolytic defluoridation was monitored by $^{19}\text{F}$ -NMR. Data are scaled to 60000 min and were fit to a first order reaction; the half-life of the corresponding $^{19}\text{F}$ -PyrBF <sub>3</sub> was calculated to be 16500 min. ....	21
<b>Figure 2.4</b> PET imaging of $^{18}\text{F}$ -labeled agents in healthy nude mice by small-animal PET. The representative 3D PET/CT images were shown at the time point of 10 min, 30 min and 60 min after being injected with the new designed RGD- $^{18}\text{F}$ -PyBF <sub>3</sub> <sup>-</sup> ( <b>2.16</b> ) The radioactivity was rapidly cleaned up from the background and then mainly excreted through urinary and digestive tract. As desired, the bone uptake was almost negligible, which clearly showed the high <i>in vivo</i> stability of this new designed $^{18}\text{F}$ -PyrBF <sub>3</sub> <sup>-</sup> radioprosthetic. I = intestine; B = bladder; H = heart. ....	28
<b>Figure 2.5</b> $^1\text{H}$ -NMR spectrum of <b>2.2</b> in $\text{CDCl}_3$ .....	32
<b>Figure 2.6</b> $^1\text{H}$ -NMR spectrum of <b>2.4</b> in $\text{CDCl}_3$ .....	33

<b>Figure 2.7</b> $^1\text{H}$ -NMR spectrum of <b>2.12</b> in $\text{CDCl}_3$ .....	35
<b>Figure 3.1</b> Organotrifluoroborates used for analysis of solvolytic stability. ....	42
<b>Figure 3.2</b> (top): $^{19}\text{F}$ -NMR kinetic analysis of the defluoridation from the $^{19}\text{F}$ - <b>3.7</b> ( $^{19}\text{F}$ -Fluoride: -121 ppm relative to $\text{CFCl}_3$ ; $^{19}\text{F}$ - <b>3.7</b> : -137 ppm relative to $\text{CFCl}_3$ ). <b>Figure 3.2</b> (bottom): Plot of relative $^{19}\text{F}$ -NMR integration of the $^{19}\text{F}$ - <b>3.7</b> as a function of all compounds ( $^{19}\text{F}$ - <b>3.7</b> + $^{19}\text{F}$ -fluoride) vs. time. Data were fit to a first order reaction, and the half-life of the corresponding $^{19}\text{F}$ - <b>3.7</b> was calculated to be 3800 min. ....	43
<b>Figure 3.3</b> Linear correlation between the logarithm of hydrolysis rate constant of organotrifluoroborates and the pKa of the corresponding carboxylic acid.....	45
<b>Figure 3.4</b> (top): $^{19}\text{F}$ -NMR kinetic analysis of the defluoridation from the $^{19}\text{F}$ -organotrifluoroborate ( $^{19}\text{F}$ -Fluoride: -121 ppm relative to $\text{CFCl}_3$ ; $^{19}\text{F}$ -organotrifluoroborate: -139 ppm relative to $\text{CFCl}_3$ ). <b>Figure 3.4</b> (bottom): Plot of relative $^{19}\text{F}$ -NMR integration of the organotrifluoroborate as a function of all compounds ( $^{19}\text{F}$ -organotrifluoroborate + $^{19}\text{F}$ -fluoride) vs. time. ....	53
<b>Figure 3.5</b> (top): $^{19}\text{F}$ -NMR kinetic analysis of the defluoridation from the $^{19}\text{F}$ -organotrifluoroborate ( $^{19}\text{F}$ -Fluoride: -121 ppm relative to $\text{CFCl}_3$ ; $^{19}\text{F}$ -organotrifluoroborate: -141 ppm relative to $\text{CFCl}_3$ ). <b>Figure 3.5</b> (bottom): Plot of relative $^{19}\text{F}$ -NMR integration of the organotrifluoroborate as a function of all compounds ( $^{19}\text{F}$ -organotrifluoroborate + $^{19}\text{F}$ -fluoride) vs. time. ....	54
<b>Figure 3.6</b> (top): $^{19}\text{F}$ -NMR kinetic analysis of the defluoridation from the $^{19}\text{F}$ -organotrifluoroborate ( $^{19}\text{F}$ -Fluoride: -121 ppm relative to $\text{CFCl}_3$ ; $^{19}\text{F}$ -organotrifluoroborate: -145 ppm relative to $\text{CFCl}_3$ ). <b>Figure 3.6</b> (bottom): Plot of relative $^{19}\text{F}$ -NMR integration of the organotrifluoroborate as a function of all compounds ( $^{19}\text{F}$ -organotrifluoroborate + $^{19}\text{F}$ -fluoride) vs. time. ....	55
<b>Figure 3.7</b> (top): $^{19}\text{F}$ -NMR kinetic analysis of the defluoridation from the $^{19}\text{F}$ -organotrifluoroborate ( $^{19}\text{F}$ -Fluoride: -121 ppm relative to $\text{CFCl}_3$ ; $^{19}\text{F}$ -	

organotrifluoroborate: -136 ppm relative to $\text{CFCl}_3$ ). <b>Figure 3.7</b> (bottom): Plot of relative $^{19}\text{F}$ -NMR integration of the organotrifluoroborate as a function of all compounds ( $^{19}\text{F}$ -organotrifluoroborate + $^{19}\text{F}$ -fluoride) vs. time. ....	56
<b>Figure 3.8</b> (top): $^{19}\text{F}$ -NMR kinetic analysis of the defluoridation from the $^{19}\text{F}$ -organotrifluoroborate ( $^{19}\text{F}$ -Fluoride: -121 ppm relative to $\text{CFCl}_3$ ; $^{19}\text{F}$ -organotrifluoroborate: -139 ppm relative to $\text{CFCl}_3$ ). <b>Figure 3.8</b> (bottom): Plot of relative $^{19}\text{F}$ -NMR integration of the organotrifluoroborate as a function of all compounds ( $^{19}\text{F}$ -organotrifluoroborate + $^{19}\text{F}$ -fluoride) vs. time. ....	57
<b>Figure 3.9</b> (top): $^{19}\text{F}$ -NMR kinetic analysis of the defluoridation from the $^{19}\text{F}$ -organotrifluoroborate ( $^{19}\text{F}$ -Fluoride: -121 ppm relative to $\text{CFCl}_3$ ; $^{19}\text{F}$ -organotrifluoroborate: -149 ppm relative to $\text{CFCl}_3$ ). <b>Figure 3.9</b> (bottom): Plot of relative $^{19}\text{F}$ -NMR integration of the organotrifluoroborate as a function of all compounds ( $^{19}\text{F}$ -organotrifluoroborate + $^{19}\text{F}$ -fluoride) vs. time. ....	58
<b>Figure 3.10</b> (top): $^{19}\text{F}$ -NMR kinetic analysis of the defluoridation from the $^{19}\text{F}$ -organotrifluoroborate ( $^{19}\text{F}$ -Fluoride: -121 ppm relative to $\text{CFCl}_3$ ; $^{19}\text{F}$ -organotrifluoroborate: -143 ppm relative to $\text{CFCl}_3$ ). <b>Figure 3.10</b> (bottom): Plot of relative $^{19}\text{F}$ -NMR integration of the organotrifluoroborate as a function of all compounds ( $^{19}\text{F}$ -organotrifluoroborate + $^{19}\text{F}$ -fluoride) vs. time. ....	59
<b>Figure 3.11</b> (top): $^{19}\text{F}$ -NMR kinetic analysis of the defluoridation from the $^{19}\text{F}$ -organotrifluoroborate ( $^{19}\text{F}$ -Fluoride: -121 ppm relative to $\text{CFCl}_3$ ; $^{19}\text{F}$ -organotrifluoroborate: -144 ppm relative to $\text{CFCl}_3$ ). <b>Figure 3.11</b> (bottom): Plot of relative $^{19}\text{F}$ -NMR integration of the organotrifluoroborate as a function of all compounds ( $^{19}\text{F}$ -organotrifluoroborate + $^{19}\text{F}$ -fluoride) vs. time. ....	60
<b>Figure 3.12</b> (top): $^{19}\text{F}$ -NMR kinetic analysis of the defluoridation from the $^{19}\text{F}$ -organotrifluoroborate ( $^{19}\text{F}$ -Fluoride: -121 ppm relative to $\text{CFCl}_3$ ; $^{19}\text{F}$ -organotrifluoroborate: -138 ppm relative to $\text{CFCl}_3$ ). <b>Figure 3.12</b> (bottom): Plot of	

relative  $^{19}\text{F}$ -NMR integration of the organotrifluoroborate as a function of all compounds ( $^{19}\text{F}$ -organotrifluoroborate +  $^{19}\text{F}$ -fluoride) vs. time. .... 61

**Figure 3.13** (top):  $^{19}\text{F}$ -NMR kinetic analysis of the defluoridation from the  $^{19}\text{F}$ -organotrifluoroborate ( $^{19}\text{F}$ -Fluoride: -121 ppm relative to  $\text{CFCl}_3$ ;  $^{19}\text{F}$ -organotrifluoroborate: -147 ppm relative to  $\text{CFCl}_3$ ). **Figure 3.13** (bottom): Plot of relative  $^{19}\text{F}$ -NMR integration of the organotrifluoroborate as a function of all compounds ( $^{19}\text{F}$ -organotrifluoroborate +  $^{19}\text{F}$ -fluoride) vs. time. .... 62

**Figure 3.14** (top):  $^{19}\text{F}$ -NMR kinetic analysis of the defluoridation from the  $^{19}\text{F}$ -organotrifluoroborate ( $^{19}\text{F}$ -Fluoride: -121 ppm relative to  $\text{CFCl}_3$ ;  $^{19}\text{F}$ -organotrifluoroborate: -139 ppm relative to  $\text{CFCl}_3$ ). **Figure 3.14** (bottom): Plot of relative  $^{19}\text{F}$ -NMR integration of the organotrifluoroborate as a function of all compounds ( $^{19}\text{F}$ -organotrifluoroborate +  $^{19}\text{F}$ -fluoride) vs. time. .... 63

**Figure 3.16** (top):  $^{19}\text{F}$ -NMR kinetic analysis of the defluoridation from the  $^{19}\text{F}$ -organotrifluoroborate ( $^{19}\text{F}$ -Fluoride: -121 ppm relative to  $\text{CFCl}_3$ ;  $^{19}\text{F}$ -organotrifluoroborate: -138 ppm relative to  $\text{CFCl}_3$ ). **Figure 3.16** (bottom): Plot of relative  $^{19}\text{F}$ -NMR integration of the organotrifluoroborate as a function of all compounds ( $^{19}\text{F}$ -organotrifluoroborate +  $^{19}\text{F}$ -fluoride) vs. time. .... 65

**Figure 4.1** TLC analysis of the fluoridation of arylborates. The starting material is less polar than the corresponding product; subsequently the starting material runs faster and can be separated from the product. Based on the fluorescence, the yield of each fluoridation reaction can be estimated semiquantitatively. .... 74

**Figure 4.2** TLC-autoradiograph, right – digital photograph, lanes 1 and 2 are from crude reaction-1 (NCA) before or after click reaction, lanes 3 and 4 are from reaction-2 (near NCA) before or after click reaction respectively; “m” refers to marker spots to correlate fluorescence with autoradiographic density. .... 77

**Figure 4.3** HPLC traces of crude  $^{18}\text{F}$ -labeled **4.16** from rxn-1 (top) and rxn-2 (bottom). The  $^{18}\text{F}$ -labeled **4.16** is indicated by red arrow. The left figures are radioactive

HPLC trace with unit of mV and the right figures are fluorescent HPLC trace at 568 nm with unit of mAU.....	78
<b>Figure 4.4</b> HPLC traces of HPLC purified <sup>18</sup> F-labeled <b>4.16</b> from rxn-1 (top) and rxn-2 (bottom). The left figures are radioactive HPLC trace with unit of mV and the right figures are fluorescent HPLC trace at 568 nm with unit of mAU. ....	79
<b>Figure 4.5:</b> Chemical structure of the fluorescent chemodosimeter. ....	82
<b>Figure 4.6</b> Fitted linear standard curve with 500 nM, 250 nM, 125 nM, 62.5 nM, 31.3 nM, 15.6 nM, 7.8 nM, 3.9 nM, and 2.0 nM of <b>4.16</b> . The blue dots indicate the values obtained from HPLC integration while the red square and green triangle show HPLC absorbance of the <b>4.16</b> peak obtained in rxn-1 and rxn-2, respectively. ....	84
<b>Figure 4.9</b> Radioactive HPLC trace of purified <sup>18</sup> F-labeled <b>4.15</b> in rxn-1.....	95
<b>Figure 5.1</b> <sup>18</sup> F- <sup>19</sup> F isotope exchange with ArBF <sub>3</sub> <sup>-</sup> .....	99
<b>Figure 5.2</b> Synthesis route of Rhodamine-ArBF <sub>3</sub> <sup>-</sup> ( <b>5.1</b> ) and RGD-ArBF <sub>3</sub> <sup>-</sup> ( <b>5.2</b> ). ....	100
<b>Figure 5.3</b> (top): Radioactive HPLC trace of <sup>18</sup> F- <sup>19</sup> F IEX of <b>5.1</b> . Two major peaks were detected, the first peak was <sup>18</sup> F-fluoride, and the second peak was the desired <sup>18</sup> F-labeled product. <b>Figure 5.3</b> (bottom): UV-Vis HPLC trace of <sup>18</sup> F- <sup>19</sup> F IEX of <b>5.1</b> . The first peak was the fluorescent peak of product, and the second peak indicated the corresponding Rhodamine-ArB(OH) <sub>2</sub> , which was the major byproduct of <sup>18</sup> F- <sup>19</sup> F IEX and could be removed by HPLC purification.....	101
<b>Figure 5.4</b> (top): Radioactive HPLC trace of <sup>18</sup> F- <sup>19</sup> F IEX of <b>5.2</b> . Two major peaks were detected, the first peak was <sup>18</sup> F-fluoride, and the second peak was the desired <sup>18</sup> F-labeled product. <b>Figure 5.3</b> (bottom): UV-Vis HPLC trace of <sup>18</sup> F- <sup>19</sup> F IEX of <b>5.2</b> . The first peak was likely DMF, while the second, very broad peak came from pyridazine buffer. The third one was the UV peak of product, and the fourth peak was the corresponding RGD-ArB(OH) <sub>2</sub> , which was the major byproduct from <sup>18</sup> F- <sup>19</sup> F IEX and could be removed by HPLC purification.....	103

- Figure 5.5** Fitted linear standard curve with HPLC injection of 200 pmol, 400 pmol, 800 pmol, 1500 pmol and 3000 pmol  $^{19}\text{F}$ -**5.2**. The black crosses indicate the values obtained from HPLC integration while the blue marks show HPLC absorbance of the **5.2** peak obtained from each radiolabeling reaction. .... 104
- Figure 5.6** *In vivo* PET/CT imaging of  $^{18}\text{F}$ -**5.2** in unblocked mouse (left three images); blocked mouse (right three images). The yellow arrows indicate the location of the tumor. For each data set, from left to right the image is transverse section, coronal section and sagittal section, respectively. .... 106
- Figure 5.7** Biodistribution of  $^{18}\text{F}$ -**5.2** (n = 3): for each data set: red bars are unblocked and black bars are pre-blocked with 100 nmol  $^{19}\text{F}$ -RGD- $\text{ArBF}_3^-$ , each mouse was injected with 100  $\mu\text{Ci}$   $^{18}\text{F}$ -**5.2** at 8 Ci/ $\mu\text{mol}$ , p-value = 0.07 for the tumor (unblocked vs. blocked), p-value = 0.1 for the muscle (unblocked vs. blocked). .... 107
- Figure 5.8** ESI-MS of HPLC purified **5.2**. .... 113
- Figure 5.9** HPLC analysis of the additional  $^{18}\text{F}$ - $^{19}\text{F}$  IEX of **5.2**. **Left:** Labeling with 50 nmol  $^{19}\text{F}$ -**5.2** and 891 mCi NCA  $^{18}\text{F}$ -fluoride: Top: crude radiotracer; Bottom: UV-Vis trace at 229 nm with the units of mAU. **Right:** Labeling with 50 nmol  $^{19}\text{F}$ -**5.2** and 1027 mCi NCA  $^{18}\text{F}$ -fluoride: Left: crude radiotracer; right: UV-Vis trace at 229 nm with the units of mAU. .... 115
- Figure 6.2** (left): Radioactive (top) and fluorescent (bottom) trace of HPLC purification of crude Rhodamine- $\text{ArBF}_3^-$ . Peaks of Rhodamine- $\text{ArBF}_3^-$  and Rhodamine- $\text{ArB}(\text{OH})_2$  are indicated, respectively. **Figure 6.2** (right): Radioactive (top) and fluorescent (bottom) HPLC trace of reinjection of sep-pak purified Rhodamine- $\text{AMBF}_3$ . Peaks of Rhodamine- $\text{AMBF}_3$  is indicated, and Rhodamine- $\text{AMB}(\text{OH})_2$  is almost undetectable. .... 122
- Figure 6.3** (left): Radioactive HPLC trace following mice plasma incubation of  $^{18}\text{F}$ -radiolabeled **6.7**. The incubation time is 0, 80 and 150 min, respectively. **Figure 6.3** (right): Biodistribution of  $^{18}\text{F}$ -labeled agents in healthy nude mice by small-animal PET. The representative 3D PET/CT images were shown at the time point of 10

min, 30 min and 60 min after being injected with the newly designed Rhodamine- <sup>18</sup> F-AMBF <sub>3</sub> ( <b>6.7</b> ).....	124
<b>Figure 6.5</b> Chemical structure of B9858-AMBF <sub>3</sub> .....	125
<b>Figure 6.6</b> (Left): B9858- <sup>18</sup> F-AMBF <sub>3</sub> images (1 h post-injection) of NODSCID/IL2RKO mouse bearing B1R-positive (red arrow) and B1R-negative (white arrow) tumour. <b>Figure 6.6</b> (right): Biodistribution of B9858- <sup>18</sup> F-BF <sub>3</sub> at 60 mins post injection after injection in tumour-bearing mice (n=4).....	126
<b>Figure 6.7</b> Chemical structures of <b>6.8</b> , <b>6.9</b> and <b>6.10</b> . ....	127
<b>Figure 6.8</b> PET/CT images (20 min post-injection) of mouse bearing HT-29 tumour (white arrow) with <sup>18</sup> F-labeled <b>6.8</b> . The left image is the pure PET image, and the right image is the hybrid PET/CT image. ....	128
<b>Figure 6.9</b> MALDI spectrum of B9858-AMBF <sub>3</sub> . ....	131
<b>Figure 6.10</b> <sup>1</sup> H-NMR (CD <sub>3</sub> OD, 25 °C) spectrum of compound <b>6.6</b> . ....	135
<b>Scheme 7.1</b> Synthetic route of TATE- <sup>18</sup> F-AMBF <sub>3</sub> .....	143
<b>Figure 7.1</b> (top): HPLC UV-trace at 277 nm of Sep-Pak purified TATE- <sup>18</sup> F-AMBF <sub>3</sub> ; (bottom): HPLC radioactive trace of Sep-Pak purified TATE- <sup>18</sup> F-AMBF <sub>3</sub> .....	144
<b>Figure 7.2</b> Measurement of the inhibition constant (K <sub>i</sub> ) of TATE-AMBF <sub>3</sub> . Here is a representative competitive binding assay curve by using human sstr2 receptors expressed on CHO membranes. The constant (K <sub>i</sub> ) of TATE-AMBF <sub>3</sub> was measured to be 0.13±0.03 nM. Meanwhile the binding affinity of TATE-DOTA-Ga was 0.7±0.2nM at the identical condition. ....	145
<b>Figure 7.3</b> <i>In vivo</i> imaging of TATE- <sup>18</sup> F-AMBF <sub>3</sub> in the nude mice with AR42J tumors. The top images are the pure PET images and the bottom images are the hybrid PET/CT images. The radioactivity specifically accumulated in the AR42J tumor and was successfully blocked in the presence of a competitor. The excretion is	

predominantly through the urinary system with insignificant kidney retention, and the bone uptake is undetectable and there is minimal background activity (t = tumour; g = gallbladder; k = kidney; b = bladder).....	146
<b>Figure 7.4</b> Time activity curves (TAC) of tumors and other important tissues. ....	147
<b>Figure 7.5</b> <i>In vivo</i> biodistribution data of TATE- <sup>18</sup> F-AMBF <sub>3</sub> at 1 hour post injection following animal sacrifice.....	148
<b>Figure 7.6</b> The radioactive HPLC trace following mice plasma incubation of TATE- <sup>18</sup> F-AMBF <sub>3</sub> . The incubation time is 0, 80 and 150 min, respectively.....	151
<b>Figure 7.8</b> The HPLC traces of the reinjection of the sep-pak purified TATE-BF <sub>3</sub> . The left figures are the radioactive HPLC trace, and the right figures are the corresponding UV-Vis HPLC trace at 277 nm. ....	156
<b>Figure 7.7</b> Standard curve with 200 pmol (16.5 mAU), 400 pmol (34.1 mAU), 800 pmol (68.5 mAU), 1500 (125.4 mAU), 2500 pmol (217 mAU) and 4000 pmol (338 mAU) TATE-BF <sub>3</sub> .....	158
<b>Figure 7.8</b> Fitted linear standard curve, the blue marks are the integrations of the HPLC injection of TATE- <sup>19</sup> F-AMBF <sub>3</sub> . The yellow marks show HPLC UV absorbance of the TATE- <sup>18</sup> F-AmBF <sub>3</sub> peak during radiolabelling 1~3. ....	159
<b>Figure 8.1</b> <b>A)</b> <sup>18</sup> F-labeled <b>8.6</b> following elution from Sep-Pak in 50% ethanol-PBS in vial (275 mCi); <b>B)</b> QC radiotrace of 1.8 mCi of Sep-Pak eluted tracer; <b>C)</b> The corresponding UV-Vis trace at 568 nm of the same sample. ....	164
<b>Figure 8.2</b> The radioactive HPLC trace following mice plasma incubation at 37 °C of BisRGD-Rhodamine- <sup>18</sup> F-BF <sub>3</sub> at 0, 60 and 120 min, respectively. ....	165
<b>Figure 8.3</b> Fitted linear standard curve with HPLC injection of 35 pmol (8.5 mAU), 100 pmol (25.1 mAU), 350 pmol (86.1 mAU) , 400 pmol (101 mAU) and 1000 pmol (253 mAU) <sup>19</sup> F- <b>8.6</b> . The blue symbols indicate the values obtained from HPLC	

integration while the blue marks show HPLC absorbance of the **8.6** peak obtained from each radiolabeling reaction. .... 166

**Figure 8.4** Fluorescent microscopy of  $\alpha_v\beta_3$  integrin binding: **A**) negative control with HT29 cells (**8.6** at 960 nM); **B**) positive control with U87M cells. The red exterior is seen in U87M cells as expected. DAPI (blue) stains nuclei in both panels. Cells were washed briefly before plating..... 167

**Figure 8.5** PET-CT images: T (tumor), K (kidney), B (bladder), left mouse imaged with **8.6** at 3 Ci/ $\mu$ mol, right mouse imaged with **8.6** at 0.01 Ci/ $\mu$ mol (three-dimension rendering increases appearance of blocking); bottom right inset: pure CT image showing tumors..... 168

**Figure 8.6** *In vivo* PET/CT imaging of  $^{18}\text{F}$ -**8.6** in blocked mouse (left three images); unblocked mouse (right three images). The white arrows indicate the location of the tumor. For each data set, from left to right the image is transverse section, coronal section and sagittal section, respectively. .... 169

**Figure 8.7** (top): *Ex vivo* fluorescence in organs to which **8.6** clears: liver, kidney, and tumor; **A**: organs from mouse that received no tracer (control); **B**: organs from mouse injected with **8.6** at 3 Ci/ $\mu$ mol; **C**: organs from the mouse injected with **8.6** at 0.01 Ci/ $\mu$ mol. **Figure 8.7** (bottom): Limitation of detection (LOD) measurement. The LOD of our optic scanner is  $\sim 20$  pmol. .... 171

**Figure 8.8** MALDI-TOF analysis of unlabeled **8.6**: three peaks were seen at 2421.15, 2422.10 and 2423.16..... 177

**Figure 8.9** Pure PET image: left mouse shows minimal bone uptake in a pure-PET image (no CT overlay). While small amounts of uptake are seen in the knee joints and lower spine and skull, these are completely blocked in the right mouse suggesting that bone uptake may reflect presence of the integrin receptor in marrow and/or bone..... 179

**Figure 8.10** TACs (Time Activity Curves) from each of the imaged mice (n = 3): B = blocked, N = non-blocked..... 180

**Figure 8.11** *In vivo* biodistribution analysis (n = 3) for all mice from which organs were collected and analyzed %ID/g at 120 min. Error bars are shown however blocking is not expected because typically to achieve statistically significant blocking ratios, >100  $\mu\text{g}$  per mouse must be used. Instead we wished to show that reasonable tumor uptake values can be achieved at specific activities as low as 0.01 Ci/ $\mu\text{mol}$  (~20  $\mu\text{g}$ ) which is not enough to achieve blocking..... 181

## List of schemes

<i>Scheme 2.1</i> Synthetic routes of the proposed organotrifluoroborates as candidates that would enable more facile bioconjugation. ....	19
<i>Scheme 2.2</i> Synthesis route of fluorescent organotrifluoroborates .....	23
<i>Scheme 2.3</i> Synthesis route of bioconjugated organotrifluoroborates. ....	25
<i>Scheme 4.1</i> Synthetic route of fluorescent $\text{ArBF}_3^-$ ( <b>4.7</b> ). ....	69
<i>Scheme 4.2</i> Synthetic route of fluorescent $\text{PyBF}_3^-$ ( <b>4.13</b> ). ....	70
<i>Scheme 4.3</i> Radiosynthesis of $^{18}\text{F}$ -Rhodamine- $\text{ArBF}_3^-$ .....	76
<i>Scheme 8.1</i> Seamless bench-to-bed translation.....	161
<i>Scheme 8.2</i> Synthesis route of <b>8.6</b> .....	163

## List of abbreviations and symbols

%ID/g	percentage of injected radioactive dose per gram of tissue
°C	degrees Celsius
~	approximate
2D	two dimensional
3D	three dimensional
AcOH	acetic acid
Anal.	analytical
ANOVA	analysis of variance
atm	atmosphere
biomolecule	vector, biovector, targeting vector, (e.g. antibody, peptide)
Bn	benzyl
Boc <sub>2</sub> O	di- <i>tert</i> -butyl-dicarbonate
br	broad (NMR), e.g. br s (broad singlet)
calcd.	Calculated
Ci	Curie
cm <sup>-1</sup>	wavenumber
CT	computed tomography
d	day(s) or doublet (NMR)
DCC	N,N'-Dicyclohexylcarbodiimide
DCM	dichloromethane
DFT	density functional theory
DMF	dimethylformamide
DMSO	dimethylsulfoxide
DOTA	1,4,7,10-tetraazacyclododecane- <i>N,N',N'',N'''</i> -tetraacetic acid
EDC	1-Ethyl-3-(3-dimethylaminopropyl)carbodiimide
EDTA	ethylenediaminetetraacetic acid
equiv.	equivalent(s)
ESI-MS	electrospray ionization mass spectrometry
EtOAc	ethyl acetate
EtOH	ethanol
eV	electron volt
FDA	Food and Drug Administration (USA)
FDG	<sup>18</sup> F-2-deoxy-2-fluoro-D-glucose
g	gram
h	hour(s)
HPLC	high performance liquid chromatography
Hz	hertz (s <sup>-1</sup> )
ID	injection dose
<i>J</i>	coupling constant (NMR)

k	kilo
L	litre or ligand
LC-MS	liquid chromatography-mass spectrometry
m	milli- or medium or multiplet
M	molar (moles/litre) or mega
<i>m/z</i>	mass per unit charge
MALDI-TOF	matrix assisted laser desorption/ionization-time of flight
MeCN	acetonitrile
MeOH	methanol
min	minute (s)
mol	mole
MRI	magnetic resonance imaging
MS	mass spectrometry
n	nano ( $10^{-9}$ ) or number of unit
NBS	<i>N</i> -bromosuccinimide
NHS	<i>N</i> -hydroxysuccinimide
NIR	near infrared
nM	nanomolar ( $10^{-9}$ M)
NMR	nuclear magnetic resonance
NOTA	1,4,7-triazacyclononane-1,4,7-triacetic acid
p.i.	post injection
PBS	phosphate buffered saline
Pd/C	palladium on carbon (10% by weight)
PET	positron emission tomography
pH	$-\log[\text{H}_3\text{O}^+]$
pM	picomolar ( $10^{-12}$ M)
ppm	parts per million
q	quartet (NMR)
r.t.	room temperature
RCY	radiochemical yield
$R_f$	retention factor
RGD	Arginine-Glycine-Aspartic Acid-peptide
$R_t$	retention time
s	singlet (NMR)
SA	specific activity
SPECT	single photon emission computed tomography
t	triplet (NMR) or time
<i>t</i> -Boc	<i>tert</i> -butoxycarbonyl
$t_{1/2}$	half-life
TATE	[Tyr <sup>3</sup> , Thr <sup>8</sup> ]-octreotide
<i>t</i> BuOH	<i>tert</i> -butanol
TFA	trifluoroacetic acid

THF	tetrahydrofuran
TLC	thin layer chromatography
$t_R$	retention time (HPLC)
UV	ultraviolet
V	volt
$\beta^-$	beta particle
$\beta^+$	positron
$\delta$	delta or chemical shift in parts per million (NMR)
$\mu$	micro ( $10^{-6}$ )
$\mu\text{M}$	micromolar ( $10^{-6}$ M)
$\gamma$	gamma ray

## **Acknowledgement**

First of all, I must thank my supervisor Dr. Perrin for his endless trust and support to my PhD study. He is the one who actually guided me into the world of science and the world of western society. To be honest, I am not even sure my languages would be good enough to express my extreme gratefulness. His passion about great science is always the original driving force of my project; His critical and straight comments have kept rising the standard of my scientific works; His great generosity has given me the opportunities for attending several international conferences, where I met a lot of friends and collaborators; And his patience has kept tolerating my unthoughtful mistakes and immature behaviors through my graduate life. If personality is an unbroken series of successful gestures being a great mentor, then I believe there is something gorgeous about Dr. Perrin.

I also want to give my heartfelt thanks to my collaborators Dr. Kuo-Shyan Lin and Dr. François Bénard for their extraordinarily generous help. Without them, my research would never go this far. In addition, I sincerely thank the lab members in BC Cancer Agency for friendships and helping me since I worked in BC Cancer Agency two years ago: Dr. Jinhe Pan, Dr. Zhengxing Zhang, Drs. Silvia Jenni, Maral Pourghiasian, Joseph Lau, Gemma Dias, Guillaume Amouroux, Jennifer Greene, Nadine Colpo, Julius Klug, Guillaume Langlois, Milan Vuckovic, Navjit Hundal and Wade English.

Thank-you to UBC faculty members for providing scientific advices and discussion over the years: Prof. Marco Ciufolini, Prof. Hongbin Li, Prof. David Chen, and Prof. Russ Algar. Thank-you to my defense examiners for their very helpful suggestions: Dr. Hank Kung, Dr. Chris Orvig, Dr. Michael Fryzuk and Dr. Michel Roberge. In particular, I would like to thank Prof. Chris Orvig for his help on my thesis writing. I feel that Prof. Orvig deserves credit for giving the instruction with the utmost professionalism, patience, and care.

Thank-you to my collaborators in TRIUMF for introducing me to the world of radiochemistry: Dr. Paul Schaffer, Dr. Thomas Ruth, Dr. Mike Adam, Dr. Hua Yang, Dr. Qing Miao and Christine Takhar.

Thank-you to my talented undergraduate students for inputting essential contributions to my PhD study: Jag Deep, M. Alex Radtke, Christalle Chow, Dan Cojocar and Daniel Chao.

Thank-you to Perrin group members for sharing the happiness and the pain, for struggling together for great science, and also for the deep friendship: Yajun Wang, Erkai Liu, Wenbo Liu, Jerome Lozada, Emily Miller, Antoine Blanc, Abid Hasan, Kaveh Matinkhoo, Dr. Eric Largy, Dr. Marleen Renders, Dr. Christine Dyrager, Dr. David Dietrich, Dr. Curtis Lam, Dr. Ying Li and Dr. Liang Zhao.

Thank-you to UBC staffs who have been crucial to solve my problems: Sheri Harbour, Kelly Turner and Marjan Molouk-Zadeh in main office; Dr. Paul Xia and Maria Ezhova in the NMR labs; Dr. Yun Ling, Marshall Lapawa, Derek Smith, and Marco Yeung in the MS labs; Dr. Elena Polishchuk in Biological Service Laboratory; and Dr. Emily Seo in SIF.

Thank-you to my best friends who are still somehow idealistic as me, and who are still sharing the dream with me: Ru Li in University of British Columbia, Lingxing Meng in Shanghai Institute of Organic Chemistry, Kuo Liao in Princeton University, Peng Zheng in Harvard University, Wei Sun in Tianjin University and Xiaojian Jiang in Yancheng

At last, utmost thank-you to my family and partner for their boundless love, trust and support through the last four years.

## **Dedication**

To my family, partner, friends and mentors for their trust and endless support.

I am also deeply indebted to the philosophy of I Ching for helping me to maintain a peaceful mind and balanced life.

# Chapter 1: Introduction

## 1.1 Molecular imaging

Molecular imaging can allow quantitative, noninvasive, and reproducible assessments of biological processes at the cellular and subcellular level in living organisms.<sup>1-4</sup> Compared to conventional techniques such as X-ray, CT, and ultrasound, molecular imaging has the advantage of supplying biological information in an intact living subject with dynamic spatial-temporal resolution.<sup>5,6</sup> Based on different reporter modalities, molecular imaging can be divided into morphological/anatomical imaging and molecular imaging technologies. Computed tomography (CT), magnetic resonance imaging (MRI), and ultrasonography are the main morphological or anatomical imaging techniques. While these three possess many advantages including high spatial resolution, they all suffer the disadvantage of not being able to detect diseases based on molecular phenomena, at least not until such phenomena lead to gross structural changes in the tissue.<sup>7</sup> In contrast, molecular imaging technologies, which consist of optical imaging, positron emission tomography (PET),<sup>8</sup> and single photon emission computed tomography (SPECT) (with radiotracers injected at nanomolar blood concentrations), offer the potential to detect molecular and cellular changes of diseases. Various imaging modalities are summarized below.

**Optical imaging** generally refers to fluorescence imaging and bioluminescence imaging, which in turn rely on the detection of visual light that is emitted by the imaging probes, that is generated through incident excitation or reaction with chemical cofactors.<sup>9-12</sup> A significant attraction of optical imaging is the lack of ionizing radiation.<sup>13</sup> In addition, optical imaging may benefit from comparatively low instrumentation costs, high sensitivity, and general availability. However, both fluorescence imaging and bioluminescence imaging have the problem of poor tissue penetration, which is due to the high degree of light scattering and absorption/quenching by overlying tissues.<sup>14</sup> In addition to the difficulty of deep tissue detection, autofluorescence from normal tissues also increases background signals and hence diminishes the contrast of optical images.<sup>15</sup> New approaches to circumvent these issues typically involve developing near-IR

fluorophores. Yet while these may correct some limitations, new issues are introduced including relatively low quantum yields,<sup>16</sup> chemical reaction of the fluorophore with biological reductants and reactive oxygen species, as well as the inability to visualize emission with the human eye, which can be important for surgery-related applications.

**Ultrasound images** are achieved by recording the reflection (echo) of ultrasound waves from tissues. The ultrasound pulse is produced by using an ultrasound transducer, and the subsequent waves then reflect and echo off parts of the tissue. Ultrasonography is effective for imaging soft tissues in the body and is widely used in medicine. It is relatively lower in cost,<sup>15</sup> free of ionization radiation, and portable. Additionally, ultrasonography provides images in real-time without an acquisition/processing delay. Nevertheless, a diagnosis based on ultrasonography relies on skilled operators and also has the inherent difficulty of providing images behind bone.

**Computed tomography (CT)** provides high-resolution images based on the differentiable absorption of X-rays. The advantage of a CT scan is its high spatial resolution, especially for diagnosing the disease in bone. Nevertheless, CT is limited in providing useful information regarding pathologies localized in soft tissues because the density of tissues mainly determines the X-ray absorption and within soft tissue, density differences can be insignificant.<sup>17,18</sup> Regardless of its poor soft-tissue contrast and lack of specific-targeted probe, CT is broadly used in medicine, especially when combined with other imaging technologies. It is noted that CT is not without significant radiation doses to the patient.<sup>19</sup>

**Magnetic resonance imaging (MRI)** provides great details for the internal body structures by measuring the rates of relaxation of hydrogen atoms in high magnetic fields, particularly in terms of tissue-specific water content.<sup>20-22</sup> MRI is free of ionizing radiation, and as such is considered to be safer compared to other radiological imaging techniques. However, because of the nature of strong magnetic fields, MRI is not applicable to patients who have pacemakers or metal implants.<sup>20</sup> In order to make MRI target-specific, relatively high doses of imaging agents are required.<sup>21</sup> While these are not

radioactive, their use may result in unwanted biological effects as they can bind physiological targets. Besides the concern of a magnetic field, MRI has several other drawbacks, namely, low sensitivity, long acquisition time, and limited contrast.<sup>23</sup>

**Single photon emission computed tomography (SPECT)** produces images by detecting gamma rays that were directly emitted by radionuclides.<sup>24</sup> The most well-known radionuclide for SPECT is <sup>99m</sup>Tc however several others are now used.<sup>25</sup> As the radionuclides used by SPECT typically have relatively long half-lives, this affords the added advantage of convenience for radiosynthesis and coordinated distribution to longer distances, most notably hospitals that cannot usually produce the radionuclides. Nevertheless, whereas a long half-life makes radiosynthesis more reproducible in terms of yields and specific activity, the same results in relatively higher radiation doses to the patient. For image acquisition, a scanner must specifically filter the gamma rays of certain energies.<sup>26-28</sup> Hence a collimator is installed between the cameras and patient, through which passes a small amount of gamma rays and subsequently reduces the sensitivity of SPECT. Moreover, to generate high quality SPECT images, a relatively high dose of radiotracer as well as long scanning time are usually administered, both of which result in a high radiation dose for the patient.<sup>25,29</sup>

**Positron emission tomography (PET)** is a fast-expanding non-invasive imaging technology that can quantitatively provide essential *in vivo* data for tracing the biochemical changes in body tissue.<sup>30,31</sup> The imaging is achieved by detecting the gamma rays of certain energy, which are generated from the annihilation of positrons that are emitted from a judiciously chosen PET-useful radionuclide.<sup>16</sup> This technology helps clinicians detect disease at an early stage and is particularly useful compared to computed tomography (CT) and magnetic resonance imaging (MRI) which are often not able to discern the evidence of the abnormality.<sup>32</sup> The unparalleled sensitivity of PET assists researchers in fundamental understanding of diseases, as well as in the design of new drugs and treatments within the fields of cardiology, oncology, neurology and inflammatory diseases. However, as with the other nuclear imaging technologies, patient radiation dose is a concern for PET. Furthermore, with the requirement of a high-priced

cyclotron to produce the PET radionuclides, PET imaging remains one of the most costly molecular imaging technologies.

As a summary, a brief comparison of the advantages and disadvantages of these imaging modalities is listed in **Table 1.1**.

**Table 1.1** Summary of imaging modalities.<sup>3,4,20-22,24,33</sup>

Modality	Sensitivity (M)	Spatial resolution (mm)	Temporal resolution	Penetration depth	Advantages	Disadvantages
Optical imaging	$10^{-9}$ - $10^{-17}$	2-5	sec to min	mm	High-throughput screening; High sensitivity	Limited clinical translation; Low depth penetration
Ultrasonography	-	0.05-0.5	sec to min	mm-cm	High spatial and temporal resolution; Low costs	Operator dependency; Targeted imaging limited to vascular compartment
CT	-	0.025-0.2	min	no limitation	High spatial resolution (bone/lung); Clinical translation	No target-specific imaging; Radiation; Poor soft-tissue contrast
MRI	$10^{-3}$ - $10^{-5}$	0.025-0.1	min	no limitation	High resolution and soft-tissue contrast	Costs; Imaging time
SPECT	$10^{-10}$ - $10^{-11}$	0.5-1.5	min	no limitation	Unlimited depth penetration	Radiation; Limited spatial resolution
PET	$10^{-11}$ - $10^{-12}$	3-7	sec to min	no limitation	High sensitivity with unlimited depth penetration	Radiation; Cost

## 1.2 PET imaging

PET, as mentioned in the previous section, provides images with both high spatial and temporal information of diseased tissues at high resolution by detecting the emission of positrons that emit from a PET-relevant nuclide that is typically affixed to a high affinity molecular ligand that is specific for a given pathology.<sup>30,31</sup> Once emitted, the positron travels a short distance through the electron cloud that makes up the tissue (as well as all matter), during which time it loses most of its energy and finally reacts with an electron to annihilate resulting in two photons of 511 keV (**Figure 1.1**). Those photons, following the laws of conservation of charge and momentum, are emitted simultaneously in opposite directions. The detector of the PET scanner detects these two photons without need for collimation and subsequently generates three-dimensional images based on the detection of these photons which can be correlated with the distribution of radioactivity in the tissue and which can ultimately be used to reconstruct an image.

A unique advantage of PET imaging is its high sensitivity.<sup>31</sup> The two high-energy gamma ray photons allow the PET scanner to generate quality images with the radiotracers injected at nanomolar blood concentrations. As previously described, the positron will travel through the tissue for a certain distance before annihilation; hence, the site of positron emission always originates from the site of detection. This distance is defined as positron range, which is directly related to the positron energy. In general, higher positron energy results in longer positron range, which results in lower spatial resolution. For this reason, to achieve a high resolution PET image, radionuclides of low positron energy are preferred.

### 1.3 Radionuclides for PET imaging

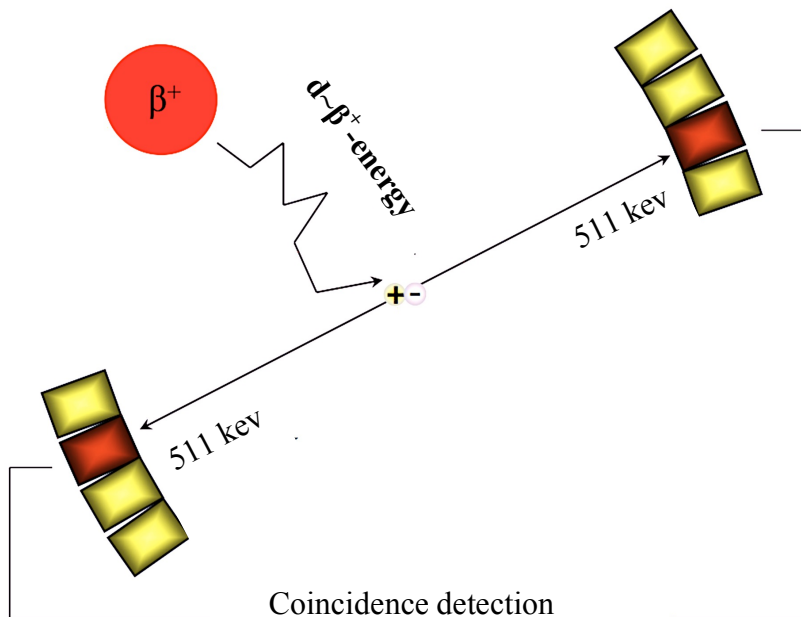


**Figure 1.1** An illustration of PET acquisition process.

Alongside the ever-expanding applications of PET imaging, numerous positron-emitting radioisotopes have been developed for use in nuclear medicine.<sup>34</sup> Some of the most frequently used radioisotopes are listed in **Table 1.2** with their radioactive properties.<sup>35,36</sup> In general, an effective PET imaging probe consists two essential parts: a functional targeting moiety and a radionuclide. In most cases, radiotracers share the same targeting moiety but will employ different radionuclides which results in significant differences in terms of biological evaluation i.e. tumor uptake, clearance rates, and contrast ratios. Therefore, it is crucial to choose an appropriate radionuclide for the acquisition of each PET image, in accordance with the following principles: a) a reasonable half-life that allows both of the preparation of radiotracers and the *in vivo* background clearance; b) low positron energy that affords high image resolution; c) acceptable radiation dosimetry to the patient; d) sufficient and on-demand production of radioisotopes;<sup>37</sup> e) a

reproducible and reliable labeling method to incorporate the said radionuclide into the bioligand with a satisfactory radiochemical yield. Meeting all of these specifications is a major undertaking for which there is no immediate or obvious solution and hence to do so requires the application of a multidisciplinary approach to nuclear medicine. My thesis represents efforts towards addressing some of these concerns.

**Table 1.2** Some positron-emitting radionuclides for PET imaging.<sup>2,34,38,39</sup>

Nuclide	Half-life (min)	Maximum Energy (MeV)	Mode of decay (%)	Theoretical specific activity (Ci/ $\mu$ mol)
<sup>18</sup> F	110	0.64	$\beta^+$ (97%)	1720
<sup>11</sup> C	20.3	0.97	$\beta^+$ (99%)	9280
<sup>13</sup> N	10	1.2	$\beta^+$ (100%)	19100
<sup>15</sup> O	2	1.9	$\beta^+$ (100%)	92800
<sup>76</sup> Br	972	4	$\beta^+$ (57%)	195
<sup>68</sup> Ga	68	2.14	$\beta^+$ (87.7%)	2766
<sup>64</sup> Cu	762	0.655	$\beta^+$ (41%)	245

Among the radionuclides listed in **Table 1.2**, Carbon-11 (<sup>11</sup>C) is one of the most widely used radioisotopes in hospitals. However, despite the prevalence of carbon in biological substances, <sup>11</sup>C-labeled agents have been used less frequently as of late, partly because the short half-life (20 minutes) inherent to <sup>11</sup>C requires very rapid syntheses to produce pure products with high specific activity.<sup>40-42</sup>

Recently Gallium-68 ( $^{68}\text{Ga}$ ) has been recognized as an attractive radioisotope for PET imaging. In addition to its moderate half-life and high positron yield, a significant advantage of  $^{68}\text{Ga}$  is its simple production from commercially available  $^{68}\text{Ge}$  generators.<sup>43</sup> In addition, some  $^{68}\text{Ga}$ -radiolabeled biomolecules demonstrate very promising *in vivo* performances and are currently in clinical trials as well as in the clinic in several institutions.<sup>23,44</sup> Nevertheless,  $^{68}\text{Ga}$ -PET imaging is not widely available due to limited availability of  $^{68}\text{Ga}$  and the current lack of FDA-approved  $^{68}\text{Ge}/^{68}\text{Ga}$  generators.

On the other hand,  $^{18}\text{F}$ -fluoride presents several attractive properties for imaging and is produced on a daily basis in large quantities in hundreds of cyclotrons based in hospitals or radiopharmacies worldwide. Yet the challenges of labeling peptides with  $^{18}\text{F}$ -fluoride are significant. Primarily, both the low chemical reactivity of  $^{18}\text{F}$ -fluoride in water and its relatively short half-life (109.8 min) are obstacles for  $^{18}\text{F}$ -labeling of peptides that are generally soluble only in water or aqueous co-solvents.<sup>45-47</sup> As a result, fluoride must be dried and reacted in dry solvents at high temperature, usually to radiolabel an intermediate radioprosthesis that is then conjugated to a peptide precursor. This necessitates the use of multistep reactions.<sup>48-52</sup> While multistep  $^{18}\text{F}$ -labeling reactions are now relatively commonplace, the comparatively short half-life of  $^{18}\text{F}$ -fluoride often impedes the application of multistep reactions in clinical use, particularly in terms of ensuring high specific activity  $> 1 \text{ Ci}/\mu\text{mol}$  in under 1 hour.

### 1.3 $^{18}\text{F}$ -based radiopharmaceutical designs

Besides the success of PET and increasing interests of  $^{18}\text{F}$ -radiochemistry, a kit-like, one-step  $^{18}\text{F}$ -labeling method, which can be broadly applied to small biomolecules to provide functional *in vivo* images has been a long-standing challenge. Most of the  $^{18}\text{F}$ -conjugations, either well established or newly developed, are relatively onerous and lengthy processes.<sup>53</sup> For instance, small compounds are typically radiolabeled in two or three steps, which could involve the radiosynthesis of the prosthetic groups and further conjugation or purification of the desired radiotracers. Furthermore, such a multi-step strategy also compromises the radiochemical yield of the synthesized imaging agent. To combat this problem, several publications have detailed the late stage radiofluorination

via  $^{18}\text{F}$ -trifluoromethylation or C- $^{18}\text{F}$  bond formation.<sup>54,55</sup> These various methodological developments are promising as they are able to radiolabel a bona-fide drug without altering the chemical structure.<sup>56-61</sup> However, these strategies still suffer from either low specific activity or lack of simple purification,<sup>62</sup> which would essentially slow down the progress of radiolabelling and thereby weaken the quality of the acquired PET image.<sup>63</sup> Previously, several new  $^{18}\text{F}$ -radioprosthesis such as  $^{18}\text{F}$ -SiFA or Al- $^{18}\text{F}$ -NOTA have been developed.<sup>51,64-73</sup> They can be  $^{18}\text{F}$ -radiolabelled in one step and then imaged with relative success.

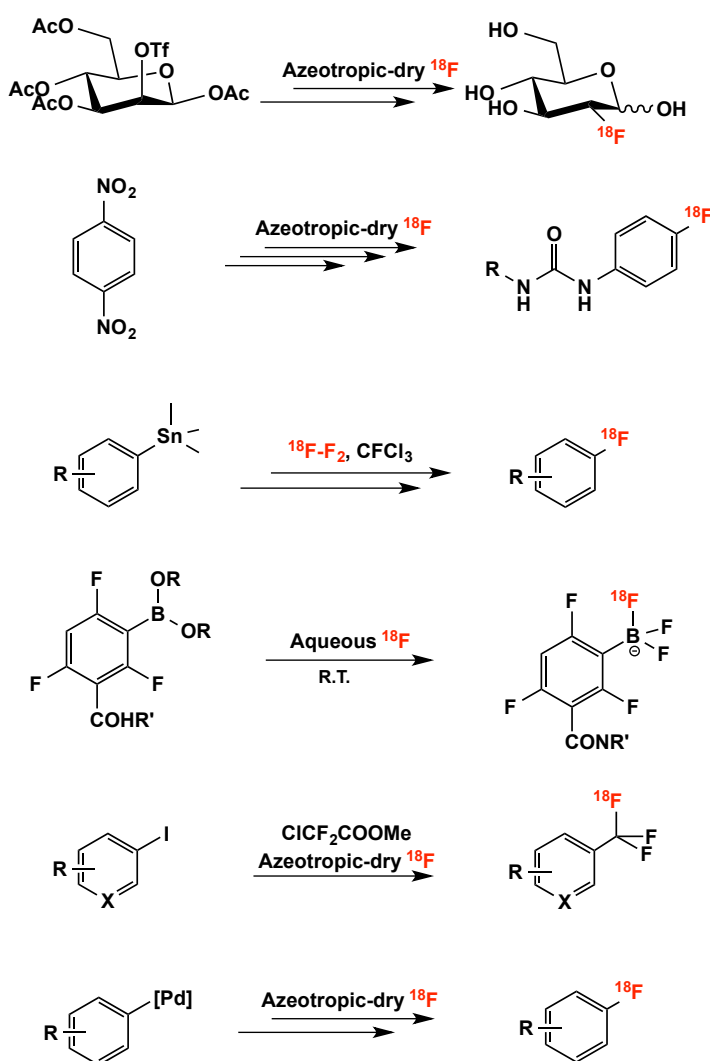


**Figure 1.2** Representative  $^{18}\text{F}$ -radiolabeling methods.<sup>54-61</sup>

## 1.4 Key-properties of $^{18}\text{F}$ -radioprosthethics

### 1.4.1 *In vivo* stability of $^{18}\text{F}$ -radioprosthethics

The *in vivo* stability of  $^{18}\text{F}$ -radioprosthethics is, of course, of paramount importance. The *in vivo* concentration of a PET tracer is sub-nanomolar; hence, an  $^{18}\text{F}$ -radiotracer of poor stability would irreversibly lose free  $^{18}\text{F}$ -fluoride during circulation. Calcium-rich bone is a well-known fluorophilic organ, and therefore free  $^{18}\text{F}$ -fluoride accumulates to a significant degree in the bone and results in high unspecific bone uptake. While such may be tolerated in the case of certain imaging agents and indeed has been seen with both new and standard  $^{18}\text{F}$ -labeling methods, ultimately such may prevent the detection of bone metastasis, which would ultimately contraindicate the use of solvolytically/metabolically unstable tracers. Furthermore, a PET radiotracer of poor bio-orthogonality might be metabolized in living subjects, and subsequently lose its *in vivo* targeting ability.

### 1.4.2 Specific activity

Specific activity, defined as  $\text{Ci}/\mu\text{mol}$ , represents a quantitative measurement of radiotracer quality.<sup>52</sup> Generally, high specific activity is thought to result in high contrast images that are needed for early detection.<sup>74-76</sup> The amount of radiotracer injected is generally constant for each patient ( $\sim 7$  mCi).<sup>77</sup> Although the amount may vary depending on clearance rates, it is generally determined by the maximal radiation dose allowable. High specific activity means that low chemical amounts of radiotracer will be injected. This means that low-abundance targets are unlikely to be saturated and therefore all binding events are linearly proportional to the amount of target present. This feature enables quantitative or at least semi-quantitative measurements of target concentration and therefore an assessment of tumor load. By contrast, at low specific activity, relatively high chemical amounts of tracer will be used and targets may be saturated. In this case, unbound tracer will give rise to a high background while unlabeled carrier, which may also bind, does not result in imaging signals. Therefore PET tracers of low specific activity generally exhibit poorer signal-to-noise ratios and lower image quality. For this reason, high specific activity can be very important for achieving high quality PET imaging. Moreover, high specific activity is particularly crucial for early cancer detection

where target concentration is low, <sup>78-85</sup> and based on FDA regulations to avoid pharmacological effects, the radiotracer concentration must be used at concentrations that ensure that the target is less than 10% saturated ( $0.1 \times K_d$ ) so that <10% target is bound.

### 1.4.3 Operational simplicity of <sup>18</sup>F-radiolabelling

Given the short half-life of <sup>18</sup>F, operational simplicity is another essential requisite to design broadly applicable <sup>18</sup>F-radioprosthesis.<sup>73,83,86-88</sup> Conventionally, <sup>18</sup>F-labelling of biomolecules can be a laborious and lengthy process, particularly given the short half-life (110 min) of <sup>18</sup>F.<sup>89-101</sup> Due to the poor aqueous nucleophilicity of <sup>18</sup>F-fluoride, the <sup>18</sup>F-radiosynthesis typically starts with a time-consuming step by azeotropically drying <sup>18</sup>F-fluoride with MeCN several times (2-6 times).<sup>55</sup> Another significant deficiency of current <sup>18</sup>F-labelling methods is the requirement of byproduct/precursor separation. In most cases, those separations are performed via HPLC purification, which may need at least 20 min. If all the aforementioned steps are removed from the radiosynthetic, the total synthesis time could be reduced, thereby increasing the radiochemical yield. In addition, the improved operational simplicity would also diminish the radio-dose for radiochemists, and allow the translation from manual synthesis into automated synthesis and microfluidic development.

## 1.5 Mini-review of B-<sup>18</sup>F labeling

In a radical departure from all other <sup>18</sup>F-labeling methods, in 2005 Ting and Perrin proposed to use boron to capture aqueous <sup>18</sup>F-fluoride in a single step thereby obviating many of the encumbrances typically encountered with <sup>18</sup>F-labeling.<sup>102-109</sup> They showed that <sup>18</sup>F-aryltrifluoroborates can be synthesized under mild aqueous conditions, conditions that are compatible for direct use with biomolecules (i.e. peptides), therefore making this type of moiety potentially interesting for usage in the development of <sup>18</sup>F-labeled radiotracers. In light of this, Perrin *et al.* hypothesized that hot fluoride (<sup>18</sup>F) could be captured by arylboronates to form <sup>18</sup>F-ArBF<sub>3</sub><sup>-</sup> compounds, which would be

potentially applicable for PET imaging. Moreover, compared to other labeling methods, radio-synthesis of an  $^{18}\text{F}$ -labeled  $\text{ArBF}_3^-$  exhibits the following advantages:

- (1) The radiolabelling condition is mild and aqueous, which is especially suitable for direct labeling of sensitive biomolecules;
- (2) One step radio-synthesis;
- (3) Specific activity of the  $^{18}\text{F}$ - $\text{ArBF}_3^-$  is triple that of the  $^{18}\text{F}$ -fluoride used for radio-synthesis.

Encouraged by these hypothetical advantages, Perrin and coworkers proposed the use of arylboronates in the context of radiolabeling. It was soon appreciated, however, that the  $^{18}\text{F}$ - $\text{ArBF}_3^-$  must spontaneously decompose under pH-neutral aqueous conditions and release free  $^{18}\text{F}$ -fluoride and arylboronic acid.<sup>86,110</sup> This solvolytic decomposition would almost surely be irreversible under conditions of high dilution that are characteristic of use in imaging, i.e. 1 nmol of tracer in 7 liters of blood. More generally, it is appreciated that all bond dissociation events, not just B-F bond dissociation, must always be characteristic of a radiotracer at high dilution. The simple reason is that at high dilution there can be no back reaction. Therefore, whereas the synthesis of a radiotracer must be dictated by both kinetic facility (high rates) and thermodynamic favorability (high yields), attributes for which conditions may be judiciously chosen or identified through screening, the regime for evaluating imaging utility is only dictated by the kinetic stability at physiological pH.

This conclusion led to an insightful secondary hypothesis that if kinetically stable  $\text{ArBF}_3^-$  compositions could be identified, and if these could be prepared relatively rapidly and in high yield, they might prove very useful for  $^{18}\text{F}$ -capture and thereby useful for PET imaging. When considering the stability of an aryltrifluoroborate to solvolytic defluoridation, Ting *et al.* developed a mechanistic hypothesis based on stereoelectronic considerations for the loss of fluoride from an  $\text{ArBF}_3^-$  that reflects pseudo-first order kinetics (shown below):

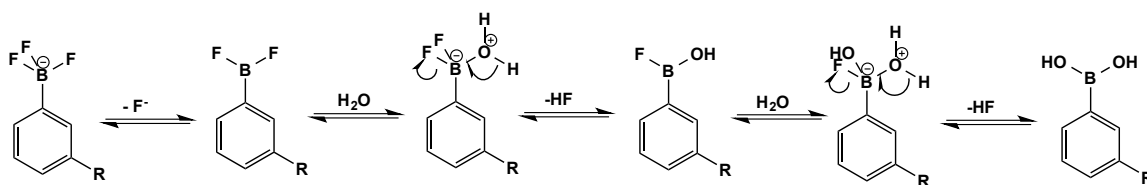


**Figure 1.3** Hypothetical mechanism for the hydrolysis of an  $\text{ArBF}_3^-$ .

Both steric encumbrance at the ortho-positions, and electronic character of all substituents can play roles in fluoride loss and judicious use of functional groups on the aryl ring can result in the design of  $\text{ArBF}_3^-$ s that are exceedingly stable to solvolysis. For PET imaging, as noted above, the kinetic stability of the tracer is essential for its development and utility.

To solve this problem, in 2008, Perrin and coworkers showed that at neutral pH or higher, aryltrifluoroborates solvolyze in a nearly pH-independent mechanism that is consistent with much earlier reports on pH-independent solvolysis of a tetrafluoroborate. Loss of the first fluorine atom was rate-limiting and no intermediate mono- or di-fluorinated species could be detected, suggesting ephemeral lifetimes for these species. The main contribution to solvolysis was determined by the electronic nature of ring substituents. By analogy to substituted benzyltosylates and cumyl chlorides, delocalization of electron density from the arene pi-system into the empty p-orbital on boron would weaken the B-F bond and concomitantly lead to the release of a fluoride atom leaving a difluoroborane that is so unstable that it immediately undergoes hydration and further solvolysis. Hence, pi-donating groups on the aryl ring greatly enhance aryltrifluoroborate solvolysis while electron-withdrawing substituents retard it. A linear free energy relationship ( $\log[k/k_0] = \rho\sigma$ ) was established for which  $\rho$  was found to be  $\sim -1$ . N-heterocycles, which are even more electron deficient by comparison, showed profoundly retarded solvolysis rates.<sup>111</sup> Based on this conclusion, 2,4,6-trifluorobenzoic acid-4-trifluoroborate was selected as the aryl ring of choice from a series of EWG-substituted  $\text{ArBF}_3^-$ s, as this exhibited a solvolytic half-life of approximately 850 minutes, or  $\sim 8$  times that of  $^{18}\text{F}$ -decay.

In the next several years, the newly identified  $\text{ArBF}_3^-$  compound was conjugated to several bioligands, each of which was radiolabelled in a single step as hypothesized, and

*in vivo* images of varied quality were achieved.<sup>110,112,113</sup> However, in most cases, the PET images incorporating this  $\text{ArBF}_3^-$  still showed some bone uptake (for example, see **Figure 1.4** and **Figure 1.5**). Therefore, other more stable and alternatively useful  $\text{ArBF}_3^-$ s are needed to further improve the PET imaging quality as well as extend this method to enable fine-tuning of various pharmacokinetic properties. In Chapter 2, some newly designed organotrifluoroborates will be disclosed and the general method for studying the stability of organotrifluoroborates will be discussed.

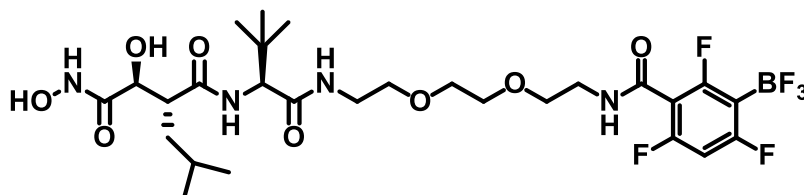
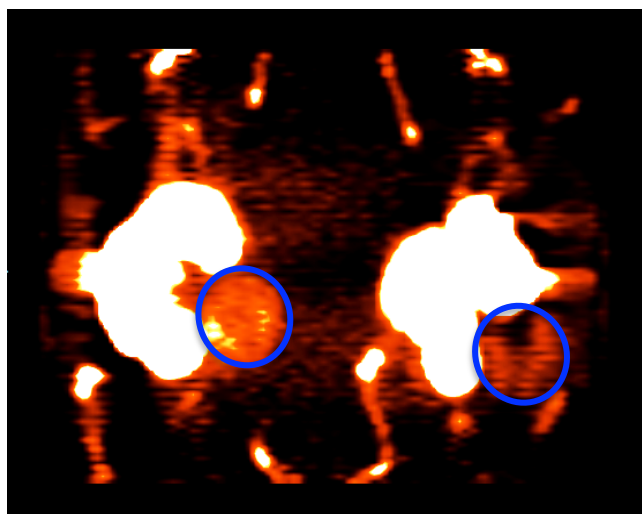


**Figure 1.4** Chemical structure of marimastat- $\text{ArBF}_3^-$ .



Unblocked

Blocked

**Figure 1.5** *In vivo* PET imaging of MMPs in murine breast carcinomas with  $^{18}\text{F}$ -labeled Marimastat. Both of the mice were directly injected with  $100\ \mu\text{Ci}$   $^{18}\text{F}$ -labeled Marimastat at  $0.39\ \text{Ci}/\mu\text{mol}$ , but the right mice was pre-blocked with  $100\ \mu\text{g}$  unlabeled Marimastat to validate the binding specificity of the radiotracer. In this experiment,  $^{18}\text{F}$ -labeled Marimastat demonstrated visible tumor uptake (blue circled) with specificity.

In addition, prior to the work described in this thesis, reports from the Perrin lab did not achieve high specific activity. The highest reported specific activity was 0.39 Ci/ $\mu\text{mol}$ ,<sup>86,104,110</sup> whereas “high specific activity” is generally considered to be around 2 Ci/ $\mu\text{mol}$ . The main problem was both the inability to work with high levels of activity that are available in clinics and the need to add a fair amount of carrier fluoride to drive the synthesis of the  $^{18}\text{F}\text{-ArBF}_3^-$ . In Chapter 4, the fluorescent screen will be presented, that has been developed to access high specific activity by radiosynthesis of aryltrifluoroborate ( $\text{ArBF}_3^-$ ).

In order to diagnose cancerous tissue, early tumor-targeting biomolecules should be introduced into the radiotracers. It is well known that bioligands such as peptides can exhibit high affinity for a certain extracellular marker present in the early stages of specific cancers (see **Figure 1.5**). Therefore, we have synthesized several conjugates of bio-ligands with the  $^{18}\text{F}\text{-ArBF}_3^-$  moieties, and some have provided very promising *in vivo* PET images.

## 1.5 The goal of this dissertation

The goal of this dissertation is to address the development a new generic  $^{18}\text{F}$ -labelling method based on B-F bond formation. This new strategy needs to be robust, rapid, and reproducible. In addition, the labeling condition needs to be mild and water-friendly, which allows for the direct labeling of most biomolecules. Finally, as with all methods related to *in vivo* use, new compounds are needed to fully explore and evaluate the design concepts that are employed to develop new bioactive compounds. In this thesis, all the aspects discussed above will be addressed in steps, and the biological applications are going to be presented.

# Chapter 2: Synthesis and Evaluation of Kinetically Stable Aryl/Alkyltrifluoroborates

## 2.1 Introduction

*In vivo* stability is usually an essential consideration during the development of new radiosynthons.<sup>103,111,114</sup> That is not to say that complete metabolic stability is required, as tracers have been reported with only modest tumor uptake even though both metabolisms have resulted in degradation and loss of fluoride with uptake to the bone.<sup>57,87</sup> Notwithstanding such cases, when considering stability, one must be concerned with all aspects of metabolic stability that include destruction of the ligand, cleavage of the linker arm and/or destruction of the radioprosthesis that erodes imaged tumor uptake values and causes the isotope to clear. All of these can result in significantly reduced tumor uptake. Hence, in most cases, the *in vivo* performance of the radiotracer is less promising when *in vivo* stability is poor.<sup>114</sup> In addition, in cases where the free radioisotope is liberated either because of dissociation from the prosthetic simply due to mass action or through metabolic interception of the prosthetic, the isotope may accumulate in certain organs, resulting in high unspecific uptake and difficulties in detecting tumor metastasis in the corresponding organs.

Since 2005, Dr. Perrin and co-workers have been working on developing a strategy to stably chelate <sup>18</sup>F-fluoride atoms based on B-F bond formation<sup>103,107,111</sup> The B-F bond is known as one of the strongest single bonds between any two non-identical atoms on the periodic table, with both C-F and Si-F bonds of comparable energies (150 kcal/mol). Yet this oft-cited value is actually based on bond homolysis rather than heterolysis. This distinction is often overlooked. For example the C-H bond of an alkyne is estimated at 133 kcal/mol while the C-H bond of an alkane is only 102 kcal/mol yet when treated with strong base such as LDA, heterolysis occurs only on the alkyne. Under physiological conditions, Ting and Perrin were the first to demonstrate a striking liability of the B-F bonds which readily heterolyze in many cases due to the high energy of solvation of a fluoride ion.<sup>45</sup> Nevertheless when thinking about bond-scission in terms of radiotracer

development, irrespective of whether a bond breaks homolytically (uncommon in biology) or heterolytically to be solvated as ions in water, at high dilution the dissociation of all bonds is always thermodynamically favored because once dissociated there can be no back reaction. It is perhaps understated therefore in the world of radiotracers that the only consideration of bond stability is kinetic. Moreover, while the design of a radioprosthesis is largely focused on the bond that connects the isotope to the prosthetic, such consideration ultimately extends to all bonds within the entire tracer, some of which, of course are labialized by the action of metabolic enzymes.

In order to develop a kinetically stable, boron-based  $^{18}\text{F}$ -radiosynthon, Ting et al. identified aryltrifluoroborate ( $\text{ArBF}_3^-$ ) derivatives to both trap  $^{18}\text{F}$ -fluoride in aqueous conditions and then hold onto  $^{18}\text{F}$ -fluoride once diluted in blood. To enhance the hydrolytic stability of  $\text{ArBF}_3^-$ s, the aryl ring was functionalized with Electron-withdrawing groups (EWGs) to give an electron-poor environment that would stabilize the negatively charged trifluoroborate. A good example of this methodology is 2,4,6-trifluoro-3-benzoic acid trifluoroborate (**2.1**), which was developed as a stable  $\text{ArBF}_3^-$  from various candidates.<sup>102,104</sup> Related animal studies were performed, and **2.1** and its derivatives were shown to be useful *in vivo* stability with limited bone uptake.

To develop an aryltrifluoroborate with superior stability, a Hammett analysis was performed, and a linear free energy relationship ( $\log[k/k_0] = \rho\sigma$ )  $\sim -1$  was identified.<sup>103</sup> Briefly, this linear correlation demonstrated that pi-donating substituents greatly enhance aryltrifluoroborate solvolysis while electron-withdrawing substituents retard it.

Based on this relationship, Ting et al. designed the  $\text{ArBF}_3^-$  **2.1** based on its apparent stability in phosphate buffer pH 7.5, as gauged by  $^{19}\text{F}$ -NMR; the half-life of **2.1** was measured to be  $\sim 1200$  min in phosphate buffer, resulting in  $\sim 3.5\%$  decomposition in the first 60 min. When labeled for *in*



*vivo* use,  $^{18}\text{F}$ -fluoride can be released from a radiotracer, and most of it will accumulate in the bone or clear to the bladder. Hence, unspecific bone uptake is often a good indication of *in vivo* defluoridation. As mentioned, several animal studies have been performed

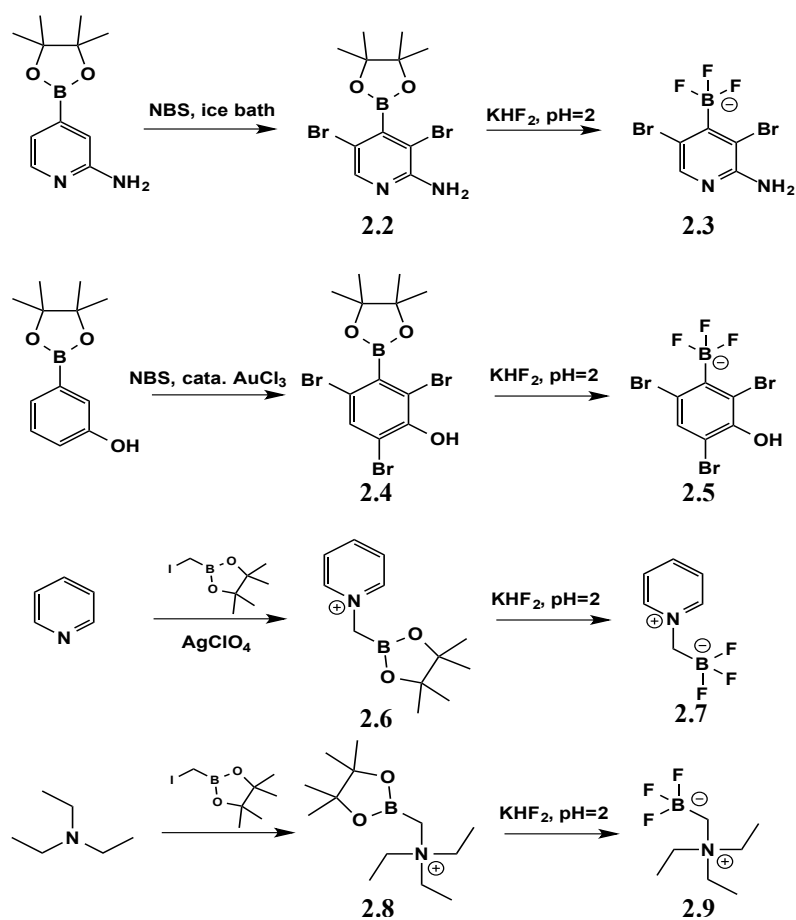
using **2.1**. In spite of the difficulties encountered with the ligands we used, the results were encouraging. However, there is room for improvement as bone uptake was  $\sim 1\%$  ID/g,<sup>113,115-120</sup> which is slightly higher than other  $^{18}\text{F}$ -radioprosthetics. In addition, based on the time activity curve (TAC), the bone uptake of the  $^{18}\text{F}$ -ArBF<sub>3</sub><sup>-</sup> tracers increased after 60 min post injection, while the uptake of other organs decreased. This abnormal phenomenon potentially demonstrated the *in vivo* defluoridation of **2.1**-mediated tracers and addressed the requirement of organotrifluoroborates to exhibit higher physiological stability. Assuming the *in vivo* defluoridation rate was similar to that observed in phosphate buffer, then it would not be surprising that the bone uptake was in the neighborhood of  $\sim 1\%$  ID/g. In order to diminish the bone uptake to an acceptable level ( $\sim 0.5\%$  ID/g), a suitable organotrifluoroborate radiotracer should decompose less than 1% in 60 min, resulting in a half-life of more than 4200 min in phosphate buffer.

In light of the Hammett analysis that Ting performed, Li expanded the number of candidates that might be useful for  $^{18}\text{F}$ -fluoride labeling through the synthesis and screening of several heteroaryltrifluoroborates (hetArBF<sub>3</sub><sup>-</sup>).<sup>111</sup> As expected, such ArBF<sub>3</sub><sup>-</sup>s were suitably stabilized due to the extremely electron-poor environment of the heteroaryl ring, and subsequently, stronger hydrolytic stability has been detected. However, harsh conditions have generally been used during the preparation of these aryltrifluoroborates, which makes the appendage of functional group for biochemical conjugation difficult. In our hands, we saw this as somewhat of a limitation in their use for bioconjugation. In addition, we also noticed that the corresponding boronic acid was rather base-labile and would give protodeboronated arenes (data not shown), which further complicated their use in peptide coupling.

Notwithstanding the arguable stability of **2.1**, the synthesis of previous ArBF<sub>3</sub><sup>-</sup>s is stepwise and challenging, which could be problematic for research centers lacking a synthetic chemist. Nevertheless, the Perrin lab has been greatly encouraged by the general success in one-step labeling at reasonable specific activity with a growing number of publications that show successful imaging. Hence when I began this work, I had worked alongside Dr. Ying Li in helping her generate images of bombesin and

bisRGD, which resulted in two publications that are not presented in this thesis due to the fact that I have chosen new work on which I have been or will be the first author.

In order to broaden the application of newly designed organotrifluoroborate radiosynths, the precursors of the radiotracers should be achieved through more simplified syntheses. Moreover, the conjugation between the radio-reporter and bioligand should be facile, robust, and bio-orthogonal, which would empower the researchers to utilize this technology for radiolabeling with sensitive and fragile bioligands (i.e. aptamers). Hence encouraged by the previous work of others in the Perrin lab achieved, I took to developing several new organotrifluoroborates that I have studied in terms of their stabilities under both *in vitro* and *in vivo* conditions. These initial steps to expanding the number of available boron-based radioprosthesis are presented in this chapter.



**Scheme 2.1** Synthetic routes of the proposed organotrifluoroborates as candidates that would enable more facile bioconjugation.

## 2.2 Results

### 2.2.1 Assessing the hydrolytic stability of organotrifluoroborates

As shown in *Scheme 2.1*, the precursors of newly designed organotrifluoroborates were achieved in one or two steps a step synthesis from commercially available starting materials. The chemical yields were gratifying, ranging from 75% to 95%. The purity and chemical identity were confirmed via mass spectrometry and  $^1\text{H-NMR}$  (See experimental session).

The organoborates were successfully converted into the corresponding organotrifluoroborate salts via incubation with excess  $\text{KHF}_2$  at  $45\text{ }^\circ\text{C}$  for 2 hours. The product was purified using silica gel via a Pasteur pipette silica column to give pure product in quantitative yield.<sup>104,107,111</sup> The resulting fluoride-free organotrifluoroborates were ready for  $^{19}\text{F-NMR}$  study to assess the solvolytic stability.<sup>121</sup>

As illustrated in *Figure 2.1*, the solvolytic stability of 2-amino-3,5-dibromopyridyl-4-trifluoroborate (**2.3**) was tested by using  $^{19}\text{F-NMR}$  spectroscopy. The  $^{19}\text{F}$ -fluoride nucleus is known to be very sensitive to nuclear magnetic excitation and therefore  $^{19}\text{F-NMR}$  spectroscopy provides a sensitive means to determine solvolytic stability.<sup>122,123</sup> At relatively high dilution ( $\sim 5\text{ mM}$ ), solvolysis of organotrifluoroborates is formally a third order reaction yet proceeds irreversibly at  $\text{pH}=7.5$  with apparent pseudo-first order kinetics, owing to the fact that the release of the first fluoride is rate limiting.<sup>103,104</sup> More interestingly, the hydrolytic defluoridation rate of organotrifluoroborates was relatively independent of the concentration of free fluoride. This may imply that the potential intermediate, such as mono- and/or bis-fluoroborates, tends to decompose rather than revert back to organotrifluoroborate at  $\text{pH}=7.5$ . Hence, this assay further shows that only the  $^{19}\text{F}$ -organotrifluoroborate is stable at  $\text{pH } 7.5$  and thus no other  $^{19}\text{F}$ -labeled species can be isolated following radiosynthesis. Gratifyingly, we found that **2.3** solvolyzed extremely slowly: the time dependent decomposition was fitted to a first order decay equation from which was extracted an apparent rate constant of  $4.2 \pm 0.03 \cdot 10^{-5}\text{ min}^{-1}$  and an apparent solvolytic half-life of  $16500 \pm 500\text{ min}$  (*Figure 2.1*).

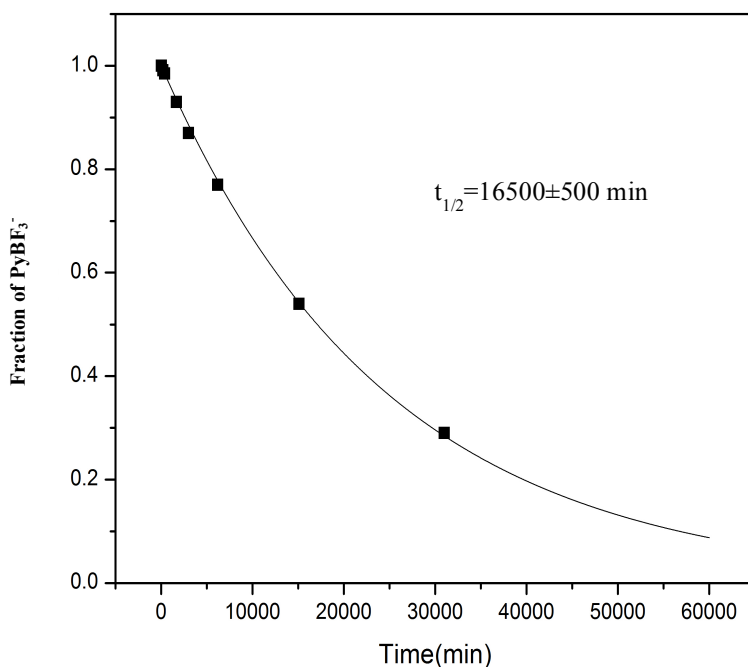


**Figure 2.1** Plot of relative integration of the  $^{19}\text{F}$ -PyrBF<sub>3</sub> as a fraction of ( $^{19}\text{F}$ -fluoride) vs. time. The solvolytic defluoridation was monitored by  $^{19}\text{F}$ -NMR. Data are scaled to 60000 min and were fit to a first order reaction; the half-life of the corresponding  $^{19}\text{F}$ -PyrBF<sub>3</sub> was calculated to be 16500 min.

As displayed, the  $^{19}\text{F}$ -NMR spectroscopy assay of the re-designed organotrifluoroborates is summarized in **Table 2.1**. These results are encouraging as the half-life is significantly longer than that of the ArBF<sub>3</sub><sup>-</sup>s we reported previously. Especially for **2.3** and **2.9**, for which half-lives were measured to be >15,000 min resulting in <0.5% decomposition in the first 60 min. Unless the radioprosthetic (taken to be the immediate group of atoms through which the B-F bond is stabilized) is metabolized, these organotrifluoroborates are promising  $^{18}\text{F}$ -radiosynthons showing excellent *in vivo* stability. As such, imaging agents have been conjugated with fluorophores/peptides to evaluate stability under various conditions. I also note that as I took over this project, I often prepared conjugates to ArBF<sub>3</sub><sup>-</sup> (**2.1**) to standardize many procedures because as new prosthetics were advancing,

we sought to evaluate these with a prosthetic that could be used as a positive control for all aspects of this work. Hence the readers will find that herein and throughout, I will often use **2.1** to advance this work and then make comparisons in some cases to new prosthetics.

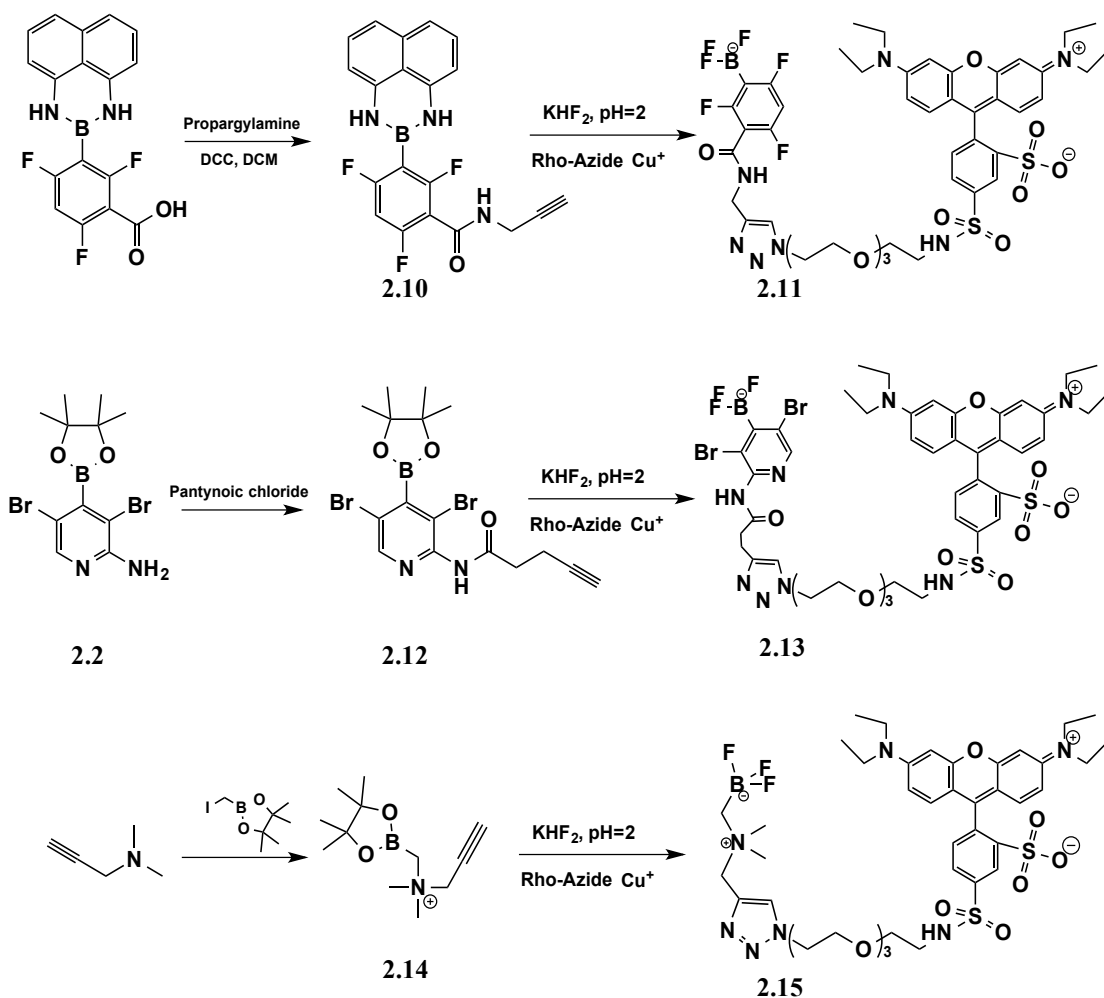
**Table 2.1** Summary of solvolytic stability of all the new organotrifluoroborates.

Compound #	half-life (min)	k (min <sup>-1</sup> )	Calculated decomposition in first 60 min
<b>2.3</b>	16500	4.20·10 <sup>-5</sup>	0.52%
<b>2.5</b>	1580	3.91·10 <sup>-4</sup>	2.60%
<b>2.7</b>	10350	6.70·10 <sup>-5</sup>	0.40%
<b>2.9</b>	19500	3.55·10 <sup>-4</sup>	0.21%

## 2.2.2 *In vitro* stability evaluation

### 2.2.2.1 Fluorescent TLC analysis

As shown in *Scheme 2.2*, compounds **2.1**, **2.3** and **2.9** were successfully modified into “clickable” versions and then conjugated to Rhodamine-azide. The purity and chemical identity were confirmed by <sup>1</sup>H-NMR and ESI-MS. The synthetic information is detailed in the experimental.



**Scheme 2.2** Synthesis route of fluorescent organotrifluoroborates

A fluorescent TLC assay was used to analyze and evaluate conditions of fluoridation, because it provided visible results by detection with the naked eye, and did not involve any time-consuming radioactive procedures. In this manner we could screen many conditions including solvents, pH, buffers, temperatures, and various additives. In addition, researchers can access fluorophores with great flexibility of time and location. In contrast, working with radioactivity,  $^{18}\text{F}$  especially, requires specialized facilities in addition to collaboration with trained operators. In addition, working with the radioisotope is not feasible without a considerably laborious preparation. Considering the operational simplicity to working with fluorescence compared to radioactivity, a fluorescent TLC assay was highly desired for defining optimal or near-optimal conditions

before confirming labeling by radioactive assays. In addition, a pre-analysis by fluorescence is helpful in optimizing the procedure for the radioactive experiment, which would simplify the operation in the hot cell and subsequently reduce the radiation dose.

In addition, the TLC method could be used to screen for serum stability. For example, Rhodamine-ArBF<sub>3</sub><sup>-</sup> (**2.11**, A, 50 nmol), Rhodamine-PyBF<sub>3</sub><sup>-</sup> (**2.13**, B) and Rhodamine-AMBF<sub>3</sub> (**2.15**, C) were re-suspended into 1:4 ethanol/PBS solution (50 μL) to create a stock solution. 10 μL of each stock solution was diluted into 100 μL mouse plasma, 100 μL human plasma and 100 μL PBS buffer to give samples 1, 2, and 3, respectively. These samples were incubated at 37 °C for 2 hours, and then quenched with 200 μL acetonitrile. The precipitate was removed by centrifuge and the supernatant was further filtered before being loaded on the TLC plate.

By accurately transferring the same volume of supernatant for each sample, a consistent amount of fluorescent organotrifluoroborate was loaded on the TLC plate. All the TLC plates were developed with 1:4 methanol/DCM. The Rhodamine-ArBF<sub>3</sub><sup>-</sup> and Rhodamine-PyBF<sub>3</sub><sup>-</sup> were slightly above the baseline owing to their high polarity, and the Rhodamine-AMBF<sub>3</sub> ran higher with an R<sub>f</sub> value of ~0.3. For sample A, ~10% of Rhodamine-ArBF<sub>3</sub><sup>-</sup> was lost during the incubation (estimated by fluorescence). No significant difference was seen between the experiments in human plasma, mouse plasma, or PBS buffer. For sample B, much less decomposition was detected, but more than one byproduct was displayed on TLC plate. The one that was shared by B1, B2, and B3 was thought to be the corresponding boronic acid. This assumption has been confirmed by LC-MS. The remaining unknown byproducts will be assessed in the following discussion. For sample C, encouragingly, none of the three experiments showed detectable decomposition, displaying its strong resistance to either solvolysis or metabolism.

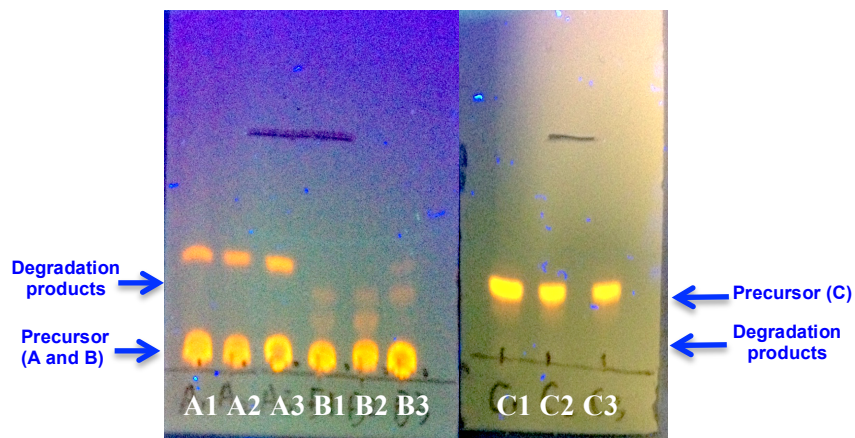
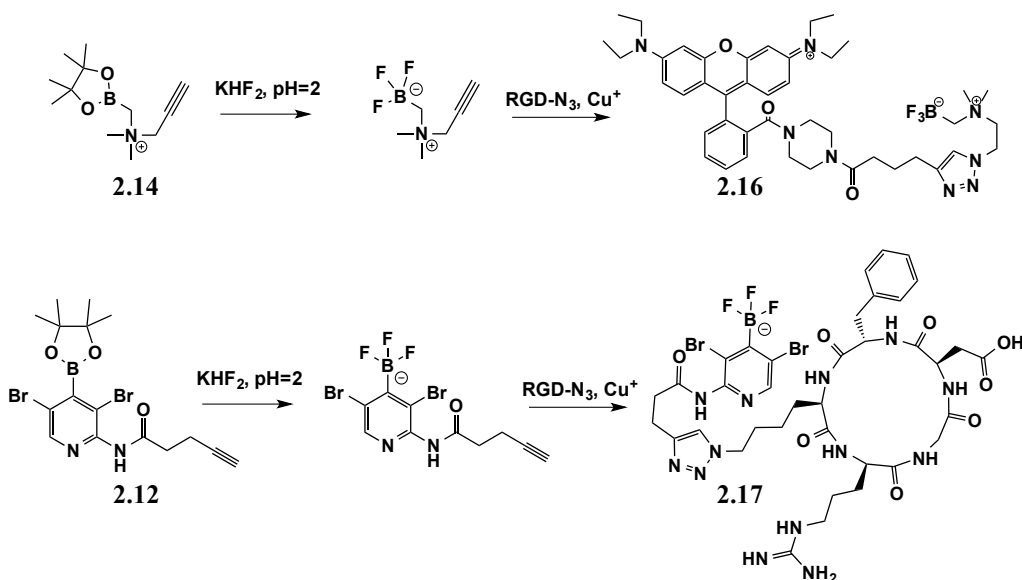


**Figure 2.2** Fluorescent TLC analysis of the plasma stability of new designed organotrifluoroborates. 10  $\mu\text{L}$  of each stock solution was diluted into 100  $\mu\text{L}$  mouse plasma, 100  $\mu\text{L}$  human plasma and 100  $\mu\text{L}$  PBS buffer to give sample 1, 2 and 3, respectively. A, B, C stands for **2.11**, **2.13** and **2.15**, respectively.

#### 2.2.2.2 Radioactive HPLC analysis



**Scheme 2.3** Synthesis route of bioconjugated organotrifluoroborates.

To begin to evaluate the stability of these new organotrifluoroborates under physiological conditions in the context of real radiotracers,  $\text{PyBF}_3^-$  and  $\text{AMBF}_3^-$  were conjugated to different ligands (**Scheme 2.4**) and then radiolabeled through  $^{18}\text{F}$ - $^{19}\text{F}$  isotopic exchange

(IEX). The  $^{18}\text{F}$ -labelled tracers were first incubated in plasma at 37 °C to assess the *in vitro* stability, and followed by animal studies for *in vivo* stability evaluation. Here, RGD-PyBF<sub>3</sub><sup>-</sup> was used as an example to illustrate how we performed this experiment. Our rationale for labeling RGD is based on two considerations: 1) RGD is perhaps the most commonly imaged peptide and its synthesis is still of current interest;<sup>87,89</sup> 2) use of RGD represents a clinically relevant tracer where the biodistribution achieved in our studies can be directly compared to other reports.<sup>112,124</sup>

**2.17** was re-suspended in DMF (15 µL), distilled water (15 µL), and pyridazine-HCl buffer (pH = 2, 15 µL). This cocktail was withdrawn into a 100 µL tuberculin syringe wherein it was stored until labeling. In the meantime the syringe was placed in the hot cell just prior to  $^{18}\text{F}$ -production by  $^{18}\text{O}$ -water bombardment. Following  $^{18}\text{F}$ -fluoride concentration by anion-exchange trapping and elution, the peptide cocktail was injected into the vial containing the  $^{18}\text{F}$ -fluoride (800-1000 mCi activity was measured at the beginning of synthesis). The reaction vial was then mixed by gentle rocking with the robotic arm manipulators. The vial was placed for 20 min in a temp block set at 45 °C and then the reaction was quenched by injection with 2 mL 5% NH<sub>4</sub>OH in 50:50 MeCN/H<sub>2</sub>O. Approximately 2.5% of the quenched reaction mixture (50 µL, ~20 mCi) was removed from the hot cell and loaded onto an analytical HPLC RP-C18 column for purification according to method C. Due to the lack of an automated fraction collector, the radiolabeled product was manually collected at 15 min following HPLC resolution and a portion of the collected fraction was re-analyzed for radiochemical purity.<sup>125</sup> The active fraction was then diluted with 15 mL distilled water whereupon the solution was passed through a C18 sep-pak cartridge and washed with 5 mL of distilled water to remove residual MeCN and free  $^{18}\text{F}$ -fluoride anion. The  $^{18}\text{F}$ -**2.17** radiotracer was then eluted with ethanol (0.3 mL) in 6 fractions (~50 µL each), diluted into phosphate buffered saline (2 mL), and sent for PET scanning. A small amount was retained for a plasma stability assay.

Purified  $^{18}\text{F}$ -**2.17** was diluted in saline (1 mL). For each assay, the saline solution was added into 500 µL mice plasma and incubated at 37 °C for 0, 80, and 150 min. Following incubation at the noted time points, the reaction was quenched by adding 1 mL MeCN to

precipitate the protein from the solution. The quenched reactions were spun at 13,000 rpm to remove insoluble material. The supernatant was isolated, filtered, and then loaded into HPLC. As expected, the radiochemically pure  $^{18}\text{F}$ -**2.17** showed very high stability with <2% degradation and/or solvolytic defluoridation in 150 min (**Figure 2.3**). This compares favorably to the plasma stability of the previous aryltrifluoroborate radiosynthon (~10% decomposition in 2 hours).

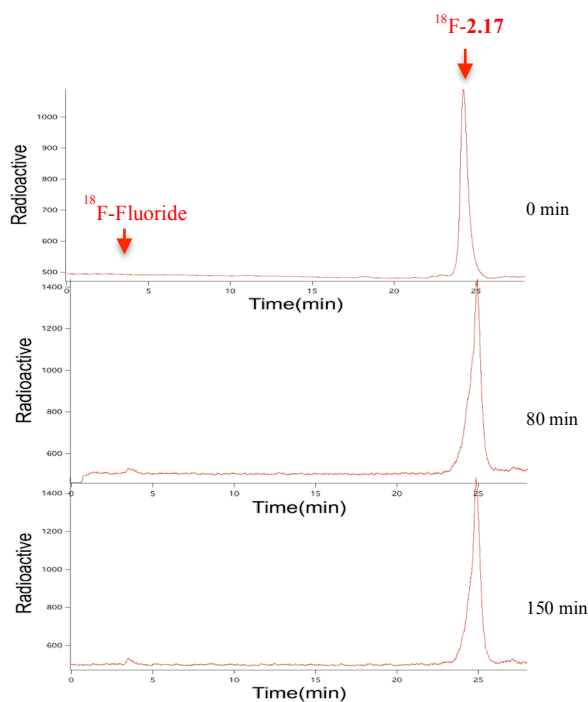


**Figure 2.3** The radioactive HPLC trace following mice plasma incubation of **2.17**. The incubation time is 0, 80 150 min, respectively. After being incubated in plasma at 37 °C for 150 min, small amount (~2%) free  $^{18}\text{F}$ -fluoride (red arrow) was detected based on radio-HPLC analysis.

### 2.2.3 *In vivo* stability assay

The *in vivo* stability of  $^{18}\text{F}$ -**2.17** was tested as following: two mice were humanely anesthetized and then injected with 100  $\mu\text{Ci}$  of labeled peptide. Dynamic scans were run and images were acquired at 10, 30, and 60 min that demonstrated significant and rapid clearance to the bladder and liver (**Figure 2.4**). Here bone uptake was calculated to be approximately 0.5%, which is on par with previous reports from our lab and others.<sup>71</sup>

In addition,  $^{18}\text{F}$ -**2.16** also showed excellent *in vitro* stability under the same conditions. There was minimal  $^{18}\text{F}$ -fluoride (<0.5%) as detected by HPLC analysis after plasma incubation for 150 min. An animal study was also performed using  $^{18}\text{F}$ -**2.16**. The results showed that most of the radioactivity was excreted through the hepatobiliary system due to high lipophilicity of the Rhodamine. The observed bone uptake was minimal which demonstrated the extraordinary stability of  $\text{AMBF}_3$ . Further details of  $\text{AMBF}_3$  will be presented in Chapter 5. No tumor imaging was performed in this case as we did not believe that tumor uptake itself would be essential criteria for evaluating a new radioprosthesis. Indeed tumor uptake can prove quite tricky and can depend on several factors of which the radioprosthesis composition is only one.

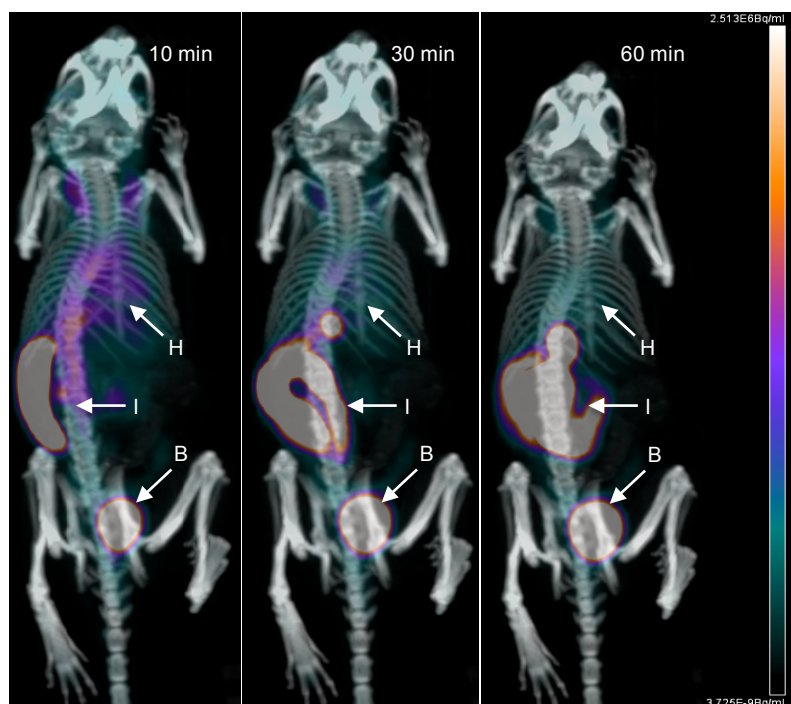


**Figure 2.4** PET imaging of  $^{18}\text{F}$ -labeled agents in healthy nude mice by small-animal PET. The representative 3D PET/CT images were shown at the time point of 10 min, 30 min and 60 min after being injected with the new designed  $\text{RGD-}^{18}\text{F-PyBF}_3^-$  (**2.16**). The radioactivity was rapidly cleaned up from the background and then mainly excreted through urinary and digestive tract. As desired, the bone uptake was almost negligible, which clearly showed the high *in vivo* stability of this new designed  $^{18}\text{F-PyrBF}_3^-$  radioprosthesis. I = intestine; B = bladder; H = heart.

## 2.3 Discussion

As described in *Scheme 2.2*, all newly designed organotrifluoroborates radiosynthons can be achieved within two steps in good yield from commercially available starting materials. During the past few years, the relative difficulty of synthesizing **2.1** and its derivatives had introduced significant difficulties for studying ligand with a pendant  $^{18}\text{F}$ - $\text{ArBF}_3^-$ . With these greatly simplified synthetic protocols, more researchers will be empowered to radiolabel their imaging probes via radiosynthesis of  $^{18}\text{F}$ -organotrifluoroborates.

Based on  $^{19}\text{F}$ -NMR spectroscopic assay,  $\text{PyBF}_3^-$  and  $\text{AMBF}_3$  displayed similar solvolytic stability with the half-life of  $\sim 18000$  min at  $\text{pH}=7.4$ . However,  $\text{PyBF}_3^-$  showed faster decomposition than  $\text{AMBF}_3$  during plasma incubation. A possible reason could be some currently unknown metabolic action such as reduction or conjugation to glutathione that would change the electronics of the pyridyl ring such that the B-F bond would weaken. In contrast,  $\text{AMBF}_3$  has consistently shown stability in either *in vitro* or *in vivo* conditions, demonstrating its inertness against biochemical processing. Therefore,  $\text{AMBF}_3$  would be a stronger candidate to be an ideal  $^{18}\text{F}$ -radioprosthetic.

Generally, bone uptake values are the standard for evaluating *in vivo* stability of radiotracers:  $<1\%$  ID/g is always the sign of good stability.<sup>57</sup> Based on time activity curve we got from this experiment, **2.17** showed 2.5% bone uptake at 5 min post injection, and the bone uptake went down to 1.7% at 120 min post injection. Here I want to argue that the time activity curve (TAC) of bone uptake would be slightly more reasonable and reliable in measuring the *in vivo* stability. Bone uptake is commonly measured through *ex vivo* analysis of biodistribution or PET imaging, which is in both cases affected by blood uptake due to the blood in the bone marrow. If a radiotracer clears from the blood relatively slowly, the bone uptake value of this radiotracer would appear to be high, even though this tracer is actually stable *in vivo*.<sup>114,126</sup> In contrast, the TAC of a stable tracer would continually diminish along with the clearance from blood and organs, but a tracer with poor stability would show a TAC that eventually increases.<sup>83</sup> In addition, for the radiotracers labeled with alternative isotopes, bone uptake would not be a useful

indication. For instance, free  $^{68}\text{Ga}$  mainly accumulates in the tumor and  $^{123}\text{I}$  is always trapped in the thyroid.

## 2.4 Conclusion

We have developed a three new organotrifluoroborates that are candidates as  $^{18}\text{F}$ -radioprothetics. These organotrifluoroborate radiosynthons can be readily obtained from commercially available starting materials, and can be conjugated with various bio-ligands via coupling reactions or copper-catalyzed click reactions.<sup>92,99,127-134</sup> In addition, systematic evaluations have been done to assess the *in vivo* stability of the organotrifluoroborates, namely  $^{19}\text{F}$ -NMR stability assays, plasma stability assays, and *in vivo* bio-distribution. Consequently,  $\text{PyBF}_3^-$  and  $\text{AMBF}_3$  have been selected as new  $^{18}\text{F}$ -radioprothetics for further molecular imaging studies. Among them,  $\text{AMBF}_3$  is preferred due to its higher metabolic stability.

## 2.5 Materials and synthesis

### 2.5.1 General information

Reagents and solvents were purchased from Fischer, Sigma-Aldrich, Alfa-Aesar, Novabiochem or Oakwood unless stated otherwise.  $^{18}\text{F}$  Trap & Release Columns were purchased from ORTG Inc. (Oakdale, TN) and C18 sep-pak cartridge (Vac 1cc, 50 mg) was obtained from Waters. Deuterated solvents were purchased from Cambridge Isotope Laboratories.

### 2.5.2 HPLC methods

Gradients for purification are listed below:

Gradient A: Agilent Eclipse XDB-C18 5  $\mu\text{m}$  9.2 x 250 mm semi-prep column. Solvent A: 0.04 M ammonium formate pH 6.8; solvent B: MeCN; 0 to 5 min: 0% to 5% B, 5 to 7 min: 5% to 35% B, 7 to 12 min, 35% to 45% B, 15 to 20 min: 45% to 100% B, 15 to 20 min: 100% to 100% B, 20 to 22 min: 100% to 20% B, 22 to 24 min: 20% to 0% B; flow rate: 3 mL/min, column temperature: 19 to 21  $^\circ\text{C}$ ;

Gradient B: Agilent Eclipse XDB-C18 5  $\mu$ m 9.2 x 250 mm semi-prep column. Solvent A: 0.04 M ammonium formate pH 6.8; solvent B: MeCN; 0 to 5 min: 0% to 5% B, 5 to 7 min: 5% to 35% B, 7 to 15 min, 35% to 45% B, 15 to 18 min: 45% to 100% B, 18 to 20 min: 100% to 100% B, 20 to 22 min: 100% to 20% B, 22 to 24 min: 20% to 0% B; flow rate: 3 mL/min, column temperature: 19 to 21 °C;

Gradient C: Phenomenex Jupiter 10m C18 300Å 4.6 x 250 mm analytical column. Solvent A: 0.04 M ammonium formate pH 6.8; solvent B: MeCN; 0 to 5 min: 0% to 5% B, 5 to 10 min: 5% to 35% B, 10 to 20 min, 35% to 45% B, 20 to 22 min: 45% to 100% B, 22 to 28 min: 100% to 100% B, 28 to 30 min: 100% to 20% B, 30 to 33 min: 20% to 5% B; flow rate: 1 mL/min, column temperature: 19 to 21 °C.

Gradient D: Phenomenex Jupiter 10m C18 300Å 4.6 x 250 mm analytical column. Solvent A: 0.1% TFA water; solvent B: MeCN; 0 to 2 min: 5% to 5% B, 2 to 7 min, 5% to 20% B, 7 to 20 min, 20% to 100%, 20 to 22 min, 100% to 5% B. Flow rate: 1 mL/min, column temperature: 19 to 21 °C.

### **2.5.3 Preparation and synthesis**

#### **Synthesis of 2-amino-3,5-dibromo-4-pyridylboronic acid pinacol ester (2.2)**

4-pyridylboronic acid pinacol ester (220 mg, 1.0 mmol) and N-bromosuccinimide (389.4 mg, 2.2 mmol) were dissolved into 5 mL 1:1 dichloromethane/N,N-dimethylformamide (DCM/DMF) and placed at 0-4 °C (ice bath) for 2 hours. The reaction warmed to room temperature and stirred overnight. The crude was concentrated under vacuum and then directly purified by flash silica column chromatography using 10:1 DCM/methanol. 320 mg white powder was obtained as pure product. Yield: 85%. ESI-MS:  $[M+H]^+$  379.2 (100%).  $^1\text{H-NMR}$ : 1.51 (s, 12H), 4.90 (s, 2H), 8.12 (s, 1H).

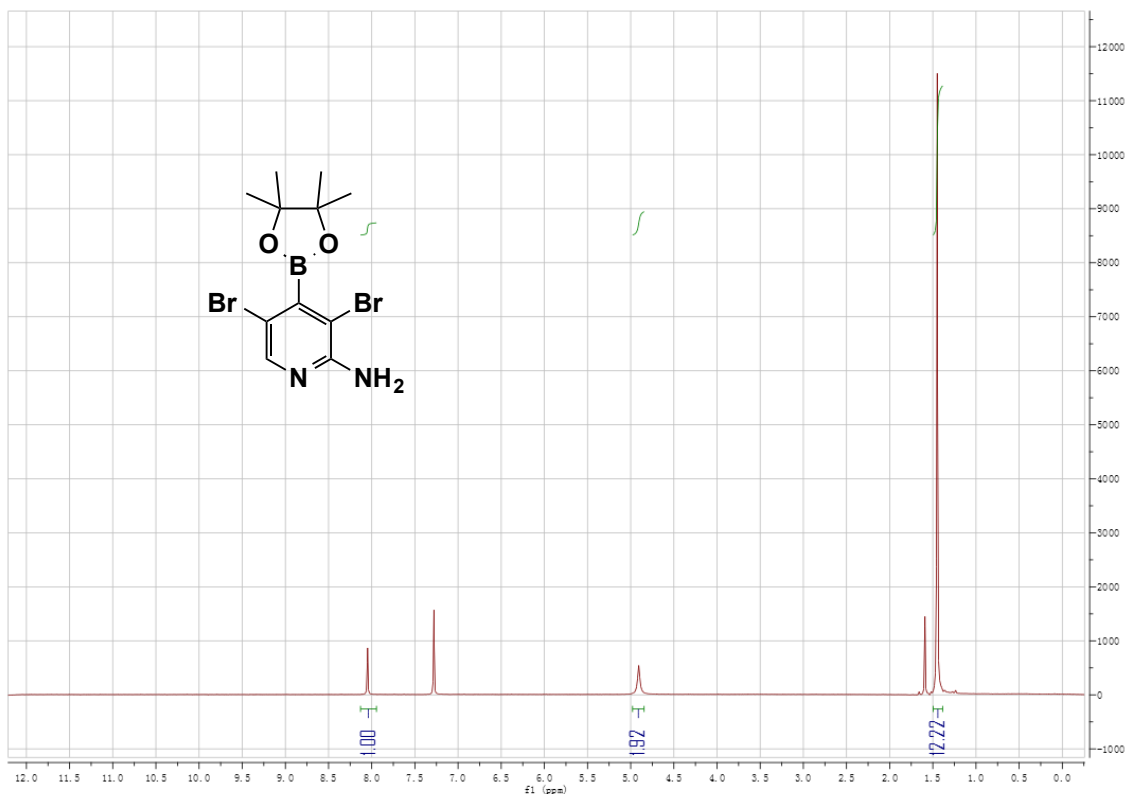


**Figure 2.5**  $^1\text{H}$ -NMR spectrum of **2.2** in  $\text{CDCl}_3$ .

### Synthesis of 2-amino-3,5-dibromo-4-pyridyltrifluoroborates (**2.3**)

In a 15 mL falcon tube, **2.2** (18.9 mg 50  $\mu\text{mol}$ ) was fluoridated with  $\text{KHF}_2$  (aq, 3 M, 100  $\mu\text{L}$ ), DMF (200  $\mu\text{L}$ ) and HCl (aq, 4 M, 100  $\mu\text{L}$ ). The reaction was incubated at 45  $^\circ\text{C}$  for 2 hours and then concentrated under vacuum at 45  $^\circ\text{C}$ . Following this concentration, the crude reaction contents were quenched with  $\text{NH}_4\text{OH}$  (1:1 MeCN/water, 5%, 1 mL). The purification was performed by a self-assembled silica pipette column to give a  $^{19}\text{F}$ -NMR pure **2.3**. Yield: 95%. ESI-MS:  $[\text{M}]^-$  305.87 (100.0%), 303.88 (51.4%), 307.87 (48.6%).  $^{19}\text{F}$ -NMR: -137 ppm (b, 3F)

### Synthesis of 2,4,6-tribromo-3-(4,4,5,5-tetramethyl-1,3,2-dioxaborolan-2-yl)phenol (**2.4**)

A flame-dry round bottom flask was charged with 3-(4,4,5,5-tetramethyl-1,3,2-dioxaborolan-2-yl)phenol (330 mg, 1.5 mmol), 3.2 equiv. of N-bromosuccinimide (854

mg, 4.8 mmol) and 0.02 equiv. AuCl<sub>3</sub> (10 mg, 0.03 mmol) along with 3 mL dry 1,2-dichloroethane (DCE). The reaction was heated up to 80 °C for 12 hours before quenching with 20 mL water. The aqueous layer was extracted twice with another 20 mL DCM. The organic layer was combined and concentrated under vacuum. The crude residue was then chromatographed on using a gradient (0-20%) ethyl acetate in hexane to give 410 mg 2.2 as a white powder. Yield: 64%. ESI-MS: [M]<sup>-</sup> 457.85 (100%). <sup>1</sup>H-NMR: 1.49 (s, 12H), 2.05 (t, 1H), 2.64 (m, 2H), 2.95 (t, 2H), 7.96 (s, 1H), 8.44 (s, 1H).

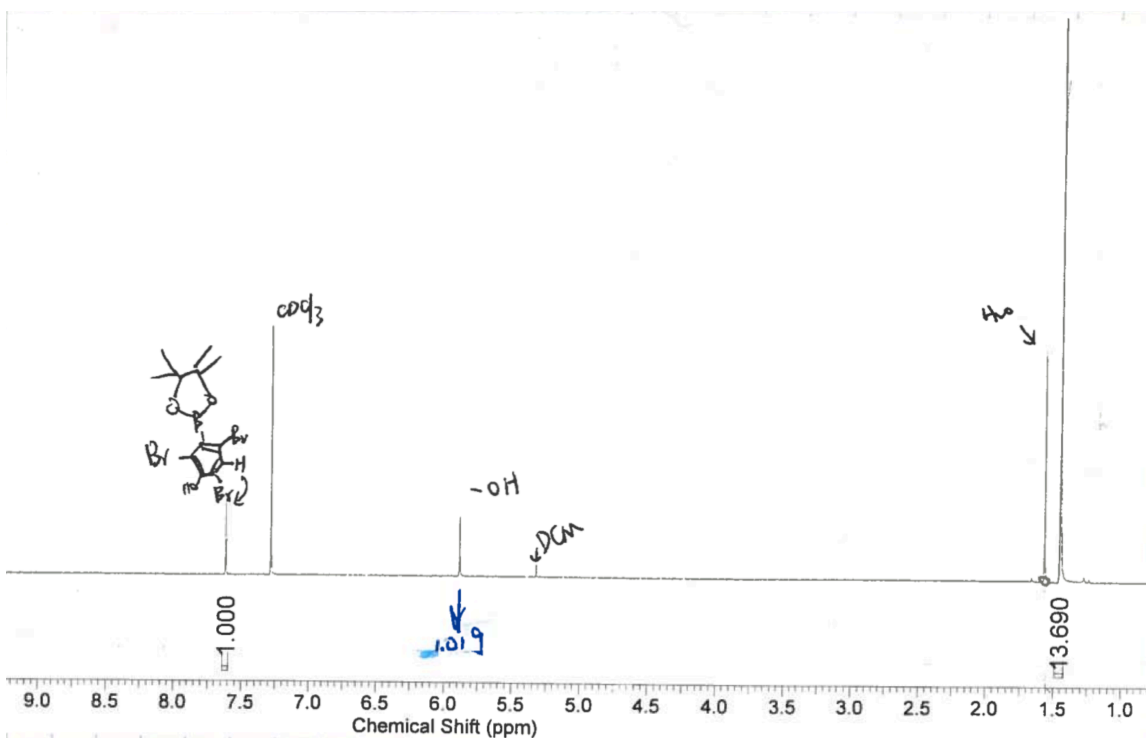


**Figure 2.6** <sup>1</sup>H-NMR spectrum of 2.4 in CDCl<sub>3</sub>.

### Synthesis of pyridium methyltrifluoroborate (2.7)

AgClO<sub>4</sub> (225 mg, 1.1 mmol) was dissolved into dry MeCN (5 mL) in a flame-dried round bottom flask. Behind a blast shield, iodomethylborate pinacol ester (182 μL, 1.0 mmol) was added dropwise to achieve a clear yellowish solution. Pyridine (804 mL, 10 mmol) was previously diluted in MeCN (10 mL) and then slowly added into the flask via syringe. A large amount of yellow precipitation was observed and then removed by centrifuge. The supernatant was concentrated and followed by fluorinating with KHF<sub>2</sub> (6

M  $\text{KHF}_2$  water solution, 1 mL, 6 mmol). The crude reaction was purified by MeCN/diethyl ether precipitation to give compound 2.7 (82 mg, 51% yield). ESI:  $[\text{M-F}]^+$  152.0.

### **Synthesis of N,N,N-triethylaminomethyltrifluoroborate (2.9)**

Triethylamine (139  $\mu\text{L}$ , 1.0 mmol) was dissolved into anhydrous diethyl ether (5 mL) in a flame-dried round bottom flask. At room temperature, iodomethylborate pinacol ester (182  $\mu\text{L}$ , 1.0 mmol) was added dropwise into the solution over 5 min. The alkylated product was precipitated from the solution as a fluffy white powder, which was achieved via filtration and then dried under vacuum. This alkylated boronic ester was fluorinated with  $\text{KHF}_2$  (6 M  $\text{KHF}_2$  water solution, 1 mL, 6 mmol) and purified by a self-assembled silica column to give compound 2.9. ESI:  $[\text{M-F}]^+$  obtained: 136.1.

### **Synthesis of Rhodamine- $^{19}\text{F}$ -ArBF $_3^-$ (2.11)**

2.10 (50  $\mu\text{mol}$ ) was converted to the corresponding alkyne-modified- $^{19}\text{F}$ -ArBF $_3^-$  through the addition of DMF (60  $\mu\text{L}$ ),  $\text{KHF}_2$  (3M, 30  $\mu\text{L}$ ) and HCl (4M, 30 $\mu\text{L}$ ) at 40-45  $^\circ\text{C}$  for 1 hour and then concentrated with speed-vac at 45  $^\circ\text{C}$ . The reaction was quenched with  $\text{NH}_4\text{OH}$  (1:1 MeCN/water, 5%, 100  $\mu\text{L}$ ) and directly used for copper-click reaction without further purification. A 1:1 MeCN/water solution that contained  $\text{CuSO}_4$  (7.5  $\mu\text{mol}$ ), sodium ascorbate (15  $\mu\text{mol}$ ) and Rhodamine-azide (5  $\mu\text{mol}$ ) was added and the reaction was warmed up to 45  $^\circ\text{C}$  for 2 hours. The crude was then purified by HPLC with method A to isolate chemically pure product. ESI-MS:  $[\text{M+H}]^+$  1038.3 (100%).

### **Synthesis of 4-pentynoylchloride**

Pentynoic acid (490 mg, 5.0 mmol) was mixed with excess thionyl chloride (2 mL) at room temperature for 2 hours. After then, the solvent and byproduct were removed by rotoevaporation to give a yellowish oil that was used directly without further purification. Yield: 80%.

### Synthesis of Alkynyl-2-ammonio-3,5-dibromo-4-pyridylboronate pinacol ester (2.12)

2-amino-3,5-dibromo-4-pyridylboronic acid pinacol ester (75.8 mg, 0.2 mmol), 1.2 equivalent 4-pentynoyl chloride (27.8 mg, 0.24 mmol) and triethylamine (1.2 eq. 23.1 mg, 0.24 mmol) was dissolved in 2 mL CH<sub>2</sub>Cl<sub>2</sub>. Stir at room temperature overnight. Then the reaction was washed with distilled water for three times and then with brine. The organic phase was then concentrated by rotoevaporation. The crude residue was purified by column chromatography using 10:1 DCM/methanol. Yield: 60%. ESI-MS: [M+H]<sup>+</sup> 459.0 (100%). <sup>1</sup>H-NMR: 1.49 (s, 12H), 2.05 (t, 1H), 2.64 (m, 2H), 2.95 (t, 2H), 7.96 (s, 1H), 8.44 (s, 1H).

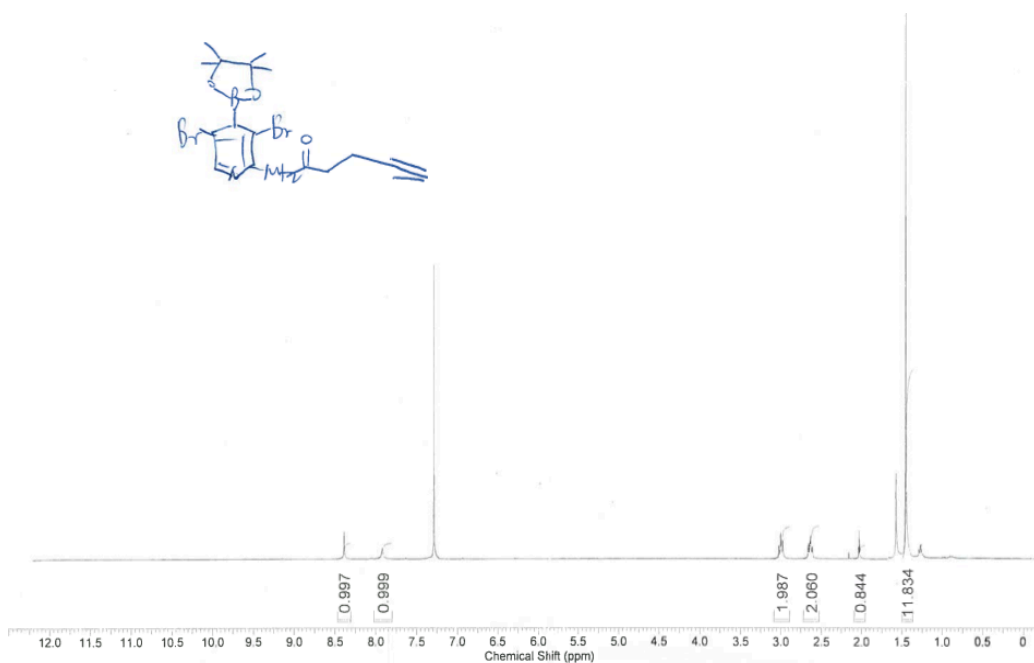


**Figure 2.7** <sup>1</sup>H-NMR spectrum of **2.12** in CDCl<sub>3</sub>.

### Synthesis of Rhodamine-<sup>19</sup>F-PyBF<sub>3</sub><sup>-</sup> (2.13)

**2.12** (50 μmol) was converted to the corresponding alkyne-modified-<sup>19</sup>F-PyBF<sub>3</sub><sup>-</sup> through the addition of DMF (60 μL), KHF<sub>2</sub> (3M, 30 μL) and HCl (4M, 30 μL) at 40-45 °C for 1 hour and then concentrated with speed-vac at 45 °C. The reaction was quenched with NH<sub>4</sub>OH (1:1 MeCN/water, 5%, 100 μL) and directly used for copper-click reaction

without further purification. A 1:1 MeCN/water solution that contained CuSO<sub>4</sub> (7.5 μmol), sodium ascorbate (15 μmol) and Rhodamine-azide (5 μmol) was added and the reaction was warmed up to 45 °C for 2 hours. The crude was then purified by HPLC with method A to isolate chemically pure product. ESI-MS: [M+H]<sup>+</sup> 1158.1 (100%).

#### **Synthesis of N,N-dimethylpropargylaminomethylboronic pinacol ester (2.14)**

N,N-dimethylpropargylamine (102 μL, 1.0 mmol) was dissolved into anhydrous diethyl ether (5 mL) in a flame-dried round bottom flask. At room temperature, iodomethylborate pinacol ester (182 μL, 1.0 mmol) was added dropwise into the solution over 5 min. The alkylated product was precipitated from the solution as a fluffy white powder, which was achieved via filtration and then dried under vacuum. ESI: [M]<sup>+</sup> 224.2 (100%).

#### **Synthesis of Rhodamine-<sup>19</sup>F-AMBF<sub>3</sub> (2.15)**

**2.14** (50 μmol) was converted to the corresponding alkyne-modified-<sup>19</sup>F-PyBF<sub>3</sub><sup>-</sup> through the addition of DMF (60 μL), KHF<sub>2</sub> (3M, 30 μL) and HCl (4M, 30 μL) at 40-45 °C for 1 hour and then concentrated with speed-vac at 45 °C. The reaction was quenched with NH<sub>4</sub>OH (1:1 MeCN/water, 5%, 100 μL) and directly used for copper-click reaction without further purification. A 1:1 MeCN/water solution that contained CuSO<sub>4</sub> (7.5 μmol), sodium ascorbate (15 μmol) and Rhodamine-azide (5 μmol) was added and the reaction was warmed up to 45 °C for 2 hours. The crude was then purified by HPLC with method A to isolate chemically pure product. ESI-MS: [M+H]<sup>+</sup> 923.4 (100%).

#### **Synthesis of Rhodamine-<sup>19</sup>F-AMBF<sub>3</sub> (2.16)**

**2.14** (50 μmol) was converted to the corresponding alkyne modified-<sup>19</sup>F-PyBF<sub>3</sub><sup>-</sup> through the addition of DMF (60 μL), KHF<sub>2</sub> (3M, 30 μL) and HCl (4M, 30 μL) at 40-45 °C for 1 hour and then concentrated with speed-vac at 45 °C. The reaction was quenched with NH<sub>4</sub>OH (1:1 MeCN/water, 5%, 100 μL) and directly used for copper-click reaction without further purification. A 1:1 MeCN/water solution that contained CuSO<sub>4</sub> (7.5 μmol), sodium ascorbate (15 μmol) and Rhodamine-azide (5 μmol) was added and the reaction was warmed up to 45 °C for 2 hours. The crude was then purified by HPLC with method A to isolate chemically pure product. ESI-MS: [M+H]<sup>+</sup> 802.5 (100%).

## Synthesis of RGD-<sup>19</sup>F-PyBF<sub>3</sub><sup>-</sup> (2.17)

2.12 (50 μmol) was converted to the corresponding alkyne-modified-<sup>19</sup>F-PyBF<sub>3</sub><sup>-</sup> through the addition of DMF (60 μL), KHF<sub>2</sub> (3M, 30 μL) and HCl (4M, 30 μL) at 40-45 °C for 1 hour and then concentrated with speed-vac at 45 °C. The reaction was quenched with NH<sub>4</sub>OH (1:1 MeCN/water, 5%, 100 μL) and directly used for copper-click reaction without further purification. A 1:1 MeCN/water solution that contained CuSO<sub>4</sub> (7.5 μmol), sodium ascorbate (15 μmol) and Rhodamine-azide (5 μmol) was added and the reaction was warmed up to 45 °C for 2 hours. The crude was then purified by HPLC with method B to isolate chemically pure product. ESI-MS: [M+H]<sup>+</sup> 1029.2 (100%).

### 2.5.4 Animal protocol

All animal studies were performed in accordance with the Canadian Council on Animal Care Guidelines and were reviewed and approved by the University of British Columbia Animal Care Committee. While under 2% isoflurane anesthesia, Rag2M mice were injected with ~200 μCi of radiotracer via catheter in the tail vein right before PET acquisition started and within 20 min of packaging. Following scanning the mice were euthanized, while under anesthesia, by isoflurane overdose followed by cervical dislocation. The list-mode data were histogrammed, and reconstructed by an iterative reconstruction algorithm (3D OSEM/MAP) using the Inveon Acquisition Workplace Software (Siemens), applying normalization, dead time, random and attenuation correction. The attenuation correction map was obtained from the CT scan data that were acquired prior to injection.

# Chapter 3: Organotrifluoroborate Hydrolysis: Implications for Suzuki-Miyaura Coupling and The Design of *In Vivo* Stable PET Tracers

## 3.1 Introduction

Organotrifluoroborates are receiving increasing attention as one of the most important *in situ* sources of organoboronic acids in Suzuki-Miyaura cross coupling reactions,<sup>36,135-138</sup> which are some of the most oft-used transition-metal catalyzed processes for C-C bond formation. Organotrifluoroborates can be readily synthesized and are always more stable for storage and commercialization than the corresponding organoboronic acids from which they are readily prepared.<sup>135,139</sup> Indeed, for Suzuki-Miyaura coupling reactions, it is known that direct use of organoboronic acids or their esters results in side reactions such as oxidation, protodeboronation, and dehydrative cyclotrimerization and such reactions can also occur prior to use.<sup>140</sup> In contrast, because of the overall stability organotrifluoroborates, their use can reduce most unwanted byproducts. Once added to a cross coupling reaction, the organotrifluoroborate slowly releases the requisite organoboronic acid *in situ* under coupling conditions.<sup>141</sup> However, this slow-release is valuable as a “strategy” only when the hydrolysis rate of the organotrifluoroborate is comparable to the rate of Pd-catalyzed turnover.<sup>107,138,140-146</sup> For example, when organotrifluoroborates hydrolyze too rapidly, the boronic acid accumulates and can undergo unwanted side reactions. By the same token, if organotrifluoroborates hydrolyze too slowly, transmetalation is hindered because the trifluoroborate is not able to coordinate to the metal and hence other metal-mediated side reactions can predominate. Therefore, inasmuch as trifluoroborate solvolysis must occur to supply the reaction with the needed organoboronic acid, understanding the molecular components that govern the hydrolytic stability of organotrifluoroborates is of critical importance.<sup>140</sup>

While the chemistry of organoboronic acids may be of great interest to mainstream organometallic chemists, the need to predict and control the hydrolytic stability of organotrifluoroborates has shown to be important for other applications that form the

basis of this thesis. In the Perrin lab, organotrifluoroborates are being developed as radioprosthesis for *in vivo* PET imaging.<sup>102,103,107,111</sup> As demonstrated in Chapter 2, slow solvolytic stability of organotrifluoroborates, which might actually be disadvantageous for Suzuki-Miyaura coupling, is of paramount importance for developing a successful <sup>18</sup>F-radiosynthon. Otherwise, poor solvolytic stability can result in higher than expected and unspecific bone uptake of the <sup>18</sup>F-fluoride, which might in turn significantly prevent the detection of bone metastasis.<sup>125</sup>

In 2008, Perrin and coworkers showed that at neutral pH or higher, aryltrifluoroborates solvolyze in a nearly pH-independent mechanism that is consistent with much earlier reports on pH-independent solvolysis of a tetrafluoroborate.<sup>103,111</sup> Loss of the first fluorine atom was rate-limiting and no intermediate mono- or di-fluorinated species could be detected, suggesting ephemeral lifetimes for these species. The main contribution to solvolysis was determined by the electronic nature of ring substituents. By analogy to substituted benzyltosylates and cumyl chlorides, delocalization of electron density from the arene pi-system into the empty p-orbital on boron would weaken the B-F bond and concomitantly lead to the release of a fluoride atom leaving a difluoroborane that is so unstable that it immediately undergoes hydration and further solvolysis. Hence, pi-donating groups on the aryl ring greatly enhance aryltrifluoroborate solvolysis while electron-withdrawing substituents retard it. A linear free energy relationship ( $\log[k/k_0] = \rho\sigma$ ) was established for which  $\rho$  was found to be  $\sim -1$ .<sup>103</sup> N-heterocycles, which are even more electron deficient by comparison, showed profoundly retarded solvolysis rates.<sup>103</sup>

In 2012, Lloyd-Jones and coworkers published their remarkable work on the hydrolysis rates of organotrifluoroborates under conditions initially described by Molander for metal-catalyzed cross coupling.<sup>140</sup> In that work, they found a similar linear correlation that corroborates Dr. Perrin's discovery.<sup>103</sup> Yet hydrolytic solvolysis of aryltrifluoroborates is easily understood because it mainly depends on the relationship between the pi-electron cloud of the aromatic ring and its overlap into an empty p-orbital on boron. However, we cannot extend such linear correlation to non-aromatic organotrifluoroborates, for which the hydrolytic stability is determined through inductive effects (*-I*) of adjacent functional groups.

In order to identify a relationship between composition and solvolytic stability/liability, nonaromatic organotrifluoroborates must be considered separately from aryltrifluoroborates to establish a viable mechanistic understanding. While Jones *et al.* investigated several organotrifluoroborates comprising both aromatic and nonaromatic moieties, in considerable detail by application of Swain-Lupton parameters, the correlation with substituent effects was not immediately forthcoming in that work.<sup>140,142</sup> Indeed, substituent effects on the rate of nonaromatic organotrifluoroborate hydrolysis have not been systematically explored to date. Notwithstanding the lack of a stability study, an increasing amount of work has involved a plethora of nonaromatic organotrifluoroborates in C-C bond formations via Suzuki-Miyaura reactions.<sup>142,147</sup> We hypothesized that nonaromatic organotrifluoroborates could be used as <sup>18</sup>F-radiosynthons provided that a suitably stable organotrifluoroborate could be found. Hence the search for stable organotrifluoroborates would take on a new and heightened direction in this thesis in the race towards a fully clinical application that would feature one-step <sup>18</sup>F-labeling via a pendent <sup>18</sup>F-organotrifluoroborate radioprosthesis. To do this, we methodically studied the relationships between the solvolytic stability and the substituents on various nonaromatic organotrifluoroborates.

Prior to this analysis, we realized that the substituent parameters of most nonaromatic organotrifluoroborates are uncertain or difficult to measure or even calculate. Simply stated, there was no report in the vast literature that ever described the molecular components that would alter the solvolysis rate of a nonaromatic organotrifluoroborate. Indeed, when I took on this specific project, as it related to my thesis, I found myself in entirely uncharted waters. In order to describe the electronic properties of various substitutes, we needed to conceive of a qualitative if not a quantitative molecular understanding through which we could ultimately teach others how to develop suitably substituted organotrifluoroborates for PET imaging. To begin, we considered the pKa of the corresponding carboxylic acids they often relate the chemical composition of neighboring substituents to the fundamental property of acidity. As known, an adjacent electron-withdrawing group can increase the acidity of carboxylic acid. Yet unknown to anyone was to what extent such an electron-withdrawing group would also stabilize an adjacent trifluoroborate under aqueous conditions. Even if one might have suggested that

this would be the case, there was no understanding as to what the magnitude of the stabilizing effect would be, if at all. Simply put, no one had ever measured this. We therefore hypothesized that the acidity of a given carboxylic acid would provide a suitable correlating variable for estimating hydrolytic stability of the corresponding organotrifluoroborate. There are two main reasons for this: (1) The pKa of most acetic acids have been accurately measured and determined for many different substituents and hence the pKa of a given carboxylic acid can be correlated with a given substituent; 2) Unlike substituent parameters ( $\sigma$ ), a pKa is a comprehensive value which represented not only the electronic environment of the side chain, but also reflects the potential field and steric effects.

In this chapter, our goal is to develop a practical molecular rubric to estimate the hydrolytic stability of nonaromatic organotrifluoroborates. Towards this end, assorted organotrifluoroborates were synthesized and studied through  $^{19}\text{F}$  NMR analysis. Through this work we discovered a heretofore unknown linear correlation between the log of the pseudo-first order solvolytic rate constant for a given organotrifluoroborate,  $\log k_{\text{solv}}(\text{B-F})$  and the pKa of the corresponding carboxylic acids. This linear correlation was unexpected and the details of its discovery are presented herein.

## 3.2 Results

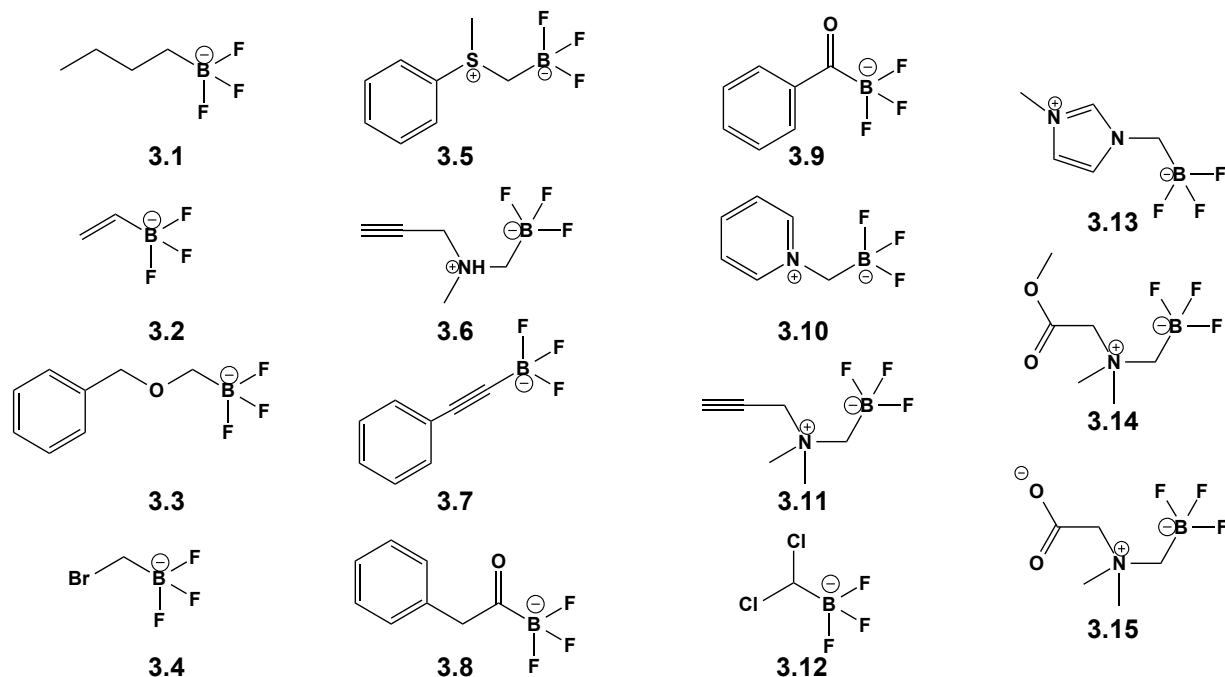


**Figure 3.1** Organotrifluoroborates used for analysis of solvolytic stability.

In order to address a comprehensive conclusion, a number of organotrifluoroborates are proposed for analysis shown in **Figure 3.1**. Their  $\alpha$ -substituents range from electron-donating groups to electron-withdrawing groups. Indeed, the most representative categories of organotrifluoroborates have been included (e.g. halo, ammonio, alkynyl, and acyl groups). Among the organotrifluoroborates, **compound 3.1**, **3.2**, **3.7**, **3.8** and **3.9** were purchased from commercial suppliers and then purified by flash silica chromatography (*via infra*). The rest of organotrifluoroborates were synthesized in our lab by me or several undergraduates who were supervised by Dr. Perrin and me. The procedures are detailed in the experimental session. In most cases, organotrifluoroborates were prepared according to previous reports, in near quantitative yields, by addition of a large excess of  $\text{KHF}_2$ , which is readily removed either by quick flash chromatography or by selective precipitation. Hence, we employed silica gel via a Pasteur pipette column to give pure, fluoride-free product, which was ready for  $^{19}\text{F}$ -NMR study to assess solvolytic stability.  $^{19}\text{F}$ -Purity and chemical identity were confirmed with ESI and  $^{19}\text{F}$ -NMR.

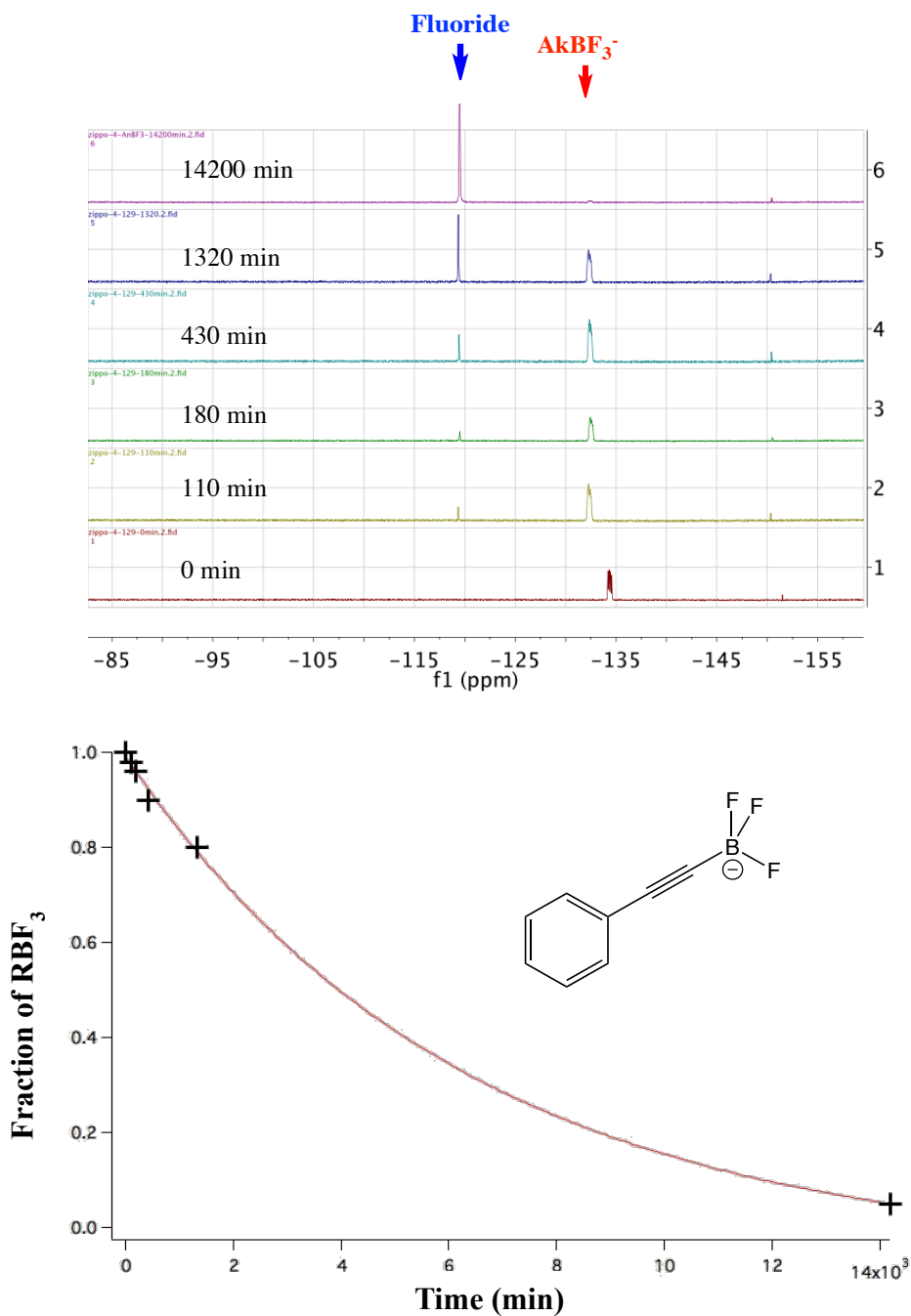


**Figure 3.2** (top):  $^{19}\text{F}$ -NMR kinetic analysis of the defluoridation from the  $^{19}\text{F}$ -**3.7** ( $^{19}\text{F}$ -Fluoride: -121 ppm relative to  $\text{CFCl}_3$ ;  $^{19}\text{F}$ -**3.7**: -137 ppm relative to  $\text{CFCl}_3$ ). **Figure 3.2** (bottom): Plot of relative  $^{19}\text{F}$ -NMR integration of the  $^{19}\text{F}$ -**3.7** as a function of all compounds ( $^{19}\text{F}$ -**3.7** +  $^{19}\text{F}$ -fluoride) vs. time. Data were fit to a first order reaction, and the half-life of the corresponding  $^{19}\text{F}$ -**3.7** was calculated to be 3800 min.

**Table 3.1** Summary of hydrolysis rate constant of organotrifluoroborates and the pK<sub>a</sub> of the corresponding carboxylic acid.

Half-life (min)	k <sub>(solv)</sub> (min <sup>-1</sup> )	pK <sub>solv.</sub>	pK <sub>a</sub> of acid	Compound #
2.3	3.1 • 10 <sup>-2</sup>	0.523	4.81	<b>3.1</b>
7.1	9.8 • 10 <sup>-2</sup>	1.01	4.25	<b>3.2</b>
145	4.8 • 10 <sup>-3</sup>	2.32	3.53	<b>3.3</b>
266	2.6 • 10 <sup>-3</sup>	2.57	NA	<b>3.15</b>
658	1.05 • 10 <sup>-3</sup>	2.98	2.86	<b>3.4</b>
3800	1.81 • 10 <sup>-4</sup>	3.74	2.45	<b>3.7</b>
4053	1.70 • 10 <sup>-4</sup>	3.77	2.34	<b>3.6</b>
8100	8.51 • 10 <sup>-5</sup>	4.07	2.35	<b>3.8</b>
10500	6.57 • 10 <sup>-5</sup>	4.18	2.15	<b>3.9</b>
10700	6.44 • 10 <sup>-5</sup>	4.19	2.14	<b>3.10</b>
22000	3.13 • 10 <sup>-5</sup>	4.50	1.83	<b>3.11</b>
150000	4.62 • 10 <sup>-6</sup>	5.34	1.29	<b>3.12</b>
460000	1.51 • 10 <sup>-6</sup>	5.82	NA	<b>3.5</b>

A representative <sup>19</sup>F-NMR spectroscopic analysis is shown in **Figure 3.2** to demonstrate the solvolytic stability assay of compound **3.7**. Solvolysis is formally a third order reaction. However, under dilute conditions solvolysis proceeds irreversibly at pH=7.4 whereby buffer removes the 2 equivalents of HF that are released thereby rendering the entire reaction irreversible.<sup>140</sup> Hence this proceeds with apparent pseudo-first order kinetics, owing to the fact that the release of the first fluoride is the rate-limiting step.<sup>103</sup> More interestingly, the hydrolytic defluoridation rate of organotrifluoroborate is essentially independent of the concentration of free fluoride, at least up to 100 mM F<sup>-</sup>, at pH 7 (data not shown). This implies that any intermediate mono- and/or difluoroborate will decompose rather than revert back to the organotrifluoroborate at pH=7.4. As shown,

the  $^{19}\text{F}$ -NMR signal of compound **3.7** (-137 ppm) decreases over a period of hours while the corresponding signal of free  $^{19}\text{F}$ -fluoride (-121 ppm) increases (**Figure 3.2 top**). The time dependent decomposition was fitted to a first order decay equation (**Figure 3.2 bottom**) with an apparent rate constant of  $(1.82\pm 0.13)\cdot 10^{-4}\text{ min}^{-1}$ , which gives an apparent solvolytic half-life of  $3800\pm 200\text{ min}$ .

Under the same protocol, 14 other organotrifluoroborates were studied and the measured half-life and rate constant  $k_{\text{sol}}$  are listed in **Table 3.1**. To simplify the correlation with the pKa of corresponding carboxylic acids, we defined  $-\log(k_{\text{sol}})$  as  $\text{pk}_{(\text{B-F})}$  to describe the stability of organotrifluoroborates. The larger the value of  $\text{pk}_{(\text{B-F})}$ , the longer the half-life and the more stable the organotrifluoroborate would be under aqueous conditions at  $\text{pH}=7.5$ . In addition, pKa values of the corresponding carboxylic acids are summarized and listed in **Table 3.1** as well. As desired, **Table 3.1** demonstrates that the more acidic the carboxylic acid becomes, the higher the solvolytic stability is afforded to the organotrifluoroborate. An increased pKa value gives a decreased  $\text{pk}_{(\text{B-F})}$  value. Eventually, to our great surprise, a nearly linear relationship is displayed when pKa and  $\text{pk}_{(\text{B-F})}$  are correlated (**Figure 3.3**).

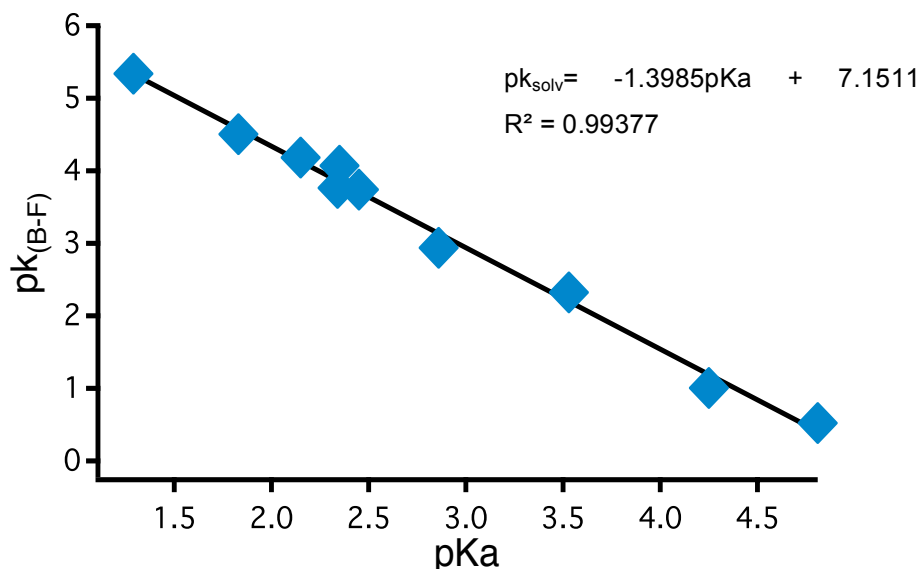


**Figure 3.3** Linear correlation between the logarithm of hydrolysis rate constant of organotrifluoroborates and the pKa of the corresponding carboxylic acid.

### 3.3 Discussion

Prior to my work on this project, this linear relationship was neither obvious nor easily predictable and its disclosure is unprecedented to the best of my knowledge. Hence we need to be critical with the collected data in order to address any and all inaccurate conclusions due to research error. Indeed, all organotrifluoroborates were purified using the same procedure and the  $^{19}\text{F}$ -NMR studies were performed under same conditions; the phosphate buffer, NMR instrument, brand of NMR tube, and room temperature ( $20 \pm 2$  °C) were kept consistent across all experiments. In order to achieve statistically reliable data to assess the hydrolytic stability of organotrifluoroborates and to calculate the  $\text{pk}_{(\text{B-F})}$  values, more than 5 time points were collected for each  $^{19}\text{F}$ -NMR assay and statistical errors have been considered as shown in **Table 3.1**. Another major error could potentially be introduced through an incorrectly measured pKa value.

Lloyd-Jones et al. previously studied organotrifluoroborate hydrolysis with B-F bond length analysis by DFT (density functional theory) calculations in order to provide insight with regards to the Suzuki-Miyaura reaction.<sup>140</sup> Their results led to a grouping of organotrifluoroborates based on whether the organotrifluoroborates would exhibit “fast”, “slow”, or “very slow” hydrolysis rates, which led to grouping the organotrifluoroborates into three classes. Class I organotrifluoroborates, of which the substituents are alkyl, cycloalkyl, alkenyl, or electron-rich aryls, undergo very rapid hydrolysis under Suzuki-Miyaura coupling conditions and even more rapidly in phosphate buffer. These organotrifluoroborates can generate the corresponding boronic acids far faster than they are consumed in coupling reactions, resulting in the generation of byproducts and lower chemical yields in regards to the Suzuki-Miyaura reaction. Class II organotrifluoroborates, of which the half-life is between 1-24 hours under Suzuki-Miyaura coupling conditions, or 10-100 min in phosphate buffer (pH=7.4), afford controlled release of boronic acids under Suzuki-Miyaura coupling conditions. These types of organotrifluoroborates generated fewer by-products and subsequently afforded higher chemical yields. Class III organotrifluoroborates, which are rather hydrolytically resistant and have the half-life of >1 day under Suzuki-Miyaura coupling conditions,

require days or weeks for conversion of the boronic acid, and may proceed via a different mechanism that remains to be fully understood for Suzuki-Miyaura coupling reactions.<sup>148</sup>

It is clear that knowing the hydrolytic stability of certain organotrifluoroborates can be very helpful in order to estimate their chemical reactivity for the Suzuki-Miyaura coupling reaction.<sup>142,147</sup> Yet while assessing hydrolytic stability of organotrifluoroborates is doable, the experimental procedure can be time consuming or even impractical. This problem is particularly serious when a vast number of organotrifluoroborates may be required for testing or in cases where the trifluoroborate is too precious to waste. To avoid this issue, here I suggest an alternative solution of using the pKa value of a certain carboxylic acid as a surrogate for classifying a given organotrifluoroborate. Using the correlation in **Figure 3.3**, I summarize three pKa windows of carboxylic acids, of which the corresponding organotrifluoroborates participated in Suzuki-Miyaura coupling reactions under three pathways (*via infra*): (1) for a carboxylic acid of pKa >4.28, the corresponding organotrifluoroborate will undergo very fast hydrolysis and belong to class I; (2) for a carboxylic acid whose pKa ranges between 3.57 to 4.28, the half-life of the corresponding organotrifluoroborate will range from 10 min to 100 min, thus belonging to class II; (3) for a carboxylic acid of pKa below 3.57, the hydrolysis of corresponding organotrifluoroborates can be remarkably slow and therefore belongs to class III.

Besides the broad application in assessing the reactivity of organotrifluoroborates under Suzuki-Miyaura coupling conditions, this linear correlation between pKa and  $pK_{(B-F)}$  also empowers us to identify and then develop the most promising organotrifluoroborate PET tracer from the organotrifluoroborate candidates. To be an ideal <sup>18</sup>F-radioprosthesis of great *in vivo* stability, the decomposition probably needs to be <2% in first 60 min at *in vivo* conditions otherwise non-negligible bone uptake would be detected during PET scanning.<sup>103,111,125</sup> Accordingly, an *in vivo* stable organotrifluoroborate candidate should have a half-life of >4700 min based on <sup>19</sup>F-NMR spectroscopic analysis, which implies that the corresponding carboxylic acids should have a pKa of <2.37. Meanwhile, based on previous labeling studies using <sup>18</sup>F-<sup>19</sup>F isotope exchange (IEX), the greater solvolytic stability that an organotrifluoroborate exhibits, the more slowly it will undergo IEX and therefore may afford a lower radiochemical yield. This negative correlation between

solvolytic stability and radiochemical yield is simply a restatement of the law of microscopic reversibility. However to date there is no good correlation between  $pK_{(B-F)}$  and the rate of isotope exchange or maximum yield in a 15 minute labeling and establishing this relationship would require additional study. Currently, we can routinely work with 1 Curie of  $^{18}\text{F}$ -fluoride; hence, a 10% radiochemical yield would still generate multiple patient doses that should be satisfactory for use as a new PET radioprosthesis used in one-step labeling for PET.<sup>89</sup> While I have identified organotrifluoroborates with solvolytic half-lives as long as 100000 min, generally those with a half-life of  $\sim 20000$  have in our hands provided sufficiently high radiochemical yields with sufficiently high specific activity. Hence I suggest that any organotrifluoroborate designed from a corresponding carboxylic acid with a  $pK_a$  of  $\sim 2.40$  or less would behave suitably *in vivo* and therefore would be useful for PET imaging. To wit, in the following chapters this assertion would be tested and ultimately validated *in vivo* with excellent tumor images. In summary, in order to develop a new trifluoroborate radiosynthon that enables a combination of good *in vivo* stability and satisfying radiochemical performance, organotrifluoroborate compositions will be preferred based on corresponding carboxylic acids with  $pK_a$ 's in the range of 1.80-2.35.

### 3.4 Conclusion

In this work, I used  $^{19}\text{F}$ -NMR spectroscopic analysis to successfully establish an unexpected correlation between the solvolytic rate constant of a nonaromatic organotrifluoroborate with the  $pK_a$  of a corresponding carboxylic acid. This linear correlation demonstrates that the  $pK_a$  of acetic acids can be a powerful tool for assessing the solvolytic stability of organotrifluoroborates. Depending on the  $pK_a$ , organotrifluoroborate may be divided into three classes, with each class of organotrifluoroborates undergoing a different pathway during Suzuki-Miyaura coupling reactions. In addition, another important application of this correlation has been established as shown in the development of new organotrifluoroborate radioprosthesis for PET imaging. Using this newly identified molecular relationship; we have designed the first  $^{18}\text{F}$ -labeled organotrifluoroborate radioprosthesis and tested its properties *in vivo*.

## 3.5 Experimental

### 3.5.1 Synthesis

#### Synthesis of benzyloxymethyltrifluoroborate (3.3)

A flame-dried round bottom flask was charged with a mixture of NaH (0.18 g, 7.5 mmol) and THF (12 mL). This slurry was cooled to 0 °C and followed by drop-wise addition of benzylalcohol (0.73 mL, 7.5 mmol) to give a mixture which was incubated in an ice bath for 30 min. Bromomethyltrifluoroborate (0.5 g, 2.5 mmol) was then added in one portion, and the temperature raised to room temperature for 3 hours. The alkylation was monitored by <sup>19</sup>F-NMR, and the solvent was removed under vacuum when the reaction was completed. The residue was extracted with MeCN (3 x 20 ml). All the extractions were combined and concentrated under vacuum. Compound **3.3** was achieved through MeCN/diethyl ether precipitation, and the purity and chemical identity were confirmed with <sup>19</sup>F-NMR and mass spectrometry. ESI: [M]<sup>-</sup> calculated: 189.07 obtained: 189.1.

#### Synthesis of bromomethyltrifluoroborate (3.4)

CH<sub>2</sub>Br<sub>2</sub> (0.38 mL, 5.5 mmol) and triisopropylborate (1.22 mL, 5.3 mmol) were added to a flame-dried round bottom flask along with anhydrous THF (12 mL). The mixture was cooled to -78 °C and followed by drop-wise addition of butyllithium (3.2 mL, 5.1 mmol). The reaction was stirred at -78 °C for another 2.5 hours and then quenched with anhydrous HCl (0.63 mL, 2.5 mmol). The reaction was allowed to warm up to 0 °C and followed by fluorination with 3 equiv. KHF<sub>2</sub> (1.17 g, 15 mmol) at room temperature for 2 hours. The solvent was removed via rotary-evaporation and the residue was purified through MeCN/diethyl ether precipitation to give compound **3.3** (0.4465 g, 2.79 mmol). Yield: 53%. ESI: [M]<sup>-</sup> calculated: 160.94 obtained: 161.0.

#### Synthesis of S-methylphenylsulfoniomethyltrifluoroborate (3.5)

AgClO<sub>4</sub> (225 mg, 1.1 mmol) was dissolved in dry MeCN (5 mL) in a flame-dried round bottom flask. Behind a blast shield, iodomethylborate pinacol ester (182 μL, 1.0 mmol) was added drop-wise to achieve a clear yellowish solution. Methylphenylthioether (1.17

mL, 10 mmol), previously diluted in MeCN (10 mL), was then slowly added into the flask via syringe. A large amount of yellow precipitation was observed and then removed by centrifuge. The supernatant was concentrated and followed by fluorination with KHF<sub>2</sub> (6 M KHF<sub>2</sub> water solution, 1 mL, 6 mmol). The crude reaction was purified by MeCN/diethyl ether precipitation to give compound **3.5** (180 mg, 87% yield). ESI: [M+K]<sup>+</sup> calculated: 245.05; obtained: 245.05.

### **Synthesis of N-methylpropargylaminomethyltrifluoroborate (3.6)**

N-methylpropargylamine (102  $\mu$ L, 1.0 mmol) was dissolved in anhydrous THF (5 mL) in a flame-dried round bottom flask. At room temperature, iodomethylborate pinacol ester (91  $\mu$ L, 0.5 mmol) was added drop-wise into the solution over 5 min. The reaction was incubated at room temperature for 30 min and subsequently the solvent was removed by rotary-evaporation. The residue was fluorinated with KHF<sub>2</sub> (6 M KHF<sub>2</sub> water solution, 1 mL, 6 mmol) and purified by MeCN/diethyl ether precipitation to give compound **3.6**. ESI: [M-F]<sup>+</sup> calculated: 132.08; obtained: 132.1.

### **Synthesis of pyridinomethyltrifluoroborate (3.10)**

AgClO<sub>4</sub> (225 mg, 1.1 mmol) was dissolved into dry MeCN (5 mL) in a flame-dried round bottom flask. Behind a blast shield, iodomethylborate pinacol ester (182  $\mu$ L, 1.0 mmol) was added drop-wise to achieve a clear yellowish solution. Pyridine (804 mL, 10 mmol) was previously diluted in MeCN (10 mL) and then slowly added into the flask via syringe. A large amount of yellow precipitation was observed and then removed by centrifuge. The supernatant was concentrated and followed by fluorinating with KHF<sub>2</sub> (6 M KHF<sub>2</sub> water solution, 1 mL, 6 mmol). The crude reaction was purified by MeCN/diethyl ether precipitation to give compound **3.10** (82 mg, 51% yield). ESI: [M-F]<sup>+</sup> calculated: 142.93; obtained: 143.0.

### **Synthesis of N,N-dimethylpropargylaminomethyltrifluoroborate (3.11)**

N,N-dimethylpropargylamine (102  $\mu$ L, 1.0 mmol) was dissolved into anhydrous diethyl ether (5 mL) in a flame-dried round bottom flask. At room temperature, iodomethylborate pinacol ester (182  $\mu$ L, 1.0 mmol) was added drop-wise into the solution over 5 min. The

alkylated product was precipitated from the solution as a fluffy white powder, which was achieved via filtration and then dried under vacuum. This alkylated boronic ester was fluorinated with  $\text{KHF}_2$  (6 M  $\text{KHF}_2$  water solution, 1 mL, 6 mmol) and purified by a self-assembled silica column to give compound **3.6**. ESI:  $[\text{M-F}]^+$  calculated: 146.09; obtained: 146.1.

### **Synthesis of dichloromethyltrifluoroborate (3.12)**

Butyllithium (0.32 mL, 0.5 mmol) was added drop-wise to diisopropylamine (0.085 mL, 0.6 mmol) in 10 mL anhydrous THF cooled in a dry ice/acetone bath. To this cold solution of lithium diisopropylamide (LDA), DCM (0.038 mL, 0.55 mmol) was added drop-wise via a syringe and the mixture was incubated at  $-78\text{ }^\circ\text{C}$  for 1 hour.

After that, trimethylborate (0.057 mL, 0.5 mmol) was slowly added in a flame-dry round bottom flask and the mixture was allowed to warm up to  $0\text{ }^\circ\text{C}$ . This was followed by fluorination with  $\text{KHF}_2$  (0.3 mL 6 M  $\text{KHF}_2$  water solution, 1.8 mmol) at room temperature for 2 hours. The solvent was removed via rotary-evaporation and the residue was purified through MeCN/diethyl ether precipitation to give compound **3.12** (0.045 g, 0.298 mmol). Yield: 60%. ESI:  $[\text{M}]^-$  calculated: 150.95 (100.0%), 152.95 (63.9%), obtained: 151.0 (100.0%), 153.0 (63.9%).

### **Synthesis of N-methylimidazolymethyltrifluoroborate (3.13)**

$\text{AgClO}_4$  (123 mg, 0.6mmol) was dissolved into dry MeCN (5 mL) in a flame-dried round bottom flask. Behind a blast shield, iodomethylborate pinacol ester (91  $\mu\text{L}$ , 0.5 mmol) added drop-wise to achieve a clear yellowish solution. N-methylimidazole (398  $\mu\text{L}$ , 5 mmol) was diluted previously in MeCN (10 mL) and then slowly added into the flask via syringe. A large amount of yellow precipitation was observed and then removed by centrifuge. The supernatant was concentrated and followed by fluorinating with  $\text{KHF}_2$  (6 M  $\text{KHF}_2$  water solution, 0.5 mL, 3 mmol). The crude reaction was and purified by a self-assembled silica column to give compound **3.13**. ESI:  $[\text{M-F}]^+$  calculated: 145.07; obtained: 145.1.

### **Synthesis of N,N-dimethylglyciniomethyltrifluoroborate methyl ester (3.14)**

N,N-dimethylglycine methyl ester (125  $\mu\text{L}$ , 1.0 mmol) was dissolved in anhydrous diethyl ether (5 mL) in a flame-dried round bottom flask. At room temperature, iodomethylborate pinacol ester (182  $\mu\text{L}$ , 1.0 mmol) was added drop-wise into the solution over 5 min. The alkylated product was precipitated from the solution as a fluffy white powder, which was achieved via filtration and then dried under vacuum. This alkylated boronic ester was fluorinated with  $\text{KHF}_2$  (6 M  $\text{KHF}_2$  water solution, 1 mL, 6 mmol) and purified by a self-assembled silica column to give compound **3.6**. ESI:  $[\text{M-F}]^+$  calculated: 180.10; obtained: 180.1.

### **Synthesis of N,N-dimethylglycine methyltrifluoroborate (3.15)**

N,N-dimethylglycine methyltrifluoroborate methyl ester (19.9  $\mu\text{L}$ , 0.1 mmol) was dissolved into the mixture of NaOH (2 M, 100  $\mu\text{L}$ , aq) and MeCN (100  $\mu\text{L}$ ) in a 1.5 mL Eppendorf tube. The reaction was incubated at 45  $^\circ\text{C}$  for 2 hours and then purified by a self-assembled silica column to give compound **3.15**. ESI:  $[\text{M}]^-$  calculated: 184.08; obtained: 184.1.

### 3.5.2 $^{19}\text{F}$ -NMR analysis of the solvolysis of organotrifluoroborates

To assess the hydrolytic stability of the following organotrifluoroborates, I used the same experimental protocol that has been detailed in Chapter 2.

#### 3.5.2.1 Butyltrifluoroborate (3.1)

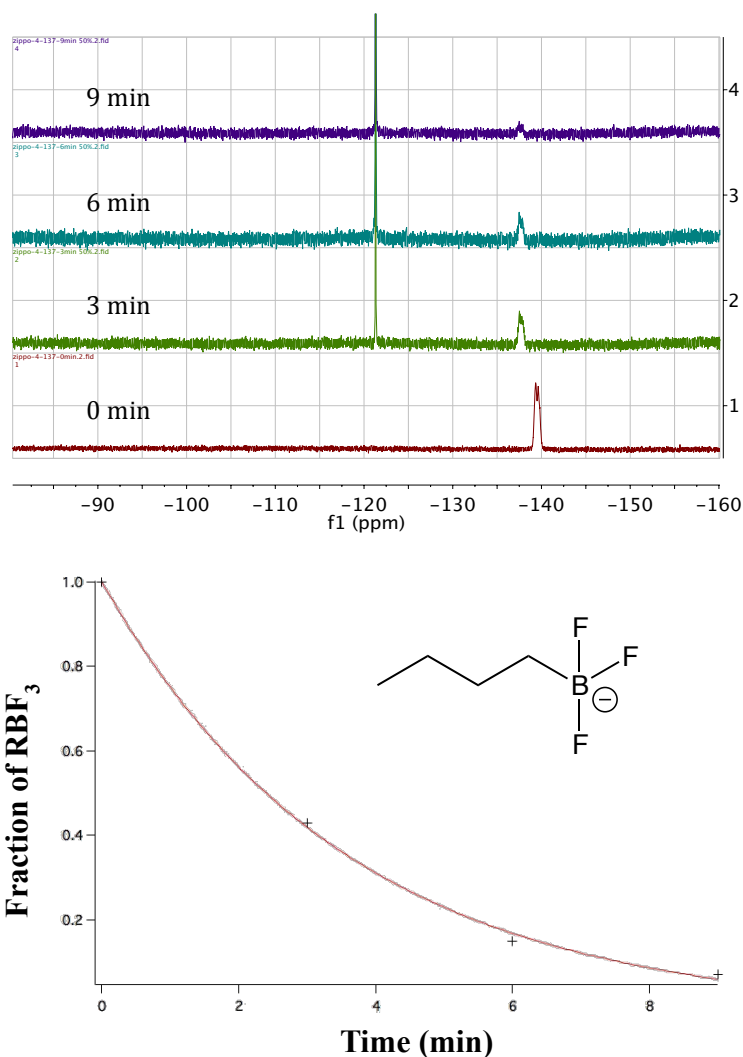


**Figure 3.4** (top):  $^{19}\text{F}$ -NMR kinetic analysis of the defluoridation from the  $^{19}\text{F}$ -organotrifluoroborate ( $^{19}\text{F}$ -Fluoride: -121 ppm relative to  $\text{CFCl}_3$ ;  $^{19}\text{F}$ -organotrifluoroborate: -139 ppm relative to  $\text{CFCl}_3$ ). **Figure 3.4** (bottom): Plot of relative  $^{19}\text{F}$ -NMR integration of the organotrifluoroborate as a function of all compounds ( $^{19}\text{F}$ -organotrifluoroborate +  $^{19}\text{F}$ -fluoride) vs. time.

### 3.5.2.2 Vinyltrifluoroborate (3.2)

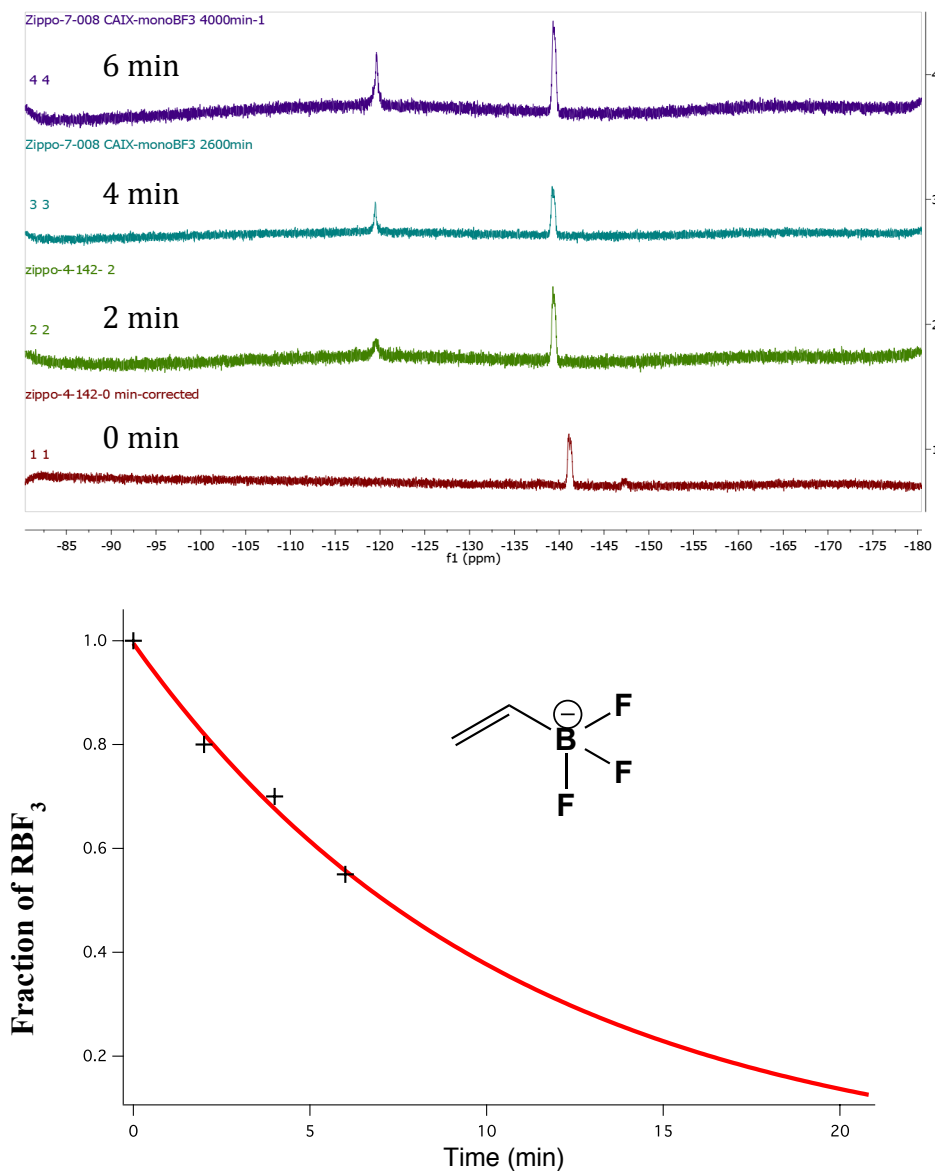


**Figure 3.5** (top):  $^{19}\text{F}$ -NMR kinetic analysis of the defluorination from the  $^{19}\text{F}$ -organotrifluoroborate ( $^{19}\text{F}$ -Fluoride: -121 ppm relative to  $\text{CFCl}_3$ ;  $^{19}\text{F}$ -organotrifluoroborate: -141 ppm relative to  $\text{CFCl}_3$ ). **Figure 3.5** (bottom): Plot of relative  $^{19}\text{F}$ -NMR integration of the organotrifluoroborate as a function of all compounds ( $^{19}\text{F}$ -organotrifluoroborate +  $^{19}\text{F}$ -fluoride) vs. time.

### 3.5.2.3 Bromomethyltrifluoroborate (3.4)

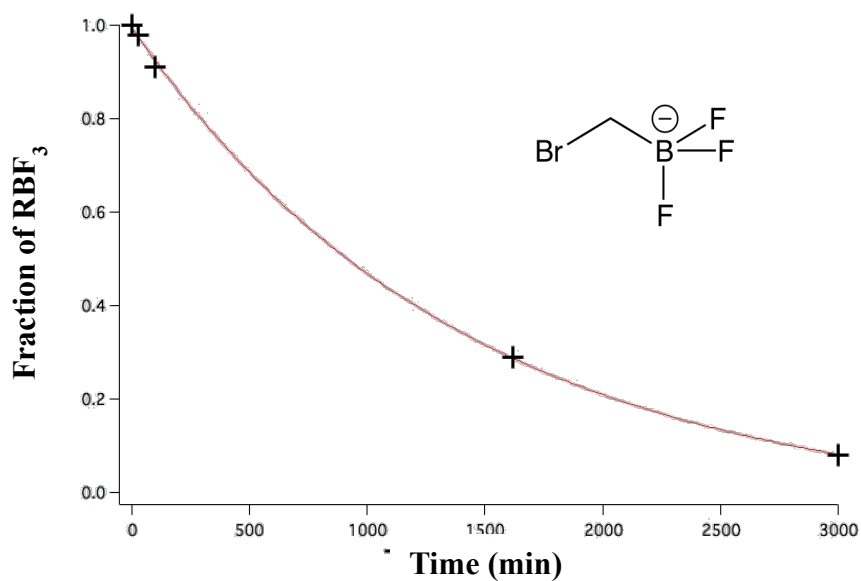
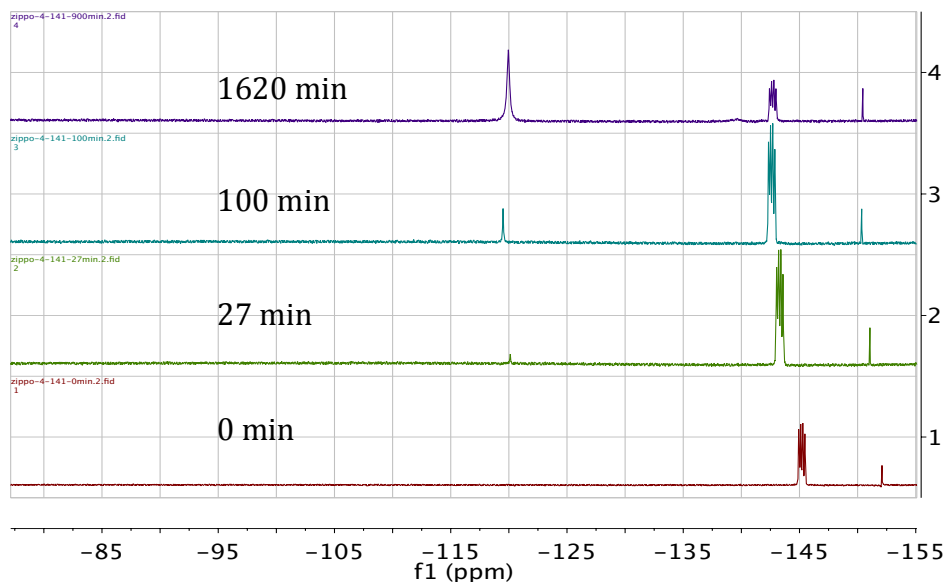


**Figure 3.6** (top):  $^{19}\text{F}$ -NMR kinetic analysis of the defluorination from the  $^{19}\text{F}$ -organotrifluoroborate ( $^{19}\text{F}$ -Fluoride: -121 ppm relative to  $\text{CFCl}_3$ ;  $^{19}\text{F}$ -organotrifluoroborate: -145 ppm relative to  $\text{CFCl}_3$ ). **Figure 3.6** (bottom): Plot of relative  $^{19}\text{F}$ -NMR integration of the organotrifluoroborate as a function of all compounds ( $^{19}\text{F}$ -organotrifluoroborate +  $^{19}\text{F}$ -fluoride) vs. time.

### 3.5.2.4 Sulfoniummethyltrifluoroborate (3.5)

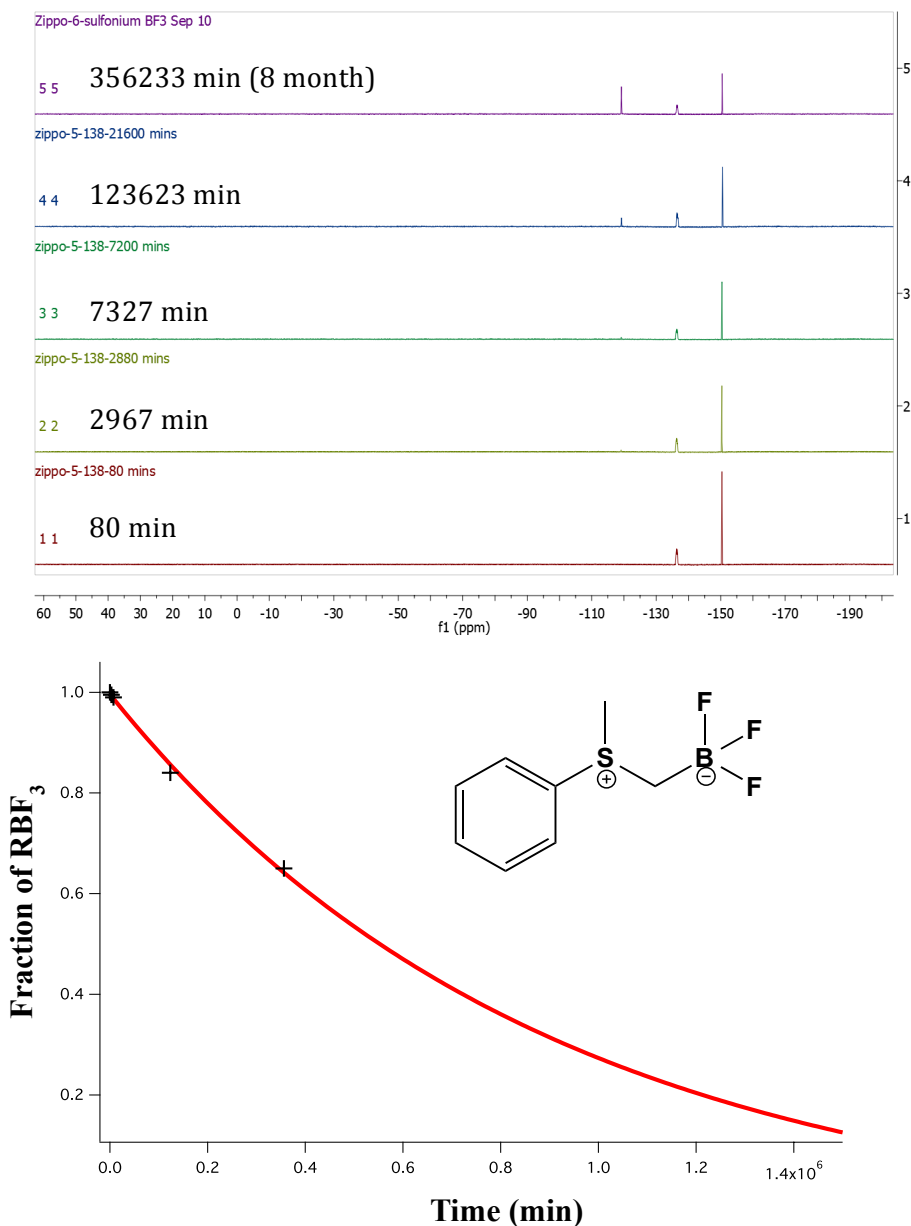


**Figure 3.7** (top):  $^{19}\text{F}$ -NMR kinetic analysis of the defluoridation from the  $^{19}\text{F}$ -organotrifluoroborate ( $^{19}\text{F}$ -Fluoride: -121 ppm relative to  $\text{CFCl}_3$ ;  $^{19}\text{F}$ -organotrifluoroborate: -136 ppm relative to  $\text{CFCl}_3$ ). **Figure 3.7** (bottom): Plot of relative  $^{19}\text{F}$ -NMR integration of the organotrifluoroborate as a function of all compounds ( $^{19}\text{F}$ -organotrifluoroborate +  $^{19}\text{F}$ -fluoride) vs. time.

### 3.5.2.5 Ammoniomethyltrifluoroborate (3.6)

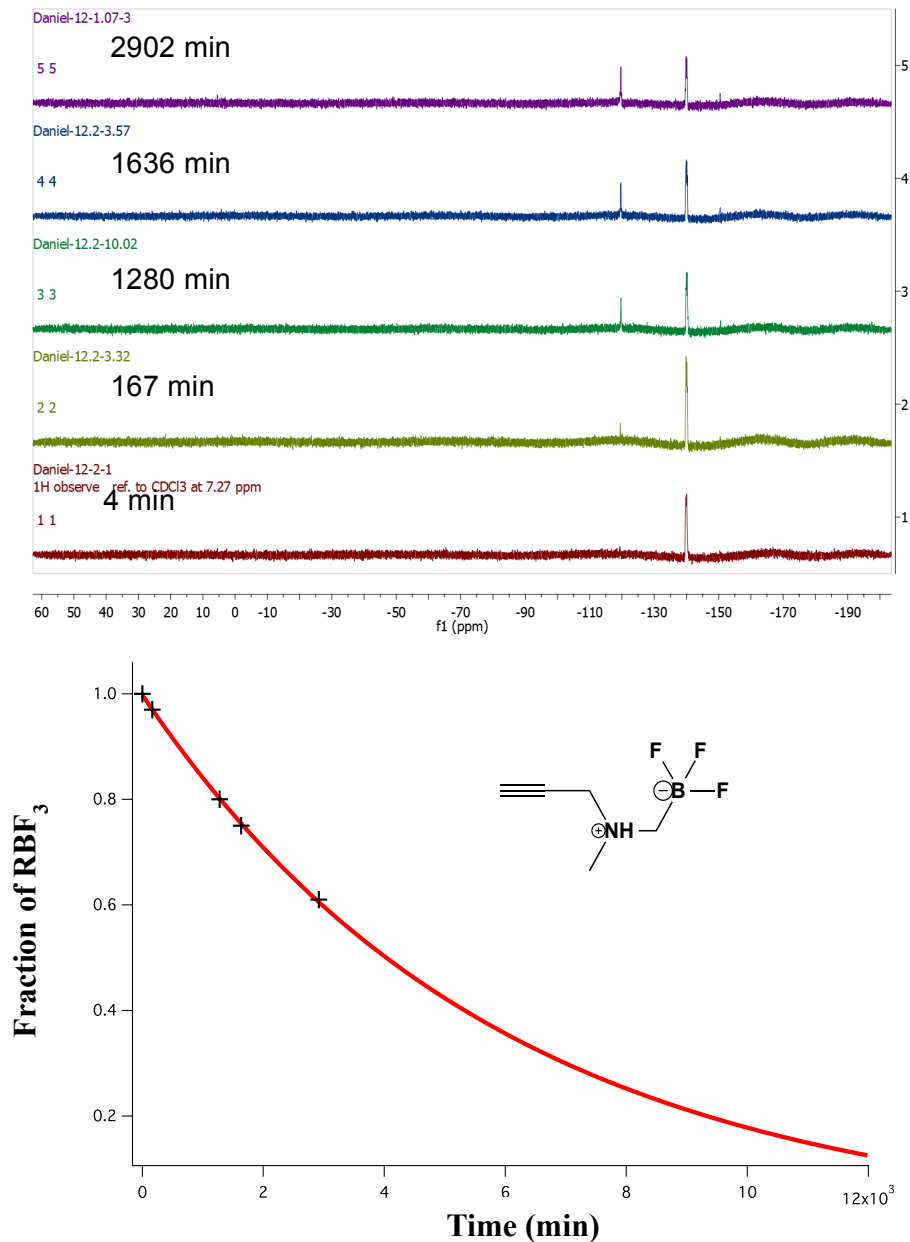


**Figure 3.8** (top):  $^{19}\text{F}$ -NMR kinetic analysis of the defluoridation from the  $^{19}\text{F}$ -organotrifluoroborate ( $^{19}\text{F}$ -Fluoride: -121 ppm relative to  $\text{CFCl}_3$ ;  $^{19}\text{F}$ -organotrifluoroborate: -139 ppm relative to  $\text{CFCl}_3$ ). **Figure 3.8** (bottom): Plot of relative  $^{19}\text{F}$ -NMR integration of the organotrifluoroborate as a function of all compounds ( $^{19}\text{F}$ -organotrifluoroborate +  $^{19}\text{F}$ -fluoride) vs. time.

### 3.5.2.6 Phenacylmethyltrifluoroborate (3.8)

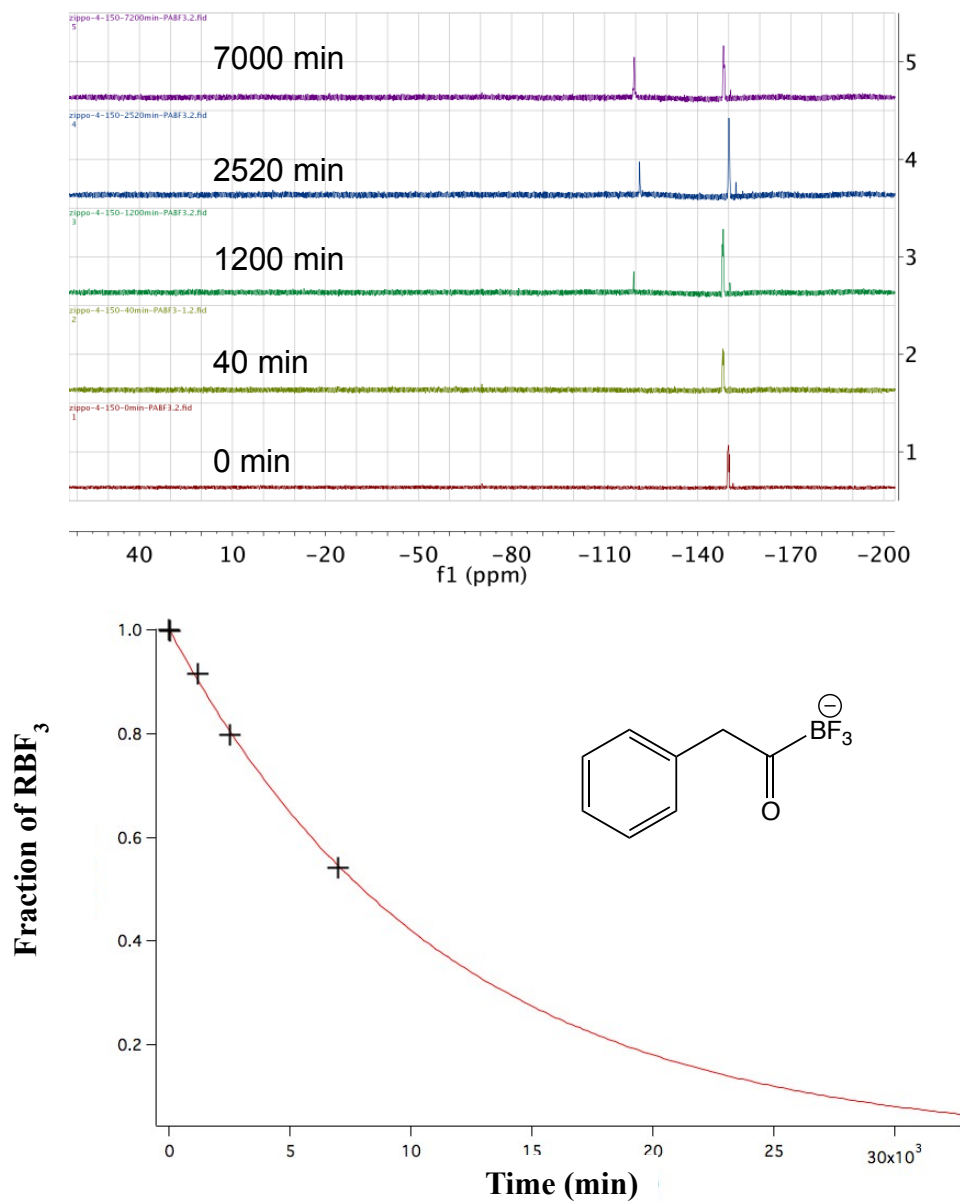


**Figure 3.9** (top):  $^{19}\text{F}$ -NMR kinetic analysis of the defluoridation from the  $^{19}\text{F}$ -organotrifluoroborate ( $^{19}\text{F}$ -Fluoride: -121 ppm relative to  $\text{CFCl}_3$ ;  $^{19}\text{F}$ -organotrifluoroborate: -149 ppm relative to  $\text{CFCl}_3$ ). **Figure 3.9** (bottom): Plot of relative  $^{19}\text{F}$ -NMR integration of the organotrifluoroborate as a function of all compounds ( $^{19}\text{F}$ -organotrifluoroborate +  $^{19}\text{F}$ -fluoride) vs. time.

### 3.5.2.7 Benzoylmethyltrifluoroborate (3.9)

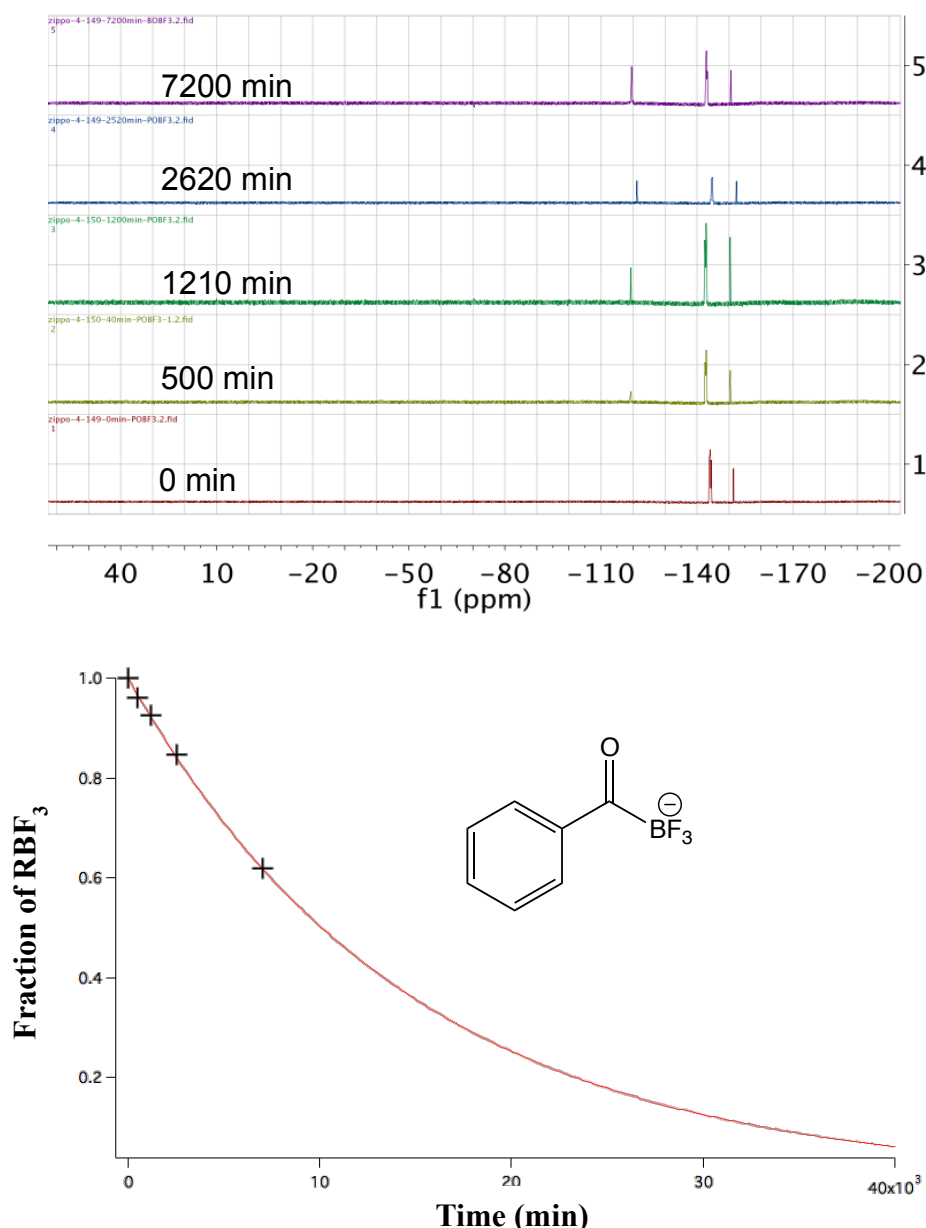


**Figure 3.10** (top):  $^{19}\text{F}$ -NMR kinetic analysis of the defluoridation from the  $^{19}\text{F}$ -organotrifluoroborate ( $^{19}\text{F}$ -Fluoride: -121 ppm relative to  $\text{CFCl}_3$ ;  $^{19}\text{F}$ -organotrifluoroborate: -143 ppm relative to  $\text{CFCl}_3$ ). **Figure 3.10** (bottom): Plot of relative  $^{19}\text{F}$ -NMR integration of the organotrifluoroborate as a function of all compounds ( $^{19}\text{F}$ -organotrifluoroborate +  $^{19}\text{F}$ -fluoride) vs. time.

### 3.5.2.8 Pyridiniummethyltrifluoroborate (3.10)

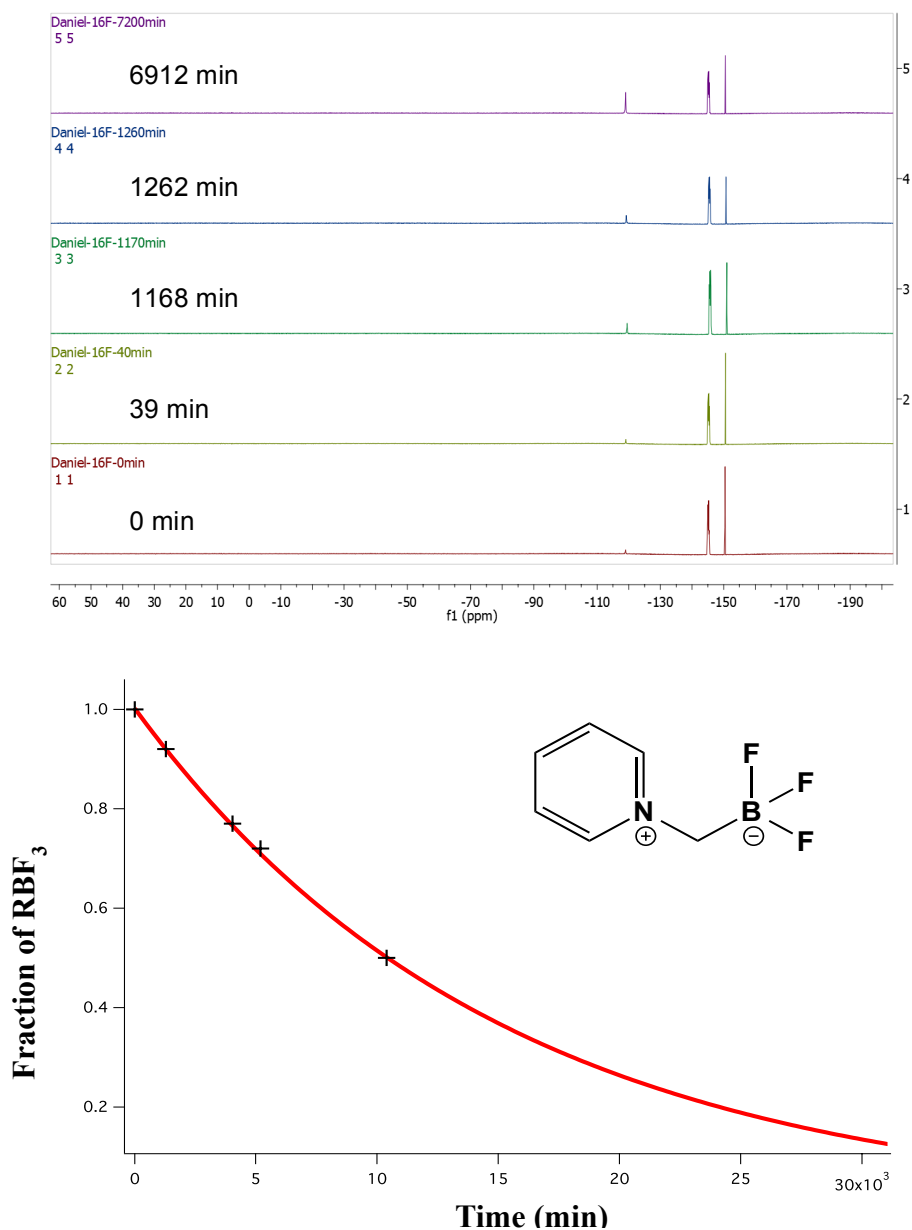


**Figure 3.11** (top):  $^{19}\text{F}$ -NMR kinetic analysis of the defluoridation from the  $^{19}\text{F}$ -organotrifluoroborate ( $^{19}\text{F}$ -Fluoride: -121 ppm relative to  $\text{CFCl}_3$ ;  $^{19}\text{F}$ -organotrifluoroborate: -144 ppm relative to  $\text{CFCl}_3$ ). **Figure 3.11** (bottom): Plot of relative  $^{19}\text{F}$ -NMR integration of the organotrifluoroborate as a function of all compounds ( $^{19}\text{F}$ -organotrifluoroborate +  $^{19}\text{F}$ -fluoride) vs. time.

### 3.5.2.9 Ammoniomethyltrifluoroborate (3.11)

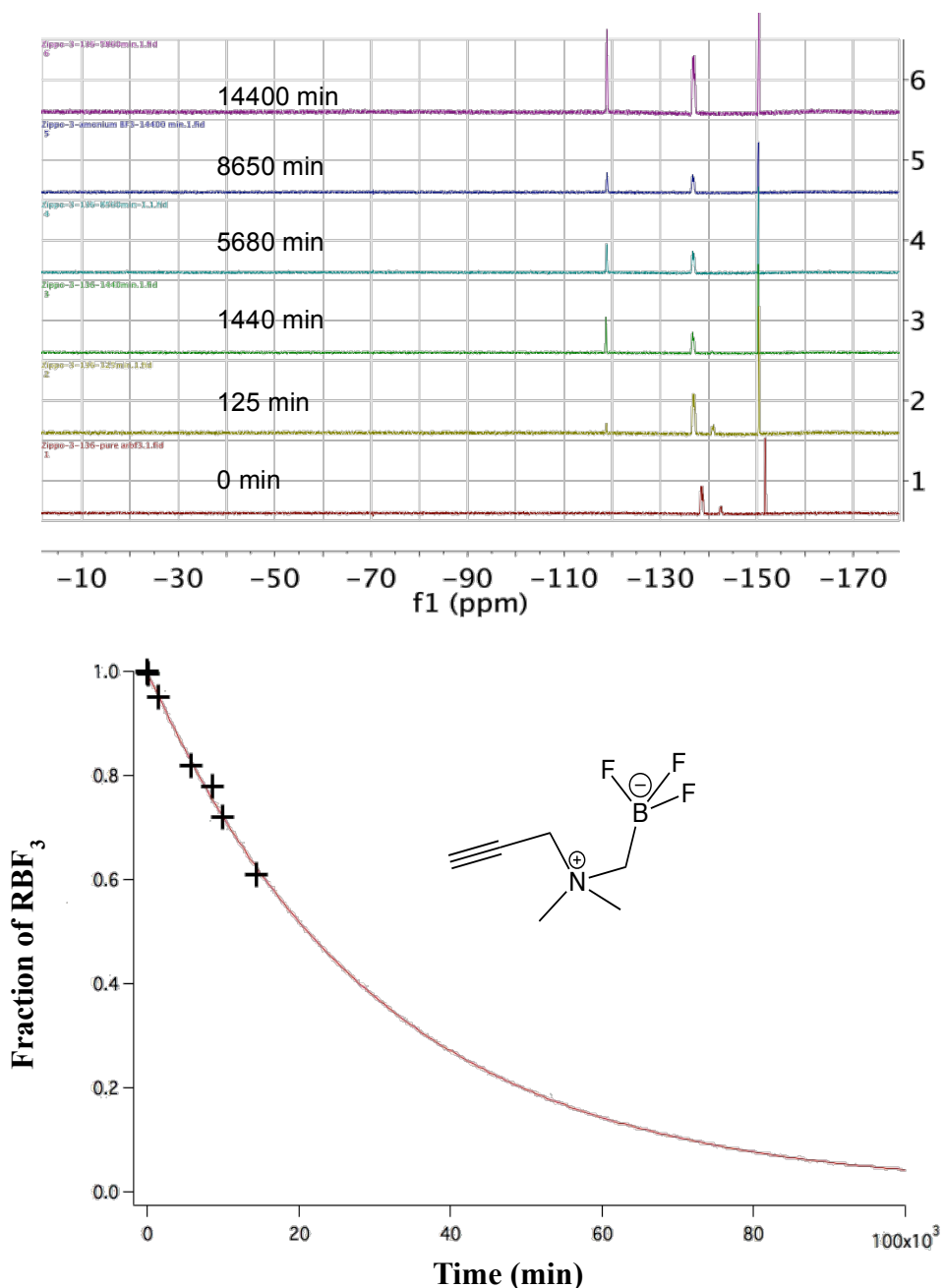


**Figure 3.12** (top):  $^{19}\text{F}$ -NMR kinetic analysis of the defluoridation from the  $^{19}\text{F}$ -organotrifluoroborate ( $^{19}\text{F}$ -Fluoride: -121 ppm relative to  $\text{CFCl}_3$ ;  $^{19}\text{F}$ -organotrifluoroborate: -138 ppm relative to  $\text{CFCl}_3$ ). **Figure 3.12** (bottom): Plot of relative  $^{19}\text{F}$ -NMR integration of the organotrifluoroborate as a function of all compounds ( $^{19}\text{F}$ -organotrifluoroborate +  $^{19}\text{F}$ -fluoride) vs. time.

### 3.5.2.10 Dichloromethyltrifluoroborate (3.12)

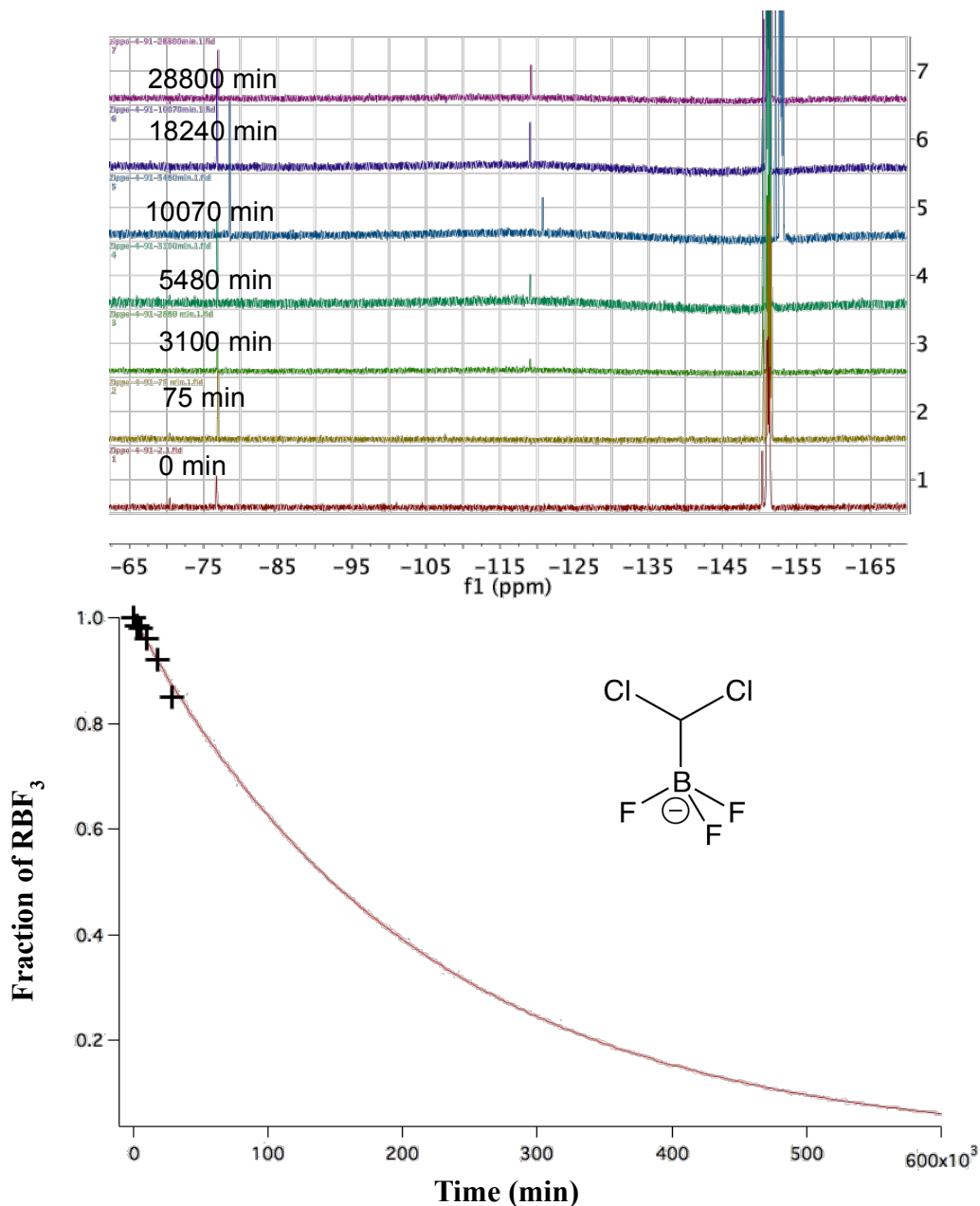


**Figure 3.13** (top):  $^{19}\text{F}$ -NMR kinetic analysis of the defluoridation from the  $^{19}\text{F}$ -organotrifluoroborate ( $^{19}\text{F}$ -Fluoride: -121 ppm relative to  $\text{CFCl}_3$ ;  $^{19}\text{F}$ -organotrifluoroborate: -147 ppm relative to  $\text{CFCl}_3$ ). **Figure 3.13** (bottom): Plot of relative  $^{19}\text{F}$ -NMR integration of the organotrifluoroborate as a function of all compounds ( $^{19}\text{F}$ -organotrifluoroborate +  $^{19}\text{F}$ -fluoride) vs. time.

### 3.5.2.11 Imidazolymethyltrifluoroborate (3.13)

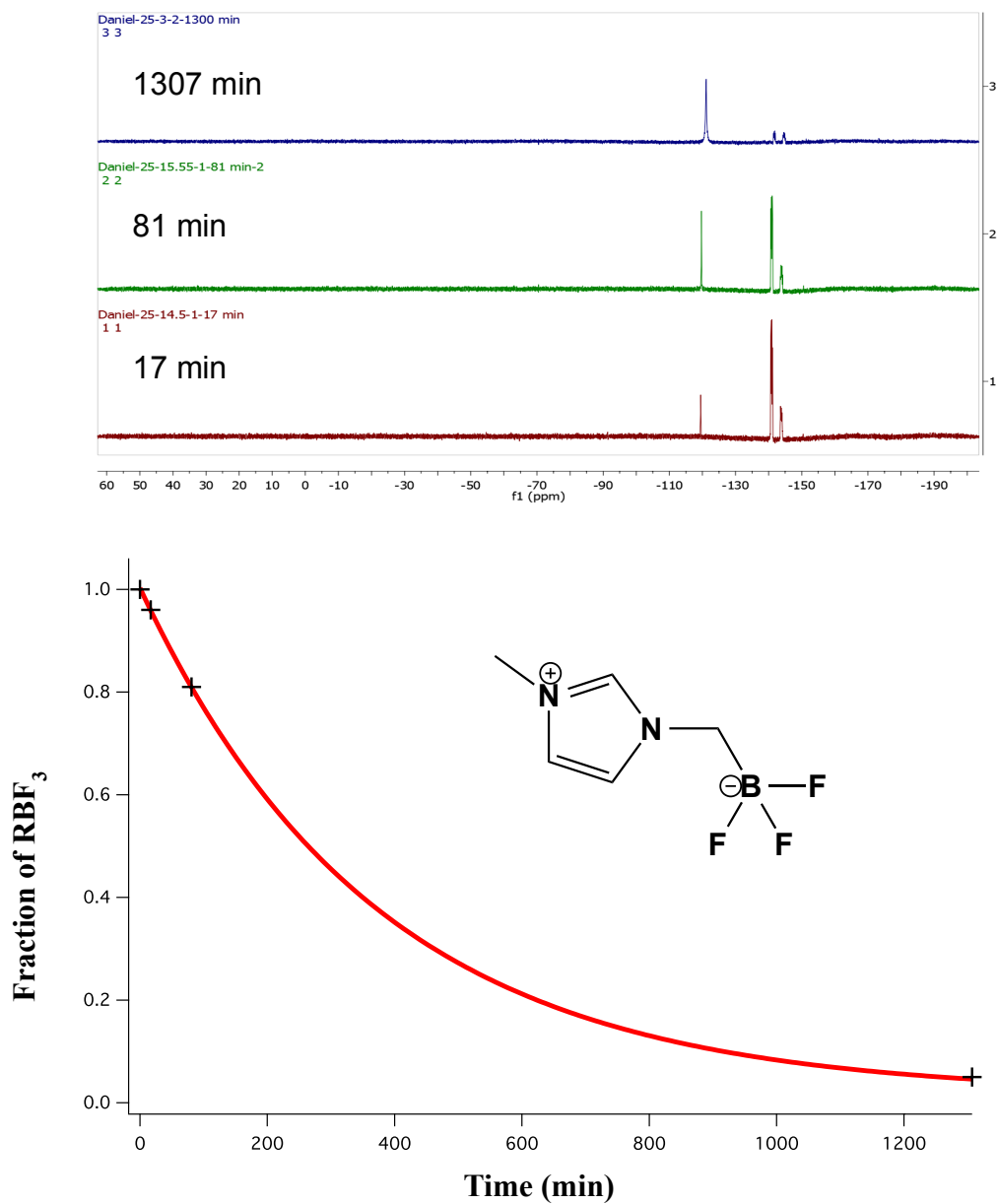


**Figure 3.14** (top):  $^{19}\text{F}$ -NMR kinetic analysis of the defluoridation from the  $^{19}\text{F}$ -organotrifluoroborate ( $^{19}\text{F}$ -Fluoride: -121 ppm relative to  $\text{CFCl}_3$ ;  $^{19}\text{F}$ -organotrifluoroborate: -139 ppm relative to  $\text{CFCl}_3$ ). **Figure 3.14** (bottom): Plot of relative  $^{19}\text{F}$ -NMR integration of the organotrifluoroborate as a function of all compounds ( $^{19}\text{F}$ -organotrifluoroborate +  $^{19}\text{F}$ -fluoride) vs. time.

### 3.5.2.12 Ammoniomethyltrifluoroborate (3.14)

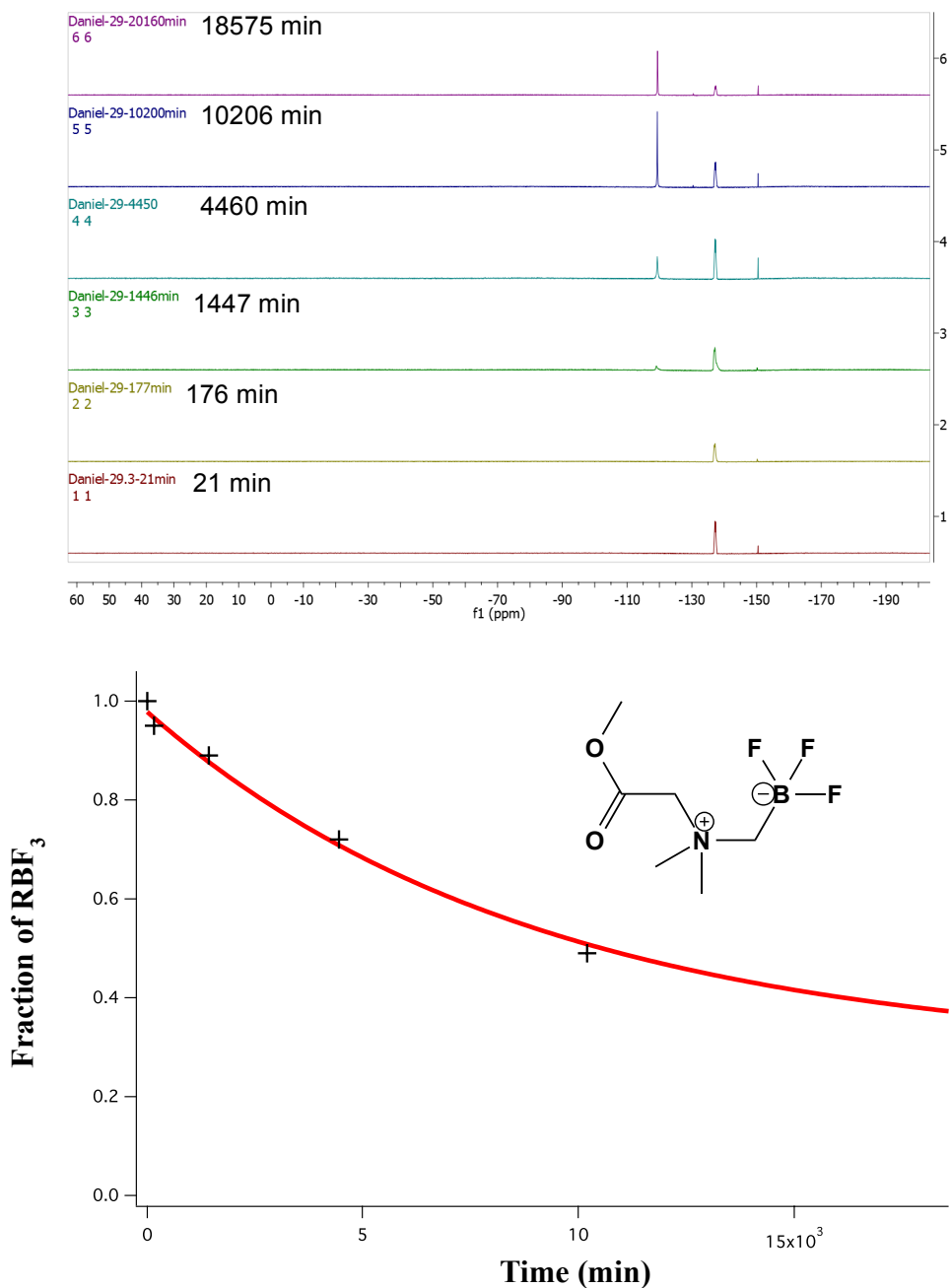


**Figure 3.15** (top):  $^{19}\text{F}$ -NMR kinetic analysis of the defluoridation from the  $^{19}\text{F}$ -organotrifluoroborate ( $^{19}\text{F}$ -Fluoride: -121 ppm relative to  $\text{CFCl}_3$ ;  $^{19}\text{F}$ -organotrifluoroborate: -136 ppm relative to  $\text{CFCl}_3$ ). **Figure 3.15** (bottom): Plot of relative  $^{19}\text{F}$ -NMR integration of the organotrifluoroborate as a function of all compounds ( $^{19}\text{F}$ -organotrifluoroborate +  $^{19}\text{F}$ -fluoride) vs. time.

### 3.5.2.13 Ammoniomethyltrifluoroborate (3.15)

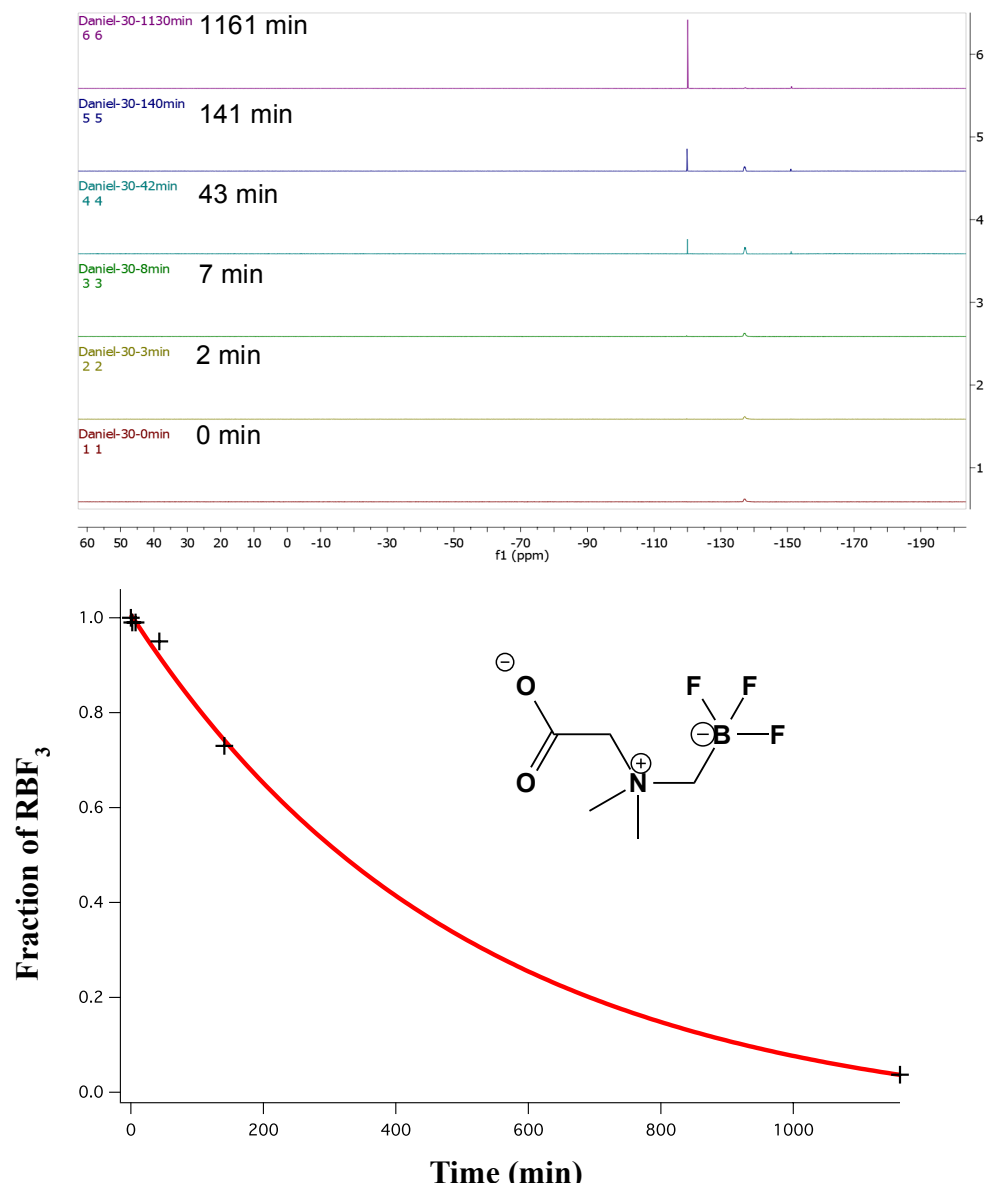


**Figure 3.16** (top):  $^{19}\text{F}$ -NMR kinetic analysis of the defluoridation from the  $^{19}\text{F}$ -organotrifluoroborate ( $^{19}\text{F}$ -Fluoride: -121 ppm relative to  $\text{CFCl}_3$ ;  $^{19}\text{F}$ -organotrifluoroborate: -138 ppm relative to  $\text{CFCl}_3$ ). **Figure 3.16** (bottom): Plot of relative  $^{19}\text{F}$ -NMR integration of the organotrifluoroborate as a function of all compounds ( $^{19}\text{F}$ -organotrifluoroborate +  $^{19}\text{F}$ -fluoride) vs. time.

## Chapter 4: Direct $^{18}\text{F}$ -Fluoridation With No-Carrier-Added (NCA) $^{18}\text{F}$ -Fluoride

### 4.1 Introduction

Irrespective of the isotope or labeling method, the specific activity of a radiotracer, defined as  $\text{Ci}/\mu\text{mol}$  radiotracer, represents an impartial measure of radiotracer quality.<sup>81</sup> Generally, high specific activity is thought to result in high contrast images that are needed for early detection.<sup>36</sup> As the amount of radiotracer injected is generally constant for each patient ( $\sim 7$  mCi), high specific activity means that low chemical amounts of radiotracer will be injected. In this case, low-abundance targets are unlikely to be saturated, and hence the fraction of bound radiotracer is linearly proportional to the amount of receptor, which enables quantitative or at least semi-quantitative measurements of target concentration in vivo.<sup>149,150</sup>

In contrast, at low specific activity, relatively high *chemical* amounts of tracer will be used leading to target saturation, but with unlabeled material which therefore does not contribute to image data. Hence, unbound tracer will give rise to high background while unlabeled carrier that also binds does not result in imaging signals. Therefore, PET tracers of low specific activity generally exhibit poorer signal-to-noise ratios and an overall lower image quality suggesting that high specific activity is very important to achieve high quality PET imaging. The other issue with regards to high specific activity relates to the total chemical dose of an imaging agent and its potential physiological effects on the patient. As many peptide tracers bind receptors that may lead to signaling, if the tracer is present in the patient at a concentration greater than  $0.1 K_d$ , it is likely that it will elicit a physiological response, something that is undesirable if imaging is to be truly passive. Therefore, very high specific activity is usually essential to ensure delivery of microdoses i.e. (1% of a therapeutic dose that results in concentrations well below the  $K_d$  of the target such that pharmacological effects are avoided).<sup>26,78,84,151</sup>

Given that the half-life of  $^{18}\text{F}$ -fluorine is 109.8 min, the defined specific activity of carrier-free  $^{18}\text{F}$  is  $1720 \text{ Ci}/\mu\text{mol}$ . Nevertheless, the specific activity of no-carrier added

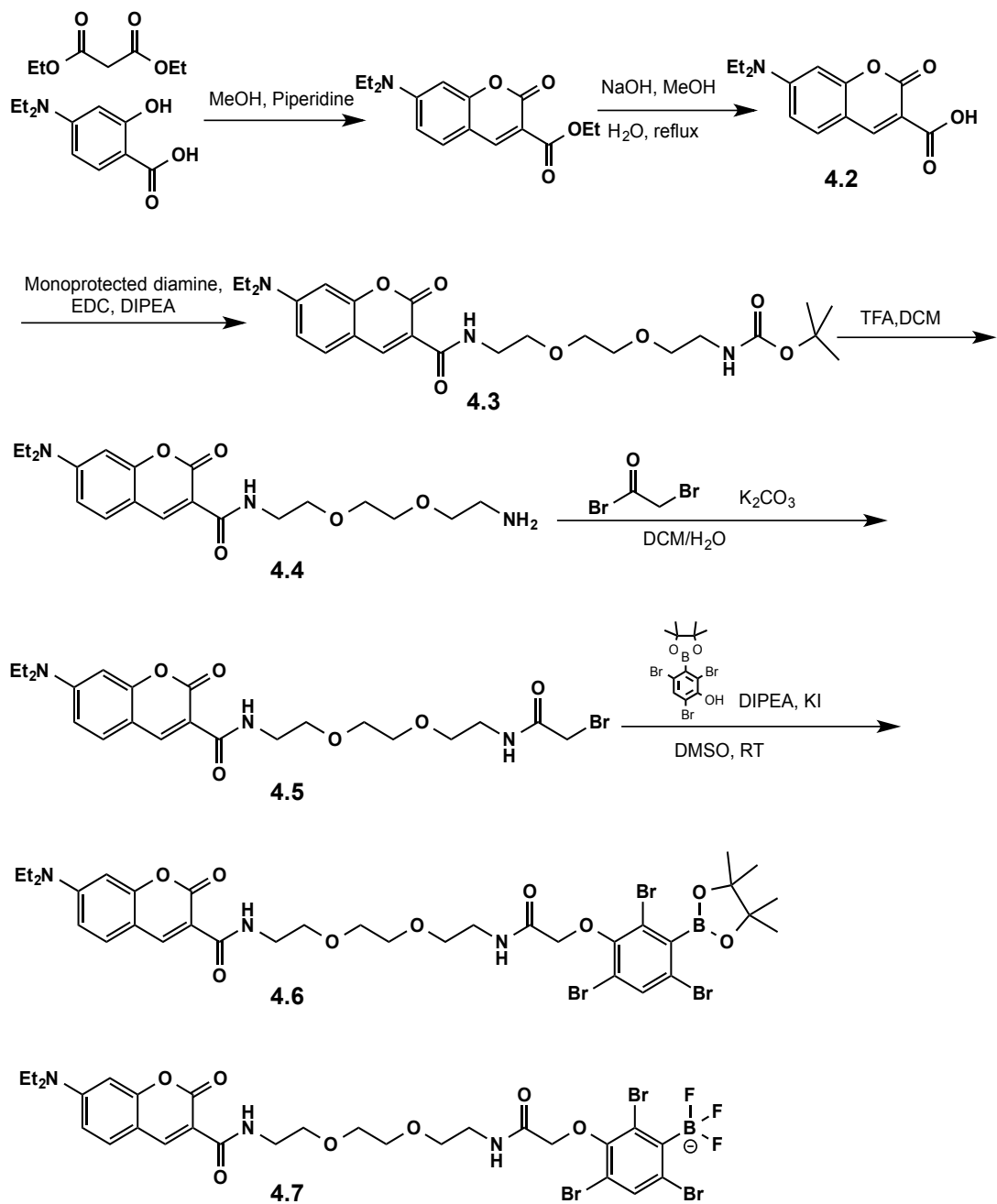
(NCA)  $^{18}\text{F}$ -fluoride ion in irradiated water directly following bombardment is rarely higher than  $40\text{ Ci}/\mu\text{mol}$ .<sup>48</sup> The specific activity decreases further to approximately  $5\text{-}10\text{ Ci}/\mu\text{mol}$  following anion exchange trapping and elution, which is required to remove contaminating radiometals and concentrate the fluoride. The result is that most small molecule tracers,<sup>56,142,151-155</sup> as well as radioprosthesis, are labeled using NCA  $^{18}\text{F}$ -fluoride that is obtained at  $\sim 8\text{ Ci}/\mu\text{mol}$  or lower.<sup>97,151,156,157</sup> By the time a relatively long radiosynthesis is executed (typically  $100\text{-}180\text{ min}$ ) for  $^{18}\text{F}$ -labelled peptides, there are few examples of labeling at specific activities in excess of  $3\text{ Ci}/\mu\text{mol}$ .<sup>151</sup>

As discussed in Chapter 1, when I took on this project, no one had ever labeled an  $^{18}\text{F}\text{-ArBF}_3^-$  at the high specific activity that is normally achieved with standard radiolabeling methods. Over the past few years,  $^{18}\text{F}\text{-ArBF}_3^-$  radioprosthesis have been used to label biotin, Marimastat, and RGD, for which the specific activities were calculated to be  $0.1\text{-}0.39\text{ Ci}/\mu\text{mol}$ , values which are considered at the low end of what is considered useful. Nevertheless, it is important to note three points: (1) The required specific activity of most radiotracers is approximately  $1\text{ Ci}/\mu\text{mol}$  and based on reports over the years, values greater than these are considered to be high,<sup>46,52,53,77,90-93,96-100,158-163</sup> (2) specific activities of  $0.16\text{-}0.5\text{ Ci}/\mu\text{mol}$  are considered to be good enough for PET imaging; (3) to date, in practice, the maximum specific activity of NCA (no-carrier added fluoride) is actually  $10\text{ Ci}/\mu\text{mol}$  or less,<sup>48</sup> which is presumed to be due environmental contamination by  $^{19}\text{F}$ -fluoride as carrier free  $^{18}\text{F}$ -fluoride has a defined specific activity of  $1720\text{ Ci}/\mu\text{mol}$ . It is also important to note that the specific activity of an  $^{18}\text{F}\text{-ArBF}_3^-$  is triple that of the  $^{18}\text{F}$ -fluoride used in labeling.<sup>164</sup> Therefore,  $^{18}\text{F}$ -fluoride, at a specific activity of  $1.5\text{ Ci}/\mu\text{mol}$  will provide an  $^{18}\text{F}\text{-ArBF}_3^-$  at  $4.5\text{ Ci}/\mu\text{mol}$  due to the stoichiometry of this reaction.

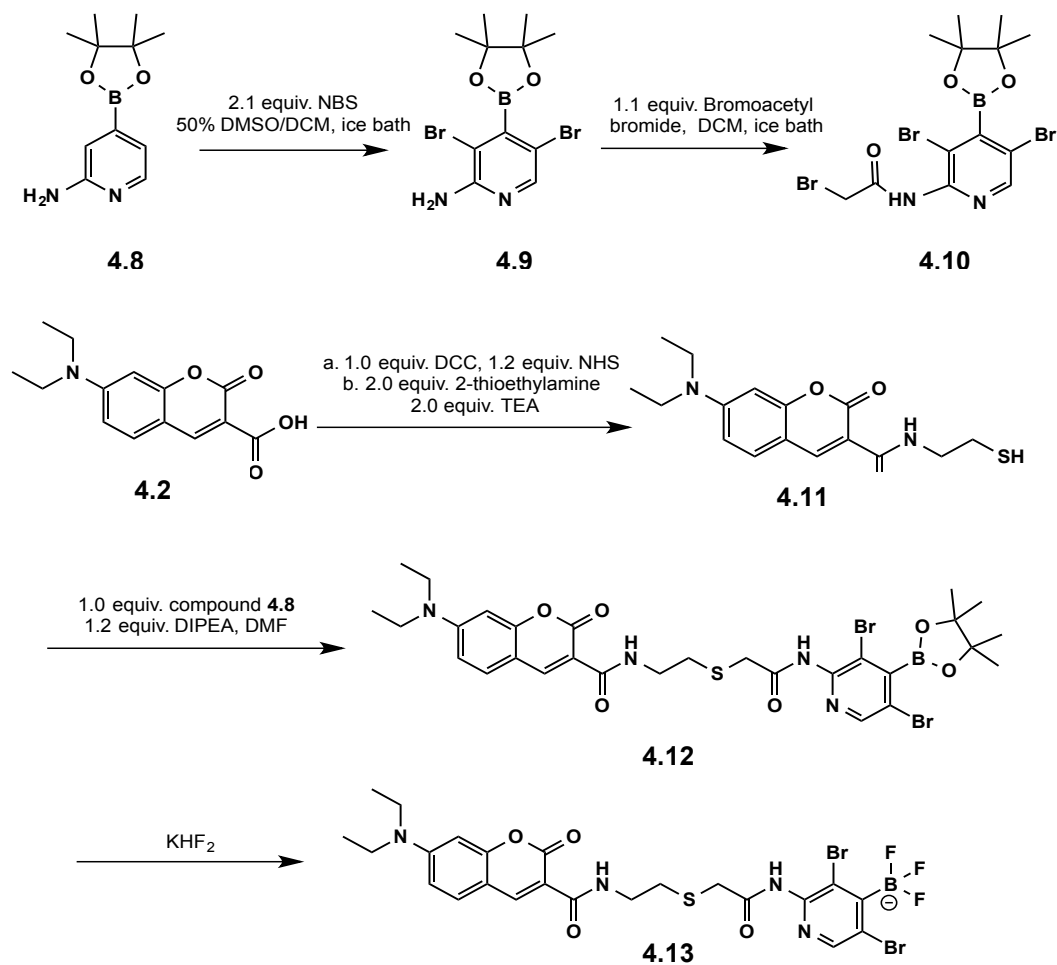
The main reason that high specific activity has not been achieved for  $^{18}\text{F}\text{-ArBF}_3^-$  is that fluoridation conditions have not been well optimized.<sup>86,107</sup> These conditions include: solvent, pH, buffer, temperature, etc. To begin to optimize the fluoridation yields under these various conditions, we hypothesized that fluorescent arylboronates might provide a rapid and semi-quantitative means of assaying these conditions for high yield at low fluoride concentrations that would imply the ability to produce organotrifluoroborate tracers at high specific activity. A quick and valuable fluorescent screen can be achieved

by simply analyzing the fluoridation crude with TLC plates using a hand-held UV lamp. The value of this is two-fold: (1) there is no use of radioactivity and therefore there are no safety concerns or issues with correcting for decay; (2) the use of a fluorescent derivative allows us to work at concentrations not unlike those that would be used for radiolabeling. When I began this work, our objective was to follow up on identifying new arylboronic acids that could be converted to *in vivo* stable aryltrifluoroborates. It was known from work by Li and Ting, that electron-withdrawing aryltrifluoroborates exhibited exalted stability.<sup>103,111</sup> Hence I prepared several candidate aryltrifluoroborates that I then linked to a fluorescent coumarin for screening in terms of their conversion to a trifluoroborate. One boronic acid was the tribromohydroxyphenylboronic acid and the other was an aminopyridyldibromoboronic acid. Their syntheses are given in the Chapter 2. Here is the brief synthetic route of fluorescent arylboronates.

Based on fluorescent screening, we rapidly verified the fluoridation of arylboronates under different conditions. Consequently, techniques for the radiosynthesis of  $^{18}\text{F-ArBF}_3^-$  were optimized such that good radiochemical yield can be achieved with NCA  $^{18}\text{F}$ -fluoride under aqueous condition. In addition, regarding the chemical composition of  $^{18}\text{F-ArBF}_3^-$  anion, the specific activity would be stoichiometrically leveraged during the radiosynthesis (*vide infra*). Herein, based on numerous conditions that were tested, we report the labeling of a radiotracer with a specific activity as high as 15 Ci/ $\mu\text{mol}$ , a value that is an order of magnitude higher than what is normally deemed to be “high” for radiotracers.<sup>82,112,113</sup>



**Scheme 4.1** Synthetic route of fluorescent  $\text{ArBF}_3^-$  (4.7).



*Scheme 4.2* Synthetic route of fluorescent  $\text{PyBF}_3^-$  (**4.13**).

## 4.2 Results and discussion

### 4.2.1 Optimization for fluoridation of arylboronates with fluorescent TLC analysis

#### 4.2.1.1 pH optimization

The following experiment presents how the fluorescent screen identified the most suitable pH for the fluoridation of arylboronates. This experiment is a good example that shows how the fluoridation conditions were optimized by using a fluorescent screen. In

the previous radiolabeling method established by Ting and Li, concentrated HCl (aq.) was used to provide acidic conditions (pH  $\approx$  0). However, this pH may not be suitable for the fluoridation of arylborates and moreover the application of a buffer was appealing in terms of standardizing conditions of labeling. Compound **4.6** was fluoridated under the following conditions to give compound **4.7**. Exactly the same amount of reaction mixture was loaded on TLC and then analyzed by fluorescence. As compound **4.7** has one more negative charge, it is more polar than compound **4.6**, and as a result, the top fluorescent spot was assumed to be the starting material (compound **4.6**), and the bottom fluorescent spot was assumed to be the corresponding aryltrifluoroborate (compound **4.7**). This assumption has been confirmed by ESI-MS.

**Table 4.1.** Experiment design of pH effect on  $\text{ArBF}_3^-$  formation.

Sample No.	[F <sup>-</sup> ]/mM	[4.6]/mM	Time/min	pH	Buffer	Yield
A1	33.3	1.0	60	1.01	0.10M HCl	25%
A2	33.3	1.0	60	2.29	300mM Anilinium <sup>+</sup>	85%
A3	33.3	1.0	60	3.01	300mM Pyridinium <sup>+</sup>	65%
A4	33.3	1.0	60	4.00	300mM Pyridinium <sup>+</sup> /pyridine	40%
A5	33.3	1.0	60	5.02	300mM Pyridinium <sup>+</sup> /Pyridine	5%
SM	33.3	1.0	60	---	----	0%

Based on the TLC analysis, reactions A2 and A3 have a significantly higher ratio of product to starting material. Therefore, the best potential pH window is 2-3 instead of pH = 0.

#### 4.2.1.2 Buffer selection

**Table 4.2** List of the buffers for the fluoridation of arylborates.

	pKa	Solubility (pH=3)/(mol/L)	Solubility (pH=2)/(mol/L)	Solubility (pH=1)/(mol/L)	LD50 (mg/kg)
Pyrazole	2.83	0.3	1.75	12	1010
Thiazole	2.72	0.32	1.29	9.59	-
Sulfamethizole	1.29	2.3*10 <sup>-3</sup>	3.2*10 <sup>-3</sup>	0.011	-
4-Fluoroaniline-HCl	4.66	1.91	10.3	10.3	-
1,2,4-Triazole-HCl	2.88/10.18	4.2	14.5	14.5	1750
2-Chloroaniline	3.54	0.042	0.3	1.57	-
3-Cyano-aniline-HCl	2.79	0.02	0.088	0.66	-
Adenosine-HCl	4.06/13.16	0.3	2.16	3.96	-
Napthalamines--HCl	β: 4.02	0.066	0.41	0.89	-
Pyridazine-HCl	3.12	8.44	12.5	12.5	2680
3-Iodo-pyridine-HCl	3.21	0.25	1.54	4.88	-
Saccharin (free acid)	1.6	0.17	0.028	0.01	-
3-Fluoropyridine	2.81	0.25	1.09	8.13	-
4-Fluoroimidazole-HCl	4.95	11.6	11.6	11.6	-
5-Fluoroimidazole-HCl	4.95	11.6	11.6	11.6	-
2-Fluoroimidazole-HCl	5.28	11.6	11.6	11.6	-
2,4-Difluoroimidazole-HCl	3.42	1.33	9.61	9.61	-
4,5-Fluoroimidazole-HCl	2.78	0.16	0.85	2.78	-

As a pH range of 2-3 (near the pKa of HF) would be optimal to fluoridate the arylborates, a buffer that provides buffer capacity in this range is subsequently necessary for the reaction. In order to develop the most optimized buffer system, a number of candidate buffers were studied as listed in **Table 4.2**. The candidates that have been tested by

fluorescent TLC analysis were highlighted, and they were selected mainly based on their pKa and solubility in water. In addition, we also considered the toxicity of the buffers with an eye to future clinical applications. As shown in **Table 4.3** and **Figure 4.1**, pyridazine buffer provided higher fluoridation yield than other buffers at certain conditions, hence it was chosen as the buffer for the  $^{18}\text{F-ArBF}_3^-$  synthesis.

**Table 4.3** Selection of buffers for the fluoridation of arylborates.

Sample No.	[F <sup>-</sup> ]/mM	[4.6]/mM	Time/min	Temp/°C	Buffer (HCl)	Estimated yield
A1	5.0	5.0	30	45	aniline	5%
A2	10.0	5.0	30	45	aniline	20%
B1	5.0	5.0	30	45	3-fluoropyridine	0%
B2	10.0	5.0	30	45	3-fluoropyridine	2.5%
C1	5.0	5.0	30	45	pyridazine	7.5%
C2	10.0	5.0	30	45	pyridazine	25%
D1	5.0	5.0	30	45	triazole	2.5%
D2	10.0	5.0	30	45	triazole	10%
E1	5.0	5.0	30	45	pyrazole	1
E2	10.0	5.0	30	45	pyrazole	5%

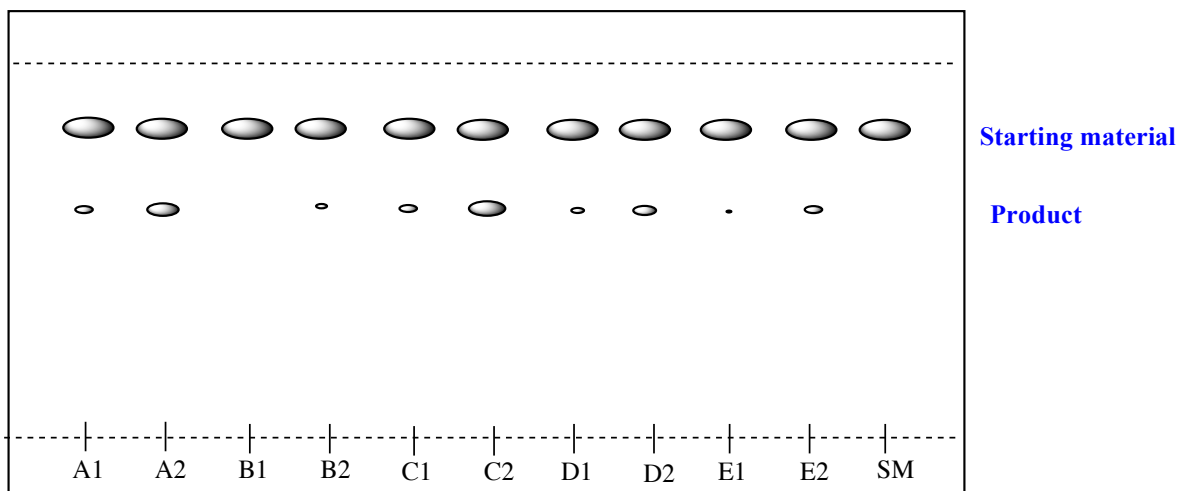


**Figure 4.1** TLC analysis of the fluoridation of arylborates. The starting material is less polar than the corresponding product; subsequently the starting material runs faster and can be separated from the product. Based on the fluorescence, the yield of each fluoridation reaction can be estimated semiquantitatively.

#### 4.2.1.3 Reaction time and reaction temperature optimization

Based on the previous study,<sup>112,113</sup> 15 mM of fluoride is the minimum concentration for obtaining a reasonable yield of  $\text{ArBF}_3^-$  at r.t. in 30 min when starting with 5 nmol or less of the boronic acid. In this experiment, we planned to study the possibility of accelerating fluoridation by elongating the reaction time or increasing the temperature. The experimental information was listed below (**Table 4.4**).

Given the short half-life of  $^{18}\text{F}$ , **Table 4.4** demonstrated that increasing the reaction time was not helpful in increasing the yield of fluoridation. At room temperature, only minimal product (~2.5%) was detected even after reaction for 160 min. In contrast, increasing the reaction temperature significantly improved the reaction yield, and ~10% chemical yield was detected within 40 min. Interestingly, both of these reactions demonstrated higher yield with longer reaction times, which means neither of two reactions had reached equilibrium.

**Table 4.4** Experiment design of temperature effect on  $\text{ArBF}_3^-$  formation.

Sample No.	[F <sup>-</sup> ]/mM	[4.6]/mM	Time/min	Temperature/°C	Estimated yield
A1	15.0	1.0	10	21±2	0%
A2	15.0	1.0	20	21±2	0%
A3	15.0	1.0	40	21±2	0%
A4	15.0	1.0	80	21±2	0%
A5	15.0	1.0	160	21±2	2.5%
B1	15.0	1.0	10	40±2	0%
B2	15.0	1.0	20	40±2	2.5%
B3	15.0	1.0	40	40±2	10%
B4	15.0	1.0	80	40±2	25%
B5	15.0	1.0	160	40±2	40%

#### 4.2.1.4 Development of an *in vacuo* method for NCA radiofluoridation

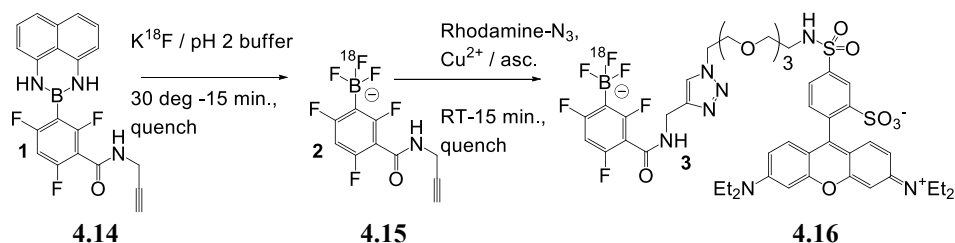
Encouraged by the success with fluorescent TLC analysis, we applied the optimized fluoridation conditions to  $^{18}\text{F}$ -radiolabelling. These new conditions resulted in improved radiochemical yields with lower amounts of added fluoride required for relatively high yields (data not shown). However, carrier  $^{19}\text{F}$ -fluoride was still needed while the specific activity was less than 1 Ci/ $\mu\text{mol}$  when using 10-50 mCi of NCA  $^{18}\text{F}$ -fluoride. In order to address this problem, we have developed a new radiolabelling method, with which the radiosynthesis of  $^{18}\text{F}\text{-ArBF}_3^-$  can be done at NCA conditions.

The protocol of this new method is to remove the solvent under reduced pressure. Therefore, even though the starting concentration ( $\sim 0.125$  mM) of fluoride was  $\sim 80$  times lower than previously reported (10 mM), the yield was found to be 10 times higher. At the same time, the specific activity of  $^{18}\text{F}\text{-ArBF}_3^-$  was increased to record levels that routinely surpassed 10 Ci/ $\mu\text{mol}$ . Typically  $^{18}\text{F}$ -fluoride is dried for use in standard labeling methods. Here we have explored the process of radio-fluoridation that relies on concentrating both the fluoride and the arylborate in the same tube. We nicknamed this method as “dry down” technology. While we have explored this for  $^{18}\text{F}\text{-ArBF}_3^-$  labeling, we believe that the same considerations may hold generally for many other  $^{18}\text{F}$ -labeling schemes.

**Table 4.5** Designed experiments to discover to new radiolabeling method. Experiment A: radiosynthesis  $^{18}\text{F}\text{-ArBF}_3^-$  with previous method. Experiment B: radiosynthesis of the same  $^{18}\text{F}\text{-ArBF}_3^-$  with “dry down” method. BOS: Beginning of the synthesis; EOS: End of synthesis.

No.	specific activity of fluoride /Ci/ $\mu\text{mol}$	Activity (EOS)/ mCi	$^{19}\text{F}\text{-F}$ /nmol	volume (BOS) / $\mu\text{L}$	volume (EOS) / $\mu\text{L}$	[fluoride] (BOS)/mM	[fluoride] (EOS)/mM	RCY
A	0.13	65	500	20	20	25	25	5%
B	4	10	2.5	20	$\sim 0$	0.125	NA	60%

#### 4.2.3 NCA $^{18}\text{F}$ -fluoridation of a fluorescent $\text{ArBF}_3^-$



**Scheme 4.3** Radiosynthesis of  $^{18}\text{F}$ -Rhodamine- $\text{ArBF}_3^-$ .

As mentioned in section 4.2, the “dry down” method provided us an opportunity to obtain a high specific activity  $^{18}\text{F-ArBF}_3^-$ . At that moment, Dr. Li in our lab had been working on the biological evaluation of radiosynthon (**4.14**), and both one-step and one-pot two-step “click” labeling had been developed.<sup>112,113</sup> Based on the evaluation, several bioligands demonstrated encouraging *in vivo* results, but high specific activity had not been achieved with the  $\text{ArBF}_3^-$ . It was known that high specific activity would often improve the *in vivo* imaging of most PET tracers. So we intended to utilize this new “dry down” labeling method with the  $\text{ArBF}_3^-$  to perform the *in vivo* study at high specific activity.

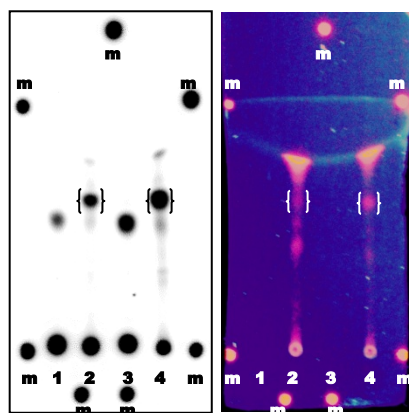


**Figure 4.2:** TLC-autoradiograph, right – digital photograph, lanes 1 and 2 are from crude reaction-1 (NCA) before or after click reaction, lanes 3 and 4 are from reaction-2 (near NCA) before or after click reaction respectively; “m” refers to marker spots to correlate fluorescence with autoradiographic density.

To efficiently develop the labeling method with the  $\text{ArBF}_3^-$ , we decided to link the  $^{18}\text{F-ArBF}_3^-$  to a fluorophore through “click” reaction. This was not only a means of showcasing the utility of click chemistry for  $^{18}\text{F-ArBF}_3^-$  labeling, but the linkage to a highly absorbent fluorophore would enable measurement of the specific activity achieved. Therefore, a new one-pot two-step method was presented to create a radiolabeled fluorescent  $^{18}\text{F-ArBF}_3^-$ . The product was then isolated and the corresponding specific activity was measured based on the law of Beer-Lambert.

As shown in **Figure 4.4**,  $^{18}\text{F}$ -Rhodamine- $\text{ArBF}_3^-$  was synthesized in two conditions: Non-Carrier Added (NCA) fluoridation (reaction-1, A1 in **Table 4.6**) and Near-NCA fluoridation (reaction-2, A2 in **Table 4.6**). The crude reaction mixtures were applied to a TLC plate which showed the correlation between fluorescence and autoradiography, as seen in **Figure 4.4** Both reactions were purified by HPLC (shown in **Figure 4.5**). From the purified fractions of **4-16**, 20% of each was re-injected into the HPLC to confirm purity (shown in **Figure 4.6**) while the remaining 80% was decayed at  $-20\text{ }^\circ\text{C}$  in order to measure the fluorescence in these fractions.

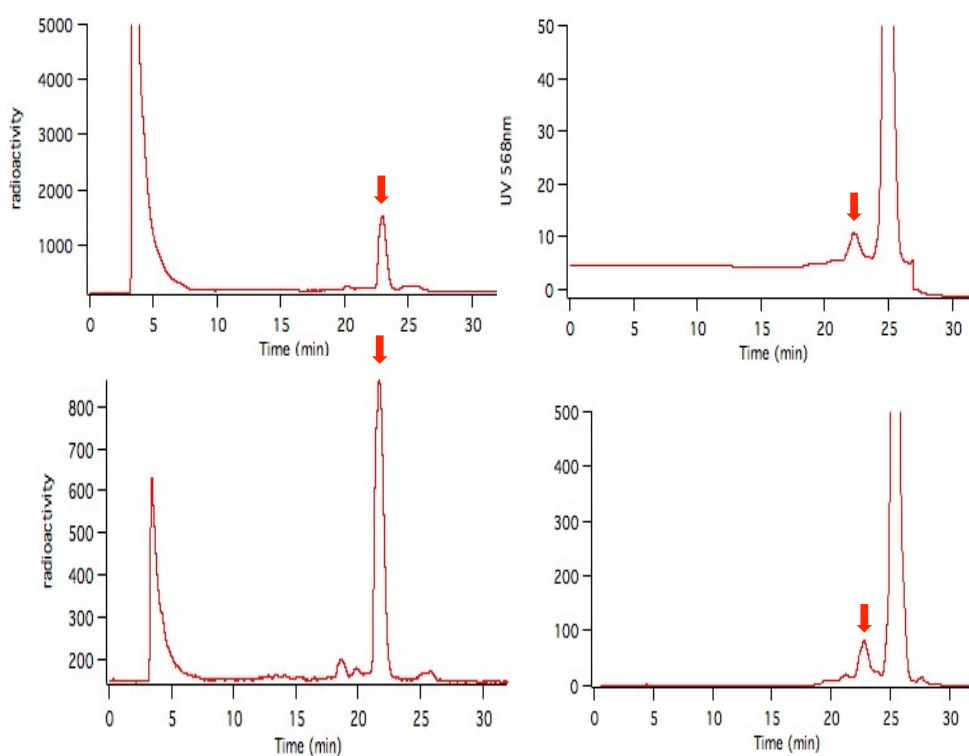


**Figure 4.3** HPLC traces of crude  $^{18}\text{F}$ -labeled **4.16** from rxn-1 (top) and rxn-2 (bottom). The  $^{18}\text{F}$ -labeled **4.16** is indicated by red arrow. The left figures are radioactive HPLC trace with unit of mV and the right figures are fluorescent HPLC trace at 568 nm with unit of mAU.

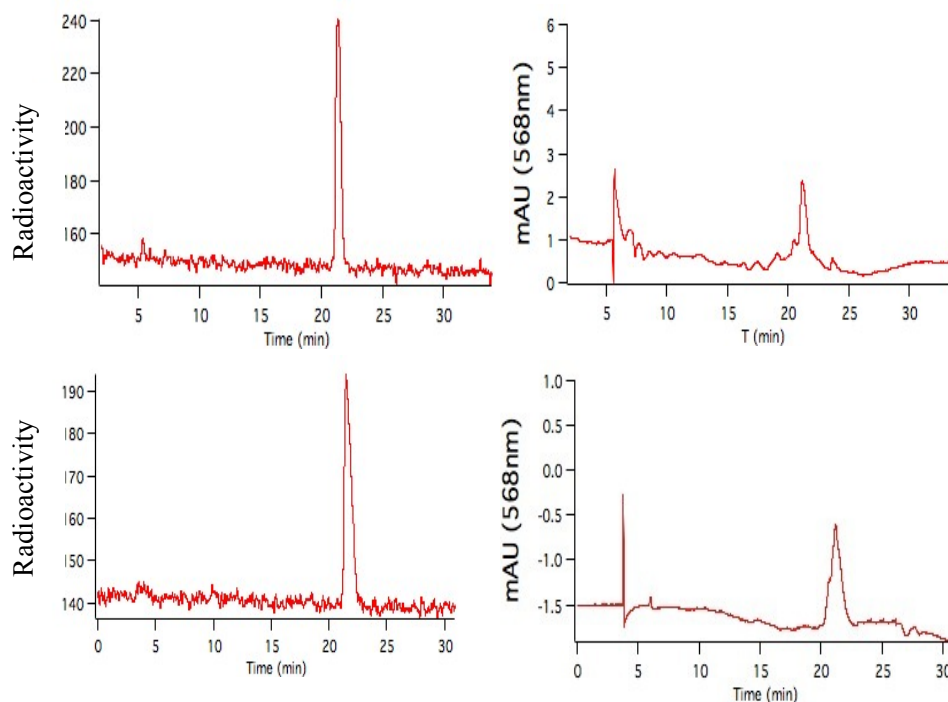


**Figure 4.4** HPLC traces of HPLC purified  $^{18}\text{F}$ -labeled **4.16** from rxn-1 (top) and rxn-2 (bottom). The left figures are radioactive HPLC trace with unit of mV and the right figures are fluorescent HPLC trace at 568 nm with unit of mAU.

### 4.3 Special discussion: stoichiometric leverage of specific activity

As demonstrated above, NCA  $^{18}\text{F}$ -fluoridation has been successfully performed by using a new “dry down” method. Hence the specific activity of  $\text{ArBF}_3^-$  was improved to be in the level of NCA  $^{18}\text{F}$ -fluoride, which was  $\sim 5 \text{ Ci}/\mu\text{mol}$  and had been achieved by several other labeling methods. Nevertheless, the special chemical nature of  $\text{ArBF}_3^-$  empowered this labeling method with a unique advantage, namely tripling the specific activity. That means the specific activity of  $^{18}\text{F}\text{-ArBF}_3^-$  can be as high as  $15 \text{ Ci}/\mu\text{mol}$ , which is almost one order of magnitude higher than other  $^{18}\text{F}$ -radiotracers have ever been produced. This statement may be controversial without deliberated explanation or solid proof, so I input a special discussion here to clarify this issue.

### 4.3.1 Mathematic explanation regarding the tripling of specific activity

The IUPAC definition of specific activity is defined as Ci/( $\mu\text{mol}$  tracer). Therefore, the specific activity of the fluoride is defined as: Ci/( $\mu\text{mol}$  fluoride) and the specific activity of  $^{18}\text{F-ArBF}_3^-$  is defined as: Ci/( $\mu\text{mol } ^{18}\text{F-ArBF}_3^-$ ).

Although the specific activities of the  $^{18}\text{F-ArBF}_3^-$  must be related to that of  $^{18}\text{F-fluoride}$  because the  $^{18}\text{F-ArBF}_3^-$  is synthesized from  $^{18}\text{F-fluoride}$ , the specific activities are *not* equivalent because the units do not match. In other words:

$$\frac{\text{Ci}}{\mu\text{mol ArBF}_3^-} \neq \frac{\text{Ci}}{\mu\text{mol F}}$$

The arithmetic relationship between the specific activity of the  $^{18}\text{F-ArBF}_3^-$  and the  $^{18}\text{F-fluoride}$  is governed by the stoichiometry of the production of the  $\text{ArBF}_3^-$ :



Specific activity units must be reconciled to reflect the relationship between the specific activity of the  $^{18}\text{F-ArBF}_3^-$  and the  $^{18}\text{F-fluoride}$ :

$$\frac{\text{Ci}}{\mu\text{mol ArBF}_3^-} = \frac{\text{Ci}}{\mu\text{mol F}} \times \frac{\mu\text{mol F}}{\mu\text{mol ArBF}_3^-} \times 3$$

This leads to a cancelling of units. However, the factor of 3, which reflects the 3-to-1 stoichiometry, remains. This is also easily understood practically in the following analysis:

Start with: 30 mCi  $^{18}\text{F}$ -fluoride at a specific activity of 5 Ci/ $\mu\text{mol}$ : this implies 6 nmol of total fluoride.

Assume a 10% radiochemical yield: 3 mCi of  $^{18}\text{F}$ -fluoride (0.6 nmol total fluoride) is converted to an  $\text{ArBF}_3^-$ .

If 0.6 nmol of  $^{18}\text{F}$ -fluoride is incorporated into an  $^{18}\text{F}\text{-ArBF}_3^-$ , how many nmol of  $\text{ArBF}_3^-$  are present?

Answer: 0.2 nmol  $^{18}\text{F}\text{-ArBF}_3^-$

What is the specific activity of this  $\text{ArBF}_3^-$ ? The specific activity of the  $^{18}\text{F}\text{-ArBF}_3^-$  is: 3 mCi/0.2 nmol  $\text{ArBF}_3^-$ : or 15 Ci/ $\mu\text{mol}$   $\text{ArBF}_3^-$ , which is triple the specific activity of the  $^{18}\text{F}$ -fluoride.

We hope all the readers will be convinced that this relationship holds true for all specific activities of fluoride that includes carrier-free, NCA, and carrier added, as this is simply a restatement of the law of conservation of mass. To further prove our statement, the specific activities of  $^{18}\text{F}\text{-4.16}$  and  $^{18}\text{F}$ -fluoride have been measured and listed in **Table 4.6**.

#### 4.3.2 Specific activity of NCA $^{18}\text{F}$ -fluoride

The specific activity of NCA  $^{18}\text{F}$ -fluoride was further assessed by a self-immolating fluorescent fluoride sensor that can accurately detect  $>0.5$  nmol Fluoride or  $>1.2$  mM Fluoride. To do this we synthesized a fluoride-specific chemodosimeter as previously reported. The chemodosimeter is shown below in **Figure 4.5**

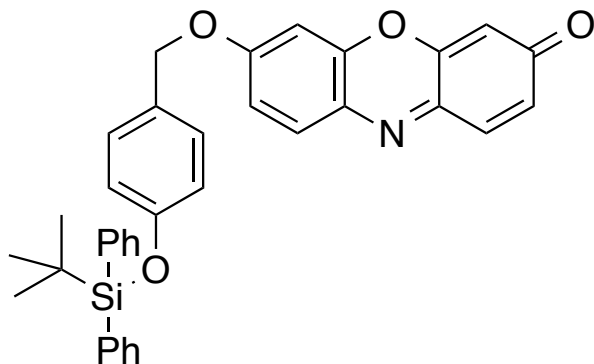


**Figure 4.5:** Chemical structure of the fluorescent chemodosimeter.

The residual  $^{18}\text{F}$ -fluoride that had been decayed following each labeling was dried on a speed vac and then re-suspended in 200 mM imidazole buffer (100  $\mu\text{L}$ ) to which was added water (100  $\mu\text{L}$ ) and 100  $\mu\text{M}$  chemodosimeter solution (200  $\mu\text{L}$ ).

To use this chemodosimeter we adapted our procedure based on the original report but included the application of a buffer. To do this, imidazole buffer pH 7.4 was obtained at 1M and diluted to 200 mM. For each analysis, fluoride samples at known concentrations were also prepared to generate a standard curve. The standard curve was generated by adding 0, 25, 50, 75, 100  $\mu\text{L}$  of a 100  $\mu\text{M}$   $\text{F}^-$  (or 50  $\mu\text{M}$   $\text{KHF}_2$ ) along with 100, 75, 50, 25, 0  $\mu\text{L}$  respectively of DI water, to which was then added 200 mM Imidazole buffer pH 7.41 (100  $\mu\text{L}$ ). These 200  $\mu\text{L}$  aqueous solutions were then mixed with a 100  $\mu\text{M}$  solution of the chemodosimeter prepared in MeCN (200  $\mu\text{L}$ ).

All samples were then incubated for 24 hours in the dark, and afterwards the samples are read for fluorescence. All fluorescence readings were acquired using Cary Eclipse Spectrofluorometer at room temperature scanning for the  $\lambda_{\text{max}}$  scan at 588 nm. The specific activity of the unused portions of NCA  $^{18}\text{F}$ -fluoride for each labeling reaction is reported in **Table 4.6**.

### 4.3.3 Specific activity of ArBF<sub>3</sub><sup>-</sup> (4.16)

The specific activity of <sup>18</sup>F-ArBF<sub>3</sub><sup>-</sup> (4.16) was determined with two different methods: calculation and standard curve measurement. The result from either method was found to corroborate the other and the details were presented herein.

#### 4.3.3.1 Calculation of specific activity from HPLC trace in UV-Vis mode

Initially, the specific activity of 4.16 was calculated from the HPLC traces (*Figure 4.6*): For the top trace, the peak height is approximately 2 mAU and the activity elutes in 2 minutes while for the bottom one, the peak height is 1.5 mAU. In order to integrate the peak area, we made a reasonable assumption that the peak shape is approximately that of a triangle. Hence, each fraction is either 0.001 OD/mL or 0.00075 OD/mL respectively. Using extinction coefficient for Rhodamine at 10<sup>5</sup> M<sup>-1</sup>cm<sup>-1</sup>, the eluted fraction has a concentration of 10 nM or 7.5 nM, respectively. With the flow rate of 1 mL/min and an elution time of 1.7 min and 2 min (21-23 minutes), respectively, the total mass collected is 17 pmol and 15 pmol, respectively. These values give non-decay corrected specific activities of 3.2 Ci/μmol at EOS+4 hours and 1 Ci/μmol at EOS+5.5 hours. Therefore the specific activities that are corrected to EOS are 14.6 Ci/μmol and 8.0 Ci/μmol, respectively.

#### 4.3.3.2 Measurement of specific activity by Fluorescence

Following decay at -20 degrees, the remaining 80% of the radiochemically pure fractions of 4.16 (224 μCi from rxn-1 and 62.4 μCi from rxn-2) were quantitatively analyzed for fluorescence. In order to do this, a standard curve was established using a known quantity of the Rhodamine azide. Because 4.15 has no chromophore that absorbs at > 400 nm, the fluorescent properties of 4.16 must be identical to those of Rhodamine itself. Therefore a solution of HPLC purified <sup>19</sup>F-labeled 4.16, as shown in *Figure 4.9*, was prepared and its concentration was determined by UV absorbance at 568 nm to be 851 nM. This solution was diluted into 50% MeCN/H<sub>2</sub>O to provide a standard sample series of 500 nM, 250 nM, 125 nM, 62.5 nM, 31.3 nM, 15.6 nM, 7.8 nM, 3.9 nM, and 2.0 nM. All the samples were read with Cary Eclipse spectrofluorometer at room temperature. Then a standard

curve was acquired based on the relationship between the fluorescence and concentration as shown in **Figure 4.6**.

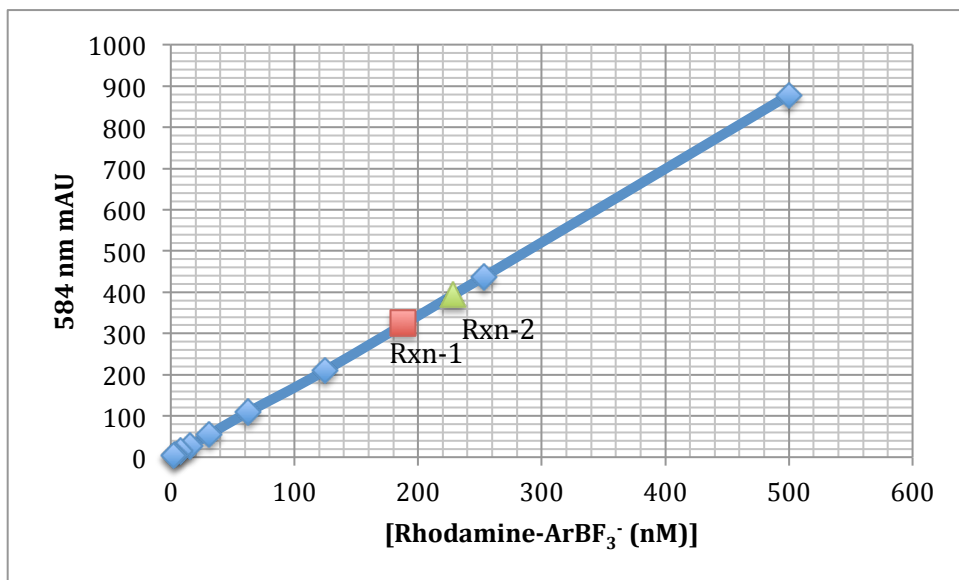


**Figure 4.6** Fitted linear standard curve with 500 nM, 250 nM, 125 nM, 62.5 nM, 31.3 nM, 15.6 nM, 7.8 nM, 3.9 nM, and 2.0 nM of **4.16**. The blue dots indicate the values obtained from HPLC integration while the red square and green triangle show HPLC absorbance of the **4.16** peak obtained in rxn-1 and rxn-2, respectively.

The samples that had decayed were approximately 1 mL in volume. The solvent of rxn-1 and rxn-2 was removed by lyophilization, and the contents of each reaction was then resuspended with 350  $\mu$ L ethanol and 300  $\mu$ L ethanol, respectively. The resulting solution of each sample was then analyzed for fluorescence and each was found to contain 325.1 mAU and 497.9 mAU for the fractions labeled in rxn-1 and rxn-2, respectively. Using the standard curve above, I calculated concentrations of 188.2 nM and 228.1 nM for the fractions labeled in rxn-1 and rxn-2, respectively. As these originally had 224  $\mu$ Ci from rxn-1 and 62.4  $\mu$ Ci from rxn-2 at EOS + 4 hours for 3 (rxn-1) and at EOS + 5.5 hours for 3 (rxn-2), the specific activities were found to be: 3.4 Ci/ $\mu$ mol and 0.91 Ci/ $\mu$ mol, respectively. Specific activities corrected to EOS are therefore 15.2 Ci/ $\mu$ mol and 7.1 Ci/ $\mu$ mol for **4.16** obtained in rxn-1 and rxn-2, respectively. The labeling was reproduced three times, and the measured specific activity of each reaction was summarized in **Table 4.6**.

#### 4.3.4 Summary

The summary of three separate labeling reactions is presented above (always paired as rxn-1: NCA and rxn-2: near NCA). Throughout this work, the specific activity of NCA  $^{18}\text{F}$ -fluoride in each case was obtained at  $\sim 5 \text{ Ci}/\mu\text{mol}$  by experimental measurement. For every trial, the specific activity of  $\text{ArBF}_3^-$  was measured to be  $\sim 15 \text{ Ci}/\mu\text{mol}$ , which was approximately 3 times higher than the specific activity of NCA  $^{18}\text{F}$ -fluoride. In addition, for rxn-2, I added a certain amount of  $^{19}\text{F}$ -fluoride to give a defined specific activity of  $\sim 2.5 \text{ Ci}/\mu\text{mol}$ . As shown in **Table 4.6**, the specific activity of the corresponding  $\text{ArBF}_3^-$  was leveraged  $\sim 3$  times as well. Similar results were obtained three times with different amount of radioactivity, subsequently demonstrating its reproducibility. I hope this experiment unambiguously addressed the concerns about achieving high specific activity with  $\text{ArBF}_3^-$ , and also proved the stoichiometric relationship between the specific activity of  $^{18}\text{F}\text{-ArBF}_3^-$  and  $^{18}\text{F}$ -fluoride.

**Table 4.6** Summary of specific activity measurement

Rxn No.	$^{19}\text{F}$ -fluoride added (nmol)	Radioactivity (mCi, BOS)	Radioactive yield	Specific activity of $\text{ArBF}_3^-$ ( $\text{Ci}/\mu\text{mol}$ ) EOS	specific activity of NCA $^{18}\text{F}$ ( $\text{Ci}/\mu\text{mol}$ ) BOS	The ratio
A1	0	10.4	11%	13.8	5.7	2.4
A2	2.5	10.4	35%	6.5	2.4	2.7
B1	0	19.3	17%	15.1	6.4	2.4
B2	4	18.7	27%	7.2	2.7	2.7
C1	0	8.1	9%	12.2	5.1	2.2
C2	2	8.4	46%	5.3	2.3	2.3

## 4.4 Conclusion

The “dry down” method has been shown to rapidly afford the target molecule with specific activities that are measured to be approximately an order of magnitude higher than previously reported. Moreover, the “dry down” method should find application in the synthesis of many radiotracers that do not necessarily rely on B-F bond formation. *Scheme 4.3* presents the one-pot two-step click radiofluoridation with this method. By using the “dry down” method, the intermediate was nearly 100% transferred into the product in 15 min with a click reaction. In conclusion, this “dry down” method provides a rapid route for preparing an  $^{18}\text{F}\text{-ArBF}_3^-$  radiosynthon at specific activities that are an order of magnitude higher than we have achieved before. Furthermore, the 3-to-1 stoichiometry in  $\text{ArBF}_3^-$  synthesis under NCA or near-NCA conditions has been proved and shown to increase specific activity of  $^{18}\text{F}\text{-ArBF}_3^-$  radioprosthetic by a factor of 3.

## 4.5 Experimental information

Materials: Chemicals were purchased from Sigma-Aldrich unless stated otherwise. The azidotriethyleneglycol-bis-sulfonylated Rhodamine was purchased from Oakwood Inc. as predominantly one of two regio-isomers. Deuterated solvents were purchased from Cambridge Isotope Laboratories. TLC analysis and preparation were performed by Silica Gel 60 F<sub>254</sub> glass TLC plates from EMD Chemicals.

### 4.5.1 General information

HPLC Conditions: Unless otherwise stated, all samples were loaded onto a Phenomenex Jupiter 10  $\mu\text{m}$  C18 300 $\text{\AA}$  4.6 mm  $\times$  250 mm column. Step gradient (solvent A: 0.04 M ammonium formate ( $\text{NH}_4\text{HCO}_2$ ), solvent B: MeCN) 0 to 5 min: 0% to 5 % B, 5 to 10 min: 5% to 35% B, 10 to 20 min: 35% to 45% B, 20 to 22 min: 45% to 100% B, 22 to 28 min: 100% to 100% B, 28 to 30 min: 100% to 20% B, 30 to 33 min: 20% to 5% B; flow rate: 1 mL/min, column temperature: 19-21  $^\circ\text{C}$ .

## 4.5.2 Synthesis

### Synthesis of Ethyl 7-diethylaminocoumarin-3-carboxylate (4.1)

Diethylamino salicylaldehyde (1.93 g, 10 mmol) and diethyl malonate (2.3 mL, 15 mmol) were dissolved in EtOH (20 mL), followed by the addition of piperidine (3 mL, 30.2 mmol). The resulting solution was heated to reflux for 4 hr and then the reaction was concentrated under vacuum. The residue was purified with flash chromatography (EtOAc:hexanes 1:2) to give a brown oil as the desired product. Yield: 1.10 g, 39%. <sup>1</sup>H NMR (300 MHz, CDCl<sub>3</sub>, rt):  $\delta$  (ppm) 1.25 (t,  $J = 7.14$  Hz, 6 H), 1.41 (t,  $J = 7.11$  Hz, 3 H), 3.45 (q,  $J = 7.14$  Hz, 4 H), 4.37 (q,  $J = 7.11$  Hz, 2H), 6.47(d,  $J = 2.29$  Hz, 1H), 6.62(dd,  $J_1 = 8.94$  Hz,  $J_2 = 2.5$  Hz, 1H), 7.37(d,  $J = 8.94$  Hz, 1 H), 8.44 (s, 1 H); <sup>13</sup>C NMR (75.5 MHz, CDCl<sub>3</sub>, rt):  $\delta$  (ppm) 12.58, 14.54, 45.25, 61.31, 96.88, 107.84, 109.14, 109.65, 131.18, 149.37, 153.01, 158.47, 158.62, 164.44; ESI-MS: [M+Na]<sup>+</sup>, 312.3 (100%).

### Synthesis of 7-Diethylaminocoumarin-3-carboxylic acid (4.2)

Compound **4.1** (1.10 g, 3.7 mmol) and NaOH (0.18 g, 4.7 mmol) were suspended in 50% aqueous MeOH (20 mL) and heated to reflux for 1 hr. The reaction was then cooled to rt and neutralized with 3 M HCl carefully to pH ~ 2. The orange precipitate was then filtered and washed with H<sub>2</sub>O and cold MeOH before being left over high vacuum to afford an orange powder Yield: 0.69 g, 75%. <sup>1</sup>H NMR (300 MHz, *d*<sub>6</sub>-DMSO, rt):  $\delta$  (ppm) 1.13 (t,  $J = 6.94$  Hz, 6 H), 3.47 (q,  $J = 6.94$  Hz, 4 H), 6.56 (s, 1 H), 6.78 (d,  $J = 8.99$  Hz, 1 H), 7.62 (d,  $J = 8.99$  Hz, 1 H), 8.57 (s, 1H); <sup>13</sup>C NMR (100.6 MHz, *d*<sub>6</sub>-DMSO, rt):  $\delta$  (ppm) 12.89, 44.97, 96.50, 107.73, 107.96, 110.64, 132.42, 150.02, 153.49, 158.48, 160.12, 165.07; ESI-MS: [M+Na]<sup>+</sup>, 284.2 (100%).

### Synthesis of tert-butyl (2-(2-(2-(7-(diethylamino)-2-oxo-2H-chromene-3-carboxamido)ethoxy)ethyl)carbamate (4.3)

Compound **4.2** (52 mg, 0.2 mmol), monoprotected diamine (54 mg, 0.22 mmol), EDC (34 mg, 0.22 mmol), and DIPEA (73  $\mu$ L, 0.44 mmol) were dissolved in DCM (10 mL). The reaction was stirred at r.t. for 16 hr and then precipitated in the mixture of DCM (20

mL) and water (20 mL). The aqueous layer was extracted with DCM (20 mL) twice. The organic layers were combined and then dried with anhydrous sodium sulfate. The organic solvent was removed with vacuum and the concentrated residue was charged with flash chromatography to give brown oil as desired product. Yield: 89 mg, 82%. ESI-MS:  $[M+H]^+$ , 492.26 (100%).

**Synthesis of N-(2-(2-(2-aminoethoxy)ethoxy)ethyl)-7-(diethylamino)-2-oxo-2H-chromene-3-carboxamide (4.4)**

In a flame-dried round bottom flask, compound **4.3** (89 mg, 0.18 mmol) was suspended in 5 mL TFA and underwent a deprotection reaction at r.t. for 2 hr. The TFA was then removed by rota-vap to give a chemically pure product. Yield: 91 mg, 100%.  $^1\text{H}$  NMR (300 MHz, *d*-CHCl<sub>3</sub>, rt):  $\delta$ (ppm) 1.4 (t, 6 H), 3.25 (t, 2 H), 3.48 (q, 4 H), 3.65 (m, 8 H), 3.82 (t 2 H), 6.55 (s, 1H), 6.78 (d, 1 H), 7.47 (d, 1 H), 8.79 (s, 1 H), 9.15 (t, 1 H); ESI-MS:  $[M+H]^+$ , 392.21 (100%).

**Synthesis of N-(2-(2-(2-(2-bromoacetamido)ethoxy)ethoxy)ethyl)-7-(diethylamino)-2-oxo-2H-chromene-3-carboxamide (4.5)**

Compound **4.4** (91 mg, 0.18 mmol) was dissolved in a mixture of DCM (10 mL) and K<sub>2</sub>CO<sub>3</sub> (1 M, 10 mL, excess). Bromoacetyl bromide (17.2  $\mu\text{L}$ , 0.20 mmol) was then added dropwise into the mixture. The reaction was completed in 30 min at r.t. The aqueous layer was extracted with DCM (20 mL) twice. The combined organic layers were concentrated under vacuum, and the resulting residue was purified with flash chromatography to give the desired product. Yield: 81 mg, 89%.  $^1\text{H}$  NMR (300 MHz, *d*-CHCl<sub>3</sub>, rt):  $\delta$ (ppm) 1.4 (t, 6 H), 3.25 (t, 2 H), 3.48 (q, 4 H), 3.65 (m, 8 H), 3.82 (t 2 H), 3.99 (s, 2 H), 6.55 (s, 1H), 6.78 (d, 1 H), 7.47 (m, 2 H), 8.79 (s, 1 H), 9.15 (t, 1 H); ESI-MS:  $[M+H]^+$ , 512.13 (100%), 514.13 (97.3%).

**Synthesis of 7-(diethylamino)-2-oxo-N-(2-(2-(2-(2-(2,4,6-tribromo-3-(4,4,5,5-tetramethyl-1,3,2-dioxaborolan-2-yl)phenoxy)acetamido)ethoxy)ethoxy) ethyl)-2H-chromene-3-carboxamide (4.6)**

A flame-dried round bottom flask was charged with a mixture of compound **4.5** (51 mg, 0.10 mmol), compound **2.6** (46 mg, 0.10 mmol), KI (1.6 mg, 0.01 mmol), and DIPEA (19.2  $\mu$ L, 0.11 mmol). The mixture was dissolved in 5 mL dry DMSO and then incubated at r.t. for 16 hr. DMSO was removed by DCM/water partition and the residue was charged onto a silica column for flash chromatography to give a brown solid as the desired product. Yield: 45 mg, 51%.  $^1\text{H}$  NMR (300 MHz, *d*- $\text{CHCl}_3$ , rt):  $\delta(\text{ppm})$  1.42 (t, 6 H), 1.51 (s, 12 H), 3.25 (t, 2 H), 3.48 (q, 4 H), 3.65 (m, 8 H), 3.82 (t, 2 H), 3.99 (s, 2 H), 6.55 (s, 1H), 6.78 (d, 1 H), 7.47 (m, 2 H), 8.79 (s, 1 H), 7.62 (s, 1 H), 9.15 (t, 1 H); ESI-MS:  $[\text{M}+\text{H}]^+$ , 888.06 (100%), 890.06 (97.3%).

**Synthesis of trifluoro(2,4,6-tribromo-3-((1-(7-(diethylamino)-2-oxo-2H-chromen-3-yl)-1,12-dioxo-5,8-dioxa-2,11-diazatridecan-13-yl)oxy)phenyl)borate (4.7)**

In a 1.5 mL eppendorf tube, compound **4.6** (8.9 mg, 0.01 mmol) was fluoridated with excess  $\text{KHF}_2$  (6 M, 50  $\mu$ L). The reaction was purified with a silica pipette column to the desired product in quantitative yield. Yield: 8.2 mg, 99%. ESI-MS:  $[\text{M}+\text{H}]^+$ , 828.97 (100%), 830.97 (97.3%).

**Synthesis of 2-bromo-N-(3,5-dibromo-4-(4,4,5,5-tetramethyl-1,3,2-dioxaborolan-2-yl)pyridin-2-yl)acetamide (4.10)**

Compound **4.9** (113.1, 0.3 mmol) was dissolved in DCM (10 mL) and placed in an ice-bath, then bromoacetyl bromide (28.6  $\mu$ L, 0.33 mmol) was added dropwise, followed by slow addition of DIPEA (57.4  $\mu$ L, 0.33 mmol). The reaction mixture was allowed to warm to ambient temperature and stirred overnight. The mixture was washed with water and then concentrated with rota-vap. The resulting residue was purified by flash chromatography and dried *in vacuo* to yield the desired product. Yield: 137 mg, 86%.  $^1\text{H}$  NMR (300 MHz, *d*- $\text{CHCl}_3$ , rt):  $\delta(\text{ppm})$  1.48 (s, 12 H), 4.46 (s, 2H), 8.45 (s, 1 H), 8.61 (b, 1 H); ESI-MS:  $[\text{M}+\text{H}]^+$ , 498.88 (100%), 500.88 (97.3%).

**Synthesis of 7-(diethylamino)-N-(2-mercaptoethyl)-2-oxo-2H-chromene-3-carboxamide (4.11)**

A 10 mL round bottom flask was charged with a mixture of compound **4.2** (131 mg, 0.50 mmol), DCC (103 mg, 0.50 mmol), N-hydroxysuccinimide (69.5 mg, 0.6 mmol), 2-thiolethylammonium chloride (112 mg, 1.0 mmol), TEA (139.2  $\mu$ L, 1.0 mmol), and DCM (20 mL). The reaction was stirred at r.t. overnight and then washed with water, followed by concentration under rota-vap. The residue was purified with flash chromatography and dried *in vacuo* to give the desired product. Yield: 78 mg, 65%.  $^1\text{H}$  NMR (300 MHz, *d*- $\text{CHCl}_3$ , rt):  $\delta$  (ppm) 1.25 (t, 6 H), 2.92 (q, 2 H), 3.48 (q, 4 H), 3.75 (q, 2 H), 6.51 (s, 1H), 6.70 (d, 1 H), 7.47 (d, 1 H), 8.45 (s, 1 H), 9.15 (t, 1 H); ESI-MS:  $[\text{M}+\text{H}]^+$ , 320.12 (100%).

**Synthesis of N-(2-((2-((3,5-dibromo-4-(4,4,5,5-tetramethyl-1,3,2-dioxaborolan-2-yl)pyridin-2-yl)amino)-2-oxoethyl)thio)ethyl)-7-(diethylamino)-2-oxo-2H-chromene-3-carboxamide (4.12)**

Compound **4.10** (49.7 mg, 0.10 mmol) and compound **4.11** (32.0 mg, 0.10 mmol) was dissolved in DMF (5 mL, dried over molecular sieves), followed by slow addition of DIPEA (11.5  $\mu$ L, 0.12 mmol). The reaction was stirred at r.t. overnight and then precipitated in water (20 mL) and DCM (20 mL). The aqueous layer was extracted with DCM (20 mL) twice, after which the organic solutions were combined and concentrated under rota-vap. The residue was purified with flash chromatography and dried *in vacuo* to give the desired product. Yield: 49 mg, 67%.  $^1\text{H}$  NMR (300 MHz, *d*- $\text{CHCl}_3$ , rt):  $\delta$  (ppm) 1.27 (t, 6 H), 1.48 (s, 12 H), 2.92 (q, 2 H), 3.48 (q, 4 H), 3.65 (s, 2 H), 3.75 (q, 2 H), 6.51 (s, 1H), 6.70 (d, 1 H), 7.47 (d, 1 H), 8.45 (s, 1 H), 8.71 (s, 1 H), 9.15 (t, 1 H), 9.39 (b, 1 H); ESI-MS:  $[\text{M}+\text{H}]^+$ , 739.07 (100%).

**Synthesis of (3,5-dibromo-2-(2-((2-(7-(diethylamino)-2-oxo-2H-chromene-3-carboxamido)ethyl)thio)acetamido)pyridin-4-yl)trifluoroborate (4.13)**

In a 1.5 mL eppendorf tube, compound **4.12** (7.4 mg, 0.01 mmol) was fluoridated with excess  $\text{KHF}_2$  (6 M, 50  $\mu$ L). The reaction was purified with a silica pipette column to the

desired product in quantitative yield. Yield: 6.8 mg, 99%. ESI-MS:  $[M+H]^+$ , 679.98 (100%).

#### **Synthesis of propargylated arylborimidine (4.14)**

Briefly, 1,3,5-trifluoro-2-carboxyphenyl-4-boronic acid was prepared according to previous reports. Instead of converting the boronate to the tetraphenylpinacolate, a diaminonaphthalene (dan) group was installed according to previous reports. The carboxylate was activated in the presence of EDC according to previous reports and condensed with propargyl amine. cpd 1 was purified by flash chromatography.

#### **Preparation of $^{19}\text{F}$ -labeled 4.15**

Following previous reports for the production of the 1,3,5-trifluoro-4- $\text{ArBF}_3^-$ , **1** (50 nmol) was dissolved in DMF (5  $\mu\text{L}$ ) to which was added 1 M pyridazine-HCl buffer (2  $\mu\text{L}$ ) in 50% DMF/ $\text{H}_2\text{O}$  and  $\text{KHF}_2$  (100 mM, 1  $\mu\text{L}$ ) aqueous solution to make a cocktail. The solvent was removed under vacuum in a speed-vac at 45  $^\circ\text{C}$ . Generally this procedure took 15 min. The residue was directly used for the next step without further purification.

#### **Rhodamine conjugated $^{19}\text{F}$ -labeled aryltrifluoroborate (4.16)**

Approximately 50 nmol of **2** was resuspended with 5%  $\text{NH}_4\text{OH}$  in 50% MeCN/ $\text{H}_2\text{O}$  (8  $\mu\text{L}$ ). A MeCN solution (5  $\mu\text{L}$ ) which contained 100 nmol Rhodamine-azide, 250 nmol  $\text{CuSO}_4$ , and 600 nmol sodium ascorbate was placed in a speed-vac at room temperature (19 degrees). After  $\sim$  10 min, a dark red solid remained. The residue was resuspended with 50% MeCN/ $\text{H}_2\text{O}$  (20  $\mu\text{L}$ ), and then applied to a TLC plate which was developed with 15% methanol in dichloromethane (see **Figure 4.8**). The TLC band, corresponding to **3** was excised and extracted into methanol. The quality control was performed by re-injecting **4.16** into HPLC, and only one single peak was observed at 568 nm. ESI-MS:  $[M]$ , 1039.7 (100%).

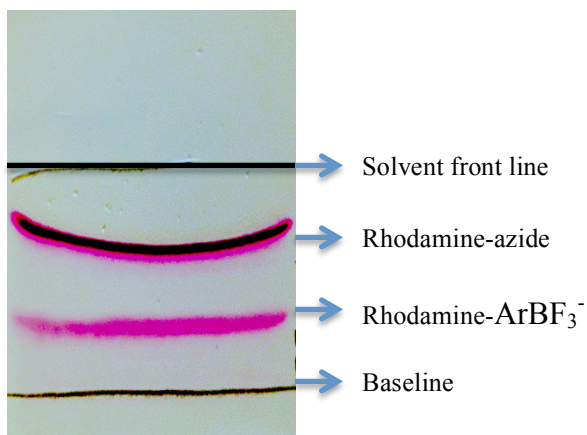


**Figure 4.7** TLC of separation of “click” reaction crude observed under visible light.

In order to verify that the molar extinction coefficient for **4.16** was equal to that of Rhodamine, the UV-Vis spectrum of **4.15** was compared to the Rhodamine spectrum, as shown below in **Figure 4.8**, where  $\text{ArBF}_3^-$  has no absorbance at  $>400$  nm.

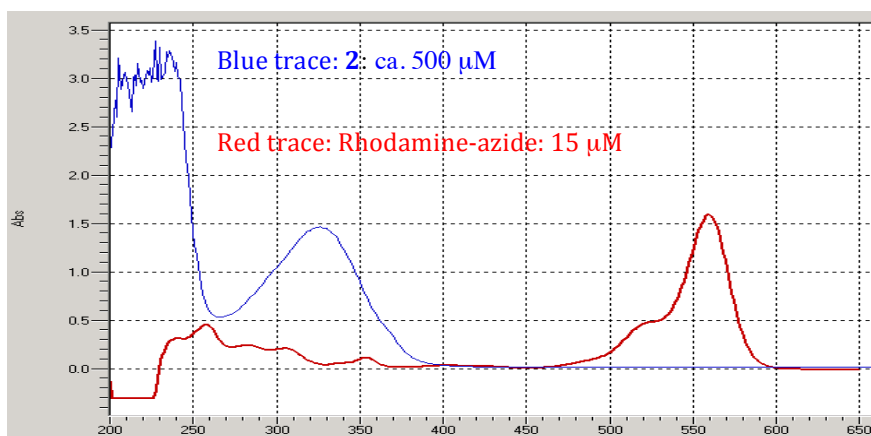


**Figure 4.8** UV-Vis spectrum of **4.15** (blue trace, 500  $\mu\text{M}$ ) and **4.16** (red trace, 15  $\mu\text{M}$ ).

### 4.5.3 Radiosynthesis of 4.15 and Radiolabeling of 4.16

#### **<sup>18</sup>F-fluoride preparation**

<sup>18</sup>F-fluoride was prepared as previously noted. A standard cartridge containing QMA anion exchange resin was converted to the chloride anion form by washing with saturated brine (NaCl) (1 mL) and then with distilled water (2 x 1 mL). In general, approximately 100 mCi <sup>18</sup>F-fluoride was obtained and applied to the column followed by elution into a plastic Falcon tube (polypropylene) with aqueous solution of NaClO<sub>4</sub> (0.3 mL / 8 mg/mL). While we recognize the utility of using <sup>18</sup>F-fluoride directly without trapping, safety regulations at TRIUMF require that contaminating radioactive metals be removed in this manner. Following the addition of MeCN (1 mL), the fluoride was azeotropically concentrated at 110 °C for 15 min; notably the fluoride is concentrated in this manner but not necessarily dried – in particular because it is re-suspended in water. Following concentration, the <sup>18</sup>F-fluoride was re-suspended in a convenient amount of distilled water, for example 45 μL to give a solution of 2.22 mCi/μL.

#### **One-pot two-step <sup>18</sup>F-radiolabeling**

For fluoridation and depending on the starting amount of activity, typically we used 8-20 mCi. Once all the components were added, each tube was counted and the time was noted. The remaining unused <sup>18</sup>F-fluoride was also counted and the cap was replaced on the falcon tube and then the tube was placed in a lead pig and allowed to decay in order to analyze this sample for residual <sup>19</sup>F-fluoride (*vide infra*). It was at this time that the beginning of synthesis (BOS) was noted. For the data reported in the manuscript, we set up two reactions each with 19.3 and 18.7 mCi, while in other cases we used slightly less (see table below). Hence, a volume of 10 μL of the re-suspended <sup>18</sup>F-fluoride cocktail was distributed to two tubes. In the tube corresponding to rxn-1 there was no <sup>19</sup>F-fluoride, whereas the tube corresponding to rxn-2 contained 4 nmol of <sup>19</sup>F-fluoride (2 μL of a 1 mM solution of KHF<sub>2</sub>). For cases where we used only 8 mCi, we added less <sup>19</sup>F-fluoride. In other words, for near-NCA labeling (rxn-2 in each case), we added small amounts of <sup>19</sup>F-fluoride to give an activity that would be ≤4 Ci/μmol.

Following the distribution of NCA fluoride to tubes for rxn-1 and rxn-2, to each reaction was then added 4  $\mu\text{L}$  of a cocktail containing **4.14** and a pyridazine-HCl buffer at pH 1.7-2. Specifically this cocktail is: 12.5 nmol of **4.14** in DMF (5  $\mu\text{L}$ ) and 1M pyridazine-HCl in  $\text{H}_2\text{O}$  (5  $\mu\text{L}$ ). Both tubes were then placed in a standard metal temp-block preheated to  $\sim 30^\circ\text{C}$ . The metal manifold was removed from the temp-block and placed in a desiccator and a vacuum was applied for 15 min. We recognize that a speed-vac would have served the same purpose however space in the hot-cell was limited. In order to prevent any evolution of gaseous HF, a trap was fitted on the vacuum line; this trap contained 4 $\text{\AA}$  sieves. This served to concentrate the reaction. The reaction was then resuspended in 16  $\mu\text{L}$  quench solution: 5%  $\text{NH}_4\text{OH}$  in 50% MeCN/ $\text{H}_2\text{O}$ . Half of the solution was then removed for both TLC and HPLC analysis. To the remainder was added 7 mL of a “click solution” prepared in the following manner: 20 mM Rhodamine-azide in MeCN (15  $\mu\text{L}$ ), 250 mM  $\text{CuSO}_4$  (3  $\mu\text{L}$ ), and 600 mM sodium ascorbate (3  $\mu\text{L}$ ) (note that the copper and ascorbate were added immediately prior to the preparation of the click solution). The tubes were again evacuated for 15 minutes in the desiccator. This procedure took around 10-15 min. The residue was re-suspended with 50% MeCN/ $\text{H}_2\text{O}$  (80  $\mu\text{L}$ ). 40  $\mu\text{L}$  was injected into HPLC for purification. Both the non-clicked  $^{18}\text{F}$ -labeled **4.15** and clicked  $^{18}\text{F}$ -labeled product **4.16** were analyzed by HPLC.

#### 4.5.4 HPLC analysis and specific activity measurement

HPLC trace

HPLC Profiles of  $^{18}\text{F}$ -labeled radiosynthon precursor **4.15** labeled in rxn-1 and rxn-2:  
Note: 50% of the labeling reaction was set aside for HPLC analysis. These fractions were loaded onto the HPLC and resolved as shown in *Figures 4.9* and *4.10*:

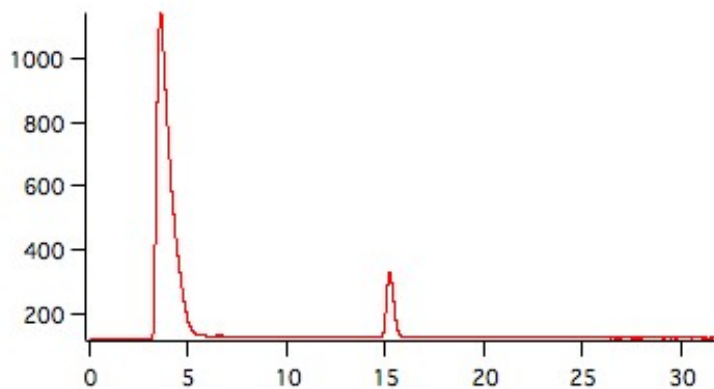


*Figure 4.9* Radioactive HPLC trace of purified  $^{18}\text{F}$ -labeled **4.15** in rxn-1.

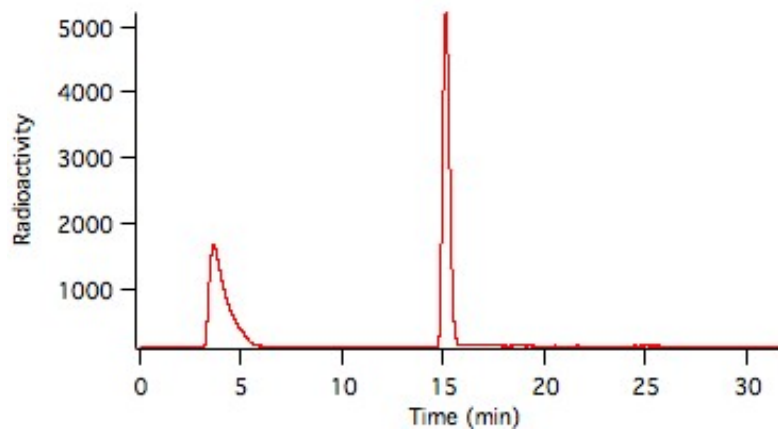


*Figure 4.10* Radioactive HPLC trace of purified  $^{18}\text{F}$ -labeled **4.15** in rxn-2

#### 4.5.5 Specific activity measurement

As these traces were obtained, product **4.16** was manually collected at approximately each 0.5 min interval starting after 21 minutes. At 25 minutes, no more fractions were collected. Each fraction was checked using a hand-held Geiger counter. Fractions at minutes 21-23.5 were pooled and estimated to contain ~80% of the total radioactivity in all fractions. We deliberately did not pool the fractions after 23.5 minutes as these might have been contaminated with azido-Rhodamine that elutes at 25 minutes.

Both rxn-1 and rxn-2 were done and then re-suspended with 50% MeCN/H<sub>2</sub>O (40  $\mu$ L) at EOS, and 6.59 mCi and 6.71 mCi was left, respectively. At EOS +2.0 hours, 38  $\mu$ L of the resulting solution was transferred into a HPLC tube for each reaction; tube 1 for rxn-1 contained 3.25 mCi, and tube 2 for rxn-2 contained 3.31 mCi. Rxn-1 was completely loaded on the HPLC at EOS +4 hours and Rxn-2 was injected 1.5 hours later. The total isolated activity from rxn-1 and rxn-2 was 280  $\mu$ Ci and 78  $\mu$ Ci, respectively. Of these pooled fractions, 20% of each was reinjected into the HPLC to check purity and estimate specific activity while the remaining 80% was decayed at -20 °C in order to measure the fluorescence in these fractions.

## Chapter 5: Developing An $^{18}\text{F}$ - $^{19}\text{F}$ Isotope Exchange (IEX) Reaction to Achieve High Specific Activity with An $\text{ArBF}_3^-$ Bioconjugate

This Chapter is an adaption of published work, and is reproduced in part with permission from Liu Z., Li Y., Lozada J., Pan J., Lin K.-S., Schaffer P., Perrin D. M., Rapid One-Step  $^{18}\text{F}$ -Labeling of Aryltrifluoroborate Conjugates by Isotope Exchange at High Specific Activity, *Journal of labelled compounds and radiopharmaceuticals* **2012**, 55 491–496 and Liu Z., Li Y., Lozada J., Wong M. Q., Greene J., Lin K.-S., Yapp D., Perrin D. M., Kit-like  $^{18}\text{F}$ -labeling of RGD- $^{19}\text{F}$ -Aryltrifluoroborate in High Yield and at Extraordinarily High Specific Activity with Preliminary *in vivo* Tumor Imaging, *Nuclear Medicine and Biology* **2013**, 40, 841-849.

### 5.1 Introduction

In Chapter 4, we improved our labeling methods to achieve exceptionally high specific activity ( $\sim 15$  Ci/ $\mu\text{mol}$ ) in good radiochemical yields under pseudo-aqueous conditions insofar as the entire reaction was dried down at room temperature.<sup>164</sup> While one could argue that this did not truly represent fully aqueous conditions as the reaction occurs on drying, I contend that essentially this method enables what no other does: namely a one-step fluoridation starting with aqueous fluoride and in which all other components are already present in water or water-compatible solvents. Hence, we directly converted a borate ester/borimidine to the corresponding  $^{18}\text{F}$ - $\text{ArBF}_3^-$  with only  $\sim 10$  mCi  $^{18}\text{F}$ -fluoride at high specific activity.<sup>113,164</sup> For the skeptics who would still argue that this represented a drying step, drying occurs *during* the reaction rather than in a separate step that presages a subsequent step or several steps. Moreover this method enables the use of a very small amount of radioactivity that makes this method broadly applicable for lab research. Nevertheless such may not be suitable for production for clinical use that will require the use of 100 mCi or more.<sup>89</sup> Previously, our lab argued that the low specific activities seen when using low levels of starting  $^{18}\text{F}$ -activity are due to the use of low levels of radioactivity in the first place e.g. 10–50 mCi of  $^{18}\text{F}$ -fluoride, and that use of

high levels of  $^{18}\text{F}$ -activity routinely produced by hospital cyclotrons would provide much higher specific activities.<sup>77,165-168</sup> Yet, the use of high levels of  $^{18}\text{F}$ -activity requires robotic manipulation in shielded hot cells, which might not be readily amenable to low reaction volumes that we have presumed will be needed to ensure good radiochemical yields. Encouraged by work by Ralf Schirmacher on isotope exchange with triorganosilylfluorides,<sup>169</sup> along with good *in vivo* tumor images gleaned from two differently linked RGD- $^{18}\text{F}$ - $\text{ArBF}_3^-$  conjugates,<sup>112,124</sup> we hypothesized that a pre-prepared  $^{19}\text{F}$ - $\text{ArBF}_3^-$  bioconjugate would undergo facile  $^{19}\text{F}$ - $^{18}\text{F}$  isotope exchange (either directly on the  $^{19}\text{F}$ - $\text{ArBF}_3^-$  or through re-equilibration with the arylboronate) to provide an  $^{18}\text{F}$ - $\text{ArBF}_3^-$  conjugate in high radiochemical and chemical yield and at high specific activity, thereby greatly simplifying radiosynthesis.

Here we sought to label at very high specific activity with good radiochemical yields in conjunction with production levels of  $^{18}\text{F}$ -activity in fully shielded hot cells. In order to measure the very high specific activity anticipated from using high levels of  $^{18}\text{F}$ -activity, I first labeled a conjugate containing a suitable chromophore that would enable accurate mass measurement from the HPLC trace, from which specific activity would be determined. Hence, I conjugated a  $^{19}\text{F}$ - $\text{ArBF}_3^-$  to Rhodamine ( $\epsilon = 100000 \text{ M}^{-1}\text{cm}^{-1}$  at 568 nm). In keeping with prior conjugation chemistries where I linked the arylboron moiety to the RGD peptide for tumor visualization, I first conjugated Rhodamine to the nonradioactive alkyne- $^{19}\text{F}$ - $\text{ArBF}_3^-$  via a copper mediated 2+3 cycloaddition “click” reaction to give the radiosynthetic precursor.

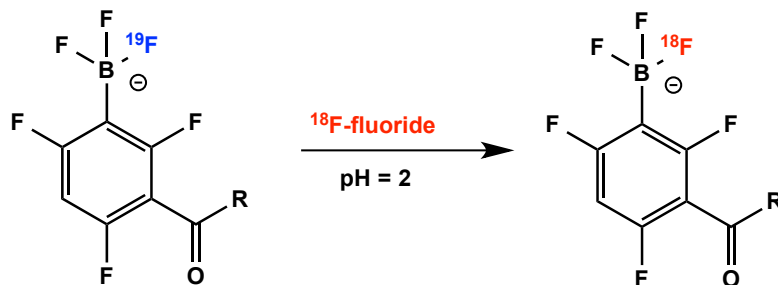


**Figure 5.1**  $^{18}\text{F}$ - $^{19}\text{F}$  isotope exchange with  $\text{ArBF}_3^-$ .

This conjugate was then subjected to a  $^{19}\text{F}$ - $^{18}\text{F}$  IEX reaction using clinical levels of NCA fluoride ( $> 0.5$  Ci) for the rapid production of a fluorescent  $^{18}\text{F}$ - $\text{ArBF}_3^-$  bioconjugate at very high specific activity. The salient advantages embodied in this labeling method are the following: (1) rapid synthesis time:  $<15$ min; (2) excellent radiochemical yields  $\sim 50\%$ ; (3) the use of aqueous conditions; (4) the use of high levels of radioactivity common to production labs; (5) a kit-like approach that uses only 50 nmol of lyophilized precursor; and (6) the production of a dual-modal  $^{18}\text{F}$ -labeled fluorophore at very high specific activity.

In addition, here I extend single-step aqueous labeling to RGD at equally high specific activities that are 3-10 fold higher than values normally described as “high” by the entire field of radiochemists.<sup>56,152,155,170</sup> RGD was chosen on two accounts: (1) its clinical relevance for animal and human images of the  $\alpha_v\beta_3$  integrin receptor a well-defined prognostic indicator for several different types of cancers,<sup>87,89</sup> and (2) the same RGD- $\text{ArBF}_3^-$  bioconjugate labeled herein had been previously imaged at quite low specific activity by direct labeling.<sup>112,124</sup> Here we demonstrate excellent radiochemical yields and extraordinarily high specific activity along with preliminary *in vivo* data that shows specific tumor uptake and we highlight the advantages of this method that include easy operation of radiolabelling in lead-shielded hot cell with up to 1000 mCi radioactivity; which would be of high interest for use in production labs. The potential advantages of routine labeling at 10 Ci/ $\mu\text{mol}$  are discussed.

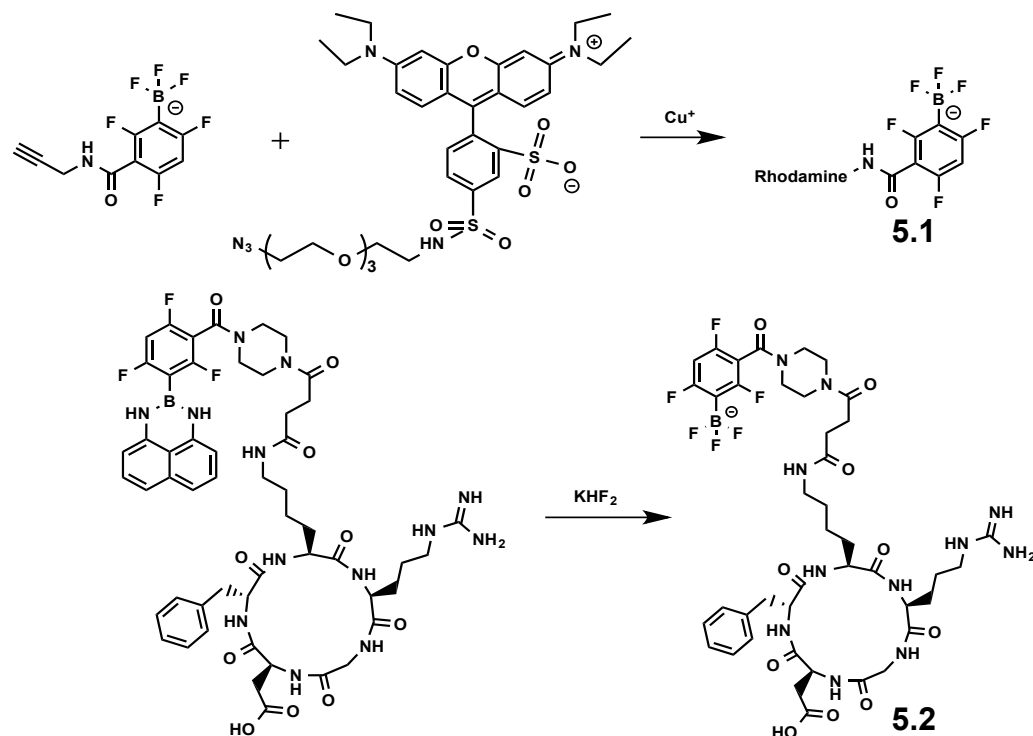


**Figure 5.2** Synthesis route of Rhodamine-ArBF<sub>3</sub><sup>-</sup> (5.1) and RGD-ArBF<sub>3</sub><sup>-</sup> (5.2).

## 5.2 Results

### 5.2.1 <sup>18</sup>F-<sup>19</sup>F IEX with a fluorescent ArBF<sub>3</sub><sup>-</sup>

The alkyne-<sup>19</sup>F-ArBF<sub>3</sub><sup>-</sup>, prepared as described in Chapter 4 is reacted with commercially available azide-triethyleneglycolyl-Rhodamine bis-sulfonate in the presence of Cu<sup>2+</sup> and ascorbate to provide the Rhodamine-<sup>19</sup>F-ArBF<sub>3</sub><sup>-</sup> bioconjugate shown in **Figure 5.2**. Following TLC and HPLC purification, the conjugate was lyophilized in aliquots of 50 nmol. For labeling, 816.5 mCi NCA <sup>18</sup>F-fluoride ion was concentrated at 100 °C for 10 min in a polypropylene tube. An aliquot of Rhodamine-<sup>19</sup>F-ArBF<sub>3</sub><sup>-</sup> (50 nmol) was re-suspended in a DMF-water solution (50 μL) containing a pyridazine-HCl buffer (pH = 2). This solution was transferred by syringe to the plastic tube containing the NCA <sup>18</sup>F-fluoride ion. After 10–15 min at 40 °C, the reaction was quenched by the addition of 2 mL 5% NH<sub>4</sub>OH in 50% MeCN/H<sub>2</sub>O, which served to re-suspend the reaction contents. About 2 h following quench, a small portion of the crude reaction (4.1 mCi) was removed and injected into the HPLC.

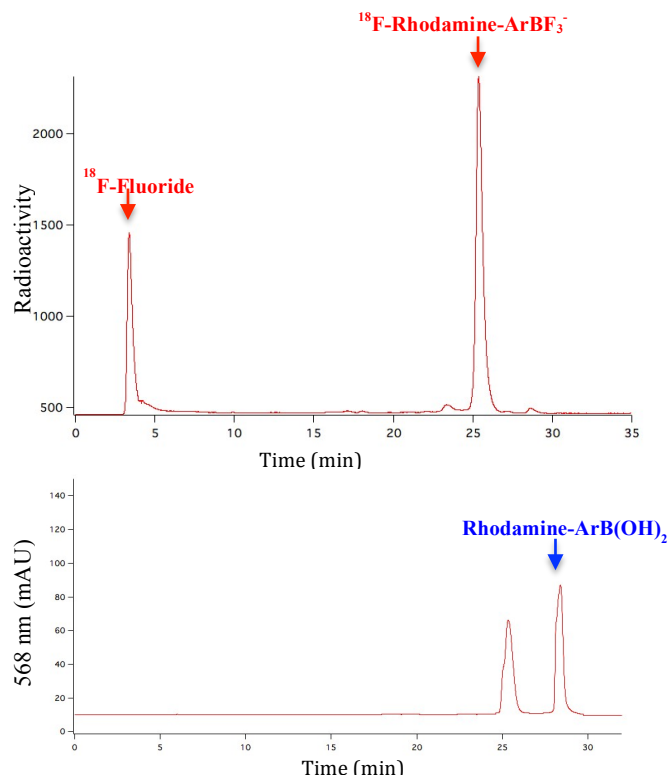


**Figure 5.3** (top): Radioactive HPLC trace of  $^{18}\text{F}$ - $^{19}\text{F}$  IEX of **5.1**. Two major peaks were detected, the first peak was  $^{18}\text{F}$ -fluoride, and the second peak was the desired  $^{18}\text{F}$ -labeled product. **Figure 5.3** (bottom): UV-Vis HPLC trace of  $^{18}\text{F}$ - $^{19}\text{F}$  IEX of **5.1**. The first peak was the fluorescent peak of product, and the second peak indicated the corresponding Rhodamine- $\text{ArB}(\text{OH})_2$ , which was the major byproduct of  $^{18}\text{F}$ - $^{19}\text{F}$  IEX and could be removed by HPLC purification.

**Figure 5.3** shows the radioactive and corresponding UV-Vis HPLC traces of the crude labeling reaction. Many observations can be made based on this result, some of which include: (1) there are only two radio-peaks, one corresponding to free  $^{18}\text{F}$ -fluoride ion and one corresponding to the desired Rhodamine- $^{18}\text{F}$ - $\text{ArBF}_3^-$ ; (2) the radiochemical yield, decay corrected to the end of synthesis, appears to be 75% (63% not decay corrected), which implies the production of >500 mCi of radiotracer starting with 816 mCi,<sup>89,118,171</sup> although isolated radiochemical yields are slightly lower, that is, 40–50%; (3) there is a

~50% chemical radiochemical yield as the UV trace shows a second, well separated fluorescent product that elutes at 28.5 min, which is the arylboronic acid whose formation competes with isotope exchange or occurs either through a re-equilibration between the arylboronic acid, the  $\text{ArBF}_3^-$  and free fluoride or by solvolysis of the  $\text{ArBF}_3^-$  to the arylboronic acid.

### 5.2.2 Specific activity measurement of $^{18}\text{F}$ -Rhodamine- $\text{ArBF}_3^-$

For the radiosynthesis featured in **Figure 5.3**, a small portion of the crude reaction that contained 4.1 mCi was loaded on the HPLC, from which was eluted 2.2 mCi (53% isolated) 25.5 min later. Integration of the visible peak at 568 nm that eluted at 25.5 min, provided a quantitative mass value of 330 pmol and therefore gave a specific activity of 6.7 Ci/ $\mu\text{mol}$  at TOC (time of collection). Correcting for the 2 h lag time between quenching and loading, the real specific activity at TOC was an extraordinary 14.3 Ci/ $\mu\text{mol}$ . The calculated specific activity of 16 Ci/ $\mu\text{mol}$  (that is, 0.8 Ci/50 nmol  $\text{ArBF}_3^-$ ), corrected to the beginning of synthesis is consistent with the specific activity that was measured. This reaction was repeated using 485 mCi and 412 mCi in radiochemical yields of 50% and 45%, respectively, and specific activities in the range of 3–7 Ci/ $\mu\text{mol}$ , corrected to TOC (see experimental section). These slightly lower specific activities are consistent with the use of commensurately lower levels of  $^{18}\text{F}$ -radioactivity. Given the success in this method and the unambiguous measurement of specific activity, I turned my attention to labeling peptides of clinical interest.

### 5.2.3 Towards a kit-like radiosynthesis of RGD- $^{18}\text{F}$ - $\text{ArBF}_3^-$ by IEX

For the radiolabeling featured in **Figure 5.4**, 927 mCi NCA  $^{18}\text{F}$ -fluoride in a polyester tube was concentrated at 110 °C for 10 min. 850 mCi remained due to decay for 10 min. A single radiosynthesis “kit” containing 50 nmol of lyophilized RGD- $^{19}\text{F}$ - $\text{ArBF}_3^-$  was re-suspended in buffered DMF-water (pyridazine-HCl buffer, pH 2.3) and combined with the NCA  $^{18}\text{F}$ -fluoride and labeled for 15 min, at which point the entire contents of the vial were re-suspended in 2 mL of quench solution at pH 7.5. As with all high-level radiosynthesis, only a small portion (~50  $\mu\text{L}$ , containing approximately 15-20 mCi) can

be safely removed from the hot cell for HPLC purification and subsequent quality control analysis following labeling.

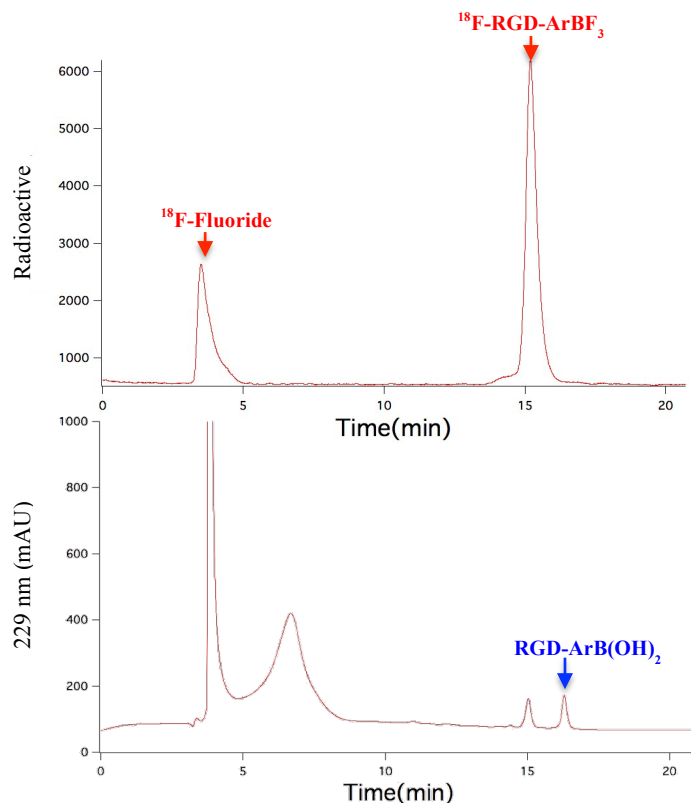


**Figure 5.4** (top): Radioactive HPLC trace of  $^{18}\text{F}$ - $^{19}\text{F}$  IEX of **5.2**. Two major peaks were detected, the first peak was  $^{18}\text{F}$ -fluoride, and the second peak was the desired  $^{18}\text{F}$ -labeled product. **Figure 5.3** (bottom): UV-Vis HPLC trace of  $^{18}\text{F}$ - $^{19}\text{F}$  IEX of **5.2**. The first peak was likely DMF, while the second, very broad peak came from pyridazine buffer. The third one was the UV peak of product, and the fourth peak was the corresponding RGD-ArB(OH)<sub>2</sub>, which was the major byproduct from  $^{18}\text{F}$ - $^{19}\text{F}$  IEX and could be removed by HPLC purification.

The radioactive and corresponding UV-Vis HPLC traces of the crude reaction are shown in **Figure 5.4**, which affords four important observations similar to those gleaned from the labeling of the Rhodamine-ArBF<sub>3</sub><sup>-</sup>: (1) Only two peaks are seen in the radiotrace: one

appears to be free  $^{18}\text{F}$ -fluoride (4-5 min) and one is the desired  $^{18}\text{F}$ -**5.2** (15 min) that was confirmed by HPLC analysis of the “cold standard”  $^{19}\text{F}$ -**5.2**; (2) In the UV-vis trace there are also only two peaks, one that coincides with the  $^{18}\text{F}$ -**5.2** peak, seen in the radiotrace (15 min), and the other corresponding to the free boronic acid i.e. RGD-ArB(OH)<sub>2</sub> (16.5 min), which was observed previously. This reflects an overall 60% chemical yield. Hence 40% of the starting  $^{19}\text{F}$ -**5.2** (20 nmol) is competitively hydrolyzed to the unwanted RGD-ArB(OH)<sub>2</sub>, which can be readily separated from the desired  $^{18}\text{F}$ -**5.2** by HPLC; (3) At the end of synthesis (EOS), the decay corrected radiochemical yield (RCY) is 65% (49% without correction). This means >400 mCi radiotracer can be produced starting with ~900 mCi of  $^{18}\text{F}$ -fluoride, where this activity has been measured following concentration to near-dryness (beginning of synthesis); (4) The specific activity value is easily calculated to be 14 Ci/ $\mu\text{mol}$  (i.e. 420 mCi is contained in 30 nmol of  $^{18}\text{F}$ -**5.2**) and a 60% chemical yield is obtained.

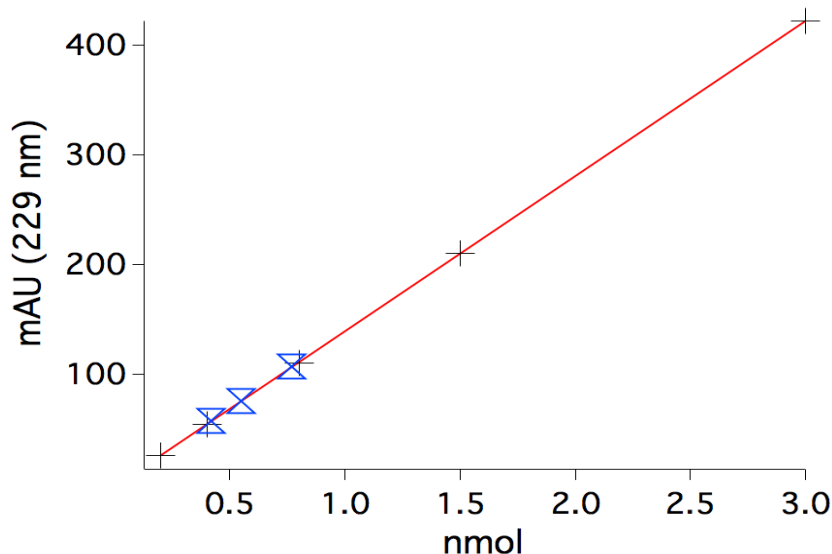


**Figure 5.5** Fitted linear standard curve with HPLC injection of 200 pmol, 400 pmol, 800 pmol, 1500 pmol and 3000 pmol  $^{19}\text{F}$ -**5.2**. The black crosses indicate the values obtained from HPLC integration while the blue marks show HPLC absorbance of the **5.2** peak obtained from each radiolabeling reaction.

#### 5.2.4 Specific activity measurement of $^{18}\text{F}$ -RGD- $\text{ArBF}_3^-$

In order to validate the calculated specific activity, we also measured the specific activity indirectly by correlating UV-absorbance to a standard curve. Firstly, we established a standard curve (**Figure 5.5**) by injecting known quantities of  $^{19}\text{F}$ -5.2 that had been determined by weight. For the radiosynthesis in **Figure 5.4**, integration of the visible peak (229 nm) that eluted at 15.1 min provided a quantitative mass value of 0.79 nmol based on the fitted linear standard curve. For this purification shown in **Figure 5.4**, 17.1 mCi was loaded on the HPLC, and 9.1 mCi was collected at ~15 min (total time ~30 min). Hence, the specific activity was measured to be 11.5 Ci/ $\mu\text{mol}$  at the time of collection.

While the specific activity value measured by standard curve analysis is slightly lower than that measured by interpolating chemical and radiochemical yields based on using a known amount of precursor (50 nmol), both analyses are based on first weighing the peptide, which may not account for associated water and ions. Nevertheless, both values (11.5 Ci/ $\mu\text{mol}$  and 14 Ci/ $\mu\text{mol}$ ) demonstrate radiolabeling at unprecedentedly high specific activities while the <20% difference between the two values may simply reflect experimental error. Finally, in order to show the reproducibility of this labeling method, the radiolabeling was performed three times and results are presented in **Table 5.1**.

**Table 5.1** Summary of measured specific activity based on standard curve analysis.

Labeling #	$^{18}\text{F}$ at BOS mCi	$^{19}\text{F}$ -5.2 (nmol)	$^{18}\text{F}$ -5.2 (HPLC analysis, mCi)	$^{18}\text{F}$ -5.2 (HPLC, analysis nmol)	SA of EOS Ci/ $\mu\text{mol}$
1	891	~50	6.4	0.47	13.6
2	1027	~50	7.3	0.54	13.5
3	927	~50	9.1	0.79	11.5

### 5.2.5 Biological evaluation of $^{18}\text{F}$ -RGD- $\text{ArBF}_3^-$ (**5.2**) at high specific activity

In order to study specific tumor uptake, six mice, of which three were pre-blocked by pre-injection of 100 nmol **5.2** prior to injection with 100  $\mu\text{Ci}$   $^{18}\text{F}$ -**5.2** for 120 min scans, were tested. Scanned mice, as well as two others to provide a cohort ( $n = 3$ ), were sacrificed for *ex vivo* biodistribution data after 120 min. This study showed tumor uptake in the unblocked mice of  $0.46 \pm 0.12\% \text{ID/g}$  and an average tumor: blood ratio of 6.6, while the average tumor uptake in the blocked mice was  $0.17 \pm 0.03\% \text{ID/g}$  and an average tumor: blood ratio of 2.4. Although uptake values are low, statistical significance is observed between the blocked and unblocked mice, thus demonstrating specific uptake, which is to be expected for labeled RGD. To corroborate these sets of data, two mice (blocked and unblocked) were imaged for 120 min by dynamic PET/CT scanning. The tumor was clearly observable whereas blocked mice had much less tumor uptake. This data are summarized in *Figure 5.6* and *Figure 5.7*.

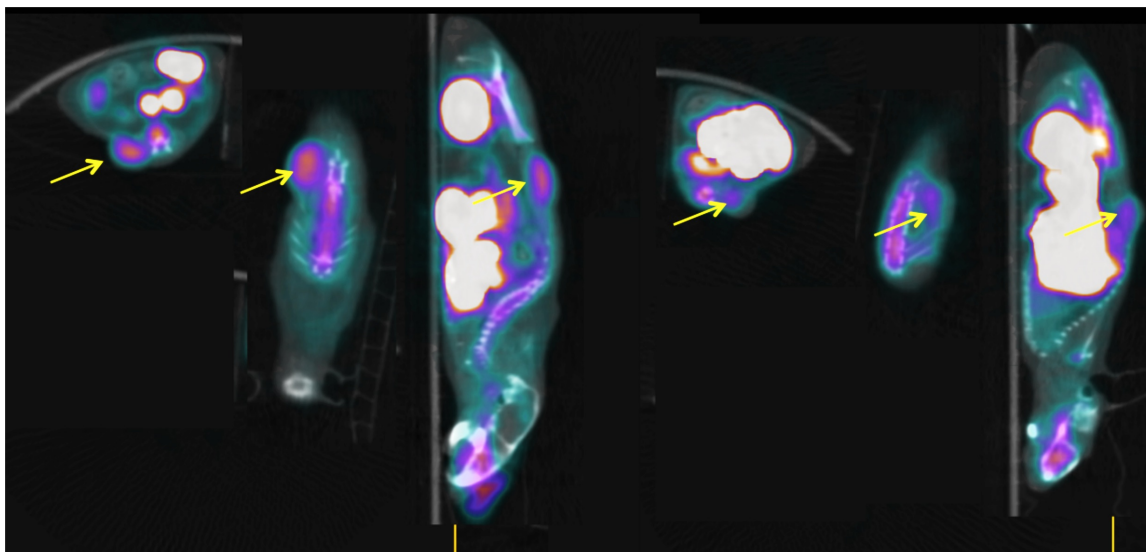


**Figure 5.6** *In vivo* PET/CT imaging of  $^{18}\text{F}$ -**5.2** in unblocked mouse (left three images); blocked mouse (right three images). The yellow arrows indicate the location of the tumor. For each data set, from left to right the image is transverse section, coronal section and sagittal section, respectively.

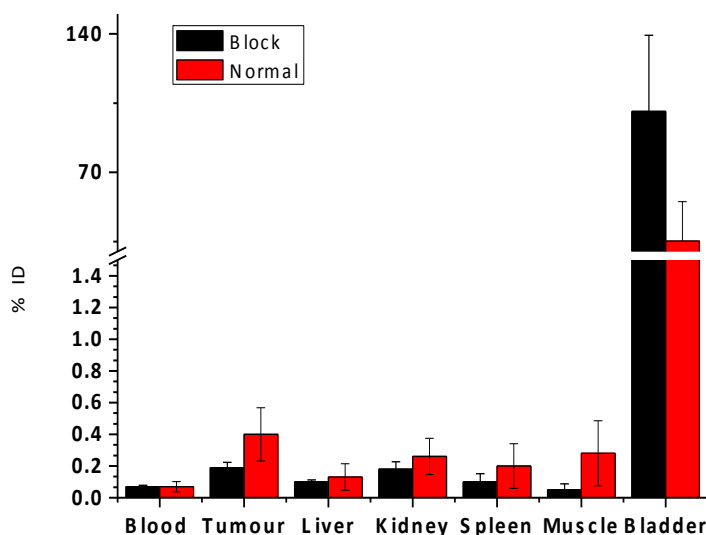


**Figure 5.7** Biodistribution of  $^{18}\text{F}$ -**5.2** ( $n = 3$ ): for each data set: red bars are unblocked and black bars are pre-blocked with  $100 \text{ nmol } ^{19}\text{F}$ -RGD- $\text{ArBF}_3^-$ , each mouse was injected with  $100 \mu\text{Ci } ^{18}\text{F}$ -**5.2** at  $8 \text{ Ci}/\mu\text{mol}$ ,  $p$ -value = 0.07 for the tumor (unblocked vs. blocked),  $p$ -value = 0.1 for the muscle (unblocked vs. blocked).

### 5.3 Discussion

Here we used 800-1000 mCi NCA  $^{18}\text{F}$ -Fluoride ion to label  $\sim 50 \mu\text{g}$  quantities of lyophilized precursor with 50% radiochemical yields within 15 min in one-step. HPLC purification, which required another 15 min, afforded a radiochemically pure tracer at specific activities of up to  $14 \text{ Ci}/\mu\text{mol}$ , a value that is nearly 10 fold higher than most other radiosynthesis. While IEX appears to provide a rapid and robust means of labeling, the appearance of free arylboronic acid suggests that  $^{18}\text{F}$ -**5.2** may arise from two different mechanisms that have yet to be addressed. The first is to simply consider complete re-equilibration of all fluoride ions (those initially bound to the  $\text{ArBF}_3^-$ , and those from the NCA  $^{18}\text{F}$ -fluoride). In this case IEX is simply a restatement of le Chatelier's principle where the equilibrium state for free fluoride,  $\text{ArBF}_3^-$  and the boronic acid is re-established

rapidly at pH 2.3 in the IEX reaction. The second mechanism presupposes non-equilibrium conditions where the  $^{19}\text{F}$ -**5.2** undergoes either IEX or solvolysis. This mechanistic nuance, which does not change the results herein, simply concerns a subtle difference between kinetic and thermodynamic parameters that govern high yielding labeling and will be the subject of further investigation.

The RGD-ArB(OH)<sub>2</sub> that forms was fortuitously removed by HPLC which gave radiochemically pure  $^{18}\text{F}$ -**5.2**. Yet had we not used HPLC, the effective specific activity of the RGD (labeled + unlabeled) would have fallen by a factor of ~2 to a still very high 6-8 Ci/ $\mu\text{mol}$  (i.e. 420 mCi/50 nmol total RGD peptide). Obviating HPLC purification reflects a recent trend in radiosynthetic cases where neither radiochemical purity nor high specific activity may be required and where, instead, time economy is of paramount importance. For example, the specific activity of bisRGD- $^{18}\text{F}$ -Al-NOTA that was calculated to be 6 Ci/ $\mu\text{mol}$  was experimentally found to be 0.16-0.8 Ci/ $\mu\text{mol}$  due to an inability to separate bisRGD- $^{18}\text{F}$ -Al-NOTA from unlabeled congeners. For the RGD- $^{18}\text{F}$ -ArBF<sub>3</sub><sup>-</sup> reported here, had we not used HPLC and instead passed the crude contents of the reaction over a sep-pak to simply remove the unincorporated  $^{18}\text{F}$ -fluoride, the effective specific activity, defined as Ci/total  $\mu\text{mol}$  ligand including unlabeled and unconjugated congeners, would have fallen 50% to 6-8 Ci/ $\mu\text{mol}$  as the tracer would have been comprised of an additional 20 nmol of unlabeled RGD-ArB(OH)<sub>2</sub>. Nevertheless, this would have saved 15 min. Notably however, specific activities of 6-8 Ci/ $\mu\text{mol}$  are on par with some of the highest specific activities reported for peptides, suggesting that a simple sep-pak step to retain the tracer would have been fully compatible with this method and in line with the current trend towards HPLC-less radiosynthesis.

Current trends notwithstanding, we contend that the 15 minutes spent on HPLC purification, which reduced radiochemical yields by ~15%, provided a tracer with unprecedentedly high specific activity and one that is two-fold higher than what could be achieved without HPLC. Furthermore, we surmise that regulatory agencies may not look favorably on tracers that are chemically and radiochemically impure. Nevertheless in terms of circumventing HPLC purification, arylboronate technology presents yet another advantage: because boronic acids have a marked affinity for diols, we envision

development of a sep-pak approach that involves a C18 cartridge to remove  $^{18}\text{F}$ -fluoride and other salts, and a diol column to trap the unlabeled arylboronic acid byproduct;<sup>137,172</sup> leaving the radiochemically and chemically pure tracer to be isolated without HPLC purification. The development of such traps is currently underway.

Despite a recent emphasis on HPLC-free radiosynthesis to increase time economy, high specific activity is of paramount importance, particularly for imaging low abundance targets where unlabeled carrier will always compete with tracer to erode image quality. Moreover, high specific activity will be essential to meet new regulatory requirements for microdosing that require that the total injected mass be 1% of a dose needed for a physiological response. Although 1 Ci/ $\mu\text{mol}$  has been described as “high”,<sup>56,152,155,170</sup> an injected dose of 10 mCi at 1 Ci/ $\mu\text{mol}$  represents 10 nmol (or 2 nM in 5L of blood), which, for a high affinity peptide drug of mol. wt.  $\sim 1600$ , is 16  $\mu\text{g}$  (a quantity that exceeds a microdose). Examples of peptide drugs where 16  $\mu\text{g}$  will be more than three times higher than the allowable microdose include clinically trialed GnRH analogs. Thus, unless specific activities increase, FDA requirements for microdosing will severely restrict clinical imaging to lower affinity tracers ( $K_{\text{dS}} > 20$  nM), such that 10 nmol still represents a microdose. At current specific activity levels, the only option for imaging such drugs would involve a deliberate reduction in affinity, provided specificity is not concomitantly diminished. Nevertheless, we also recognize counter-arguments in favor of adding carrier to improve image quality as in the case of labeled octreotate (where lower specific activity improves image quality).<sup>78</sup>

For applications where high specific activity is not needed, three new options are available to investigators: i) add more  $^{18}\text{F}$ -**5.2** to further boost chemical and radiochemical yields by IEX, ii) use less NCA  $^{18}\text{F}$ -fluoride, or iii) simply wait until the tracer decays to the desired specific activity. Furthermore those who remain satisfied with specific activities of 0.5 Ci/ $\mu\text{mol}$  must appreciate that labeling at 15 Ci/ $\mu\text{mol}$  critically enables two important possibilities: **(1)** The radiotracer distribution time window now increases to 9 hours as tracers labeled at 15 Ci/ $\mu\text{mol}$  can be transported to distant PET scanners before decaying to 0.5 Ci/ $\mu\text{mol}$ ; **(2)** Specific activity can now be routinely

standardized at 1 Ci/ $\mu$ mol by dilution with carrier ligand e.g.  $^{19}\text{F}$ -**5.2**, in accord with patient arrival for the PET scan and to ensure consistency in clinical trials.

While examples of RGD labeled at such high specific activity are, to the best of our knowledge unprecedented, the  $^{18}\text{F}$ -**5.2** studied herein did not provide particularly high tumor uptake values. While a great deal of emphasis is placed on tumor uptake values, we contend that tumor:non-tumor ratios will ultimately be more important for clinical imaging. Here, tumor:blood ratios were still quite high, although tumor:muscle ratios were a bit lower. Overall, these data are reasonably consistent with data from other labeled RGD tracers where tumor:non-tumor ratio ranges from 2-10, while %ID/g values that range from 0.27-12.0.<sup>7,173-176</sup> Interestingly, when the same compound was labeled at much lower specific activity, PET images in a single mouse indicated slightly higher tumor uptake values ( $\sim 2\%$ ID/g). It remains unexplained how much lower specific activity actually appeared to give slightly higher uptake. While this suggests that higher specific activity may not improve image data, a more thorough study will be required to define the relationship between specific activity and image quality in the case of RGD. Such a study will require extensive imaging with a large number of animals, along with specific activities that are deliberately allowed to range by at least an order of magnitude. Given the general limitations in specific activities that can be achieved in standard radiosynthesis, a study where specific activity is deliberately allowed to range from 10 Ci/ $\mu$ mol down to 0.5 Ci/ $\mu$ mol has, to the best of our knowledge, never been conducted for RGD.

While this work describes the potential for doing new studies at high specific activity, it is important to put these findings in context with contemporary developments in other labeling methods that have been elegantly developed to afford excellent radiolabeling yields, high specific activities, and ease-of-use, but which have not provided any viable images. For instance, a recent and important report highlighted a two-step strain-promoted bio-orthogonal click labeling of bisRGD with  $^{18}\text{F}$ -cyclooctyne at relatively high specific activity ( $\sim 2$  Ci/ $\mu$ mol) in 50% radiochemical yield yet no tumor uptake was observed and tumor:blood ratios were less than unity;<sup>177</sup> despite the use of a polar PEG linker designed to enhance clearance. In another example, bombesin- $^{18}\text{F}$ -SIFA was

labeled at 6 Ci/ $\mu\text{mol}$  yet was retained in blood without observable tumor uptake.<sup>57</sup> The lack of images was ascribed to the hydrophobicity of the silyl-fluoride prosthetic, and efforts now focus on increasing radiotracer polarity with PEG or cationic linkers to speed clearance. While considerable effort is now being directed towards *increasing* the polarity of some radiotracers,  $^{18}\text{F}\text{-ArBF}_3^-$  salts are inherently very polar ( $\text{pK}_{\text{oct/wat.}} = -3.9$ ), an attribute that distinguishes  $^{18}\text{F}\text{-ArBF}_3^-$  prosthetics from many other fluorinated prosthetics most of which are hydrophobic. In fact these data suggest that clearance is so rapid that uptake is lower than desired and leads to actions to reduce clearance rates through the incorporation of more hydrophobic linkers, which have been designed to retard clearance of radiometallated tracers.

As comprehensive reviews of RGD radiotracers have suggested, the polarity of the linker arm that connects RGD to a traditionally hydrophobic radioposthetic is especially important, as it must enhance pharmacokinetic properties.<sup>115,178</sup> Here, the reverse will likely be required, as new hydrophobic linkers along with the use of more hydrophobic and/or zwitterionic organotrifluoroborates will effectively reduce clearance. Nevertheless, based on these data, it is possible that other radiotracers may benefit from the very high polarity that is unique to the nature of  $^{18}\text{F}\text{-ArBF}_3^-$  prosthetic. Such tracers may include antibodies, which clear relatively slowly, as well as very hydrophobic peptides.

## 5.5 Conclusion

In this chapter, we have used isotope exchange first on microgram quantities of a fluorescent- $\text{ArBF}_3^-$  for validation of very high specific activity, and then on similar quantities of a clinically used radiotracer, in the presence of production level quantities of  $^{18}\text{F}$ -activity provides excellent radiochemical yields in near record rapidity of 15 minutes. HPLC purification provided radiochemically pure tracer at specific activities of 14 Ci/ $\mu\text{mol}$  within 15 minutes (totally synthesis time  $\sim 30\text{-}35$  min). These values are consistent with previous values obtained with a fluorescent- $^{18}\text{F}\text{-ArBF}_3^-$  and demonstrate the reliability and potential generality of this approach. While more animal studies will be required to fully quantify tumor uptake, the very high specific activity, along with rapid

clearance, gave lower tumor uptake than might be desired. Nevertheless, these findings should encourage others to consider modifying  $^{18}\text{F-ArBF}_3^-$  radiotracers in terms of linker-arm chemistries to boost tumor uptake by slightly retarding clearance. To date, this work presents the first example of  $^{18}\text{F}$ -labeling of a clinically used peptide at extraordinary high specific activity and portends the creation of kits where microgram quantities of lyophilized precursor can be labeled with great ease. The production of tracers at specific activities that are an order of magnitude higher than normal has important implications for clinical development including greater access to microdoses, increased distribution window times, and an ability to standardize specific activities for each injection through dilution with carrier.

## 5.5 Experimental section

### 5.5.1 General information

Reagents and solvents were purchased from Fischer, Sigma-Aldrich, Alfa-Aesar, Novabiochem or Oakwood unless stated otherwise.  $^{18}\text{F}$ -fluoride Trap & Release Columns were purchased from ORTG Inc. (Oakdale, TN) and C18 sep-pak cartridge (Vac 1cc, 50  $\mu\text{g}$ ) was obtained from Waters. Deuterated solvents were purchased from Cambridge Isotope Laboratories.

### 5.5.1 HPLC methods

Unless otherwise stated, all samples were resolved on a Phenomenex Jupiter 10m C18 300Å 4.6 x250 mm analytical column. Gradients for purification are listed below: Gradient A: Solvent A: 0.1% TFA water; solvent B: 0.05% TFA MeCN; 0 to 6 min: 10% to 10% B, 6 to 10 min, 10% to 15% B, 10 to 13 min: 15% to 100% B, 13 to 15 min: 100% to 10% B, 15 to 16 min: 10% to 10% B. Flow rate: 1 mL/min, column temperature: 19 to 21 °C; Gradient B: Solvent A: 0.04 M ammonium formate pH 6.8; solvent B: MeCN; 0 to 5 min: 0% to 5% B, 5 to 10 min: 5% to 35% B, 10 to 20 min, 35% to 45% B, 20 to 22 min: 45% to 100% B, 22 to 28 min: 100% to 100% B, 28 to 30 min: 100% to 20% B, 30 to 33 min: 20% to 5% B; flow rate: 3 mL/min, column temperature: 19 to 21 °C; Gradient C: Solvent A: 0.04 M ammonium formate pH 6.8; solvent B: MeCN; 0 to 5

min: 0% to 5% B, 5 to 10 min: 5% to 35% B, 10 to 20 min, 35% to 45% B, 20 to 22 min: 45% to 100% B, 22 to 28 min: 100% to 100% B, 28 to 30 min: 100% to 20% B, 30 to 33 min: 20% to 5% B; flow rate: 1 mL/min, column temperature: 19 to 21 °C.

### 5.5.3 Synthesis

#### Synthesis of RGD-ArB(tetraphenylpinacolate)

The RGD-ArB(tetraphenylpinacolate) was synthesized according to previous reports.<sup>86,104,124</sup> which highlighted both the stability of the tetraphenylpinacolate boronate ester to coupling conditions, and the excellent chromatographic behavior that it affords on HPLC to allow purification of the boronate-conjugate from other reaction components.

#### Preparation of <sup>19</sup>F-5.2 “labeling kit”

5.2 mg, 4 μmol RGD-ArB(tetraphenylpinacolate) was converted to the corresponding ArBF<sub>3</sub><sup>-</sup> through the addition of 100 μL DMF, 50 μL 3 M KHF<sub>2</sub> and 50 μL 4 M HCl at 40-45 °C for 1 hour and then concentrated with speed-vac at less than 45 °C for 1 hour as previously reported.<sup>124</sup> The reaction was quenched with 1 mL 5% NH<sub>4</sub>OH 1:1 MeCN/Water, then purified by HPLC with method B to isolate ~3 mg of chemically pure RGD-<sup>19</sup>F-ArBF<sub>3</sub><sup>-</sup> suitable for radiolabeling by IEX. After HPLC purification, the RGD-<sup>19</sup>F-ArBF<sub>3</sub><sup>-</sup> was aliquoted into portions of 50 nmol (50 μg), and lyophilized to create radiolabeling kits for routine use on demand.

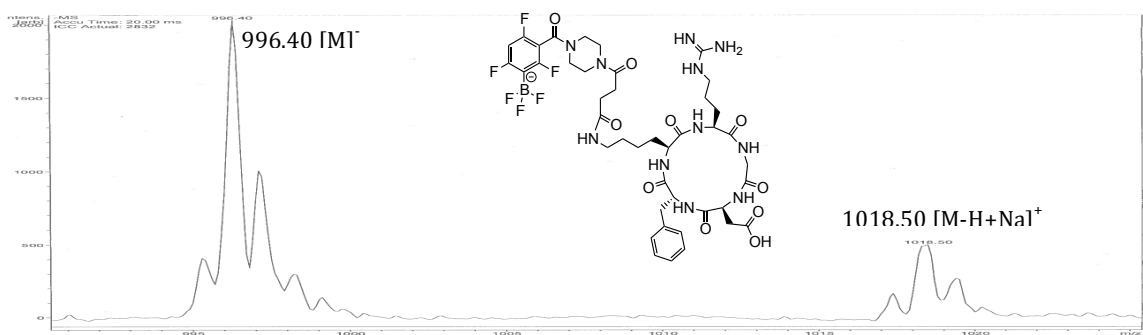


**Figure 5.8** ESI-MS of HPLC purified 5.2.

#### 5.5.4 Preparation of $^{18}\text{F}$ -fluoride

A QMA $^{18}\text{F}$  anion trap (carbonate form) was pretreated with 6 mL deionized water, 6 mL saturated brine (NaCl, aq), and 6 mL DI water to convert it to the chloride form of the resin. Approximately 1.5 mL of target water containing 800-1000 mCi was transferred within a shielded hot cell to the anion exchange resin.<sup>82</sup> The  $^{18}\text{F}$ -fluoride ion was eluted from the resin into the reaction vial using isotonic saline (0.20 mL, 150 mM). Acetonitrile (200 mL) was then added to accelerate azeotropic concentration at 110 °C in less than 10 min. Because of the aqueous conditions of this labeling method, absolute dryness is not needed; hence, in contrast to other methods, drying is simply employed to concentrate the fluoride rather than enhance its chemical reactivity, which often requires repeated azeotropic drying steps.

#### 5.5.5 Radiosynthesis of $^{18}\text{F}$ -5.2 by IEX

RGD- $^{19}\text{F}$ -ArBF $_3^-$  was re-suspended in 15  $\mu\text{L}$  DMF, 15  $\mu\text{L}$  DI water, and 15  $\mu\text{L}$  pyridazine-HCl buffer (pH = 2). This cocktail was stored in a 100  $\mu\text{L}$  tuberculin syringe that was placed in the hot cell just prior to bombardment. Following  $^{18}\text{F}$ -fluoride concentration, the peptide cocktail was injected into the vial containing the  $^{18}\text{F}$ -fluoride (800-1000 mCi activity was measured at the beginning of synthesis). The vial was placed for 20 min in a temp block set at 45 °C and then the reaction was quenched by injection with 2 mL 5% NH $_4\text{OH}$  in 50:50 MeCN/H $_2\text{O}$ . Approximately 2.5% of the quenched reaction mixture (50  $\mu\text{L}$ , ~20 mCi) was removed from the hot cell and loaded onto an analytical HPLC RP-C18 column for purification according to method C. Due to the lack of an automated fraction collector, the radiolabeled product was manually collected at 15 minutes following HPLC resolution and re-analyzed for radiochemical purity. The active fraction was then diluted with 15 mL DI water whereupon the solution was passed through a C18 sep-pak cartridge and washed with 5 mL of DI water to remove residual MeCN and free  $^{18}\text{F}$ -fluoride anion. The RGD- $^{18}\text{F}$ -ArBF $_3^-$  radiotracer was then eluted with ethanol (0.3 mL) into 6 fractions (~50  $\mu\text{L}$  each), diluted into phosphate buffered saline (2 mL), and sent for PET scanning. A small amount was also retained for quality control analysis by HPLC.

Here are the HPLC traces of the additional  $^{18}\text{F}$ - $^{19}\text{F}$  IEX of **5.2**. Reaction 1: Labeling with 50 nmol  $^{19}\text{F}$ -**5.2** and 891 mCi NCA  $^{18}\text{F}$ -fluoride: Top: crude radiotrace; Bottom: UV-vis trace at 229 nm with the units of mAU. Decay corrected specific activity: 13.6 Ci/ $\mu\text{mol}$ . Reaction 2: Labeling with 50 nmol  $^{19}\text{F}$ -**5.2** and 1027 mCi NCA  $^{18}\text{F}$ -fluoride: Left – crude radiotrace; right – UV-vis trace at 229 nm with the unit of mAU. Decay corrected specific activity: 13.5 Ci/ $\mu\text{mol}$ .

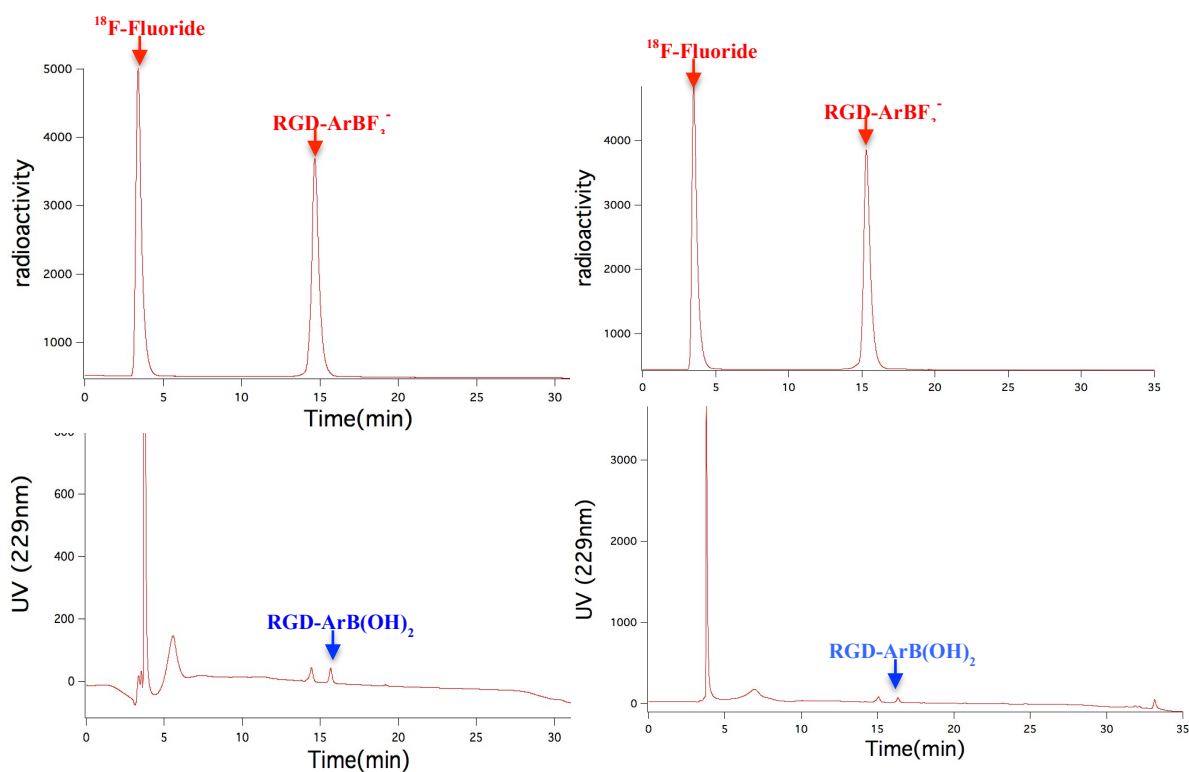


**Figure 5.9** HPLC analysis of the additional  $^{18}\text{F}$ - $^{19}\text{F}$  IEX of **5.2**. **Left:** Labeling with 50 nmol  $^{19}\text{F}$ -**5.2** and 891 mCi NCA  $^{18}\text{F}$ -fluoride: Top: crude radiotrace; Bottom: UV-Vis trace at 229 nm with the units of mAU. **Right:** Labeling with 50 nmol  $^{19}\text{F}$ -**5.2** and 1027 mCi NCA  $^{18}\text{F}$ -fluoride: Left: crude radiotrace; right: UV-Vis trace at 229 nm with the units of mAU.

### 5.5.6 Animal imaging and *in vivo* biodistribution

All animal studies were performed in accordance with the Canadian Council on Animal Care Guidelines and were reviewed and approved by the University of British Columbia Animal Care Committee. Rag2M mice (8-11 weeks old, bred in-house at the BC Cancer Research Agency) were subcutaneously inoculated with U87MG (human glioblastoma) cells into the lower back ( $5 \times 10^6$  cells). Animals were cared for according to human protocols during which time tumor growth was monitored for 2 weeks until a suitable size of 100-200 mm<sup>3</sup> was reached for tracer studies. For biodistribution studies in mice with tumors, tracer was injected via the lateral tail vein while mice were under 2% isoflurane anesthesia. Six mice were used, three of which were pre-blocked by injection of 1 mg/mL RGD-<sup>19</sup>F-ArBF<sub>3</sub><sup>-</sup> (100 μL) and then injected with 100 mCi RGD-<sup>18</sup>F-ArBF<sub>3</sub><sup>-</sup>. Prior to *ex vivo* biodistribution, one set of paired, tumor-bearing mice (blocked and unblocked) were also imaged using the Siemens Inveon multimodality small animal PET/CT scanner to evaluate the tumor-to non-target-tissue contrast for the tracer. A 10 minute CT attenuation scan followed by a 120 minute Dynamic PET scan was carried out. The list-mode data was represented with a histogram, and reconstructed by an iterative reconstruction algorithm (3D OSEM/MAP) using the Inveon Acquisition Workplace Software (Siemens), applying normalization, dead time, random and attenuation correction. The attenuation correction map was obtained from the CT scan data. Following scanning, all mice were humanely euthanized (CO<sub>2</sub>) and tissues/organs of interest were collected, rinsed, patted dry and counted in a gamma counter (Cobra-II Auto Gamma, Canberra Packard Canada). The tissue weight and associated cpm (counts per min.) were used to calculate the percentage of injected dose per gram of tissue (%ID/g).

# Chapter 6: A Broadly Applicable and Facile $^{18}\text{F}$ -labeling Method for PET Imaging

## 6.1 Introduction

Despite the success of PET and increasing interests of  $^{18}\text{F}$ -radiochemistry, a kit-like, one-step  $^{18}\text{F}$ -labeling method that can be broadly applied to small biomolecules to provide functional *in vivo* images has been a long-standing challenge.<sup>115</sup> Most known  $^{18}\text{F}$ -labeling methods, either the well established or newly developed, are relatively onerous and lengthy processes.<sup>89</sup> This is a particularly serious problem given the short half-life of  $^{18}\text{F}$ . For instance, small compounds are typically radiolabeled using a 2-3 step process.<sup>89</sup> Conceptually this approach is extended to the radiosynthesis of prosthetic groups and the further conjugation/purification of the desired radiotracer following the ultimate step involving conjugation. Recently, several beautiful reports have been released about the late-stage radiofluoridation via  $^{18}\text{F}$ -trifluoromethylation or C- $^{18}\text{F}$  bond formation.<sup>55,179</sup> Nevertheless, these strategies still suffer from either low specific activity and/or lack of a simple purification method, which would undermine the needed outcomes of radiolabeling and weaken the quality of PET imaging. Yet, progress in this domain is promising as these new compounds and methods may ultimately lead to the ability to radiolabel a real drug without changing any chemical structures. Nevertheless, many tracers will never be drugs and moreover, the very properties of blood persistence that are desirable in a drug are actually undesirable in regards to a radiotracer that is meant to associate with its target or otherwise clear from the blood. For such purposes, peptides provide a precisely scaffold that is often more suited for tracer development rather than drug development (although notably there are an increasing number of peptide drugs being developed). Hence, there is a real interest in developing a convenient  $^{18}\text{F}$ -labeling method, not just for small molecules but also for peptides and other large biomolecules that are being developed simply as tracers and not necessarily as drugs.

Conventionally, radiofluoridation needs extraordinarily dry reaction environment due to the high solvation energy of anionic fluoride in water.<sup>45</sup> Hence to use it as a nucleophile,

$^{18}\text{F}$ -fluoride must be azeotropically dried, usually twice, with acetonitrile.<sup>55</sup> This procedure is relatively time-consuming and laborious and can increase the risk of synthetic failure, particularly if either the fluoride is not completely dried or if for some reason in its dry states it fails to be resolubilized. Hence an aqueous-friendly labeling method is required to eliminate the step of azeotropic evaporation. Furthermore, to remove impurities, a time-consuming (>30 min) and laborious HPLC purification is usually needed. To date, it is not entirely clear what the standard criteria for “useful”  $^{18}\text{F}$ -labeling will be. However through my work on this thesis, I would like to forward a suggestion for this standardization; a method I have named “stamp” labeling. This analogy is in reference to the fact that stamping mail identifies the mail as “paid for” and processed, while otherwise leaving the envelope relatively unchanged. Therefore, an ideal tracer should keep its original properties after radiolabeling. As Eckelman et al. suggested, a “true” radiotracer should have nearly identical chemical composition as its original bioligand/drug.<sup>75</sup> Moreover, this “stamp” labeling should be as simple and efficient as stamping an envelope, perhaps even as a “prepaid” stamped envelope. Conclusively, “stamp” labeling is the confluence of facile radiolabeling and “true” tracer design. Following are the requirements we suggest for “stamp” labeling. Firstly, the  $^{18}\text{F}$ -radiosynthesis should be simplified as a “kit”; both bioorthogonal and *in vivo* stabilities are necessary for the  $^{18}\text{F}$ -radioprosthetics, which should not participate in any biological processes, and should function only as a reporter in the living system. Finally, as mentioned previously, the  $^{18}\text{F}$ -radioprosthetics would ideally be small in size and free of charge to limit the extent to which the prosthetic might change the biological properties of the tracer so as to ensure that the radiolabeled biomolecule performs the same as the unlabeled molecule in physiological conditions.

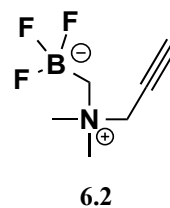
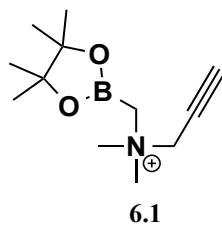
To address all these criteria and develop a “stamp” labeling method, I have continued to develop two rapid and mild radiolabeling methods based on the radiosynthesis of *in vivo* stable  $^{18}\text{F}$ -aryltrifluoroborate ( $\text{ArBF}_3^-$ ) conjugates over the past few years.<sup>82,83,164</sup> Both of the methods now achieve exceptionally high specific activity ( $\sim 15 \text{ Ci}/\mu\text{mol}$ ) and good-to-excellent radiochemical yields in 15 minutes under aqueous conditions. However, relatively dry  $^{18}\text{F}$ -fluoride along with HPLC purification was still needed when I started working on this project. To eliminate the need for these strenuous steps and develop a

real “kit” labeling method, I proposed to use  $^{18}\text{F}$ - $^{19}\text{F}$  isotope exchange in the context of a novel ammoniomethyl- $\text{BF}_3$  ( $\text{AMBF}_3$ ) (*vide infra*) that I developed. Considering the remarkable simplicity of the new designed  $\text{AMBF}_3$ , it would represent an encouraging stamp-like radiosynthon once it is assessed to be stable and bioorthogonal *in vivo*. Given the collaborative nature of this work and the successful relationships that Perrin lab established with both Dr. Francois Benard and Dr. Kuo-Shyan Lin, we were poised to evaluate this proposed  $^{18}\text{F}$ - $\text{AMBF}_3$  strategy with various bioligands using the reproducibility and promising results that have been achieved from preliminary animal studies.

## 6.2 Results and discussion

### 6.2.1 Hydrolytic stability

In Chapter 3, a broad scope of organotrifluoroborates were analyzed in term of their stability in PBS and dimethylammoniomethyltrifluoroborate (**6.2**) was chosen to due to its extraordinary hydrolytic



stability and ease of precursor preparation. NMR-pure compound **6.1** was prepared in quantitative yield by directly precipitating from the 1:1 mixing of N,N-dimethylpropargylamine and iodomethylborate pinacol ester in diethylether. Compound **6.1** is then converted to the corresponding organotrifluoroborate with  $\text{KHF}_2$  to give compound **6.2**, which is chemically stable under  $-20\text{ }^\circ\text{C}$  for at least one year and readily useful for further conjugation via CuAAC reaction. Given the effectiveness and bio-orthogonality of CuAAC reaction, this “clickable” radiosynthon has been successfully conjugated on various ligands binders, enzyme inhibitors, or other functional small molecules (*vide infra*). Prior to radiolabeling and biological evaluation, the solvolytic stability of compound **6.2** was evaluated using  $^{19}\text{F}$ -NMR spectroscopy assay: At  $\text{pH} = 7.5$  and dilute conditions ( $\sim 5\text{ mM}$ ), compound **6.2** was observed to slowly lose free fluoride in pseudo-first order kinetics, resulting in a remarkably long hydrolytic half-life:

19500±500 min (**Figure 6.1**). Indeed this is very encouraging as the half-life is almost twenty-fold longer than the  $\text{ArBF}_3^-$  compounds we reported previously.

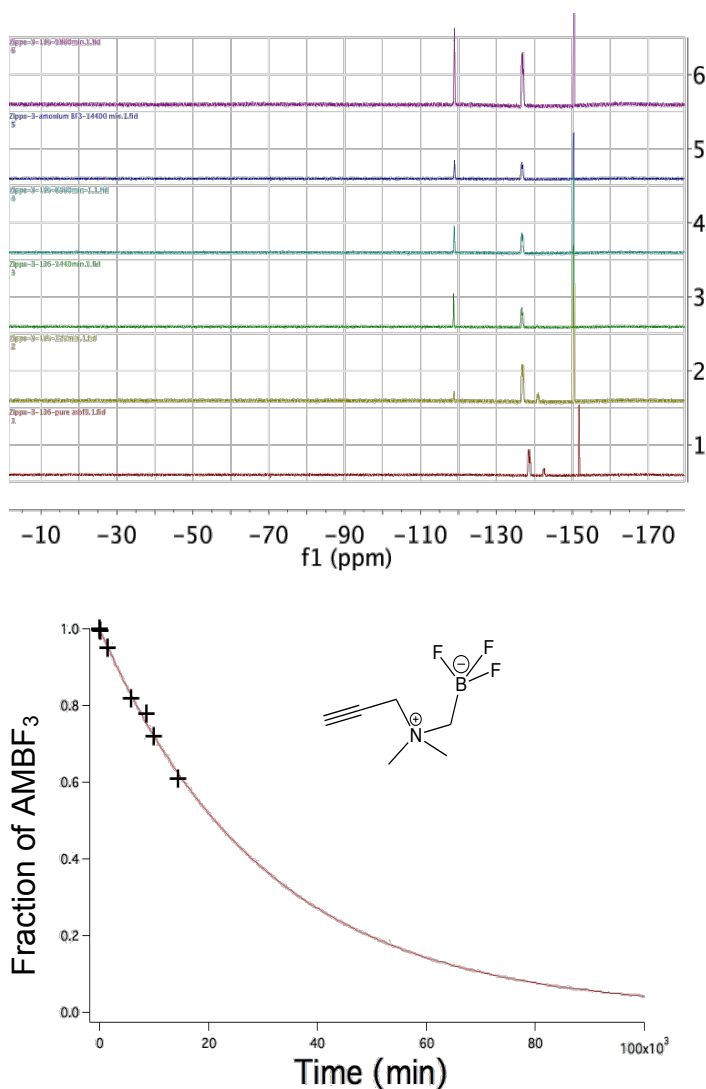


**Fig. 6.1** (Top):  $^{19}\text{F}$ -NMR (phosphate buffer, 25 °C) kinetic analysis of the defluorination from the  $^{19}\text{F}$ -AMBF<sub>3</sub> **6.1** ( $^{19}\text{F}$ -Fluoride: -121 ppm relative to  $\text{CFCl}_3$ ;  $^{19}\text{F}$ -AMBF<sub>3</sub>: -137 ppm relative to  $\text{CFCl}_3$ ). **Fig. 6.1** (bottom): Plot of relative  $^{19}\text{F}$ -NMR integration of the  $^{19}\text{F}$ -AMBF<sub>3</sub> as a function of all compounds ( $^{19}\text{F}$ -AMBF<sub>3</sub> +  $^{19}\text{F}$ -fluoride) vs. time. Data are scaled 100000 min. Data were fit to a first order reaction, and the half-life of the corresponding  $^{19}\text{F}$ -AMBF<sub>3</sub> was calculated to be 19500±500 min.

### 6.2.2 Kit-like radiolabeling

Due to the poor aqueous reactivity of  $^{18}\text{F}$ -fluoride, the  $^{18}\text{F}$ -radiosynthesis typically starts with a time-consuming step by azeotropically drying  $^{18}\text{F}$ -fluoride with MeCN up to 2 to 6 times.<sup>55,63,179</sup> In our case,  $^{18}\text{F}$ - $^{19}\text{F}$  IEX on  $\text{AMBF}_3$  is aqueous-friendly, so the dryness of  $^{18}\text{F}$ -fluoride is not a concern. In addition, we have successfully eliminated the step of drying  $^{18}\text{F}$ -fluoride along by deliberately using a micro QMA cartridge, which is assembled within a 16 gauge needle in order to reduce the dead volume during  $^{18}\text{F}$ -fluoride elution. According to this specifically designed  $^{18}\text{F}$ -release/trap column, most of the radioactivity can be efficiently released ( $>95\%$ , 1 Ci) into the reaction vial with  $<60$   $\mu\text{L}$  saline. At this rather small volume, the concentration of  $^{19}\text{F}$ -precursor is sufficiently high to enable  $^{18}\text{F}$ - $^{19}\text{F}$  IEX and subsequently no further drying is necessary.

Another significant shortfall of most current  $^{18}\text{F}$ -labeling methods is the issue of the byproduct/precursor separation.<sup>11,51,180-184</sup> For instance, considerable ( $>50\%$ ) decomposition of  $\text{ArBF}_3$  to the free  $\text{ArB}(\text{OH})_2$  was detected with our previous  $^{18}\text{F}$ - $^{19}\text{F}$  IEX method by using HPLC.<sup>82,83</sup> For those who are willing to continue using HPLC, this is not necessarily a problem as HPLC could be used to remove any boronic acid side product. However if HPLC is to be avoided, then it must be noted that the resulting  $\text{ArB}(\text{OH})_2$  cannot be simply removed by C18 cartridge as typically it will co-elute along with the desired  $^{18}\text{F}$ - $\text{ArBF}_3^-$ . Subsequently a time-consuming HPLC purification is always required to remove the byproduct (**Figure 6.2**, top). Interestingly, this disadvantage is simply remedied by using  $\text{AMBF}_3$  because of its higher stability at  $\text{pH}=2$ : in a typical labeling reaction,  $<5\%$  decomposition of biomolecule-conjugated  $\text{AMBF}_3$  was detected during most radiosyntheses (**Figure 6.2**, bottom). Therefore, the undesired HPLC purification step is replaced with a simple sep-pak elution, which is GMP friendly and results into a significant advance in clinical applications.

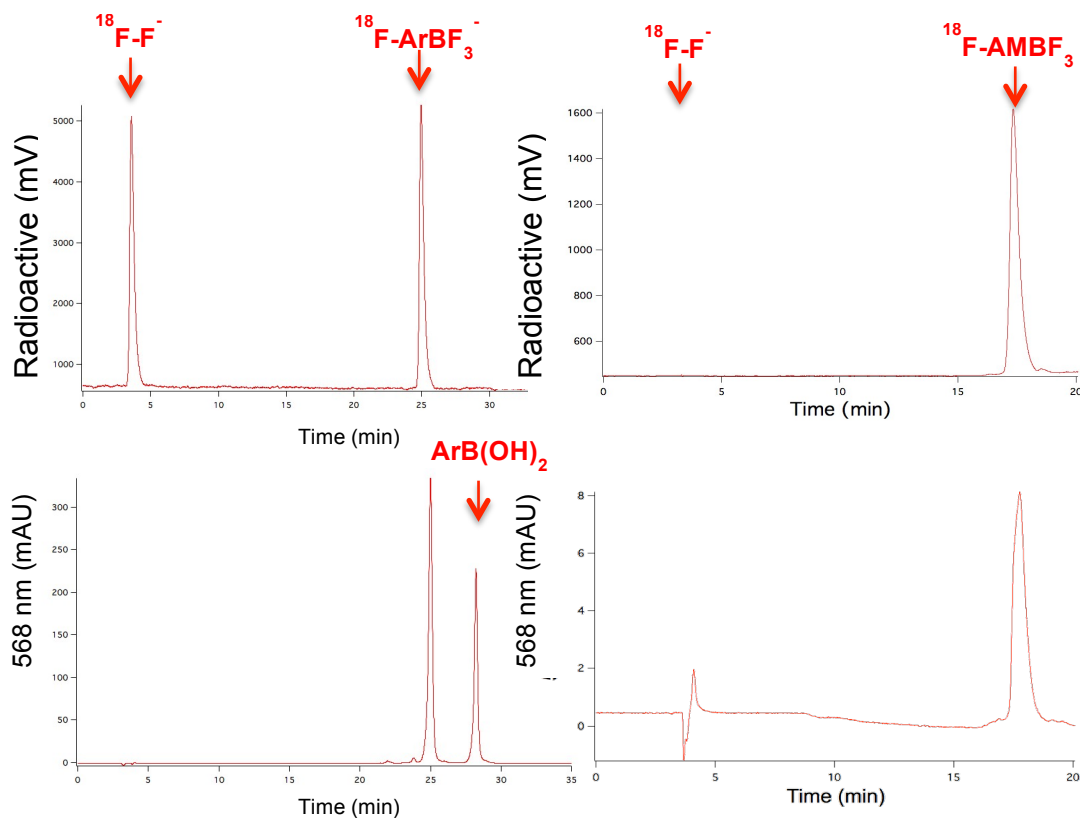


**Figure 6.2** (left): Radioactive (top) and fluorescent (bottom) trace of HPLC purification of crude Rhodamine- $\text{ArBF}_3^-$ . Peaks of Rhodamine- $\text{ArBF}_3^-$  and Rhodamine- $\text{ArB}(\text{OH})_2$  are indicated, respectively. **Figure 6.2** (right): Radioactive (top) and fluorescent (bottom) HPLC trace of reinjection of sep-pak purified Rhodamine- $\text{AMBF}_3$ . Peaks of Rhodamine- $\text{AMBF}_3$  is indicated, and Rhodamine- $\text{AMB}(\text{OH})_2$  is almost undetectable.

### 6.2.3 *In vivo* stability

The initial radiolabeling was tested with a fluorescent Rhodamine- $\text{AMBF}_3$  (**6.7**) that allows the convenient tracing of the reaction progression while also measuring the specific activity of the tracer at the end of synthesis (EOB). In terms of kit development, the purified Rhodamine- $\text{AMBF}_3$  was aliquoted in quantities of 45  $\mu\text{g}$  (~50 nmol) per labeling reaction. Prior to radiolabeling, the precursor is re-suspended in 40  $\mu\text{L}$  aqueous pyridazine buffer (pH=2.5) and then transferred into sealed polypropylene vial using a Hamilton gas-tight syringe. Afterwards, the reaction vial was placed on a heating block at 80  $^\circ\text{C}$  within a lead-shielded hot cell. 800 mCi  $^{18}\text{F}$ -fluoride was directly eluted into the

vial and the  $^{18}\text{F}$ - $^{19}\text{F}$  IEX occurs upon mixing. The radiolabeling was quenched with 2 mL PBS buffer followed by a sep-pak C18 cartridge purification. In general ( $n > 20$ ), starting with 800 mCi  $^{18}\text{F}$ -fluoride, 200 mCi ( $30.1 \pm 4.5$  % radiochemical yield, decay-corrected) of  $^{18}\text{F}$ -conjugated-AMBF<sub>3</sub> would be obtained within 25 min. The purification efficiency was confirmed with QC analysis, which shows only one predominant peak in both radioactive mode and fluorescent mode (**Figure 6.2**, right). A notable advantage of this labeling method is the reproducible high specific radioactivity: ~200 mCi radiolabeled product was acquired with 50 nmol precursor. Thus the specific radioactivity was calculated to be 4 Ci/ $\mu\text{mol}$ . This calculation was verified by a standard curve measurement and is readily translated to the radiosynthesis of other  $^{18}\text{F}$ -conjugated-AMBF<sub>3</sub>s.

Next we evaluated the stability of  $^{18}\text{F}$ -AMBF<sub>3</sub> in plasma to determine its applicability for further *in vivo* studies. As demonstrated in **Figure 6.3**, negligible decomposition was detected even after 2 hr of incubation at 37 °C, thus validating the excellent *in vitro* stability of  $^{18}\text{F}$ -AMBF<sub>3</sub>. This finding was verified by assessing the *in vivo* stability of  $^{18}\text{F}$ -Rhodamine-AMBF<sub>3</sub>. PET/CT scan demonstrated accumulation in mitochondria-rich organs (**Figure 6.4**), as most of the radioactivity quickly accumulated in mitochondria-rich organs such as the liver and heart. This is not unexpected as other Rhodamine tracers similarly track to liver and heart. The radiotracer was then slightly excreted to the intestine after 1 hr. minimal uptake of other organs was detected. While it was anticipated to observe some metabolic degradation for  $^{18}\text{F}$ -labeled small molecules,  $^{18}\text{F}$ -AMBF<sub>3</sub> appears to be metabolically stable and no measurable bone uptake was detected, showing release of free  $^{18}\text{F}$ -fluoride.

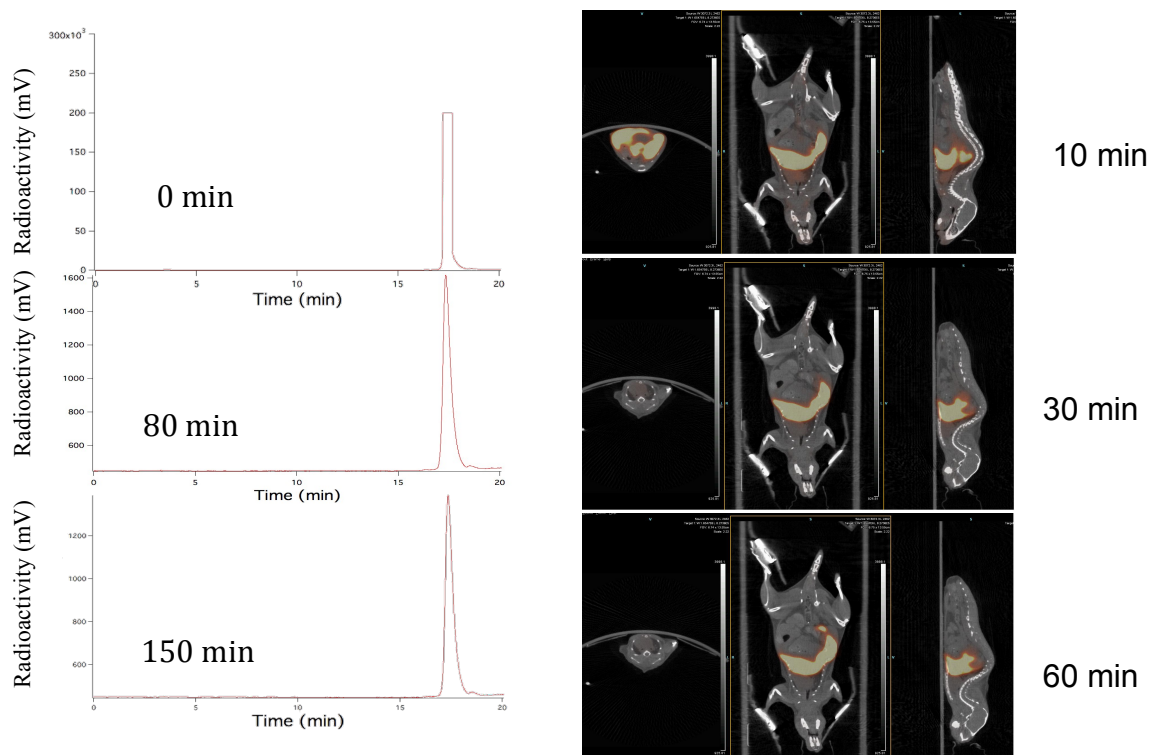


**Figure 6.3** (left): Radioactive HPLC trace following mice plasma incubation of  $^{18}\text{F}$ -radiolabeled **6.7**. The incubation time is 0, 80 and 150 min, respectively. **Figure 6.3** (right): Biodistribution of  $^{18}\text{F}$ -labeled agents in healthy nude mice by small-animal PET. The representative 3D PET/CT images were shown at the time point of 10 min, 30 min and 60 min after being injected with the newly designed Rhodamine- $^{18}\text{F}$ -AMBF<sub>3</sub> (**6.7**).

#### 6.2.4 *In vivo* tumor targeting

To further demonstrate effective biomolecule labeling, the Bradykinin B1 receptor was selected as a clinically relevant model system. The Bradykinin B1 receptor (B1R),<sup>185,186</sup> which is overexpressed in a variety of malignancies but not in normal tissues, is a promising biomarker for cancer imaging. Herein, we report the synthesis and evaluation of an  $^{18}\text{F}$ -labeled peptide derived from the potent antagonist B9858 (Lys-Lys-Arg-Pro-Hyp-Gly-Igl-Ser-D-Igl-Oic) for imaging B1R expression with PET. The precursor of radiosynthesis, B9858- $^{19}\text{F}$ -AMBF<sub>3</sub> (**Figure 6.5**), was achieved in milligram quantities from the conjugation between alkynyl-AMBF<sub>3</sub> and B9858-azide using CuAAC “click” reaction. The  $^{18}\text{F}$ -radiolabeling was performed precisely as previously described via  $^{18}\text{F}$ -



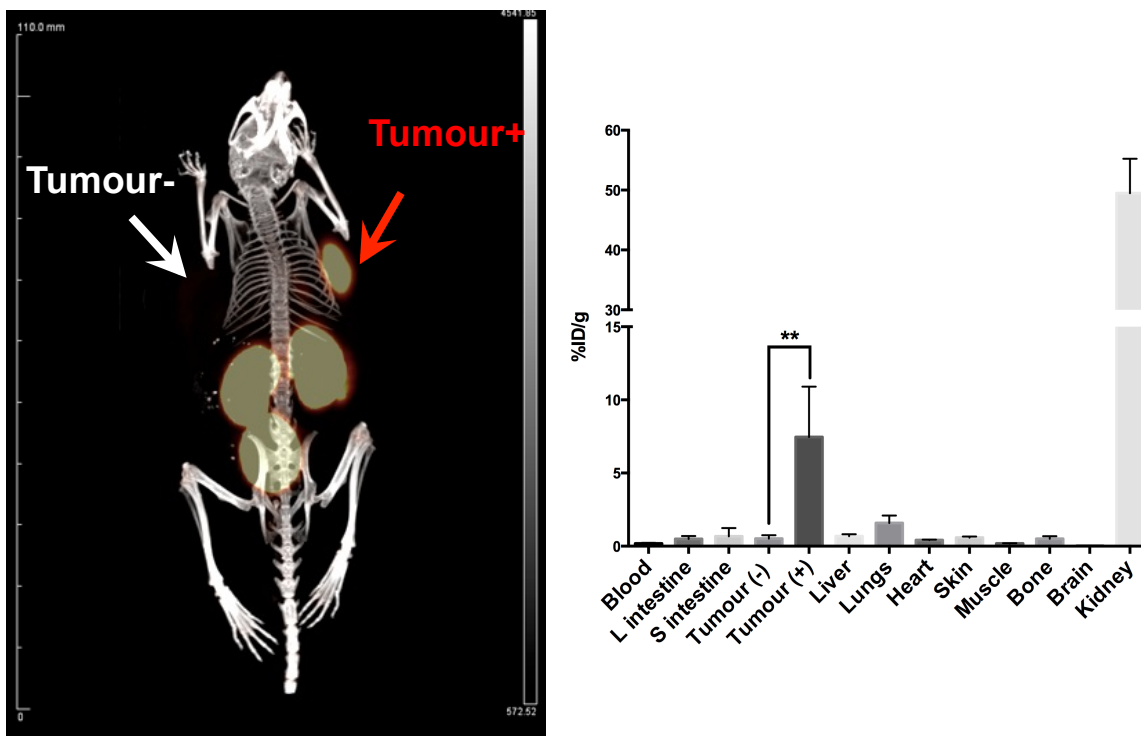


**Figure 6.6** (Left): B9858-<sup>18</sup>F-AMBF<sub>3</sub> images (1 h post-injection) of NODSCID/IL2RKO mouse bearing B1R-positive (red arrow) and B1R-negative (white arrow) tumour. **Figure 6.6** (right): Biodistribution of B9858-<sup>18</sup>F-BF<sub>3</sub> at 60 mins post injection after injection in tumour-bearing mice (n=4).

Encouraged with the success of peptide labeling, we displaced our target with smaller biomolecules to expend the utility of this <sup>18</sup>F-labeling strategy. Carbonic Anhydrase IX (CA-IX) is a surrogate marker for hypoxia and a promising diagnostic/therapeutic target for cancers.<sup>187</sup> Sulfonamide derivatives have been shown to inhibit CA-IX by binding to the Zn catalytic domain. However, as far as we know, there are very few examples of successful CA-IX PET probes that have been developed based on sulfonamide derivatives, and among them no <sup>18</sup>F-labeled radiotracer has ever been reported. Generally, the main concerns for applying a small molecule to be an <sup>18</sup>F-PET tracer are the poor pharmacokinetics and the lack of binding affinity. To overcome these drawbacks we designed a multivalent tracer with three sulfonamides that might afford greater binding affinity for CA-IX (**Figure 6.7**). Such a tracer is also less likely to cross cell membrane where it could bind to cytosolic CA isoforms I and II. The property of

membrane-impermeability would significantly reduce the background uptake in cells and subsequently improve the imaging contrast for CA-IX,<sup>114,126</sup> which is expressed on the membrane of certain tumor cells. As expected, tracer **6.8** was radiolabeled in kit-like manner and >250 mCi (31-42% non-decay-corrected yield) of <sup>18</sup>F-labeled **6.8** was obtained in 25 min from ~800 mCi <sup>18</sup>F-fluoride with >99% radiochemical purity and 2.5-3 Ci/μmol specific activity. Encouragingly, CA-IX-expressing tumor xenograft were successfully targeted by <sup>18</sup>F-radiolabeled **6.8** and clearly visible as early as 20 min post injection (**Figure 6.8**). Even though modifications are still required to reduce gastrointestinal uptake, compound **6.8** has suggested a promising strategy to unify small biomolecules into valuable <sup>18</sup>F-radiotracers.

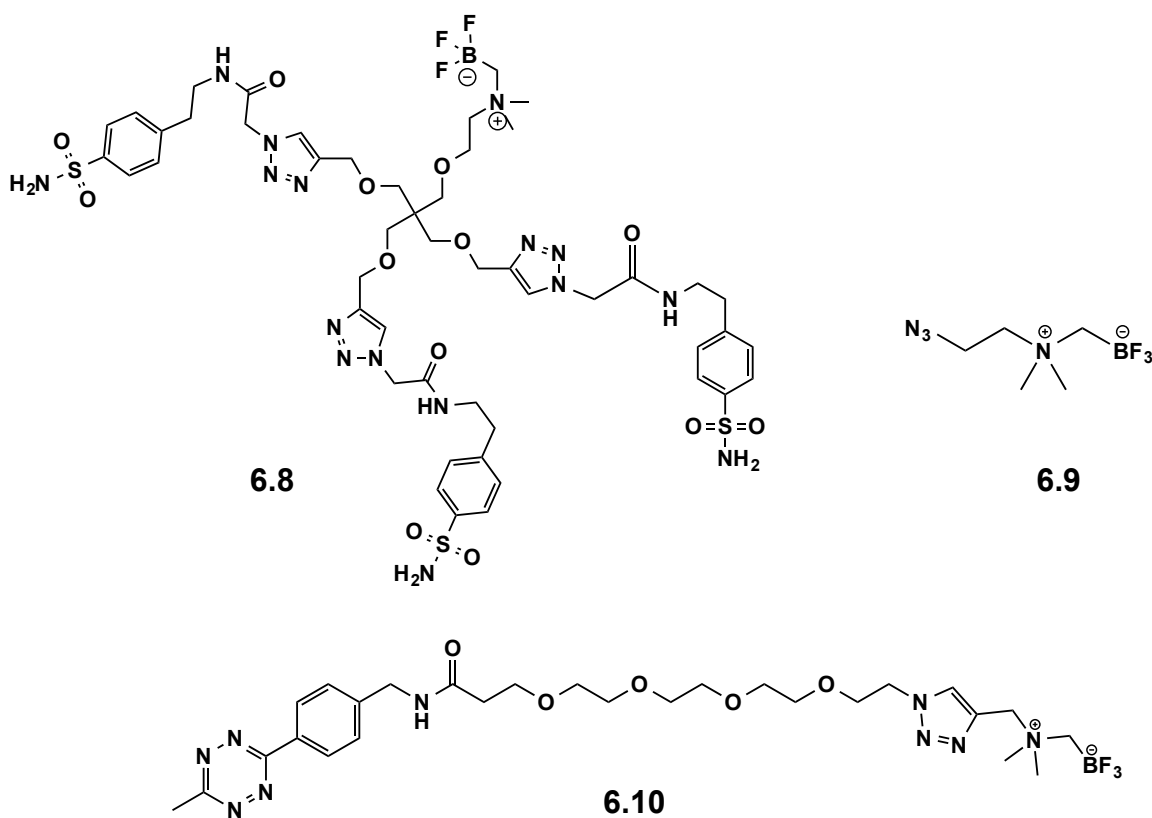


**Figure 6.7** Chemical structures of **6.8**, **6.9** and **6.10**.

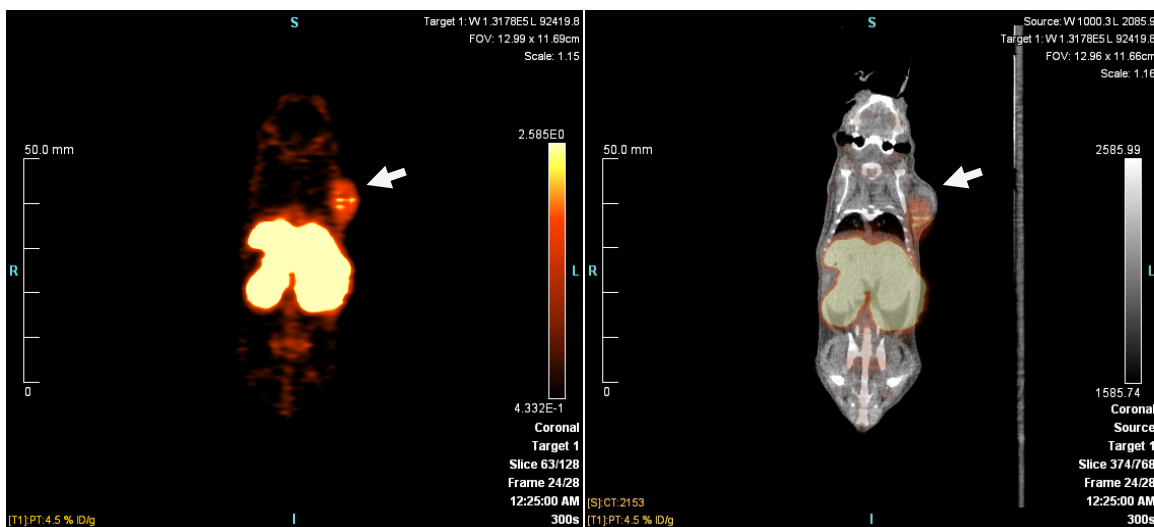


**Figure 6.8** PET/CT images (20 min post-injection) of mouse bearing HT-29 tumour (white arrow) with  $^{18}\text{F}$ -labeled **6.8**. The left image is the pure PET image, and the right image is the hybrid PET/CT image.

For more sensitive and fragile biomolecules (i.e. antibodies) that may not survive acidic radiolabeling conditions, we propose an alternative solution which would revert to a one-pot two-step strategy. In recent years, successful examples have been presented to show  $^{18}\text{F}$ -labeling of fragile biomolecules via copper-catalyzed/copper-free “click” conjugation.<sup>91,99</sup> Hence, compound **6.9** (Azido-AMBF<sub>3</sub>) and compound **6.10** (Tetrazine-AMBF<sub>3</sub>) have been radiosynthesized in good radiochemical yield and high specific activity via our  $^{18}\text{F}$ - $^{19}\text{F}$  IEX method. Given the bioorthogonality of click-tags and the high stability of  $^{18}\text{F}$ -AMBF<sub>3</sub> *in vivo*, we would suggest that a broad scale of sensitive biomolecules can be generically transferred into  $^{18}\text{F}$ -PET imaging probe along with this  $^{18}\text{F}$ -AMBF<sub>3</sub>.

### 6.3 Conclusion

In this chapter, I introduced an efficient “stamp-like” radiolabeling protocol, which allows facile  $^{18}\text{F}$ -fluorination of fluorophore, small molecule and peptide using  $^{18}\text{F}$ - $^{19}\text{F}$  isotopic exchange on a novel *in vivo* stable trifluoroborate derivative. This technology may find ample application in  $^{18}\text{F}$ -labeling pharmaceutical candidates to accelerate drug screening, especially for peptides. Moreover, as AMBF<sub>3</sub> is a zwitterion, and as such it

may hold promise for designing AMBF<sub>3</sub>-conjugated biomolecules to penetrate a regular cellular membrane or even the blood brain barrier (BBB). This radiochemistry does not need either the preparation of dry <sup>18</sup>F-fluoride or HPLC purification, and can be simply performed under production level radioactivity with low-level hand dose. Therefore, this method of <sup>18</sup>F-BF<sub>3</sub> formation should be easily applied for automated synthesizer (i.e. GE fast lab) and microfluidic development. Its operational simplicity and high *in vivo* performance can be interesting for the PET chemists.

## 6.4 Materials and methods

### 6.4.1 General information

Reagents and solvents were purchased from Advanced Chemtech, Sigma-Aldrich, Combi-Blocks, or Novabiochem. The cell lines were purchased from ATCC. <sup>18</sup>F-fluoride Trap & Release Columns were purchased from ORTG Inc. (Oakdale, TN) and C18 Sep-Pak cartridges (1cc, 50 mg) were obtained from Waters. An Endeavor 90 peptide synthesizer (Aaptec) was applied to synthesize the peptide.

### 6.4.2 HPLC gradient

The following gradients were used for HPLC purification and quality control:

Method A: Agilent Eclipse XDB-C18 5 μm 9.2 x 250 mm semi-prep column. Solvent A: 0.1% TFA water; solvent B: MeCN; 0 to 15 min: 20% to 40% B, 15 to 20 min, 40% to 20% B. Flow rate: 4.5 mL/min, column temperature: 19 to 21 °C.

Method B: Agilent Eclipse XDB-C18 5 μm 9.2 x 250 mm semi-prep column. Solvent A: 0.1% TFA water; solvent B: MeCN; 0 to 2 min: 5% to 20% B, 2 to 5 min, 20% to 30% B, 5 to 20 min, 30% to 50%, 20 to 22 min, 50% to 5% B. Flow rate: 3 mL/min, column temperature: 19 to 21 °C.

Gradient C: Agilent Eclipse XDB-C18 5 μm 9.2 x 250 mm semi-prep column. Solvent A: 0.1% TFA water; solvent B: MeCN; 0 to 2 min: 5% to 20% B, 2 to 5 min, 20% to 30% B,

5 to 20 min, 30% to 100%, 20 to 22 min, 100% to 5% B. Flow rate: 3 mL/min, column temperature: 19 to 21 °C.

Method D: Phenomenex Jupiter 10  $\mu\text{m}$  C18 300Å 4.6 x 250 mm analytical column. Solvent A: 0.1% TFA water; solvent B: MeCN; 0 to 2 min: 5% to 5% B, 2 to 7 min, 5% to 20% B, 7 to 15 min, 20% to 100%, 15 to 20 min, 100% to 5% B. Flow rate: 2 mL/min, column temperature: 19 to 21 °C.

### 6.4.3 Synthesis

#### Peptide Synthesis

The B9858 peptide was synthesized as previously described. Briefly, the NHS-ester of bromoacetic acid was coupled to the N-terminus followed by successive treatment with sodium azide to provide a B9858 derivative suitable for click-conjugation. The peptide was deprotected and cleaved from the resin by treatment with trifluoroacetic acid supplemented with trimethylsilane scavengers. Purification by HPLC with a semi-preparative column with Method A provided the final peptide in quantities of ~10 mg. The calculated mass was 1504.8 and measured at 1505.8 as  $\text{H}^+$  peak by mass spectrometry. The purity of the peptide was >99%.

#### Synthesis of B9858-AMBF<sub>3</sub>

The N-Propargyl-N,N-dimethylammonio-methylboronylpinacolate (5.0 mg, 22.3  $\mu\text{mol}$ ) was converted to the corresponding trifluoroborate (alkynyl-AMBF<sub>3</sub>) through the addition of KHF<sub>2</sub> (3 M, 30  $\mu\text{L}$  in water), HCl (4M, 30  $\mu\text{L}$  in water), deionized water (20  $\mu\text{L}$ ) and DMF (60  $\mu\text{L}$ ) at 45°C for 2 hours, and then quenched by NH<sub>4</sub>OH (conc., 10  $\mu\text{L}$ ). The crude reaction was directly used for click conjugation to B9858 azide without further purification. A mixture of B9858-azide (4.0 mg, 3.4  $\mu\text{mol}$ ), CuSO<sub>4</sub> (1.0 M, 5.0  $\mu\text{L}$ ), sodium ascorbate (1.0 M, 12.5  $\mu\text{L}$ ) and 5% NH<sub>4</sub>OH (MeCN/H<sub>2</sub>O=1:1, 50  $\mu\text{L}$ ) was added, and the new mixture was warmed up to 45 °C for 2 hours. Purification was performed by Agilent 1100 HPLC system with Gradient B to isolate 2.3 mg of chemically pure AMBF<sub>3</sub>-B9858. ESI-MS: Calculated: 1669.9; Obtained: 1670.8. For convenience and to

ensure reproducibility, the purified B9858-<sup>19</sup>F-AMBF<sub>3</sub> was diluted in ethanol and aliquoted in quantities of ~75 μg (~50 nmol) for radiolabeling.

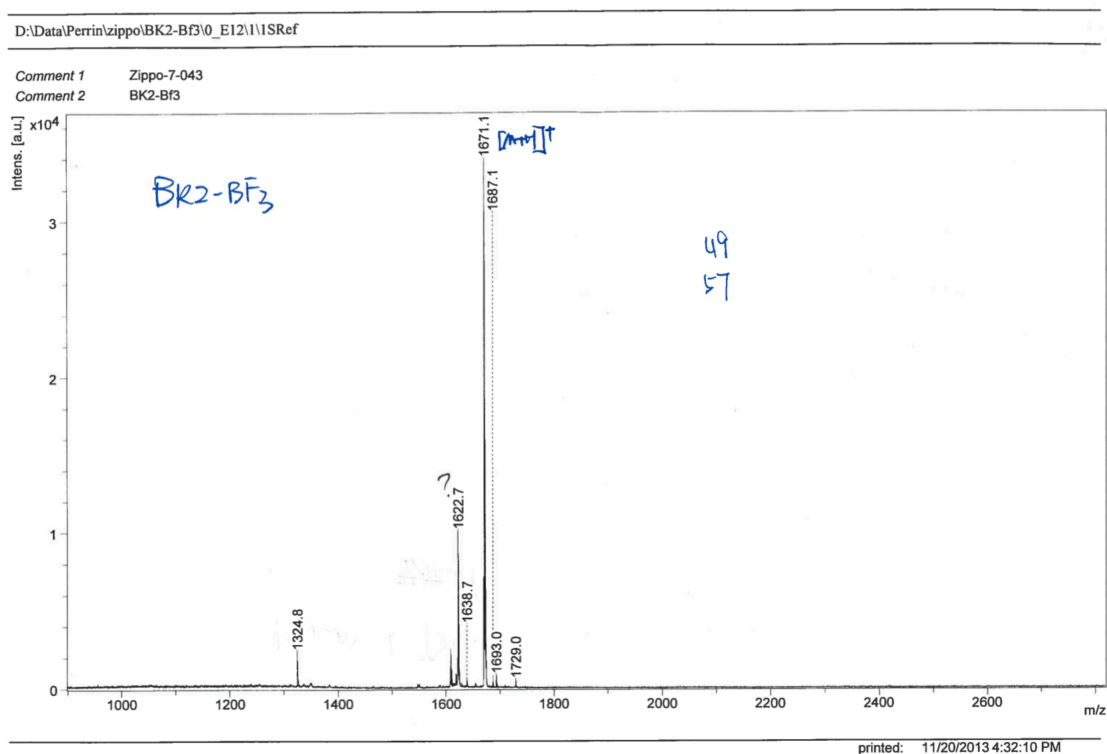


**Figure 6.9** MALDI spectrum of B9858-AMBF<sub>3</sub>.

### Synthesis of N-propargyl-N,N-dimethyl-ammoniomethyl-boronylpinacolate (6.1)

N-Propargyl-N,N-dimethyl-ammoniomethyl-boronylpinacolate (alkynyl-AMB(pin)) was synthesized by condensation of iodomethyl-boronylpinacolate and propargylamine by standard alkylative amine quaternization. Briefly, a flame-dried round bottom flask was charged with N,N-dimethylpropargylamine (98 μL, 1.0 mmol) and 2 mL anhydrous diethyl ether under argon atmosphere to which Iodomethyl-pinacolboronate (165 μL, 0.9 mmol) was added drop-wise at room temperature. On stirring, the solution became cloudy followed by the formation of a white precipitate, which was the desired product. The resulting precipitate was filtered and washed with cold diethyl ether. Then the residue was dried under high vacuum to give a fluffy white powder in 95% yield. <sup>1</sup>H NMR (300 MHz, CD<sub>3</sub>CN) δ 4.40 (d, 2H), 3.31 (s, 2H), 3.22 (s, 6H), 3.21 (t, 1H), 1.27 (s, 12H); ESI: [M]<sup>+</sup> 224.1.

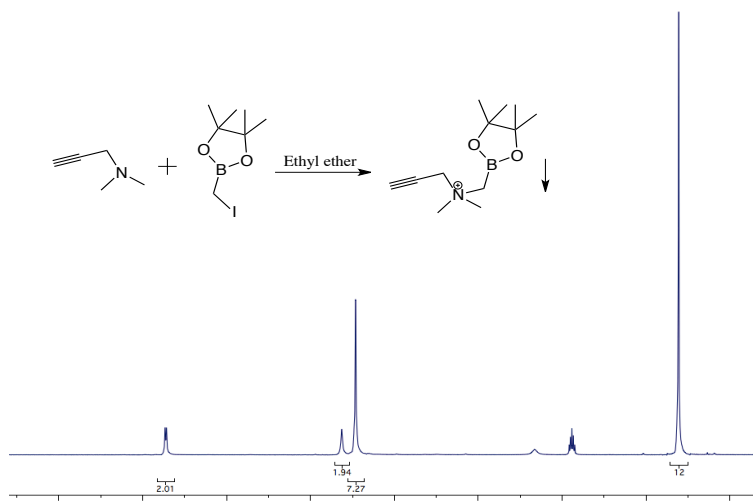


**Figure 6.10** <sup>1</sup>H-NMR (CD<sub>3</sub>CN, 25 °C) spectrum of compound **6.1**.

### Synthesis of N-propargyl-N,N-dimethyl-ammoniotrifluoroborate (**6.2**)

N,N-dimethylpropargylamine (102 μL, 1.0 mmol) was dissolved into anhydrous diethyl ether (5 mL) in a flame-dried round bottom flask. At room temperature, iodomethylborate pinacol ester (182 μL, 1.0 mmol) was added dropwise into the solution over 5 min. The alkylated product was precipitated from the solution as a fluffy white powder, which was achieved via filtration and then dried under vacuum. This alkylated boronic ester was fluorinated with KHF<sub>2</sub> (6 M KHF<sub>2</sub> water solution, 1 mL, 6 mmol) and purified by a self-assembled silica column to give compound **6.2**. ESI: [M-F]<sup>+</sup> calculated: 146.09; obtained: 146.09.

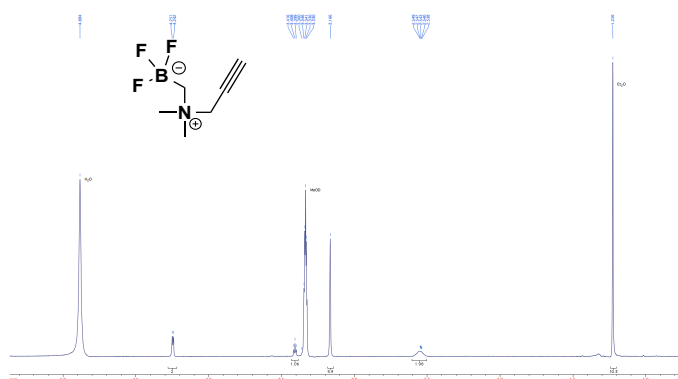


**Figure 6.11** <sup>1</sup>H-NMR (CD<sub>3</sub>CN, 25 °C) spectrum of compound **6.2**.



stirring at reflux for 24 h, a 0.1 M aqueous solution of HCl was added dropwise until gas evolution ceased. The heterogeneous solution was filtered and the retained solids were rinsed with CH<sub>2</sub>Cl<sub>2</sub> and a 4:1 CH<sub>2</sub>Cl<sub>2</sub>/MeOH solution. The combined filtrate was concentrated and the residue was dissolved in CH<sub>2</sub>Cl<sub>2</sub>, filtered to remove insoluble salts, and concentrated again. The resulting glassy solid was then partitioned between dilute aqueous NaHCO<sub>3</sub> and EtOAc. After isolation, the aqueous layer was washed with 3 additional portions of EtOAc to remove residual starting material. The retained aqueous layer was saturated with NaCl, acidified with 1 M aqueous HCl, and then extracted with multiple portions of 2:1 iso-PrOH/CH<sub>2</sub>Cl<sub>2</sub>, until a faint pink color persisted. The combined organic layers were then dried over Na<sub>2</sub>SO<sub>4</sub>, filtered, and concentrated under reduced pressure. The glassy purple solid was dissolved in a minimal amount of MeOH and precipitated by dropwise addition to a large volume of Et<sub>2</sub>O. The product was collected by filtration as a dark purple solid 120 mg, (47%). ESI: [M+H]<sup>+</sup> 511.3. NMR (500 MHz, CD<sub>3</sub>OD): δ 1.28-1.33 (t, 12H, *J*=7.5), 3.12 (br s, 4H), 3.64-3.74 (m, 12H), 6.97-6.98 (d, 2H, *J*=2.5), 7.09-7.11 (dd, 2H, *J*=2.5, 10.0), 7.26-7.27 (d, 2H, *J*=9.5), 7.51-7.54 (m, 1H), 7.76-7.80 (m, 3H).

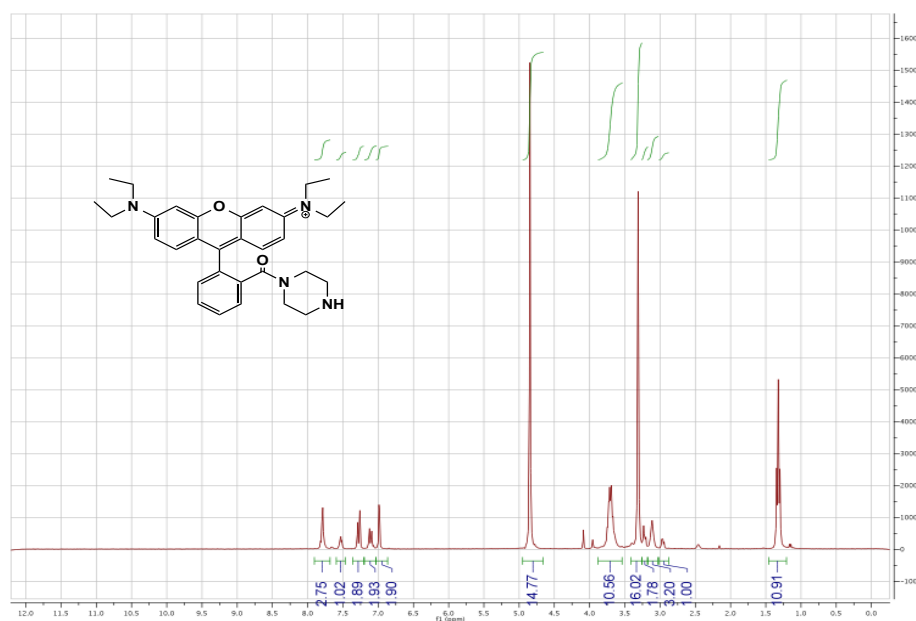


**Figure 6.12** <sup>1</sup>H-NMR (CD<sub>3</sub>OD, 25 °C) spectrum of compound 6.4.

### Rhodamine B 4-(5-hexynoylcarboxyl)piperazine amide (6.6)

Triethylamine (30  $\mu$ L, 0.2 mmol) was added to a stirred solution of **6.4** (30.5 mg, 0.059 mmol), 5-hexynoylcarboxyl NHS ester (45  $\mu$ L, 0.2 mmol), and DMF (2 mL) in  $\text{CH}_2\text{Cl}_2$  (2 mL). After stirring at room temperature for 24 h, the reaction solution was partitioned between EtOAc and 1 M aqueous  $\text{K}_2\text{CO}_3$ . The aqueous layer was washed with 3 additional portions of EtOAc. Sodium chloride was added to the isolated aqueous layer until saturation was achieved and the solution was then extracted with 2:1 isopropanol/ $\text{CH}_2\text{Cl}_2$ . The organic layer was dried over  $\text{Na}_2\text{SO}_4$ , and concentrated under reduced pressure. The resulting solid was dissolved in  $\text{CHCl}_3$  and filtered to remove insoluble salts. Upon concentration, the product was obtained as a dark solid, ESI:  $[\text{M}+\text{H}]^+$  607.8. (50% yield).  $^1\text{H-NMR}$  (300 MHz,  $\text{CD}_3\text{OD}$ ):  $\delta$  1.28-1.32 (t, 12H,  $J=6.8$ ), 1.82 (t, 2H), 2.29 (m, 2H), 2.51 (t, 2H), 2.71 (s, 1H), 3.44-3.51 (m, 8H), 3.71-3.82 (m, 8H), 7.09 (s, 2H), 7.27-7.29 (d, 2H,  $J=9.6$ ), 7.52-7.53 (d, 2H), 7.69-7.71 (m, 1H), 7.76-7.78 (m, 3H).

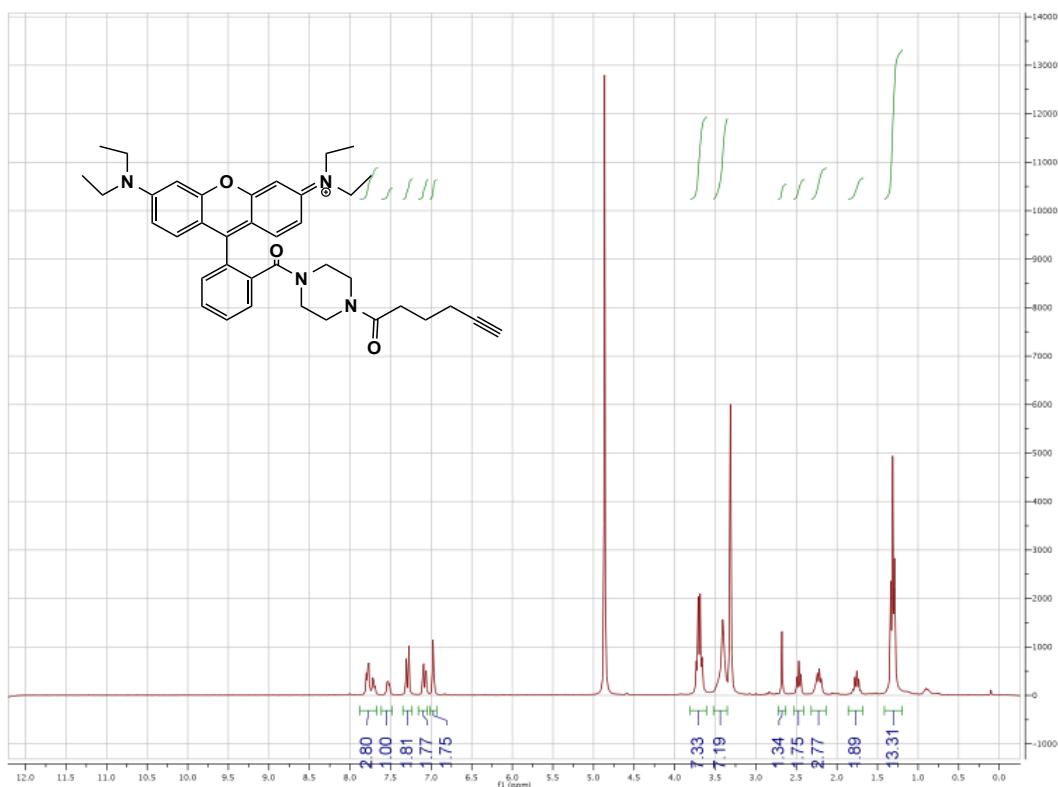


**Figure 6.10**  $^1\text{H-NMR}$  ( $\text{CD}_3\text{OD}$ , 25  $^\circ\text{C}$ ) spectrum of compound **6.6**.

### **Synthesis of Rhodamine B-AMBF<sub>3</sub> (6.7)**

The N-propargyl-N,N-dimethylammonio-methylboronylpinacolate (5.0 mg, 22.3  $\mu\text{mol}$ ) was converted to the corresponding trifluoroborate (alkynyl-AMBF<sub>3</sub>) through the addition of KHF<sub>2</sub> (3 M, 30  $\mu\text{L}$  in water), HCl (4M, 30  $\mu\text{L}$  in water), deionized water (20  $\mu\text{L}$ ) and DMF (60  $\mu\text{L}$ ) at 45°C for 2 hours, and then quenched by NH<sub>4</sub>OH (conc., 10  $\mu\text{L}$ ). The crude reaction was directly used for click conjugation to Rhodamine B-azide without further purification. A mixture of Rhodamine B-azide (4.0 mg, 3.4  $\mu\text{mol}$ ), CuSO<sub>4</sub> (1.0 M, 5.0  $\mu\text{L}$ ), sodium ascorbate (1.0 M, 12.5  $\mu\text{L}$ ) and 5% NH<sub>4</sub>OH (MeCN/H<sub>2</sub>O=1:1, 50  $\mu\text{L}$ ) was added, and the new mixture was warmed up to 45 °C for 2 hours. Purification was performed by Agilent 1100 HPLC system with Gradient B to isolate 2.3 mg of chemically pure Rhodamine-AMBF<sub>3</sub>. ESI-MS: Calculated: 801.46; Obtained: 802.5. For convenience and to ensure reproducibility, the purified Rhodamine-<sup>19</sup>F-AMBF<sub>3</sub> was diluted in ethanol and aliquoted in quantities of ~40  $\mu\text{g}$  (~50 nmol) for radiolabeling.

### **Synthesis of TrisCAIX-AMBF<sub>3</sub> (6.8)**

The trisalkynyl-boronylpinacolate (5.0 mg, 10  $\mu\text{mol}$ ) was converted to the corresponding trifluoroborate (trisalkynyl-AMBF<sub>3</sub>) through the addition of KHF<sub>2</sub> (3 M, 30  $\mu\text{L}$  in water), HCl (4M, 30  $\mu\text{L}$  in water), deionized water (20  $\mu\text{L}$ ) and DMF (60  $\mu\text{L}$ ) at 45 °C for 2 hours, and then quenched by NH<sub>4</sub>OH (conc., 10  $\mu\text{L}$ ). The crude reaction was directly used for click conjugation to CAIX-azide without further purification. A mixture of CAIX-azide (14 mg, 50  $\mu\text{mol}$ ), CuSO<sub>4</sub> (1.0 M, 5.0  $\mu\text{L}$ ), sodium ascorbate (1.0 M, 12.5  $\mu\text{L}$ ) and 5% NH<sub>4</sub>OH (MeCN/H<sub>2</sub>O=1:1, 50  $\mu\text{L}$ ) was added, and the new mixture was warmed up to 45 °C for 2 hours. Purification was performed by Agilent 1100 HPLC system with Gradient B to isolate 2.3 mg of chemically pure TrisCAIX-AMBF<sub>3</sub>. ESI-MS: Calculated: 1253.4; Obtained: 1253.6. For convenience and to ensure reproducibility, the purified TrisCAIX-<sup>19</sup>F-AMBF<sub>3</sub> was diluted in ethanol and aliquoted in quantities of ~60  $\mu\text{g}$  (~50 nmol) for radiolabeling.

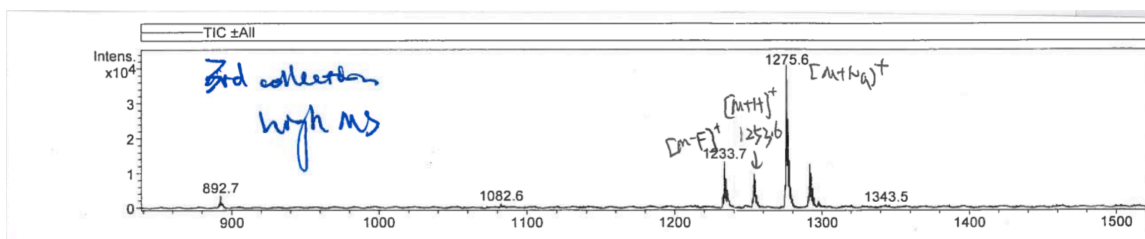


**Figure 6.14** ESI-MS spectrum of compound **6.8**.

### Synthesis of 2-azidoethyl-N,N-dimethyl-ammoniotrifluoroborate(**6.9**)

N,N-dimethyl-2-azidoethylamine (114 mg, 1.0 mmol) was dissolved into anhydrous diethyl ether (5 mL) in a flame-dried round bottom flask. At room temperature, iodomethylborate pinacol ester (182  $\mu$ L, 1.0 mmol) was added dropwise into the solution over 5 min. The alkylated product was precipitated from the solution as a fluffy white powder, which was achieved via filtration and then dried under vacuum. This alkylated boronic ester was fluorinated with  $\text{KHF}_2$  (3 M  $\text{KHF}_2$  water solution, 1 mL, 3 mmol) and purified by a self-assembled silica column to give compound **6.9**. ESI:  $[\text{M-F}]^+$  calculated: 177.09; obtained: 177.1

### Synthesis of Tetrazine-AMBF<sub>3</sub> (**6.10**)

The N-propargyl-N,N-dimethylammonio-methylboronylpinacolate (5.0 mg, 22.3  $\mu$ mol) was converted to the corresponding trifluoroborate (alkynyl-AMBF<sub>3</sub>) through the addition of  $\text{KHF}_2$  (3 M, 30  $\mu$ L in water), HCl (4M, 30  $\mu$ L in water), deionized water (20  $\mu$ L) and DMF (60  $\mu$ L) at 45°C for 2 hours, and then quenched by  $\text{NH}_4\text{OH}$  (conc., 10  $\mu$ L). The crude reaction was directly used for click conjugation to tetrazine-azide without further purification. A mixture of tetrazine-azide (2.0 mg, 4.2  $\mu$ mol),  $\text{CuSO}_4$  (1.0 M, 5.0  $\mu$ L), sodium ascorbate (1.0 M, 12.5  $\mu$ L) and 5%  $\text{NH}_4\text{OH}$  (MeCN/ $\text{H}_2\text{O}$ =1:1, 50  $\mu$ L) was added, and the new mixture was warmed up to 45 °C for 2 hours. Purification was performed by Agilent 1100 HPLC system with Gradient C to isolate 2.3 mg of chemically pure Tetrazine-AMBF<sub>3</sub>. The identity and purity was confirmed with LC-MS: Calculated: 639.33; Obtained: 640.4. For convenience and to ensure reproducibility, the purified Tetrazine-<sup>19</sup>F-AMBF<sub>3</sub> was diluted in ethanol and aliquoted in quantities of ~32  $\mu$ g (~50 nmol) for radiolabeling.

#### 6.4.4 *In vitro* binding assays

(Use TATE-AMBF<sub>3</sub> as a representative example) Membranes from Chinese Hamster Ovary cells (CHO-K1) transfected with sst2r and <sup>125</sup>I-tyr-somatostatin-14 were obtained commercially from PerkinElmer, Canada. A standard filtration binding assay was performed in 96-well filtration plates (MultiScreen, Millipore) to determine the binding affinity (K<sub>i</sub>) of AMBF<sub>3</sub>-TATE. Briefly, 0.25 μL of the membranes per well were incubated with the <sup>125</sup>I-labeled standard at a concentration of 0.05 nM, and increasing concentrations of non radioactive TATE-AMBF<sub>3</sub> (competitor), in buffer consisting of 25 mM Hepes pH 7.4, 10 mM MgCl<sub>2</sub>, 1 mM CaCl<sub>2</sub>, and 0.5% BSA. After incubation at 37 °C for 1 hour, the wells were aspirated and washed 8 times with 50 mM of ice-cold wash buffer (TRIS-HCL pH 7.4) over GF/B filters. The filters were removed and counted by a gamma counter (Cobra II, Packard). The experiment was repeated in triplicate. Data were fitted to a one-site competition model (GraphPad Prism 7.1 software) to calculate the inhibition constant (K<sub>i</sub>).

#### 6.4.5 Radiolabeling

Just prior to radiosynthesis, Rhodamine-AMBF<sub>3</sub> was re-suspended in aqueous pyridazine-HCl buffer (pH = 2) (~50 μL) in a vial (polypropylene Falcon Tube). No carrier-added <sup>18</sup>F-fluoride (800-1000 mCi) was obtained by bombardment of H<sub>2</sub><sup>18</sup>O with 18 MeV protons, followed by trapping on an anion exchange resin (9 mg, QMA, chloride form, prewashed with deionized water). The <sup>18</sup>F-fluoride was eluted with isotonic saline (70-100 μL) into the reaction vial containing Rhodamine-AMBF<sub>3</sub>. The vial was placed in a heating block set at 80 °C for 20 min whereupon the reaction was quenched by the injection of 5% NH<sub>4</sub>OH in water (2 mL). The reaction mixture was loaded onto a C18 light cartridge. The impurities (i.e. free <sup>18</sup>F-fluoride) were removed by flushing with saline (2 mL). Radiochemically pure Rhodamine-<sup>18</sup>F-AMBF<sub>3</sub> was then released into a glass vial by elution with 1:1 ethanol/saline (0.5 mL) to provide 200 mCi tracer. This solution was formulated into isotonic saline (5 mL) for imaging. A small sample was removed for quality control analysis by HPLC (**Figure 6.2**). The radiolabeling was repeated three times and the HPLC traces are shown below.

#### **6.4.6 *In vitro* stability**

The purified Rhodamine-<sup>18</sup>F-AMBF<sub>3</sub> in its saline formulation was assayed for plasma stability. For a plasma stability assay, Rhodamine-<sup>18</sup>F-AMBF<sub>3</sub> (20 μL) was added to mouse plasma (500 μL) and incubated at 37 °C for 0, 60 and 120 min. Following incubation at each time point, the reaction was quenched by adding MeCN (1 mL) to precipitate insoluble proteins from the solution. The quenched reactions were centrifuged to remove insoluble material. The supernatant was aspirated by pipette, filtered, and analyzed by HPLC using Method C.

#### **6.4.7 Animal model and biodistribution studies**

All animal studies were performed in accordance with the Canadian Council on Animal Care Guidelines and were approved by the animal care committee of the University of British Columbia. 10<sup>7</sup> CHO-K1 cells were freshly expanded in PBS/matrigel mixture and inoculated subcutaneously in female immunocompromised mice (nod scid IL2r-γ-null, bred in house). The tumors were grown for 2 weeks until they reached 5-7 mm in diameter. While under 2% isoflurane anesthesia, the mice were injected via the tail vein with 10-20 μCi of B9858-<sup>18</sup>F-AMBF<sub>3</sub> (n=5). To demonstrate the specificity of uptake *in vivo* in receptor positive tissues, 100 μg of Ga-DOTA-B9858 was pre-injected 15 minutes prior to B9858-<sup>18</sup>F-AMBF<sub>3</sub> injection as a blocking control cohort (n=4). Sixty minutes following injection, the mice were anesthetized with isoflurane and euthanized by carbon dioxide. The organs were harvested, rinsed with saline, blotted dry, and collected in previously weighted tubes. The tubes containing the organs were counted in a gamma counter (Cobra-II, Packard). The tissue weight and associated counts per minute were used to calculate the percentage injected dose per gram of tissue (%ID/g).

#### **6.4.8 PET/CT imaging**

The imaging studies were acquired using multimodality PET/CT system (Inveon, Siemens). For imaging, a baseline low-dose CT scan was obtained for localization and attenuation correction. Roughly 100 μCi of radiotracer was injected in the caudal lateral tail vein of tumor-bearing mice. A dynamic scan was acquired in list-mode for 60

minutes while the animal was kept warm by a heated pad on the scanner bed. B9858-DOTA-Ga (100  $\mu\text{g}$  per mouse) was pre-injected as a blocking agent in some animals. Following scanning, the mice were euthanized, while under anesthesia, by  $\text{CO}_2$  inhalation. The images were reconstructed by an iterative reconstruction algorithm (3D OSEM/MAP) using the Inveon Acquisition Workplace Software (Siemens), applying normalization, dead time, random, and attenuation corrections. The uptake of tumor and tissues of interest were determined by region of interest (ROI), and the %ID/g was calculated (assuming a tissue density of 1.0 g/cc). The mean %ID/g was calculated by drawing a ROI to match the tumor contours visible on CT. The peak %ID/g was calculated from the hottest 2x2 voxel cluster within the tumor.

# Chapter 7: Preclinical Evaluation of a Novel $^{18}\text{F}$ -Labeled Somatostatin Receptor-Binding Peptide

## 7.1 Introduction

Somatostatin sub-type 2 receptors (sstr2) are highly overexpressed on neuroendocrine tumors (NETs) in comparison to normal tissues. Since the incidence of NETs has rapidly increased during the last 30 years, there is considerable interest in developing high affinity somatostatin-derived ligands that bind sstr2 for radiotherapy.<sup>188</sup> These therapies have been shown to prolong survival time of patients with NETs in certain cases.<sup>189-191</sup> In order to diagnose and monitor patients with sstr2-positive tumors, advanced non-invasive imaging technologies have been developed with radiotracers based on the somatostatin family of peptides, notably octreotate (TATE) and octreotide.<sup>188,192-194</sup> Encouragingly, octreotate/octreotide mediated imaging probes have proven to be very promising for detecting small tumors and metastases that are unable to be detected by conventional means. Currently,  $^{111}\text{In}$ -DTPA-pentetreotide (Octreoscan, Mallinckrodt) is the clinical standard for imaging NETs.  $^{99\text{m}}\text{Tc}$  derivatives such as  $^{99\text{m}}\text{Tc}$ -depreotide and  $^{99\text{m}}\text{Tc}$ -hydrazinonicotinyl-Tyr(3)-octreotide ( $^{99\text{m}}\text{Tc}$ -EDDA/HYNIC-TOC) have also been used,<sup>195</sup> but have yet to be commercialized in North America. However, given the slow clearance and long half-life of  $^{111}\text{In}/^{99\text{m}}\text{Tc}$  mediated radiotracers, patients must wait at least one day after injection before getting scanned to achieve a sufficient target-to-background contrast. In addition, even with modern SPECT devices, the ability to detect small lesions that measure below 2 cm is limited, and as such the sensitivity is sub-optimal.<sup>190</sup>

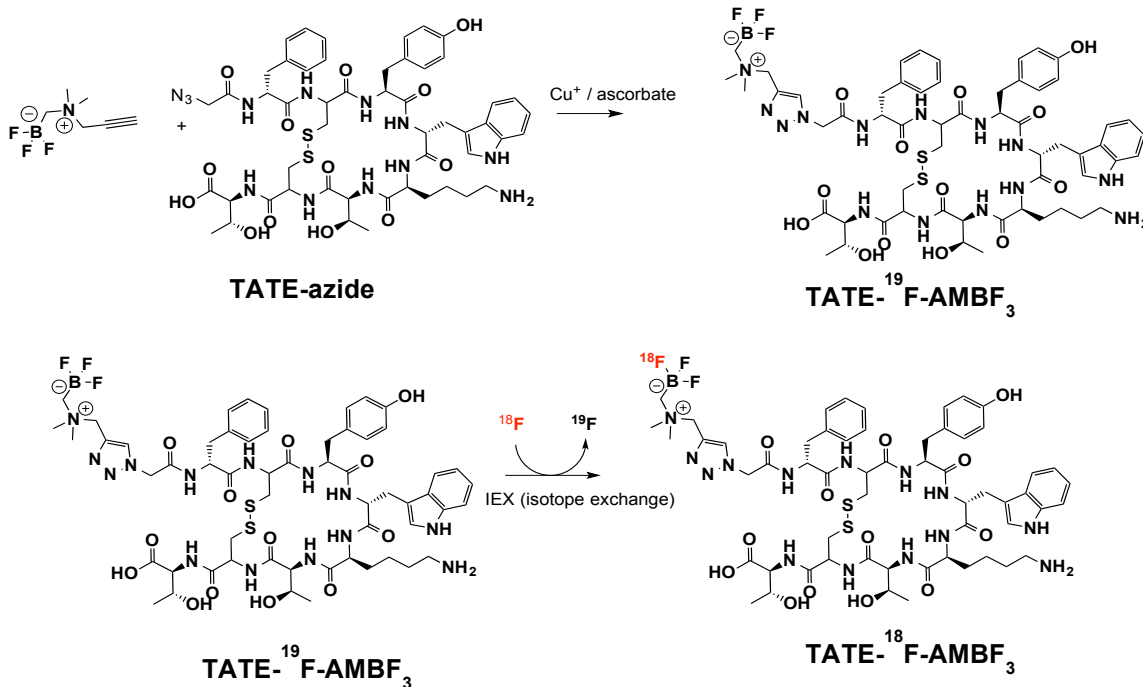
In contrast to these standard SPECT based imaging methods, PET (positron emission tomography) generally provides greater spatio-temporal resolution while requiring lower radioactivity doses owing to its higher sensitivity.<sup>26</sup> Radioisotopes such as  $^{68}\text{Ga}$ ,  $^{64}\text{Cu}$ , and  $^{18}\text{F}$ , along with various other radioprosthesis, have been conjugated to various octreotide derivatives for PET imaging.<sup>51,90,162,196-204</sup> Those radiotracers have been labeled at specific activities of 0.11~0.98 Ci/ $\mu\text{mol}$  in yields of 10~90% to give tumor images

with uptake values of 0.11~5.14% ID/g and tumor:blood contrast ratios of 0.56~25.0. Among them,  $^{68}\text{Ga}$ -labeled sstr2 ligands demonstrate the most promising performance for detection of NETs, and are used in clinical trials as well as under the local practice of pharmacy in several institutions,<sup>205-207</sup> mainly in Europe. Nevertheless,  $^{68}\text{Ga}$ -PET imaging is not widely available due to limited availability of  $^{68}\text{Ga}$  and the current lack of FDA-approved  $^{68}\text{Ge}/^{68}\text{Ga}$  generators.<sup>208</sup>

In contrast,  $^{18}\text{F}$ -fluoride presents several attractive properties for imaging including the fact that it is produced on a daily basis in large quantities in hundreds of cyclotrons based in hospitals or radiopharmacies world-wide.<sup>209,210</sup> Yet the challenges of labeling peptides with  $^{18}\text{F}$ -fluoride are significant. Primarily, both the low chemical reactivity of  $^{18}\text{F}$ -fluoride in water and its short half-life (109.8 min) represent major obstacles for  $^{18}\text{F}$ -labeling of peptides that are generally soluble only in water or aqueous co-solvents.<sup>45,211,212</sup> As a result, fluoride must be dried and reacted in dry solvents at high temperature, usually to radiolabel an intermediate radioprosthetic that is then conjugated to a peptide precursor. This necessitates the use of multistep reactions. While multi-step  $^{18}\text{F}$ -labeling reactions are now relatively commonplace, the comparatively short half-life of  $^{18}\text{F}$ -fluoride often impedes the application of multistep reactions in clinical use, particularly in terms of ensuring high specific activity i.e.  $> 1\text{Ci}/\mu\text{mol}$ . Given these challenges, an sstr2 ligand, which can be easily labeled with  $^{18}\text{F}$ -fluoride, would improve the availability of sstr2 imaging by PET, particularly if such an  $^{18}\text{F}$ -labeled octreotate could be produced in high yield and high specific activity. Towards these ends, several new  $^{18}\text{F}$ -octreotate derivatives such as  $^{18}\text{F}$ -SiFA or Al- $^{18}\text{F}$ -NOTA have been labeled in one step and then imaged with relative success.<sup>68,101,213-216</sup>

In Chapter 5, we demonstrated that certain alkyltrifluoroborates would undergo facile  $^{18}\text{F}$ -labeling by  $^{18}\text{F}$ - $^{19}\text{F}$  isotope exchange (IEX) while providing the requisite serum stability needed for PET tracer development. In light of the long-standing interest in mapping sstr2 expression with PET imaging, we conjugated the new alkyltrifluoroborate, denoted AMBF<sub>3</sub> to octreotate to give TATE- $^{19}\text{F}$ -AMBF<sub>3</sub>, which can be  $^{18}\text{F}$ -labeled in one step to produce a promising sstr2 PET tracer (**Scheme 7.1**). To our surprise, TATE- $^{19}\text{F}$ -AMBF<sub>3</sub> exhibited approximately 30-fold higher affinity than other octreotide analogs ( $K_d$

= 100 pM). This new TATE analog is easily  $^{18}\text{F}$ -labeled in record rapidity to provide a promising PET tracer for imaging *ssr2*-mediated cancers. Total synthesis, radiosynthesis, and *in vivo* properties are presented herein.



**Scheme 7.1** Synthetic route of TATE- $^{18}\text{F}$ -AMBF<sub>3</sub>.

## 7.2 Results

### 7.2.1 Radiochemistry

Starting with 800~1000 mCi  $^{18}\text{F}$ -fluoride, >200 mCi of TATE- $^{18}\text{F}$ -AMBF<sub>3</sub> was reproducibly obtained in 25 min (25±3%, n=5). As illustrated in **Figure 7.1**, the cartridge purified TATE- $^{18}\text{F}$ -AMBF<sub>3</sub> was re-injected into HPLC for quality analysis. As desired, only one dominant peak was observed in both radioactive mode and UV mode. As 200 mCi TATE- $^{18}\text{F}$ -AMBF<sub>3</sub> was obtained starting with 50 nmol of precursor, a simple calculation suggests that the specific activity is 4 Ci/μmol. To validate this calculation, a standard curve was employed and showed that the specific activity was >3 Ci/μmol. For plasma stability, TATE- $^{18}\text{F}$ -AMBF<sub>3</sub> was incubated in mouse plasma for 120 min with no detectable loss of fluoride or other decomposition.

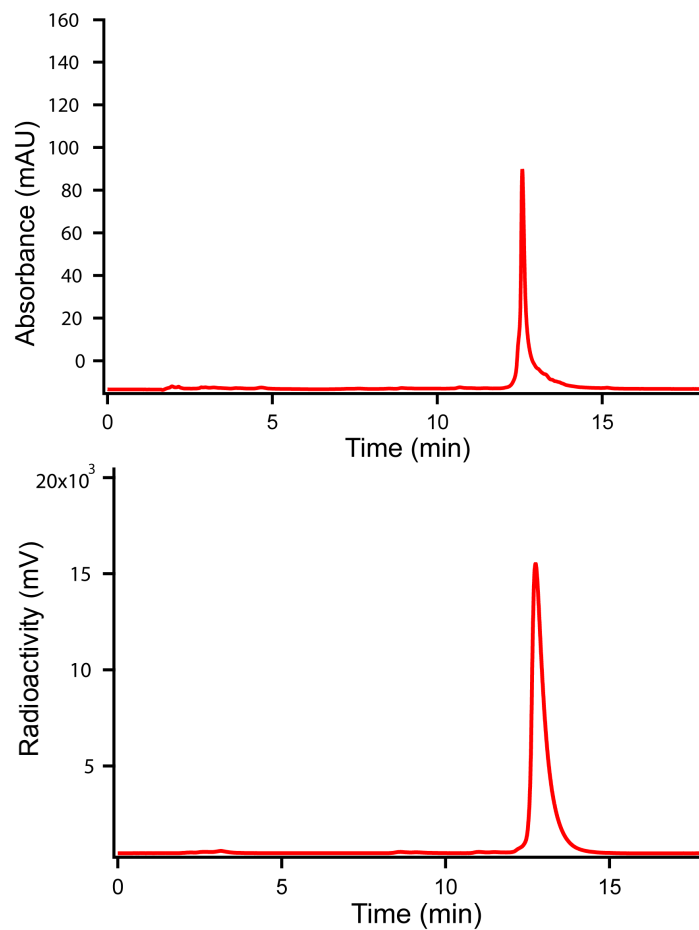


**Figure 7.1** (top): HPLC UV-trace at 277 nm of Sep-Pak purified TATE-<sup>18</sup>F-AMBF<sub>3</sub>; (bottom): HPLC radioactive trace of Sep-Pak purified TATE-<sup>18</sup>F-AMBF<sub>3</sub>.

### 7.2.2 *In vitro* affinity

The inhibition constant ( $K_i$ ) of TATE-AMBF<sub>3</sub> using human sstr2 receptors expressed on CHO membranes was  $0.13 \pm 0.03$  nM. Using identical assay conditions and the same lot of membranes, the binding affinity of TATE-DOTA-Ga was  $0.7 \pm 0.2$  nM. **Figure 7.2** shows a representative competitive binding assay curve.

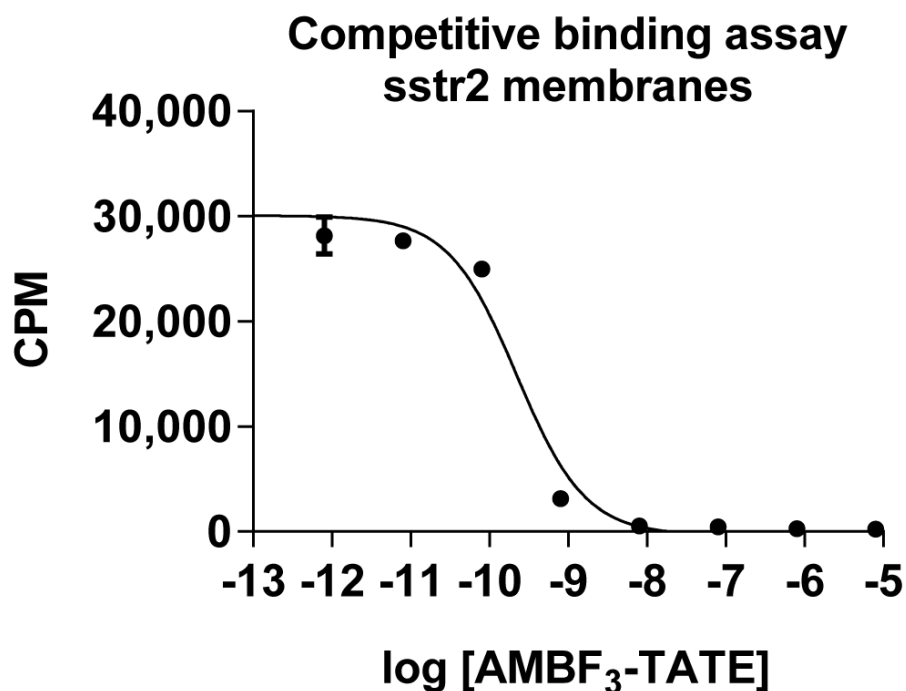


**Figure 7.2** Measurement of the inhibition constant ( $K_i$ ) of TATE-AMBF<sub>3</sub>. Here is a representative competitive binding assay curve by using human sstr2 receptors expressed on CHO membranes. The constant ( $K_i$ ) of TATE-AMBF<sub>3</sub> was measured to be  $0.13 \pm 0.03$  nM. Meanwhile the binding affinity of TATE-DOTA-Ga was  $0.7 \pm 0.2$  nM at the identical condition.

### 7.2.3 PET/CT

As shown in **Figure 7.3 left**, the radioactivity intensely accumulated in the AR42J tumor and was clearly specific as the uptake is significantly impaired in the presence of a competitor (**Figure 7.3 right**). The average tumor uptake based on the whole tumor ROI was  $10.2 \pm 2.1$  %ID/g. The average peak tumor uptake based on the hottest voxel cluster was  $47.2 \pm 3.0$  %ID/g. In contrast, the average uptake in the liver, blood pool, and muscle were  $0.83 \pm 0.16$ ,  $0.47 \pm 0.12$ , and  $0.09 \pm 0.03$  %ID/g, respectively. The excretion is predominantly through the urinary system with insignificant kidney retention. Some unexpected excretion through the gallbladder was noted, as the gallbladder is a known channel for the excretion of highly polar molecules from the body. In addition, bone

uptake is undetectable and there is minimal background activity, resulting in a very high contrast images.

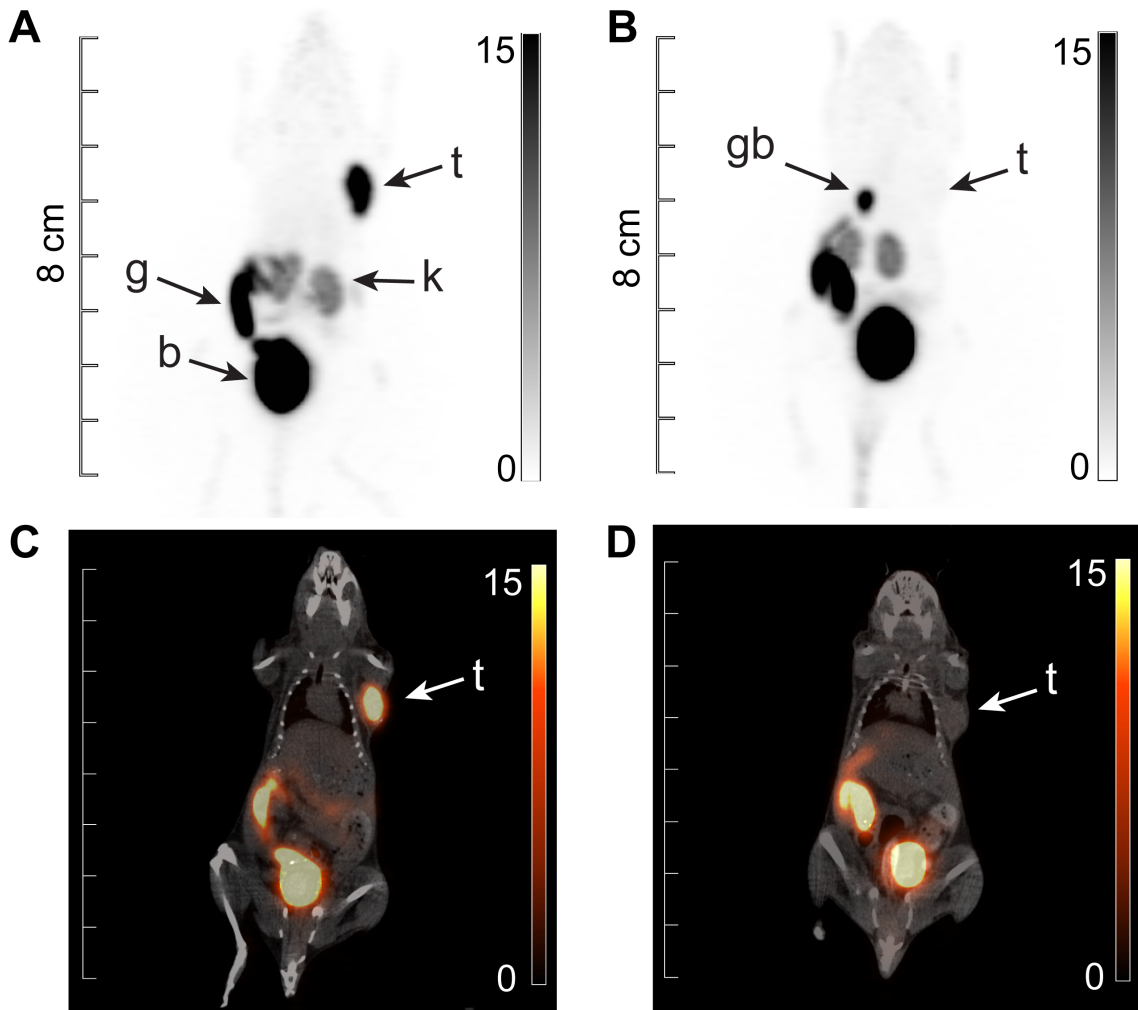


**Figure 7.3** *In vivo* imaging of TATE-<sup>18</sup>F-AMBF<sub>3</sub> in the nude mice with AR42J tumors. The top images are the pure PET images and the bottom images are the hybrid PET/CT images. The radioactivity specifically accumulated in the AR42J tumor and was successfully blocked in the presence of a competitor. The excretion is predominantly through the urinary system with insignificant kidney retention, and the bone uptake is undetectable and there is minimal background activity (t = tumour; g = gallbladder; k = kidney; b = bladder).

## 7.2.4 Time activity curve (TAC) analysis

**Figure 7.4** presents the time activity curves (TACs) of tumors and other important tissues. Time dependent tumor uptake was consistently increased to a peak voxel cluster value of 24% ID/g, which is extraordinary comparing with the other somatostatin radiotracers. As expected, the uptake in rest tissues rapidly declined after reaching the peak value at an early time point soon after intravenous administration.

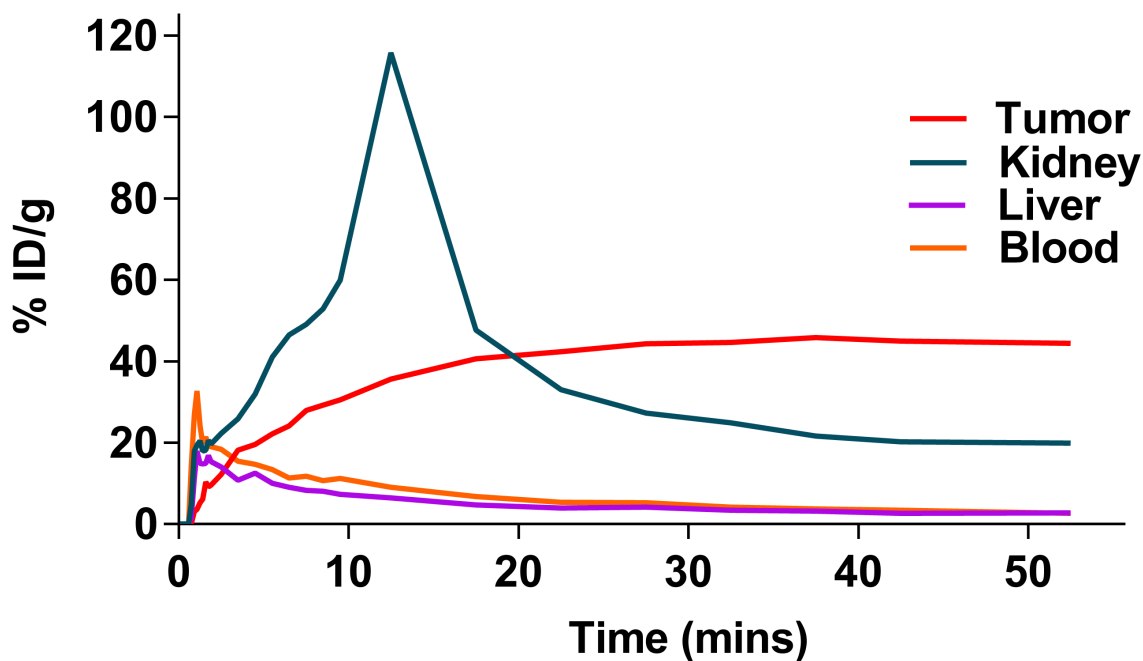


**Figure 7.4** Time activity curves (TAC) of tumors and other important tissues.

## 7.2.5 Biodistribution studies

The *in vivo* biodistribution data of TATE-<sup>18</sup>F-AMBF<sub>3</sub> at 1 hour post injection is summarized in **Figure 7.7**, and the data corroborate PET scanning data. The uptake in AR42J xenograft tumor in the unblocked mice was as high as 10.11±1.67% ID/g. As expected, with excess of competitor, the apparent tumor uptake was remarkably reduced to 0.32±0.21% ID/g, of which the blocking efficiency was up to 97%. The uptake in blood and muscle (1 hour post injection) were: 0.40±0.31% ID/g and 0.11±0.03% ID/g, respectively. This rapid clearance from the background resulted in a very high tumor-to-

blood and tumor-to-muscle ratio of  $25.10 \pm 1.00$  and  $88.96 \pm 3.05$ , respectively. Negligible bone uptake was detected ( $0.46 \pm 0.17\%$  ID/g, 1 hour after injection), specifying no *in vivo* defluoridation.

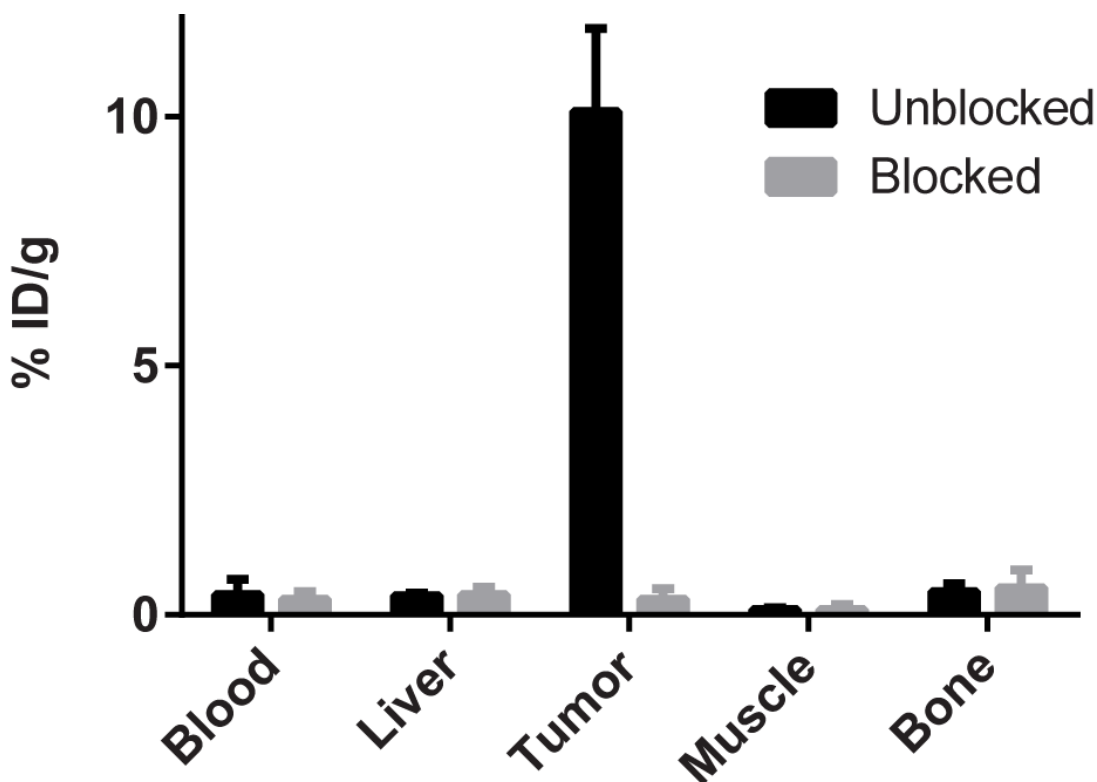


**Figure 7.5** *In vivo* biodistribution data of TATE-<sup>18</sup>F-AMBF<sub>3</sub> at 1 hour post injection following animal sacrifice.

### 7.3 Discussion

A comprehensive comparison of the most representative radiolabeled TATE derivatives is listed in **Table 7.2**.<sup>162,163,190,191,197-199,205,215,217-221</sup> As shown, among the reported TATE-based radiotracers, TATE-<sup>18</sup>F-AMBF<sub>3</sub> demonstrated one of the highest binding affinities to the ssrt2 receptors. This is indeed unexpected, as the TATE was only simply modified by adding the new-designed AMBF<sub>3</sub> via copper-catalyzed click conjugation. Based on PET/CT imaging, TATE-<sup>18</sup>F-AMBF<sub>3</sub> showed very high receptor mediated uptake in a preclinical model of neuroendocrine cancer, with essentially no background activity and exceptional targeting in the tumors. Corroborated with the *in vivo* imaging, *in vivo* biodistribution verified the high tumor uptake. In fact, the tumor uptake of TATE-<sup>18</sup>F-

AMBF<sub>3</sub> was higher in comparison with the clinically used <sup>68</sup>Ga-DOTA-TATE, and ranked among the highest reported to date.<sup>222-226</sup> In the same tumor model, TATE-<sup>18</sup>F-AMBF<sub>3</sub> also showed significantly higher tumor uptake than <sup>111</sup>In-DTPA-octreotide (OctreoScan) and <sup>18</sup>F-NOTA-AIF-TATE.

**Table 7.2** The comparison of the most representative radiolabeled TATE derivatives. In spite of the facile radiosynthesis, TATE-<sup>18</sup>F-AMBF<sub>3</sub> demonstrated one of the highest binding affinities to the ssrt2 receptors, and also one of the best tumor uptake.<sup>162,163,190,191,197-199,205,215,217-221</sup>

	Total synthesis time (min)	Specific Activity (GBq/μmol)	Binding affinity (nM)	Tumor uptake after 60 min	Tumor to muscle	Tumor to blood
<sup>111</sup> In-DTPA-Oc (Octreoscan)	>60	44.2	1.2	0.99	/	49.5
<sup>99m</sup> Tc-P829(NeoSpect)	20	37	0.32	4.81	68.00	21.0
<sup>111</sup> In-DOTA-TATE	>60	15.9	>1.67	4.12	/	51.5
<sup>99m</sup> Tc-EDDA-TATE	20	60	>1.67	5.01	/	23.85
<sup>64</sup> Cu-CB-TE1AIP-Y3-TATE	>60	48	1.8	5.11	60.00	25.0
<sup>18</sup> F-FETE-PEG-TOCA	90	5.9	12	5.14	23.74	24.15
<sup>18</sup> F-FET-βAG-TOCA	90	3.9	4.7	8.23	24.12	13.47
<sup>18</sup> F-FET-βAG-[W-c-K]	90	12.3	220	0.11	0.65	1.10
<sup>18</sup> F-AI-NOTA-OC	45	36.1	3.6	6.43	37.44	23.15
<sup>68</sup> Ga-DOTA-TATE	45	ND	0.24	2.75	2.28	0.56
TATE- <sup>18</sup> F-AMBF <sub>3</sub>	<30	111	0.14	10.11	88.96	25.10

It is well known that the liver uptake of radiometal-labeled octreotide is low on average,<sup>198,199,205,220</sup> but this is not always true for <sup>18</sup>F-labelled radiotracers.<sup>214</sup> Liver uptake, particular non-specific uptake, is worth consideration for imaging reagents as high non-specific liver uptake essentially reduces the specificity of detecting the metastasis in the liver tissue. Interestingly, as shown in PET/CT and biodistribution, the liver uptake of TATE-<sup>18</sup>F-AMBF<sub>3</sub> is low, resulting in a much higher tumor-to-liver ratio (27.21±0.79, 2 hours after injection) than the other <sup>18</sup>F-labelled TATE analogs (0.25~5.0, 2 hours after injection). Moreover, comparing with the standard “OctreoScan”, the tumor-to-liver ratio for TATE-<sup>18</sup>F-AMBF<sub>3</sub> was similar or even higher, which is uncommon for <sup>18</sup>F-labelled TATE peptides. Generally, the <sup>18</sup>F-labelled octreotide analogs, such as octreotide-<sup>18</sup>F-fluoropropionamide (logP, -0.07±0.01), displayed comparatively high lipophilicity. However, the lipophilicity of TATE-<sup>18</sup>F-AMBF<sub>3</sub> is relatively low and in the same range with TATE-NOTA-Al-<sup>18</sup>F and radiometal-labeled octreotide analogs, possibly explaining the unusually high tumor-to-liver ratio.

To assess the *in vivo* stability, a systematic and comprehensive evaluation has been performed in Chapter 2. At pH=7.4, <sup>19</sup>F-AMBF<sub>3</sub> presents excellent chemical stability in PBS buffer; the half-life was measured to be 19500±500 min, which is up to 15 times more stable than the aryltrifluoroborates being used previously.<sup>102-104</sup> A plasma stability assay was accomplished by incubating TATE-<sup>18</sup>F-AMBF<sub>3</sub> at 37 °C for 120 min (**Figure 7.6**). The decomposition was negligible and the intact radiotracer was still dominant in the plasma. In addition, minimal bone uptake (0.46±0.13% ID/g, 2 hours after injection) was observed in both PET/CT and biodistribution, resulting in high tumor-to-bone ratio of up to 21.30±3.60. This low unspecific bone uptake is particularly encouraging for the detection of bone metastasis (BM).<sup>71</sup> Moreover, this result highlights the general stability of such alkyltrifluoroborate radioprosthesis, an observation that should open the door for the development of other peptide tracers based on the same zwitterionic ammoniomethyl-BF<sub>3</sub>.

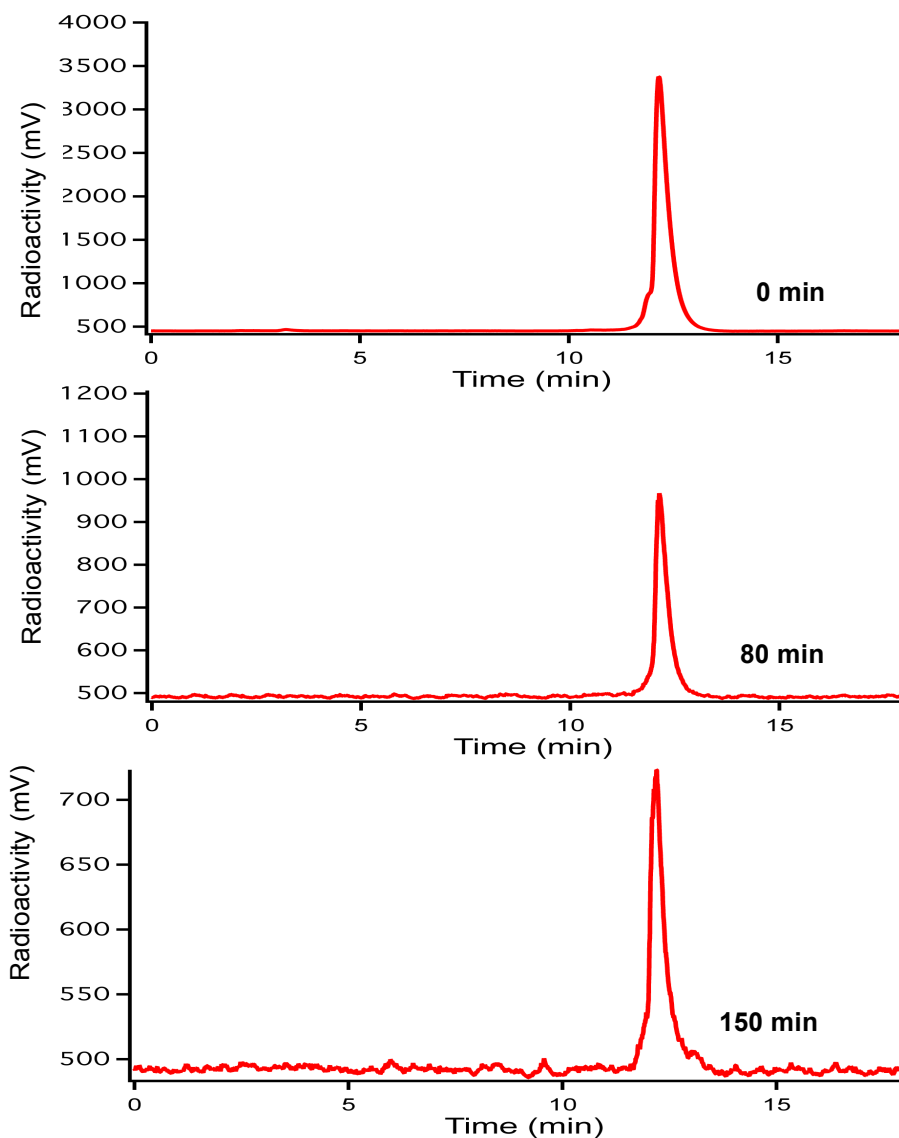


**Figure 7.6** The radioactive HPLC trace following mice plasma incubation of TATE- $^{18}\text{F}$ -AMBF $_3$ . The incubation time is 0, 80 and 150 min, respectively

By radiolabelling this newly designed B-F radioprosthesis via  $^{18}\text{F}$ - $^{19}\text{F}$  IEX, the radiosynthesis has been significantly simplified on following accounts: (1) time-consuming azeotropic  $^{18}\text{F}$ -fluoride drying was avoided as aqueous conditions were used and no-carrier-added  $^{18}\text{F}$ -fluoride was eluted with isotonic saline; (2) rapid labeling ( $\sim 15$  min); (3) sub-milligram precursors were used; (4) high specific activity was achieved; (5) time consuming HPLC purification was eliminated as radiolabelled product is chemically

identical with the precursor. In keeping the advantage of operational simplicity, all the operations were performed in a completely shielded hot cell, in which Curie-level labeling was performed to enable multiple human doses in a single run. Moreover, improvements in cyclotron power and increased market demand for  $^{18}\text{F}$ -FDG have led to clinical radiolabeling starting with multi-Curies-level of  $^{18}\text{F}$ -fluoride. Hence, this new  $^{18}\text{F}$ - $^{19}\text{F}$  IEX technology will be readily applicable to existing production facilities and in turn be promising for clinical applications.

## **7.4 Conclusion**

TATE- $^{18}\text{F}$ -AMBF<sub>3</sub> was radiolabeled in high yields and specific activity using a facile exchange reaction using nanomole quantities of precursor peptide, without HPLC purification. This methodology provides for rapid multi-dose production of a high affinity  $^{18}\text{F}$ -labeled octreotate in a single production run that should be easily amenable to automation. In addition to radiosynthetic ease, the biological evaluation of TATE- $^{18}\text{F}$ -AMBF<sub>3</sub> indicated that this tracer provides good stability, optimal pharmacokinetics, excellent binding affinity, and very high tumor to non-target tissue ratios for *in vivo* imaging.

## **7.5 Materials and methods**

### **7.5.1 General information**

Reagents and solvents were purchased from Advanced Chemtech, Sigma-Aldrich, Combi-Blocks, or Novabiochem. The AR42J cell line was purchased from ATCC.  $^{18}\text{F}$ -fluoride Trap & Release Columns were purchased from ORTG Inc. (Oakdale, TN) and C18 Sep-Pak cartridges (1 cc, 50 mg) were obtained from Waters. An Endeavor 90 peptide synthesizer (Aaptec) was applied to synthesize the peptide.

### **7.5.1 Synthesis**

#### **HPLC Analysis**

The following gradients were used for HPLC purification and quality control:

Method A: Agilent Eclipse XDB-C18 5  $\mu\text{m}$  9.2 x 250 mm semi-prep column. Solvent A: 0.1% TFA water; solvent B: MeCN; 0 to 15 min: 20% to 40% B, 15 to 20 min, 40% to 20% B. Flow rate: 4.5 mL/min, column temperature: 19 to 21  $^{\circ}\text{C}$ .

Method B: Agilent Eclipse XDB-C18 5  $\mu\text{m}$  9.2 x 250 mm semi-prep column. Solvent A: 0.1% TFA water; solvent B: MeCN; 0 to 2 min: 5% to 20% B, 2 to 5 min, 20% to 30% B, 5 to 20 min, 30% to 50%, 20 to 22 min, 50% to 5% B. Flow rate: 3 mL/min, column temperature: 19 to 21  $^{\circ}\text{C}$ .

Method C: Phenomenex Jupiter 10  $\mu\text{m}$  C18 300 $\text{\AA}$  4.6 x 250 mm analytical column. Solvent A: 0.1% TFA water; solvent B: MeCN; 0 to 2 min: 5% to 5% B, 2 to 7 min, 5% to 20% B, 7 to 15 min, 20% to 100%, 15 to 20 min, 100% to 5% B. Flow rate: 2 mL/min, column temperature: 19 to 21  $^{\circ}\text{C}$ .

## **Peptide Synthesis**

The TATE peptide was synthesized as previously described.<sup>220,227</sup> Briefly, the NHS-ester of bromoacetic acid was coupled to the N-terminus followed by successive treatment with sodium azide to provide a TATE derivative suitable for click-conjugation. The peptide was deprotected and cleaved from the resin by treatment with trifluoroacetic acid supplemented with trimethylsilane scavengers. Purification by HPLC with a semi-preparative column with Method A provided the final peptide in quantities of ~10 mg. The calculated mass was 1131.2 and measured at 1131.4 by mass spectrometry. The purity of the peptide was >99%.

## **Synthesis of N-propargyl-N,N-dimethyl-ammoniomethyl-boronylpinacolate:**

N-Propargyl-N,N-dimethyl-ammoniomethyl-boronylpinacolate (alkynyl-AMB(pin)) was synthesized by condensation of iodomethyl-boronylpinacolate and propargylamine by standard alkylative amine quaternization.<sup>228</sup> Briefly, a flame-dried round bottom flask was charged with N,N-dimethylpropargylamine (98  $\mu\text{L}$ , 1.0 mmol) and 2 mL anhydrous diethyl ether under argon atmosphere to which Iodomethyl-pinacolboronate (165  $\mu\text{L}$ , 0.9 mmol) was added drop-wise at room temperature. On stirring, the solution became cloudy followed by the formation of a white precipitate, which was the desired product.

The resulting precipitate was filtered and washed with cold diethyl ether. Then the residue was dried under high vacuum to give a fluffy white powder in 95% yield.  $^1\text{H}$  NMR (300 MHz,  $\text{CD}_3\text{CN}$ )  $\delta$  4.40 (d, 2H), 3.31 (s, 2H), 3.22 (s, 6H), 3.21 (t, 1H), 1.27 (s, 12H); ESI: calculated: 224.1; found: 224.1.

### Synthesis of TATE-AMBF<sub>3</sub>

The N-propargyl-N,N-dimethylammonio-methylboronylpinacolate (5.0 mg, 22.3  $\mu\text{mol}$ ) was converted to the corresponding trifluoroborate (alkynyl-AMBF<sub>3</sub>) through the addition of  $\text{KHF}_2$  (3 M, 30  $\mu\text{L}$  in water),  $\text{HCl}$  (4M, 30  $\mu\text{L}$  in water), deionized water (20  $\mu\text{L}$ ) and DMF (60  $\mu\text{L}$ ) at 45°C for 2 hours, and then quenched by  $\text{NH}_4\text{OH}$  (conc., 10  $\mu\text{L}$ ). The crude reaction was directly used for click conjugation to TATE-azide without further purification. A mixture of TATE-azide (4.0 mg, 3.4  $\mu\text{mol}$ ),  $\text{CuSO}_4$  (1.0 M, 5.0  $\mu\text{L}$ ), sodium ascorbate (1.0 M, 12.5  $\mu\text{L}$ ) and 5%  $\text{NH}_4\text{OH}$  ( $\text{MeCN}/\text{H}_2\text{O}=1:1$ , 50  $\mu\text{L}$ ) was added, and the new mixture was warmed up to 45 °C for 2 hours. The overall synthetic route is shown in **Scheme 7.1**. Purification was performed by Agilent 1100 HPLC system with Gradient B to isolate 2.3 mg of chemically pure AMBF<sub>3</sub>-TATE. ESI-MS: Calculated: 1297.5; Obtained: 1297.4. For convenience and to ensure reproducibility, the purified TATE- $^{19}\text{F}$ -AMBF<sub>3</sub> was diluted in ethanol and aliquoted in quantities of ~60  $\mu\text{g}$  (~50 nmol) for radiolabeling.

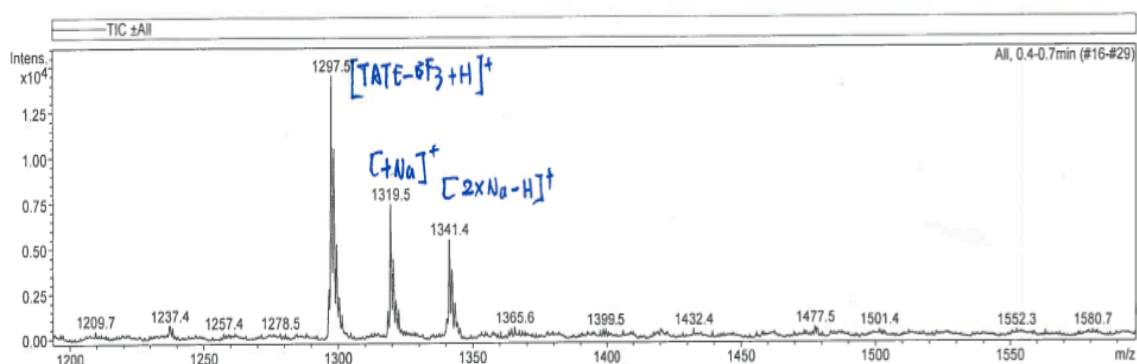


**Figure 7.7** ESI-MS spectrum of TATE- $^{19}\text{F}$ -AMBF<sub>3</sub>.

### 7.5.2 *In vitro* binding assay

Membranes from Chinese Hamster Ovary cells (CHO-K1) transfected with sst2r and [ $^{125}\text{I}$ ]Tyr-somatostatin-14 were obtained commercially from PerkinElmer, Canada. A

standard filtration-binding assay was performed in 96-well filtration plates (MultiScreen, Millipore) to determine the binding affinity ( $K_i$ ) of AMBF<sub>3</sub>-TATE. Briefly, 0.25  $\mu$ L of the membranes per well were incubated with the <sup>125</sup>I-labeled standard at a concentration of 0.05 nM, and increasing concentrations of non radioactive AMBF<sub>3</sub>-TATE (competitor), in buffer consisting of 25 mM Hepes pH 7.4, 10 mM MgCl<sub>2</sub>, 1 mM CaCl<sub>2</sub>, and 0.5% BSA. After incubation at 37 °C for 1 hour, the wells were aspirated and washed 8 times with 50 mM of ice-cold wash buffer (Tris-HCl pH 7.4) over GF/B filters. The filters were removed and counted by a gamma counter (Cobra II, Packard). A typical competition curve is shown in **Figure 7.2**. The experiment was repeated in triplicate. Data were fitted to a one-site competition model (GraphPad Prism 7.1 software) to calculate the inhibition constant ( $K_i$ ).

### 7.5.3 Radiolabeling

Just prior to radiosynthesis, AMBF<sub>3</sub>-TATE was re-suspended in aqueous pyridazine-HCl buffer (pH = 2) (~50  $\mu$ L) in a vial (polypropylene Falcon Tube). No carrier-added <sup>18</sup>F-fluoride (800-1000 mCi) was obtained by bombardment of H<sub>2</sub><sup>18</sup>O with 18 MeV protons, followed by trapping on an anion exchange resin (9 mg, QMA, chloride form, prewashed with deionized water). The <sup>18</sup>F-fluoride was eluted with isotonic saline (70-100  $\mu$ L) into the reaction vial containing AMBF<sub>3</sub>-TATE. The vial was placed in a heating block set at 80 °C for 20 min whereupon the reaction was quenched by the injection of 5% NH<sub>4</sub>OH in water (2 mL). The reaction mixture was loaded onto a C18 light cartridge. The impurities (i.e. free <sup>18</sup>F-fluoride) were removed by flushing with saline (2 mL). Radiochemically pure TATE-<sup>18</sup>F-AMBF<sub>3</sub> was then released into a glass vial by elution with 1:1 ethanol/saline (0.5 mL) to provide 200 mCi tracer. This solution was formulated into isotonic saline (5 mL) for imaging. A small sample was removed for quality control analysis by HPLC (**Figure 7.1**). The radiolabeling was repeated three times and the HPLC traces are shown below.

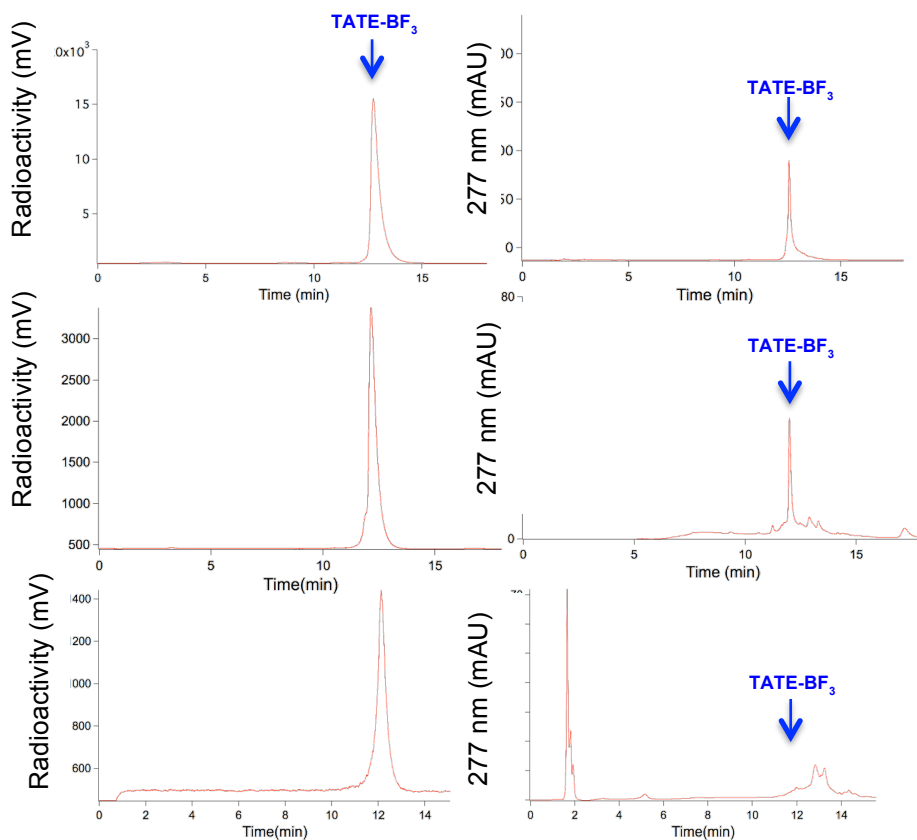


**Figure 7.8** The HPLC traces of the reinjection of the sep-pak purified TATE-BF<sub>3</sub>. The left figures are the radioactive HPLC trace, and the right figures are the corresponding UV-Vis HPLC trace at 277 nm.

#### 7.5.4 *In vitro* stability

The purified TATE-<sup>18</sup>F-AMBF<sub>3</sub> in its saline formulation was assayed for plasma stability. For a plasma stability assay, TATE-<sup>18</sup>F-AMBF<sub>3</sub> (20 μL) was added to mouse plasma (500 μL) and incubated at 37 °C for 0, 60 and 120 min. Following incubation at each time point, the reaction was quenched by adding MeCN (1 mL) to precipitate insoluble proteins from the solution. The quenched reactions were centrifuged to remove insoluble material. The supernatant was aspirated by pipette, filtered, and analyzed by HPLC using Method C.

### 7.5.5 Animal model and biodistribution studies

All animal studies were performed in accordance with the Canadian Council on Animal Care Guidelines and were approved by the animal care committee of the University of British Columbia.  $10^7$  Rat pancreatic adenocarcinoma cells (AR42J) were freshly expanded in PBS/matrigel mixture and inoculated subcutaneously in female immunocompromised mice (nod scid IL2r- $\gamma$ -null, bred in house). The tumors were grown for 2 weeks until they reached 5-7 mm in diameter. While fewer than 2% isoflurane anesthesia, the mice were injected via the tail vein with 10-20  $\mu$ Ci of TATE- $^{18}$ F-AMBF<sub>3</sub> (n=5). To demonstrate the specificity of uptake *in vivo* in receptor positive tissues, 100  $\mu$ g of TATE-DOTA-Ga was pre-injected 15 minutes prior to TATE- $^{18}$ F-AMBF<sub>3</sub> injection as a blocking control cohort (n=4). Sixty minutes following injection, the mice were anesthetized with isoflurane and euthanized by carbon dioxide. The organs were harvested, rinsed with saline, blotted dry, and collected in previously weighted tubes. The tubes containing the organs were counted in a gamma counter (Cobra-II, Packard). The tissue weight and associated counts per minute were used to calculate the percentage-injected dose per gram of tissue (%ID/g).

### 7.5.6 PET/CT imaging

The imaging studies were acquired using multimodality PET/CT system (Inveon, Siemens). For imaging, a baseline low-dose CT scan was obtained for localization and attenuation correction. Roughly 100  $\mu$ Ci of radiotracer was injected in the caudal lateral tail vein of tumor-bearing mice. A dynamic scan was acquired in list-mode for 60 minutes while the animal was kept warm by a heated pad on the scanner bed. TATE-DOTA-Ga (100  $\mu$ g per mouse) was pre-injected as a blocking agent in some animals. Following scanning, the mice were euthanized, while under anesthesia, by CO<sub>2</sub> inhalation. The images were reconstructed by an iterative reconstruction algorithm (3D OSEM/MAP) using the Inveon Acquisition Workplace Software (Siemens), applying normalization, dead time, random, and attenuation corrections. The uptake in tumor and tissues of interest were determined by region of interest (ROI), and the %ID/g was calculated (assuming a tissue density of 1.0 g/cc). The mean %ID/g was calculated by

drawing a ROI to match the tumor contours visible on CT. The peak %ID/g was calculated from the hottest 2x2 voxel cluster within the tumor.

### 7.5.7 Specific activity measurement

To assess the specific activity, a fitted linear standard curve (**Figure 7.7** and **Figure 7.8**) was achieved by chromatographing a series of known quantities of unlabeled TATE-<sup>19</sup>F-AMBF<sub>3</sub> by HPLC. The exact quantity of each injection was previously determined by absorbance at 277 nm of the stock solution. For the radiosynthesis (**Figure 7.1**), integration of the visible peak (277 nm) that eluted at 12.0 min provided a quantitative mass value of 0.46 nmol based on the fitted linear standard curve. For the re-injection, TATE-<sup>18</sup>F-AMBF<sub>3</sub> was loaded on HPLC and most of the radioactivity was collected at 12.0 min. The specific activity was measured to be 4.3 Ci/μmol at the time of collection. The same experiments were repeated three times and the results were listed in **Table 7.1**.

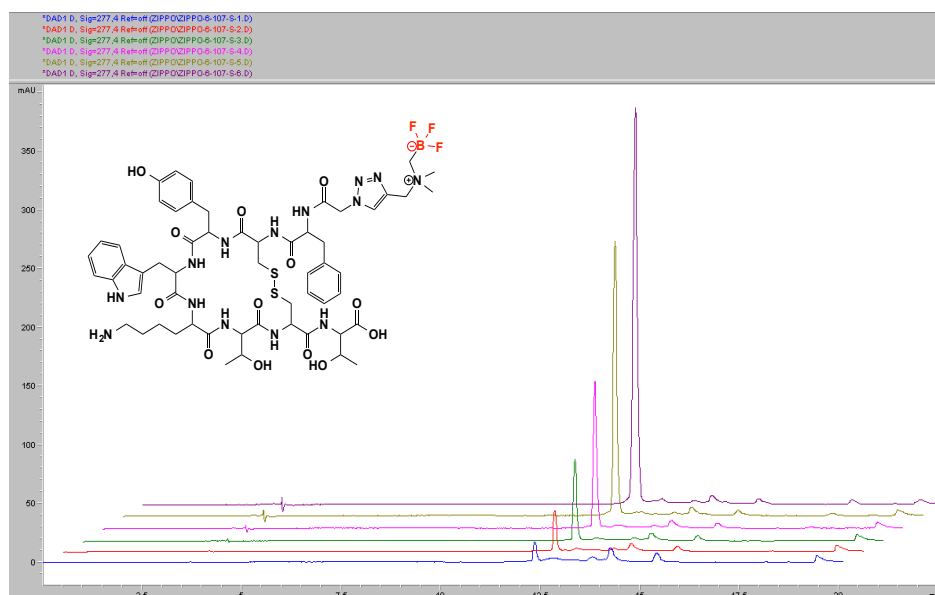


**Figure 7.7:** Standard curve with 200 pmol (16.5 mAU), 400 pmol (34.1 mAU), 800 pmol (68.5 mAU), 1500 (125.4 mAU), 2500 pmol (217 mAU) and 4000 pmol (338 mAU) TATE-BF<sub>3</sub>.

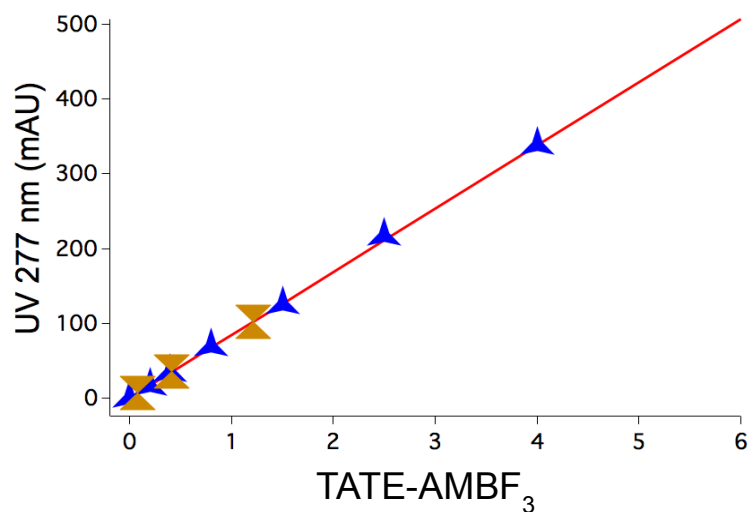


**Figure 7.8:** Fitted linear standard curve, the blue marks are the integrations of the HPLC injection of TATE-<sup>19</sup>F-AMBF<sub>3</sub>. The yellow marks show HPLC UV absorbance of the TATE-<sup>18</sup>F-AmBF<sub>3</sub> peak during radiolabelling 1~3.

**Table 7.1:** Summary of specific activity measurement of TATE-<sup>18</sup>F-AmBF<sub>3</sub>.

Labeling #	<sup>18</sup> F at BOS (mCi)	TATE <sup>19</sup> F-AMBF <sub>3</sub> (nmol)	TATE- <sup>18</sup> F-AMBF <sub>3</sub> (mCi)	TATE- <sup>18</sup> F-AMBF <sub>3</sub> (nmol)	SA of EOS (Ci/μmol)
1	1241	~100	0.33	0.076	4.3
2	586	~50	1.28	0.41	3.1
3	760	~100	3.31	1.02	3.2

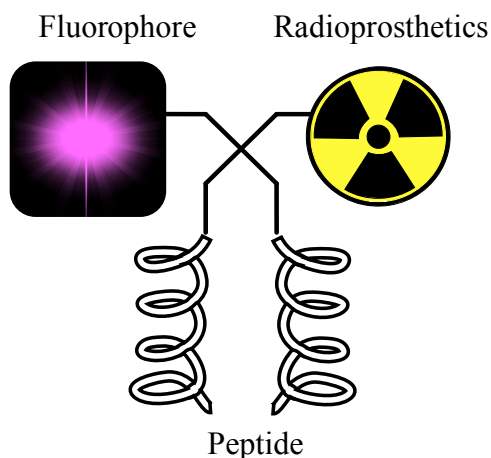
# Chapter 8: A Dual Modal Fluorescent PET Tracer

## 8.1 Introduction

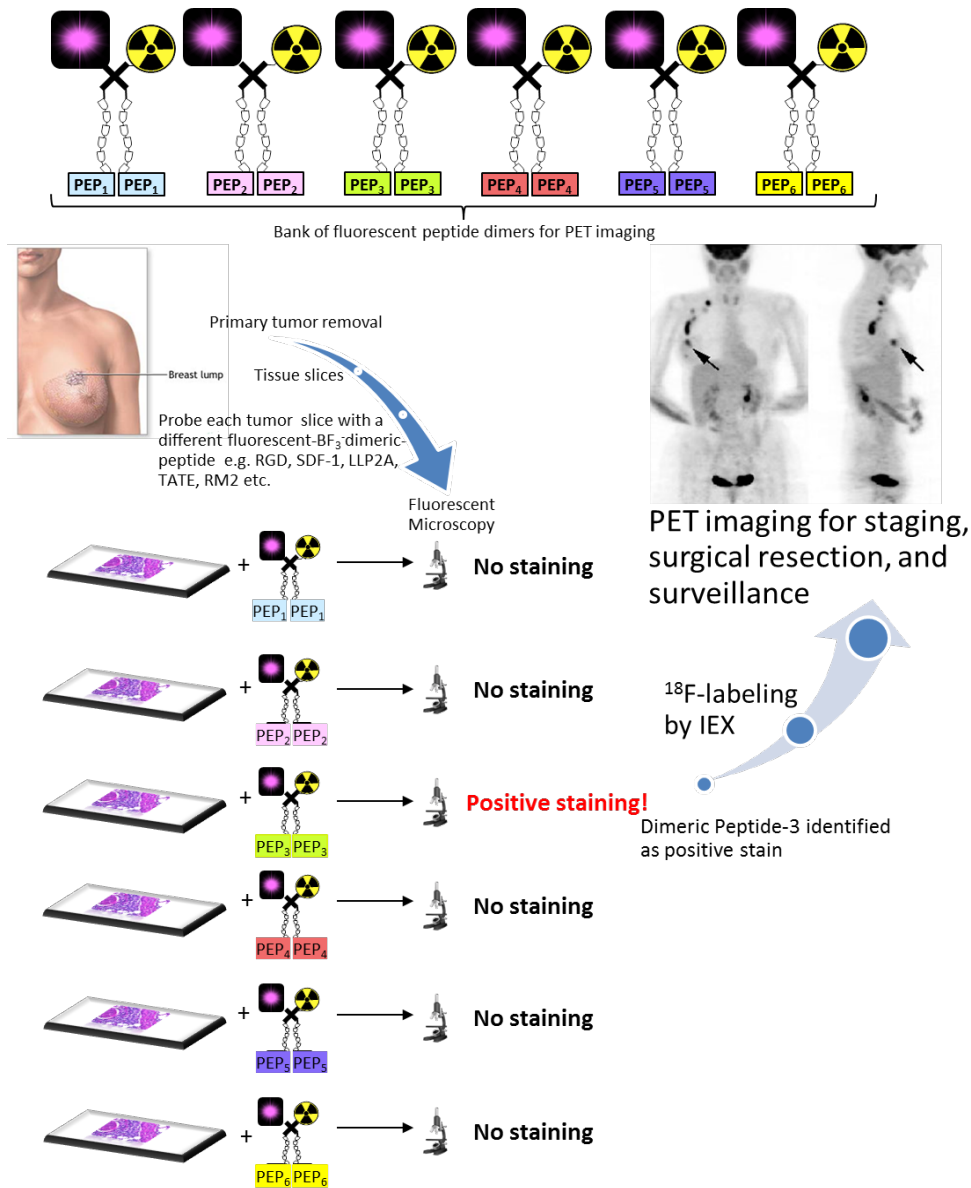
Positron Emission Tomography (PET) is routinely used for numerous clinical applications, especially in imaging the dynamic clearance, distribution, and abundance of specific pathological targets within deep tissue.<sup>229</sup> In Chapter 6, our radiolabelling method demonstrates broad applications in rapidly screening bioligands for ultimately developing novel PET tracers with very promising results. However, we need to face the challenge that the use of PET tracers has been limited primarily to macroscopic spatial and temporal imaging due to the short half-life of radioisotopes.<sup>66,230</sup> In contrast, a fluorescent probe can be visualized at the microscopic level to provide more rapid validation of new radiotracers.<sup>231</sup> Moreover this allows the combined optical and PET signals to be superimposed, supplying a micro/macroscopic hybrid image along with use in pre/post-operative applications.<sup>232</sup> Thus, a radiosynthon that empowers seamless switching between PET and fluorescence imaging would be highly desirable.<sup>10,13,231-234</sup>

To make a fluorescent PET tracer, a chemically identical molecule with singular pharmacokinetics would be used first as the fluorescent probe for histological applications and also as a PET tracer for diagnosing the disease in the same patient. This unique advantage is considered promising in order to facilitate various bench-to-clinic applications.<sup>13</sup> Indeed, interest in this approach is

underscored by numerous examples of fluorescent peptides that have been labeled by radiometal wash-in have been studied.<sup>183,235,236</sup> Nevertheless, there are rare examples of <sup>18</sup>F-labelled fluorescent PET tracers have been developed. And this dearth of <sup>18</sup>F-labelled fluorescent peptides is most likely due to the long-standing challenges of <sup>18</sup>F-labelling in high yield and high specific activity. Encouragingly, Dr. Weissleder and coworkers



recently performed a direct  $^{18}\text{F}$ -labeling of a BODIPY derivative by displacement of DMAP in water,<sup>143,237</sup> and the fluorescent radiosynthon, as an NHS ester, was then conjugated to an antibody in a second step. Similarly, Dr. Gabbai and coworkers performed  $^{19}\text{F}$ - $^{18}\text{F}$  isotope exchange on  $^{19}\text{F}$ -BODIPY-NHS that was then linked to a peptide.<sup>238</sup> Finally Dr. Tsien and



*Scheme 8.1* Seamless bench-to-bed translation.

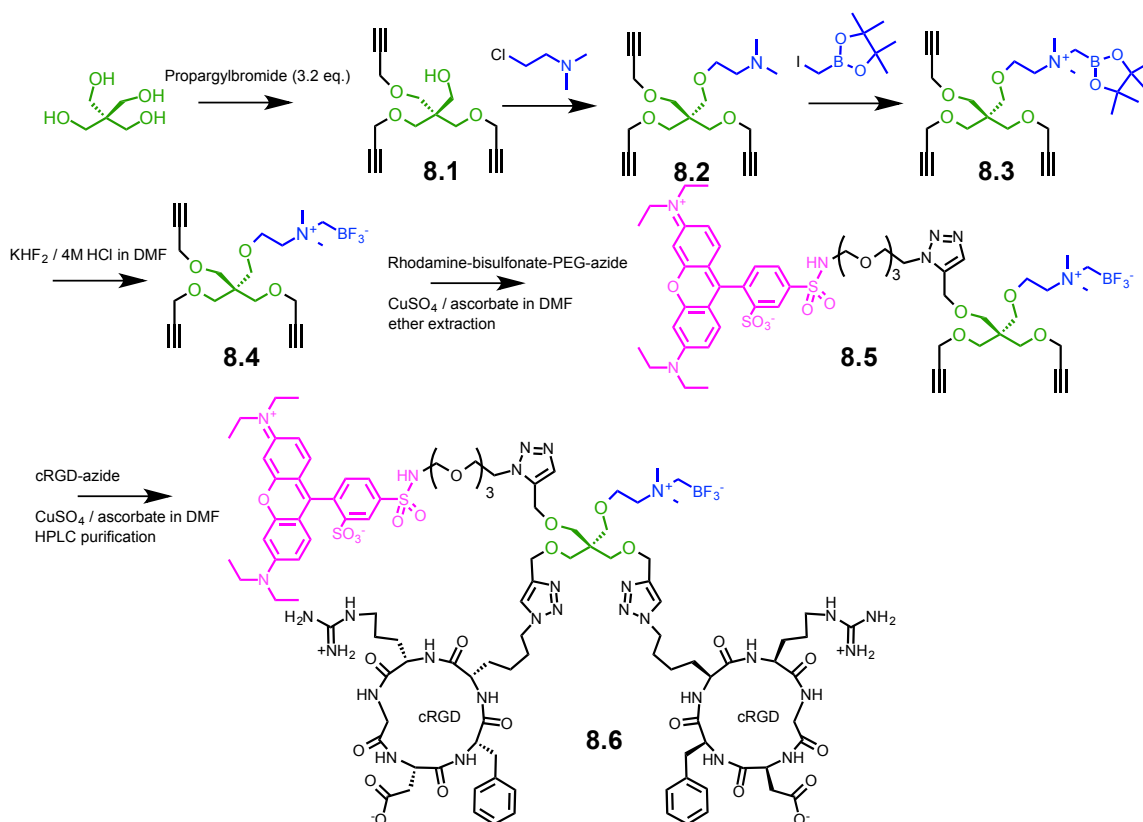
coworkers developed a tripodal arylboronate-near-IR fluorophore that was first grafted to a high molecular weight manosylated glycan.<sup>239</sup> This was then labeled in the presence of aqueous  $^{18}\text{F}$ -fluoride to convert the boronate to the  $^{18}\text{F}\text{-ArBF}_3^-$ . The conjugate provided exquisite images of the sentinel lymph node by both PET and fluorescent imaging modes. As a consequence of this work, more and more excitement surrounds the development of fluorescent PET tracers. However, excluding the two-step and multi-step radiosynthesis, to date the specific radioactivity values of all such  $^{18}\text{F}$ -labeled fluorescent tracers were useful ( $\leq 0.05$  Ci/ $\mu\text{mol}$ ), yet considered to be rather low compared to needs for PET imaging.<sup>143</sup> Nevertheless, such a low value would prove to be necessary to correlate *ex vivo* fluorescence with PET imaging (see below). Nevertheless for PET, high specific radioactivity is important. A value of  $>1$  Ci/ $\mu\text{mol}$  is generally required to ensure microdosing,<sup>36</sup> in accordance with regulatory guidelines. The interplay between high specific activity that reduces the chemical doses vs. the need for sufficiently high masses of fluorophore needed for fluorescent detection forms the basis of the investigation of this Chapter as we ask the following question, what happens when fluorescent imaging is performed with a tracer labeled at very high specific activity that is typically required for PET imaging.<sup>19,115,165,180,238,240,241</sup>

As demonstrated in Chapter 6, high specific activity has been reproducibly achieved using one-step  $^{18}\text{F}$ - $^{19}\text{F}$  IEX with *in vivo* stable organotrifluoroborates preconjugated to various peptides. It would be promising to apply the new radiolabelling method to developing a fluorescent PET tracer. In addition, dimeric-peptide conjugates are preferred for their increased avidity that often results in higher affinity.<sup>88,89</sup> To embrace all of these concerns, here we disclose for the first time a synthetic strategy that amalgamates a dimeric peptide, a fluorophore, and trifluoroborate precursor prosthetic for a facile  $^{18}\text{F}$ -labelling. This construct not only successfully provides fluorescent imaging for a qualitative cell-binding assay using confocal fluorescence microscopy, but also is labeled in high radiochemical yield and at high specific activity as a “kit”. Besides these promising chemical and radiosynthetic results, specific tumor uptake was observed by *in vivo* PET imaging whereas *in vivo* optical imaging demonstrated tumor uptake with fluorescence.

## 8.2 Results

### 8.2.1 Modular synthesis

In order to modularly build a trimeric construct that successively grafts one fluorophore and two peptides, we opted to use “click” chemistry due to its broad utility in bioconjugation,<sup>242-244</sup> and recent applications to radiotracers. Synthesis started with a standard three-fold propargylation of pentaerythritol followed by treatment with dimethyl-



*Scheme 8.2* Synthesis route of **8.6**.

(chloro-ethyl)amine. The amine was quaternized with iodomethylboronyl-pinacolate to give **8.3**, N,N-dimethyl-ammonio-N-(methylboronyl-pinacolate). Compound **8.3** was converted to the trifluoroborate with  $\text{KHF}_2$  to give **8.4**, which was treated with 1 eq. commercially available Rhodamine-PEG-azide in the presence of cuprous ion to give compound **8.5**. Compound **8.5** possessed two alkyne groups for subsequent peptide

grafting. cRGD-N<sub>3</sub> (2.5 eq.) was then conjugated to provide the corresponding dimer of cRGD as a radiotracer precursor **8.6** that would be labeled by IEX (*Scheme 8.2*).<sup>124</sup>

### 8.2.2 Radiosyntheses

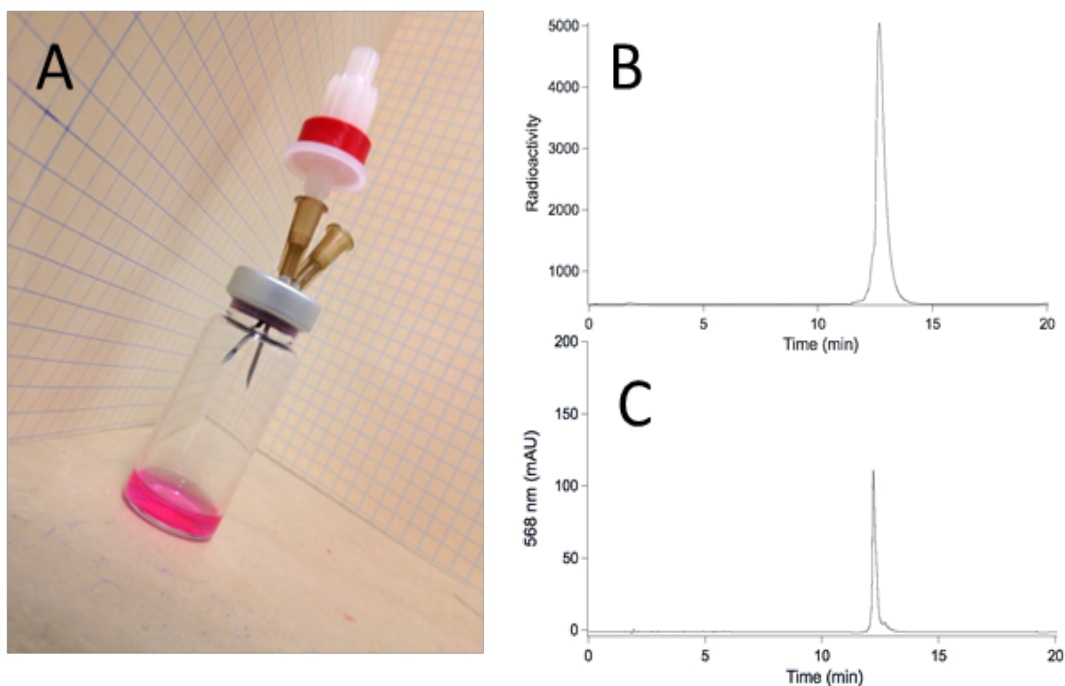


**Figure 8.1** A) <sup>18</sup>F-labeled **8.6** following elution from Sep-Pak in 50% ethanol-PBS in vial (275 mCi); B) QC radiotracer of 1.8 mCi of Sep-Pak eluted tracer; C) The corresponding UV-Vis trace at 568 nm of the same sample.

Radiolabeling generally followed previous reports on this method. Approximately 800-1200 mCi was eluted with 0.9% isotonic saline (70-100  $\mu$ L) into a polypropylene Falcon tube that had been fitted with a septum and which contained an aliquot of **8.6** (50 or 75 nmol) that had been re-suspended in DMF (30  $\mu$ L) and aqueous buffer pH 2 (30  $\mu$ L) just prior to bombardment. The tube containing the labeling reaction was then placed in a heated sand bath (85  $^{\circ}$ C) for 20 min whereupon quench solution (5% NH<sub>4</sub>OH in pure water) (2mL) was added to the reaction by syringe. The entire reaction contents were then withdrawn into a 3 mL syringe and passed over a reverse phase C18-Sep-Pak that was then washed with saline (2 mL). The tracer was then eluted into a sterile capped vial

by passage of 1:1 ethanol-PBS (2 mL). Radiochemical yields of 30-40% were achieved (n=3). As illustrated in **Figure 8.1**, the Sep-Pak purified  $^{18}\text{F}$ -AMBF<sub>3</sub>-Rhodamine-BisRGD was re-injected into HPLC for quality analysis, and only one predominant peak was observed in both radioactive mode and 568 nm. To assess plasma stability,  $^{18}\text{F}$ -AMBF<sub>3</sub>-Rhodamine-BisRGD was incubated in mouse plasma for up to 120 min with no detectable loss of fluoride or other observable decomposition products as assayed by radio-HPLC (**Figure 8.2**).

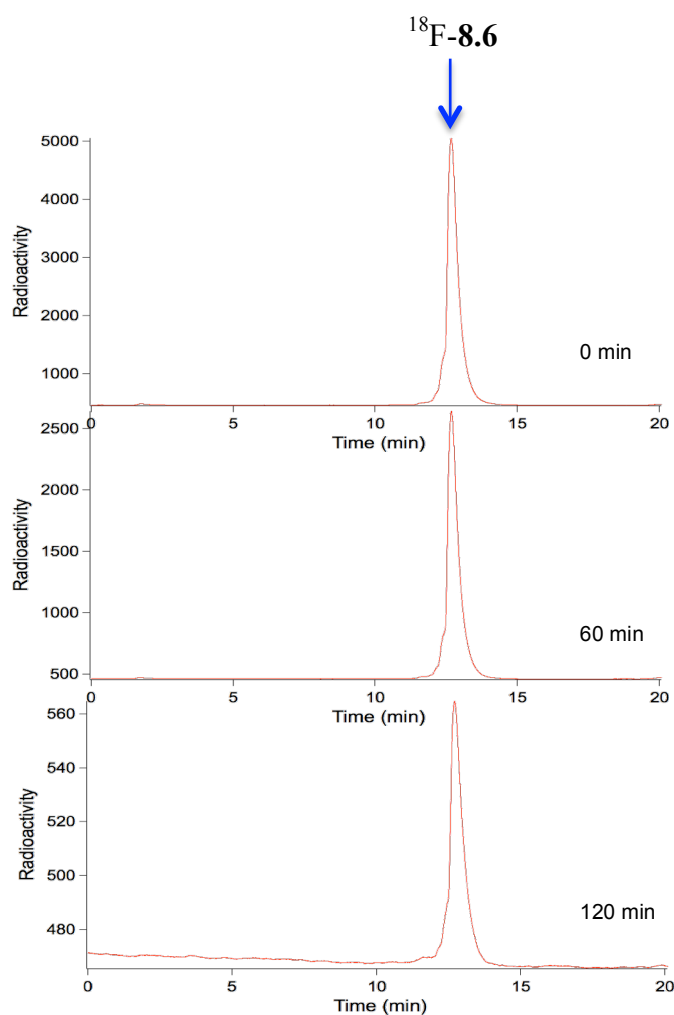


**Figure 8.2** The radioactive HPLC trace following mice plasma incubation at 37 °C of BisRGD-Rhodamine- $^{18}\text{F}$ -BF<sub>3</sub> at 0, 60 and 120 min, respectively.

### 8.2.3 Specific activity measurement

To assess the specific activity, a fitted linear standard curve (see **Figure 8.3**) was achieved by chromatographing a series of known quantities of unlabeled **8.6** by HPLC. The exact quantity of each injection was previously determined by absorbance at 568 nm of the stock solution. For the radiosynthesis (**Figure 8.1**), integration of the visible peak (568 nm) that eluted at 12.5 min provided a quantitative mass value of 0.46 nmol based on the fitted linear standard curve. For the re-injection, 1.82 mCi  $^{18}\text{F}$ -labelled **8.6** was loaded on HPLC and most of the radioactivity was collected at 12.5 min. The specific activity was measured to be 3.95 Ci/ $\mu\text{mol}$  at the time of collection. The same experiments were repeated three times and the results were listed in **Table 8.1**.

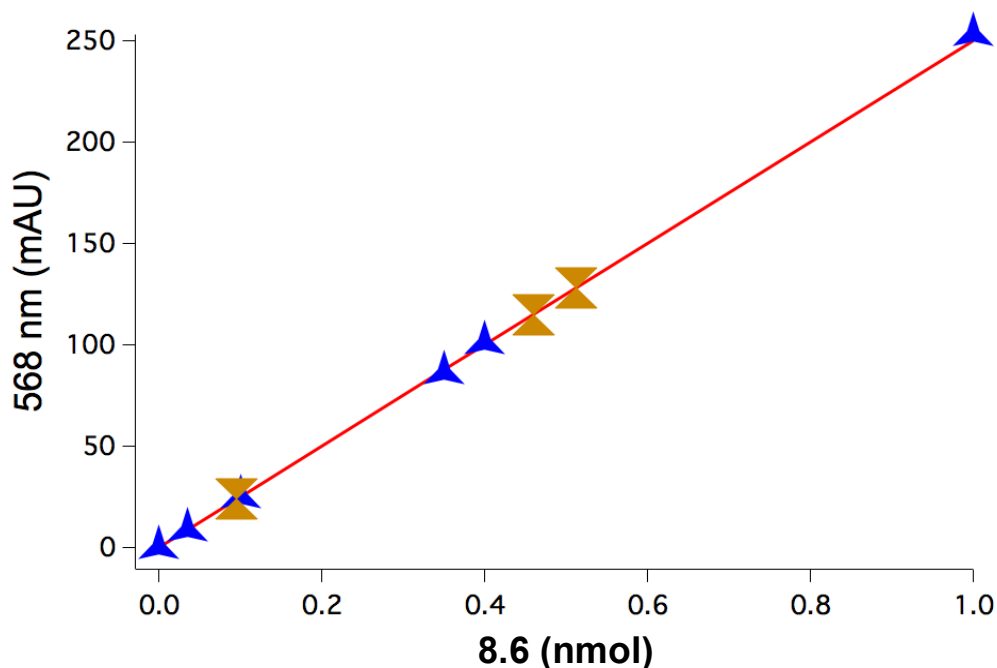


**Figure 8.3** Fitted linear standard curve with HPLC injection of 35 pmol (8.5 mAU), 100 pmol (25.1 mAU), 350 pmol (86.1 mAU), 400 pmol (101 mAU) and 1000 pmol (253 mAU)  $^{19}\text{F}$ -**8.6**. The blue symbols indicate the values obtained from HPLC integration while the blue marks show HPLC absorbance of the **8.6** peak obtained from each radiolabeling reaction.

Labeling #	$^{18}\text{F}$ at BOS (mCi)	$^{19}\text{F}$ -8.6 (nmol)	$^{18}\text{F}$ -8.6 (mCi)	$^{18}\text{F}$ -8.6 (HPLC analysis, mCi)	$^{18}\text{F}$ -8.6 (HPLC analysis, nmol)	Specific activity of EOS (Ci/ $\mu\text{mol}$ )
1	809	75	275	1.82	0.46	3.95
2	765	50	186	2.10	0.51	4.11
3	780	30	106	0.35	0.096	3.64

**Table 8.1** Summary of specific activity measurement of  $^{18}\text{F}$ -8.6.

#### 8.2.4 *In vitro* fluorescent binding assay

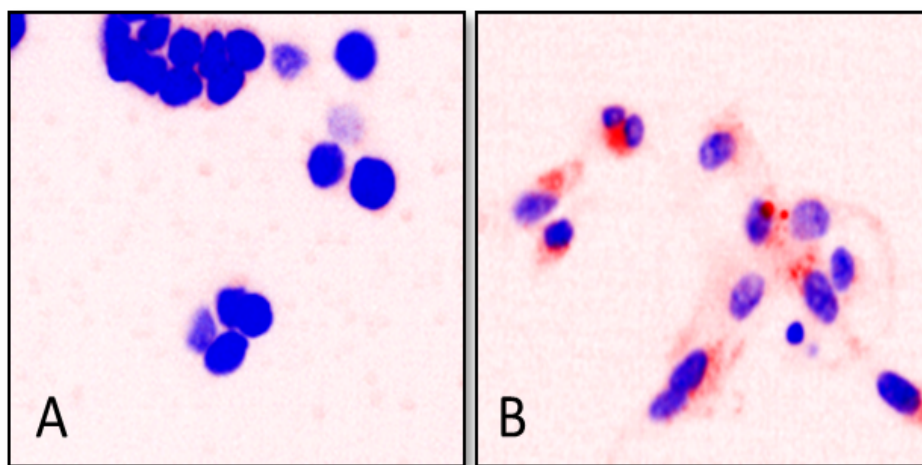


**Figure 8.4** Fluorescent microscopy of  $\alpha_v\beta_3$  integrin binding: **A)** negative control with HT29 cells (8.6 at 960 nM); **B)** positive control with U87M cells. The red exterior is seen in U87M cells as expected. DAPI (blue) stains nuclei in both panels. Cells were washed briefly before plating.

The binding affinity of AMBF<sub>3</sub>-Rhodamine-BisRGD was qualitatively evaluated with fluorescent microscopy assay using two cell lines: **A)** negative control with HT29 cells

(**8.6** at 960 nM); **B**) positive control with U87M cells (480 nM). The red exterior is seen in U87M cells as expected. DAPI (blue) stains nuclei in both panels.

### 8.2.5 *In vivo* imaging

As shown in **Figure 8.5** the radioactivity accumulated notably in the U87M tumor and the uptake was clearly specific as evidenced by reduced signal in the presence of a competitor. To be corroborated with the imaging studies, the average of the tumor uptake based on *ex vivo* biodistribution was  $3.8 \pm 1.2\%$  ID/g (n=3). In contrast, the average uptake of the liver, blood pool, and muscle were  $3.57 \pm 1.19$ ,  $2.17 \pm 1.13$  and  $0.52 \pm 0.25$  %ID/g, respectively. The excretion is predominantly renal with minimal liver uptake. Some unexpected excretion through the gallbladder was noted, as the gallbladder is a known channel for the excretion of highly polar molecules from the body. In addition, the bone uptake is undetectable and there is minimal background activity, resulting in very high contrast images.



**Figure 8.5** PET-CT images: T (tumor), K (kidney), B (bladder), left mouse imaged with **8.6** at 3 Ci/μmol, right mouse imaged with **8.6** at 0.01 Ci/μmol (three-dimension rendering increases appearance of blocking); bottom right inset: pure CT image showing tumors.

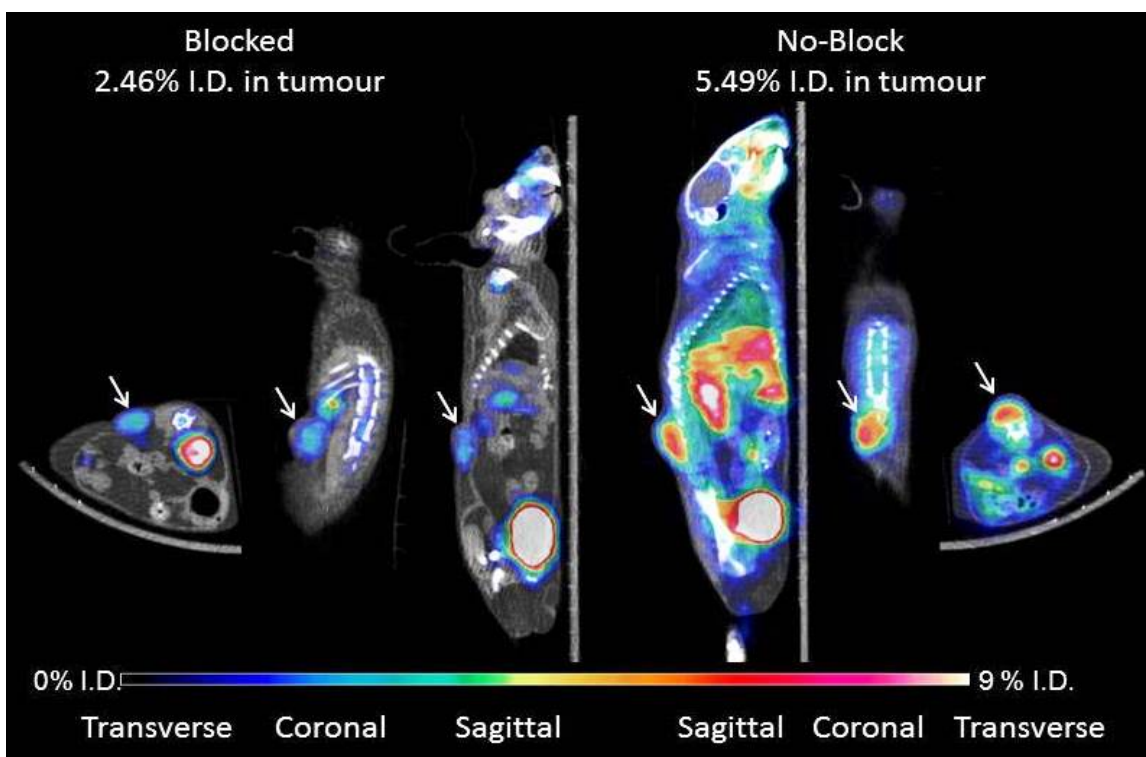


**Figure 8.6** *In vivo* PET/CT imaging of  $^{18}\text{F}$ -**8.6** in blocked mouse (left three images); unblocked mouse (right three images). The white arrows indicate the location of the tumor. For each data set, from left to right the image is transverse section, coronal section and sagittal section, respectively.

## 8.3 Discussion

### 8.3.1 Modular synthesis

The synthetic strategy that is disclosed in this work allows rapid conversion from compound **8.4** to compound **8.6** in 2 days, and results in ~10 mg precursor that can be aliquoted in portions of 30-75 nmol, each of which is then directly used for radiolabelling. RGD was deliberately chosen mainly because of the extensive number of previous studies focused on advancing various labeled RGDs for clinical applications.<sup>7,83,168,178,245</sup> By using RGD, we can avoid uncertainties related to tumor specificity and serum stability and thereby clearly make a comparison with other bisRGD

tracers on the basis of radiosynthetic ease, specific radioactivity, and *in vivo/ex vivo* biological data. Rhodamine was chosen for the fluorescent marker because of its high quantum yield, high molar extinction coefficient, *in vivo* stability, relatively long emission wavelength (compared with  $^{18}\text{F}$ -labeled BODIPY fluorophores),<sup>143,237</sup> and wide utility with microscopes, fluorimeters, and spectrophotometers. For future development, due to the broad applicability and bio-orthogonality, synthon **8.4** would be a powerful tool to rapidly screen other more experimental peptides via fluorescent binding assay and PET imaging. This approach is likely to allow one to replace Rhodamine with other fluorophores. This synthetic approach should also be adaptable to develop a target-specified “vehicle” of toxin/radiotoxin by replacing the fluorophore.<sup>11,246</sup>

### 8.3.2 Dual modal imaging: low/high specific activity

Fluorescence imaging was acquired for portions of the liver, kidney and tumour using a Maestro-2 imaging station. Tissues were analyzed at 568-570 nm with an exposure time of 1 second. Compound **8.6** was evaluated at both low specific activity ( $\sim 0.05$  Ci/ $\mu\text{mol}$ ) and high specific activity ( $\sim 3$  Ci/ $\mu\text{mol}$ ), which are shown in **Figure 8.7**.

As far as we know, fluorescent PET tracers were previously studied at low specific activity ( $\sim 0.05$  Ci/ $\mu\text{mol}$ ) due to the inability to generate such probes at high specific activity with regular labelling methods.<sup>183,235,247,248</sup> However, high specific activity is essential for PET. Generally,  $>1$  Ci/ $\mu\text{mol}$  is necessary to assure microdosing, in accordance with FDA requirements. In order to explore the potential utility of a fluorescent PET tracer at high specific activity, compound **8.6** was radiolabelled at  $\sim 3$  Ci/ $\mu\text{mol}$  and evaluated with both PET and fluorescence imaging. In PET imaging,  $^{18}\text{F}$ -labeled compound **8.6** significantly accumulated in U87M xenografts, and the tumor uptake at 60 min post injection of tracer at high specific activity and at low specific activity were  $8.5 \pm 0.25$  %ID/g and  $2.5 \pm 0.33$  %ID/g, respectively (**Figure 8.6**).

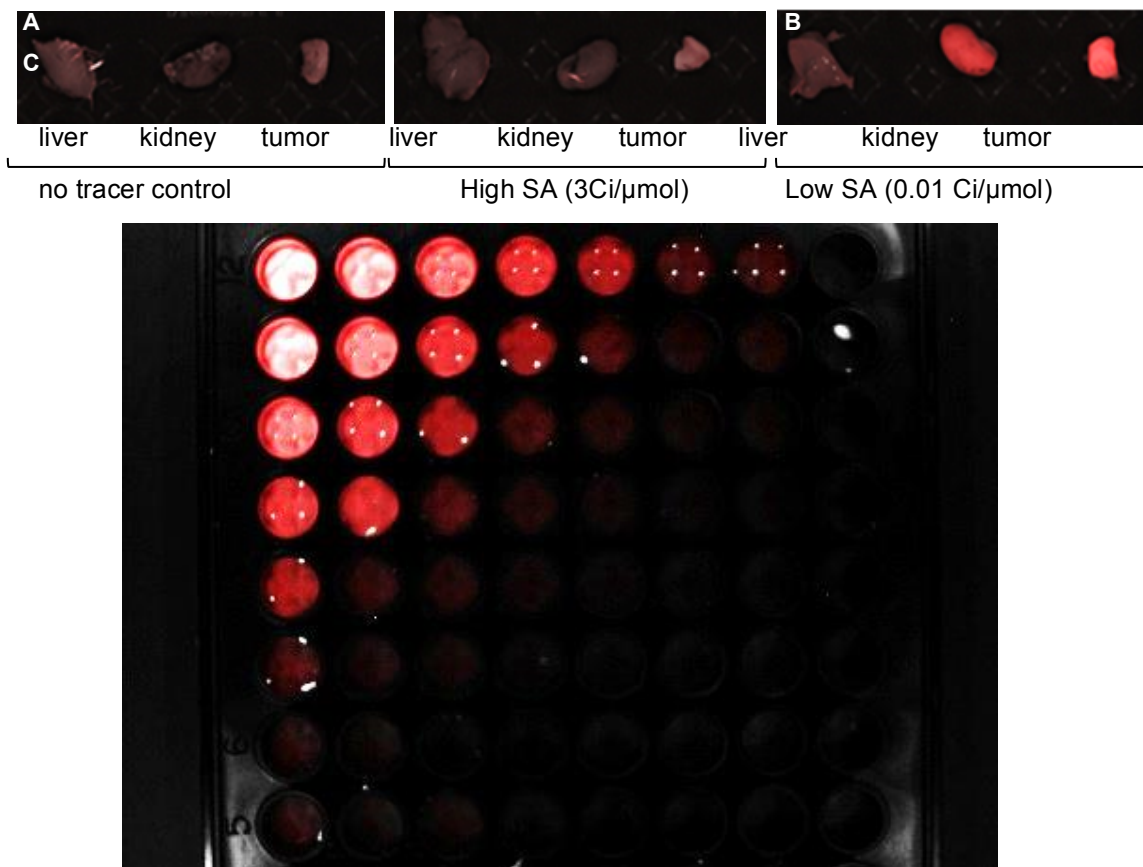


**Figure 8.7** (top): *Ex vivo* fluorescence in organs to which **8.6** clears: liver, kidney, and tumor; **A**: organs from mouse that received no tracer (control); **B**: organs from mouse injected with **8.6** at 3 Ci/ $\mu$ mol; **C**: organs from the mouse injected with **8.6** at 0.01 Ci/ $\mu$ mol. **Figure 8.7** (bottom): Limitation of detection (LOD) measurement. The LOD of our optic scanner is  $\sim$ 20 pmol.

In optical imaging, wonderful fluorescent tumour uptake was detected only in mice injected with low specific activity radiotracer. In contrast, the mice imaged with the high specific activity radiotracer demonstrated nearly invisible fluorescent uptake based on fluorescent optical scanning (**Figure 8.7**). Indeed, this is not unexpected; with 100 mCi injected and uptake of 3.8% ID/g at the time of excision, a tumor of 80 mg contains only 0.3 mCi **8.6** (decay corrected). At 3 Ci/ $\mu$ mol, this equals 100 fmol of tracer ( $\sim$ 1.2 nM in tissue), which is undetectable with a camera designed for tissue imaging (**Table 8.2**). In order to visualize a tumor under both fluorescent images and PET images, the limitations

of fluorescence imaging must be significantly lowered through advances in camera hardware and/or increases in molar extinction coefficient.<sup>11,13,168,246,249-251</sup> Otherwise, specific activities must be lowered to  $\sim 0.05$  Ci/ $\mu\text{mol}$ , which may not ensure the microdosing requirement.

**Table 8.2** Fluorescent radiotracer assessments at high/low specific activity.

<b>Experiment</b>	<b>Unblocking</b>	<b>Blocking</b>
<b>Injection dose</b>	<b>100 <math>\mu\text{Ci}</math></b>	<b>100 <math>\mu\text{Ci}</math></b>
<b>Specific activity</b>	<b>3 Ci/<math>\mu\text{mol}</math></b>	<b>0.01 Ci/<math>\mu\text{mol}</math></b>
<b>Chemical mass injected</b>	<b>33 pmol</b>	<b>10 nmol</b>
<b>Tumour uptake</b>	<b>4%</b>	<b>2.5%</b>
<b>Mass in tumour</b>	<b>105 pmol</b>	<b>20 pmol</b>
<b>Limit of detection</b>	<b>20 pmol</b>	

## 8.4 Conclusion

Notwithstanding the inability to detect fluorescence at very high specific radioactivity, **8.6** compares reasonably well to other PET radiotracers based on RGD.<sup>7,160,252</sup> An extensive body of literature reveals that most RGD-radiosynthesis achieve slightly lower specific radioactivity (0.5-1 Ci/ $\mu\text{mol}$ ), while there is a considerable range of uptake values (0.27-12% ID/g) depending on the specific RGD composition governing clearance. Particular advantages of **8.6** include: (1) one-step, efficient, aqueous, HPLC-free labeling that proceeds in near record rapidity (30 min) with good radiosynthetic yields and high specific radioactivity without dry  $^{18}\text{F}$ -fluoride; (2) rapid clearance that is

predominantly renal with minimal liver uptake; and (3) *in vivo* tumor imaging revealed similar uptake values compared to bisRGD-NOTA-Al-<sup>18</sup>F and 10-fold higher values compared to a previous report outlining a dimeric cRGD comprising of a more traditional linker and an anionic <sup>18</sup>F-ArBF<sub>3</sub><sup>-</sup> prosthetic.<sup>83,113</sup> In addition, though a simultaneous dual-modal detection is not going to be possible so far, this radiosynthetic approach should be readily adaptable to expand the color palate fluorescent radiotracers in a modular and user-friendly manner.

## 8.5 Experimental

### 8.5.1 General information

Reagents and solvents were purchased from Fischer, Sigma-Aldrich, Combi-Blocks, Novabiochem, or Clicktools. Cell lines were purchased from Stemcell and media from Invitrogen. Deuterated solvents were purchased from Cambridge Isotope Laboratories. <sup>18</sup>F-fluoride Trap & Release Columns were purchased from ORTG Inc. (Oakdale, TN) and C18 Sep-Pak cartridges (1cc, 50 mg) were obtained from Waters.

### 8.5.2 Synthesis

#### HPLC Methods

Gradient A: Agilent Eclipse XDB-C18 5 μm 9.2 x 250 mm semi-prep column. Solvent A: 0.1% TFA water; solvent B: MeCN; 0 to 2 min: 0% to 5% B, 2 to 7 min, 5% to 35% B, 7 to 15 min, 35% to 65%, 15 to 20 min, 65% to 100% B. Flow rate: 3 mL/min, column temperature: 19 to 21 °C.

Gradient B: Agilent Eclipse XDB-C18 5 μm 9.2 x 250 mm semi-prep column. Solvent A: 0.1% TFA water; solvent B: MeCN; 0 to 2 min: 5% to 20% B, 2 to 5 min, 20% to 30% B, 5 to 20 min, 30% to 100%, 20 to 22 min, 100% to 5% B. Flow rate: 3 mL/min, column temperature: 19 to 21 °C.

Gradient C: Phenomenex Jupiter 10 μm C18 300Å 4.6 x 250 mm analytical column. Solvent A: 0.1% TFA water; solvent B: MeCN; 0 to 2 min: 5% to 5% B, 2 to 7 min, 5%

to 20% B, 7 to 15 min, 20% to 100%, 15 to 20 min, 100% to 5% B. Flow rate: 2 mL/min, column temperature: 19 to 21 °C.

**Synthesis of 3-(prop-2-yn-1-yloxy)-2,2-bis((prop-2-yn-1-yloxy)methyl) propan-1-ol (compound 8.1):** 2.00 g (14.7 mmol) of pentaerythritol was suspended in DMSO (15 mL). A solution of 40% NaOH (10 mL) was added drop-wise over approximately 30 minutes. A solution of 80% propargyl bromide in toluene (5 mL, 48.0 mmol) was added drop-wise via syringe. The mixture is then stirred overnight for approximately 20 hours. Diethyl ether (100 mL) was added and the ether layer was washed with water (4 x 25 mL). Ether and toluene were then removed via rotary evaporation and the product purified by flash column chromatography (1:1 diethyl ether:petroleum ether). 30.4% yield (1.12 g, 4.47 mmol) <sup>1</sup>H NMR (300 MHz, 25°C, CDCl<sub>3</sub>) δ (ppm) 4.14 (d, J=2.4 Hz, 6H), 3.70 (d, J=6.5 Hz, 2H), 3.57 (s, 6H), 2.42 (t, J=2.4 Hz, 3H); ESI-MS: calculated: 250.3; found: 250.4.

**Synthesis of N,N-dimethyl-2-(3-(prop-2-yn-1-yloxy)-2,2-bis((prop-2-yn-1-yloxy)methyl)propoxy)ethan-1-amine (compound 8.2):** Compound **8.1** (626 mg, 2.50 mmol) was dissolved in DMSO (3 mL) to which 40% NaOH (2 mL) was added. The solution became yellow. The hydrochloride salt of N,N-dimethylaminoethyl chloride (720 mg, 5.00 mmol) was added. The pH was verified by spotting a small amount of the crude reaction on pH paper; we found that the addition of small amounts of excess NaOH was required to ensure alkaline pH (pH > 12). The mixture was stirred for 3 days. A volume of water (25 mL) was added and the product extracted into diethyl ether (3 x 5 mL). The product was then extracted into the aqueous phase from the combined ether extracts with 1M HCl (3 x 5 mL). The combined aqueous extracts were then basified to pH 13 by the addition of concentrated NaOH and the product was extracted into diethyl ether (3 x 5 mL). The ethereal extract was concentrated by rotary evaporation to give the product as yellow oil. 38.3 % yield (308 mg, 0.96 mmol) <sup>1</sup>H NMR (300 MHz, 25°C, CDCl<sub>3</sub>) δ (ppm) 4.11 (d, J=2.4 Hz, 6H), 3.52 (m, 8H), 3.42 (s, 2H), 2.49 (t, J=5.9 Hz, 2H), 2.39 (t, J=2.4 Hz, 3H), 2.26 (s, 6H) <sup>13</sup>C NMR (300 MHz, 25°C, CD<sub>3</sub>CN) δ (ppm) 81.0, 75.6, 70.9, 70.4, 69.9, 59.4, 59.3, 46.2, 45.6; ESI-MS: calculated: 321.2; found; 321.4.

**Synthesis of N,N-dimethyl-2-(3-(prop-2-yn-1-yloxy)-2,2-bis((prop-2-yn-1-yloxy)methyl)propoxy)-N-((4,4,5,5-tetramethyl-1,3,2-dioxaborolan-2-yl)**

**methyl)ethan-1-ammonium iodide (compound 8.3):** Iodomethylpinacolboronate (165 mL, 0.9 mmol) was dissolved in anhydrous diethyl ether (3 mL) in a flame-dried round bottom flask under argon atmosphere. Compound **8.2** (300 mg, 0.93 mmol), isolated as an oil, was re-dissolved in a minimum amount of anhydrous diethyl ether and added via syringe to the solution of iodomethylpinacolboronate. On stirring, the solution became turbid followed by the formation of an anomalous emulsion. Following stirring overnight, the mixture appeared to form two layers: an oil layer on the bottom and a clear ethereal layer on top. The diethyl ether was carefully decanted from the viscous oil on the bottom, and fresh diethyl ether (1 mL) was added and the oil triturated. This trituration procedure, for which a sonicator proved useful, was repeated twice for a total of three times. Following trituration, a much more viscous oil was obtained. The residue was then dried under high vacuum to give a yellow product of a thick gel/glass-like consistency in 91% yield (530mg, 0.82 mmol) <sup>1</sup>H NMR (300 MHz, 25°C, CD<sub>3</sub>CN) δ 4.11 (d, J=2.4 Hz, 6H), 3.79 (br, 2H), 3.56 (t, J=4.6 Hz, 2H), 3.45 (m, 8H), 3.21 (s, 2H), 3.16 (s, 6H), 2.72 (t, J=2.4 Hz, 3H), 1.31 (s, 12H) <sup>13</sup>C NMR (300 MHz, 25°C, CD<sub>3</sub>CN) δ (ppm) 86.4, 80.8, 75.8, 71.2, 69.8, 66.6, 66.0, 59.2, 55.3, 45.2, 24.9; ESI-MS: calculated: 462.2; found: 462.4.

**Synthesis of N-((trifluoroborato)methyl)-N,N-dimethyl-2-(3-(prop-2-yn-1-yloxy)-2,2-bis((prop-2-yn-1-yloxy)methyl)propoxy)ethan-1-ammonium (compound 8.4):** A 1.5 mL Eppendorf tube was charged with DMF (80 μL) into which compound **8.3** (5.0 mg, 8.48 mmol) was dissolved. To this, the following were added in order: 3M KHF<sub>2</sub> (40 mL), 4M HCl (20 mL), and H<sub>2</sub>O (20 mL). The solution was then mixed by vigorous vortexing and left to stand for 20 hours. The reaction was then concentrated to apparent dryness *in vacuo* via speed-vac at 65°C. The residue was then resuspended in 10% MeOH in CH<sub>2</sub>Cl<sub>2</sub> (10 mL) and purified flash silica chromatography (0.3 cm x 5 cm – in a Pasteur pipette), using 10% MeOH/CH<sub>2</sub>Cl<sub>2</sub>. R<sub>f</sub> = 0.57 (10% MeOH/CH<sub>2</sub>Cl<sub>2</sub>) to afford the product in 93.5% yield (3.2 mg, 8.94 mmol) <sup>1</sup>H NMR (300 MHz, 25°C, CDCl<sub>3</sub>) δ (ppm) 4.11 (d, J=2.4 Hz, 6H), 3.84 (t, J=4.4 Hz, 2H), 3.51 (t, J=4.4 Hz, 2H), 3.47 (m, 8H), 3.16 (s, 6H), 2.56 (br, 2H), 2.43 (t, J=2.4 Hz, 3H) <sup>13</sup>C NMR (300 MHz, 25°C, CD<sub>3</sub>CN) δ

(ppm) 80.9, 75.7, 70.9, 69.8, 66.6, 66.3, 59.3, 55.0, 45.4  $^{19}\text{F}$  NMR (300 MHz, 25°C,  $\text{CDCl}_3$ )  $\delta$  (ppm) -139.7; ESI-MS: calculated 403.2; found: 403.3.

**Synthesis of Rhodamine-bisalkynyl- $^{19}\text{F}$ -BF $_3$  (compound 8.5):** This reaction was run several times at the scale reported here. A 1.5 mL Eppendorf tube was charged with compound **8.4** (10 mg, 24.5  $\mu\text{mol}$ ), Rhodamine-triethyleneglycol-bis-sulfonate-568-azide (Click tools:  $\epsilon = 100000 \text{ M}^{-1}\text{cm}^{-1}$ ) (5 mg, 6.6  $\mu\text{mol}$ ), aqueous  $\text{CuSO}_4$  (1.0 M, 5 mL), and sodium ascorbate (1.0 M, 12.5 mL) and (5%  $\text{NH}_4\text{OH}$  in  $\text{MeCN}:\text{H}_2\text{O}$  1:1, 50 mL). This mixture was reacted at 45 °C for 2 hours and then directly loaded onto a semi-preparative HPLC column and purified (Gradient A,  $T_R = 12.1$  min) to yield chemically pure Rhodamine-bisalkynyl- $^{19}\text{F}$ -BF $_3$  in 59% yield (4.5 mg, 3.9  $\mu\text{mol}$ ). The fractions containing **8.5** were pooled and the concentration was determined by first measuring the absorbance at 568 nm and divided by the molar extinction coefficient. Portions corresponding to 1  $\mu\text{mol}$  were lyophilized *in vacuo* and stored as aliquots at -20 °C for further conjugation. ESI-MS: Calculated: 1161.49; Obtained: 1161.5.

**Synthesis of Rhodamine-bisRGD- $^{19}\text{F}$ -BF $_3$  (compound 8.6):** Several reactions were carried out under identical conditions below to provide 1 milligram of **8.6** as needed. For a typical reaction, in a 1.5 mL Eppendorf tube, compound **8.5** (1.2 mg, 1.0  $\mu\text{mol}$ ) is dissolved in 5%  $\text{NH}_4\text{OH}$  in  $\text{MeCN}/\text{H}_2\text{O}=1:1$  (30  $\mu\text{L}$ ). To this is added RGD-azide (3 mg, 4.8  $\mu\text{mol}$  in water),  $\text{CuSO}_4$  (1.0 M in water, 3 mL), and sodium ascorbate (1.0 M in water, 8.5 mL). This mixture is allowed to react at 45 °C for 2 hours, and then directly loaded onto a semipreparative HPLC column and purified by HPLC (Gradient B,  $T_R = 11.2$  min), to yield chemically pure Rhodamine-bisRGD- $^{19}\text{F}$ -BF $_3$  in 41% yield (1 mg, 0.41  $\mu\text{mol}$ ). The identity and purity was confirmed with MALDI-TOF (See **Figure 8.8**): Calculated: 2421.1; Found: 2421.3. Following lyophilization, the solution was resuspended in ethanol (200  $\mu\text{L}$ ) to give a solution of 2.1 mM. Following serial dilutions, the concentration was confirmed by UV-vis spectrophotometry using the extinction coefficient of at 568 nm. Aliquots of 50 nmol (121 mg) or 75 nmol (181 mg) were prepared, lyophilized and stored at -20° C for further use.

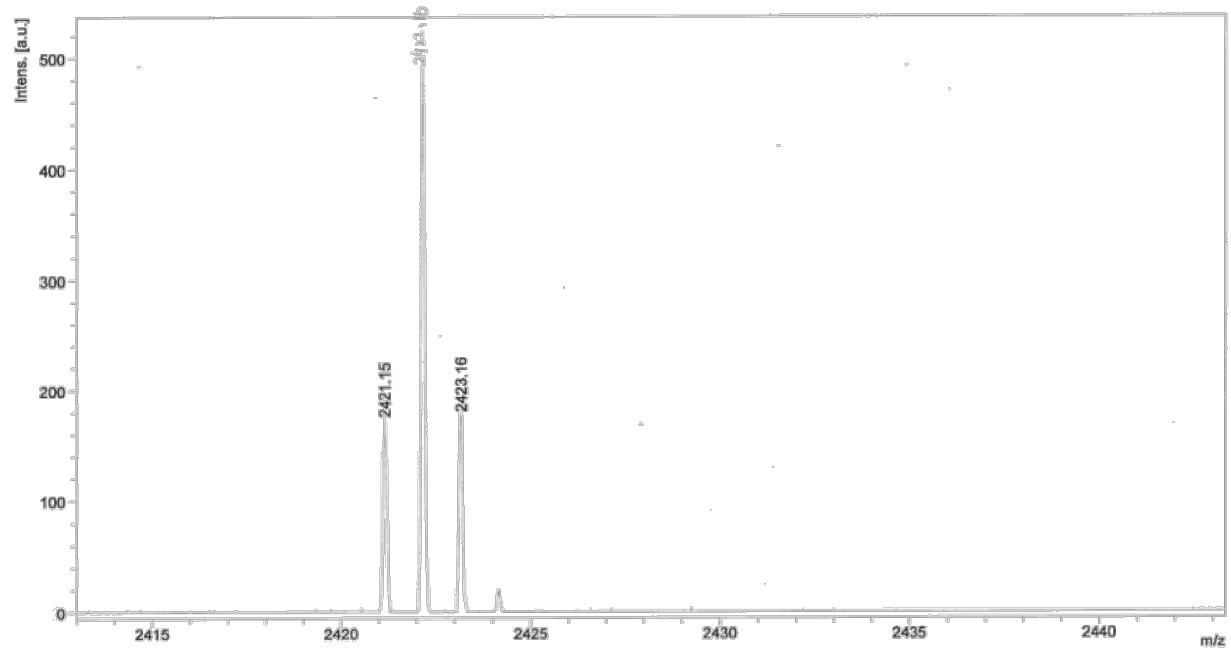


**Figure 8.8:** MALDI-TOF analysis of unlabeled **8.6**: three peaks were seen at 2421.15, 2422.10 and 2423.16.

### 8.5.2 Cell based assay

HT29 cells are grown in McCoy 5A media with 10% FBS, and 2mM L-glutamine. U87M cells were grown in DMEM supplemented with 10% FBS and 2mM L-glutamine. For visualization by fluorescent microscopy, cells in 10% fetal calf serum (100  $\mu$ L) were incubated in the presence of **8.6** (480 nM for U87M cells, positive control; or 960 nM for HT29 cells, negative control). Following 1 hour, the cells were briefly washed twice with fresh serum and visualized at 20x using a Lecia 6000B microscope.

### 8.5.3 Serum stability assay

This protocol follows our previous reports that were developed for labeled bombesin. Here, labeled **8.6**, (~2 mCi) in 50% PBS-EtOH was further diluted in saline buffer (0.5 mL). For each assay, the saline solution (100  $\mu$ L) was mixed with plasma (100  $\mu$ L), incubated at 37 °C for 0, 60, and 120 min, and quenched by the addition of 75% aqueous CH<sub>3</sub>CN (400  $\mu$ L). The resulting mixture was vortexed and then centrifuged to precipitate insoluble components. The supernatant was then decanted, filtered (0.22  $\mu$ m), and analyzed by HPLC (Gradient C) as shown in **Figure 8.2** which indicates that there is no detectable defluorination ( $T_R \sim 4$  min) or other degradation products.

### 8.5.4 Animal care and *in vivo* image acquisition

The methods used here are nearly identical to those we previously reported for imaging RGD in U87M xenograft tumors. Briefly, all animal studies were performed in accordance with the Canadian Council on Animal Care Guidelines and were reviewed and approved by the University of British Columbia Animal Care Committee. Rag2M mice (8–11 weeks old, bred in-house at the BC Cancer Research Agency) were subcutaneously inoculated with U87MG (human glioblastoma) cells into the lower back ( $5 \times 10^6$  cells). The tumors were grown to a suitable size ( $\sim 100$  mm<sup>3</sup>) within approximately two weeks and were measured by calipers. Mice were anesthetized by 2% isoflurane inhalation. For biodistribution studies in mice with tumors, the tracer was injected via the lateral tail vein with a catheter while mice were under anesthesia. Eight mice were used, four of which were set aside for a partial blocking experiment where they received 100  $\mu$ Ci of **8.6** at 0.01 Ci/ $\mu$ mol while four received 100  $\mu$ Ci of **8.6** at 3 Ci/ $\mu$ mol. Prior to *ex vivo* biodistribution, one set of paired, tumor-bearing mice (unblocked and partially blocked) were imaged using the Siemens Inveon multimodality small animal PET/CT scanner to evaluate the tumor-to-non-target-tissue contrast for the tracer. A 10 min CT attenuation scan followed by a 120 min Dynamic PET scan was carried out. The list-mode data were histogrammed and reconstructed by an iterative reconstruction algorithm (3D OSEM/MAP) using the Inveon Acquisition Workplace Software (Siemens), applying normalization, dead time, random, and attenuation

correction. The attenuation correction map was obtained from the CT scan data. Images representing pure-PET are shown here to demonstrate the lack of bone uptake (**Figure 8.9**) while combined PET-CT were acquired (3% CT overlaid on 97% PET as shown in **Figure 8.5**). A 2D image with proper scaling is shown in **Figure 8.6**. Time activity curves were also generated using the images with ROIs placed in the tissue of interest. These are shown in **Figure 8.10** herein.

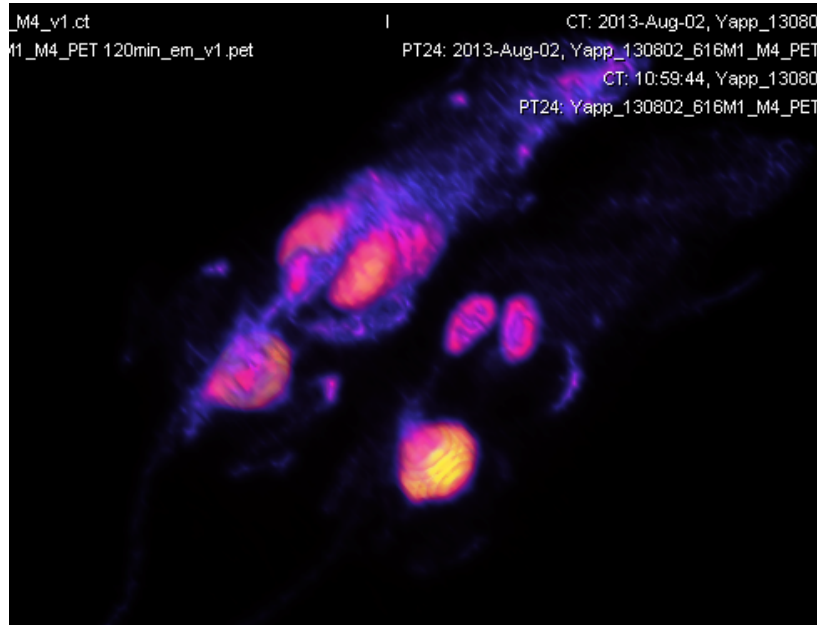


**Figure 8.9:** Pure PET image: left mouse shows minimal bone uptake in a pure-PET image (no CT overlay). While small amounts of uptake are seen in the knee joints and lower spine and skull, these are completely blocked in the right mouse suggesting that bone uptake may reflect presence of the integrin receptor in marrow and/or bone.

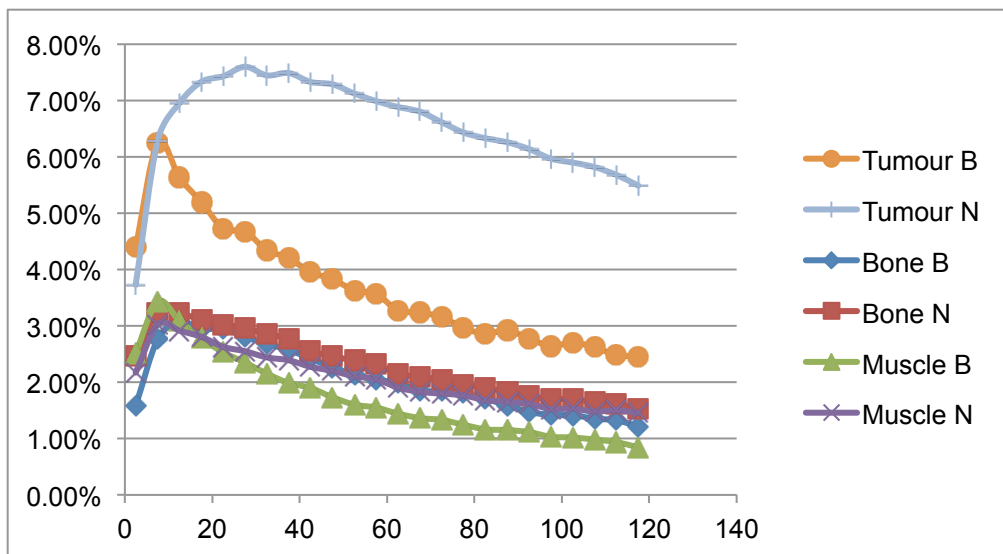


**Figure 8.10:** TACs (Time Activity Curves) from each of the imaged mice (n = 3): B = blocked, N = non-blocked.

### 8.5.5 *In vivo* biodistribution analysis

These methods largely follow our previous reports on RGD and dimeric versions thereof. Briefly, following scanning, all mice were humanely euthanized by isoflurane overdose followed by CO<sub>2</sub> inhalation and tissues/organs of interest were collected, rinsed in PBS, patted dry and counted in a gamma counter (Cobra-II Auto Gamma, Canberra Packard Canada). The tissue weight and associated cpm (counts per min.) were used to calculate the percentage of injected dose per gram of tissue (%ID/g) with decay correction. The *ex vivo* biodistribution data are shown in **Figure 8.11** In order to use sufficient chemical amounts of **8.6** for fluorescence detection yet still achieve respectable uptake of 2.6% ID/g, we intentionally administered **8.6** at low specific activity: 0.01 Ci/ $\mu$ mol (10 nmol, 24 mg). This resulted in only a partial blocking experiment (typically for good blocking one needs to use >100 mg to achieve statistically significant blocking). Hence errors on tumor uptake are not expected to be statistically significant.

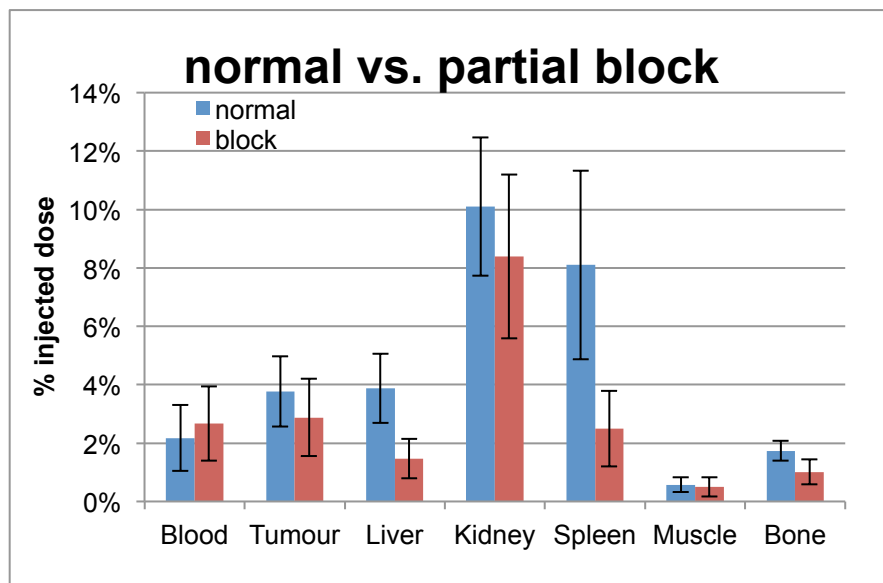


**Figure 8.11:** *In vivo* biodistribution analysis (n = 3) for all mice from which organs were collected and analyzed %ID/g at 120 min. Error bars are shown however blocking is not expected because typically to achieve statistically significant blocking ratios, >100  $\mu\text{g}$  per mouse must be used. Instead we wished to show that reasonable tumor uptake values can be achieved at specific activities as low as 0.01 Ci/ $\mu\text{mol}$  (~20  $\mu\text{g}$ ) which is not enough to achieve blocking.

## Chapter 9: Conclusion and Future Work

### 9.1 Summary

In conclusion, a broad applicable and clinical relative  $^{18}\text{F}$ -labeling method is established and presented. Although I have worked on other projects, they are not included in this thesis, as they await other results as well as consideration for patents.

In Chapter 2, I synthesized and evaluated a number of kinetically stable aryl/organotrifluoroborates under *in vivo* conditions. The *in vivo* stability of all radiosynths is essential. Therefore, significant efforts have been expended at developing new organotrifluoroborate radioprosthesis of high stability: a) Synthesis and conjugation of organotrifluoroborates radiosynths; b) Assess the hydrolytic stability of organotrifluoroborates by using  $^{19}\text{F}$ -NMR study; c) Evaluate the *in vitro* stability by incubating  $^{18}\text{F}$ -labelled organotrifluoroborates in mice plasma; and d) Biological evaluation of conjugated  $^{18}\text{F}$ -organotrifluoroborates in living animals. In the end, two new organotrifluoroborates were identified owing to their extraordinarily high *in vivo* stability.

Chapter 3 outlined a linear free energy analysis of nonaromatic organotrifluoroborates. In this chapter, the goal is to address a practical method to estimate the hydrolytic stability of alkyltrifluoroborates. Towards this end, assorted alkyltrifluoroborates have been synthesized and even more have been studied using  $^{19}\text{F}$ -NMR analysis. Consequently, an unexpected linear correlation is discovered between the hydrolytic stability and the acidity of the corresponding acetic acid. This discovery is of fundamental importance, for both Suzuki-Miyaura coupling and new organotrifluoroborates radiotracer design.

Chapter 4 and Chapter 5 discussed a direct  $^{18}\text{F}$ -fluorination at extraordinary high specific activity. A fluorescent screen was developed to identify conditions for achieving high specific activity. These conditions include: solvent, pH, buffer, temperature, and the use of reduced pressure. The results of the aforementioned fluorescent screen were verified in a radiochemical context by using no-carrier added (NCA)  $^{18}\text{F}$ -fluoride to prepare radiolabelled  $^{18}\text{F}\text{-ArBF}_3^-$ . The radiochemically pure, fluorescent  $^{18}\text{F}\text{-ArBF}_3^-$  was HPLC

purified and by virtue of the appended fluorophore, we were able to directly measure the specific activity. Consequently, the specific activity was measured to be 15 Ci/ $\mu\text{mol}$ , which is about a magnitude higher than normal maximum. In addition, a new labeling method was invented based on  $^{18}\text{F}$ - $^{19}\text{F}$  isotope-exchange. Given the operational simplicity, all of the procedures can be completed in a shielded hot cell. By exploiting this fact, Curie-level radioactivity was utilized for the radiosynthesis of  $^{18}\text{F}$ -organotrifluoroborates and subsequently high specific activity was achieved. Lastly, *in vivo* PET imaging of  $^{18}\text{F}$ -ArBF<sub>3</sub>-bioconjugates was performed at high specific activity.

Chapter 6 demonstrated a facile and broadly applicable  $^{18}\text{F}$ -fluoridation for PET imaging is developed: This radiochemistry does not need either the preparation of dry  $^{18}\text{F}$ -fluoride or HPLC purification, and can be simply performed under production level radioactivity with low-level hand dose. Therefore, this method of  $^{18}\text{F}$ -ArBF<sub>3</sub><sup>-</sup> synthesis is readily suitable for automated synthesizers and microfluidic development. Its operational simplicity and high *in vivo* performance is of high interest for PET chemists.

Chapter 7 demonstrated a preclinical evaluation of a novel  $^{18}\text{F}$ -Labelled somatostatin receptor-binding peptide. In light of the long-standing interest in mapping sstr2 expression with PET imaging, we conjugated the new alkyltrifluoroborate to octreotate to give  $^{19}\text{F}$ -AMBF<sub>3</sub>-TATE, which can be  $^{18}\text{F}$ -labeled in one step to produce a promising sstr2 PET tracer. To our surprise, TATE-AMBF<sub>3</sub> exhibited approximately 30-fold higher affinity than other octreotide analogs. This new TATE analog is easily  $^{18}\text{F}$ -labeled in record rapidity to provide a promising PET tracer for imaging sstr2-mediated cancers. Total synthesis, radiosynthesis, and *in vivo* properties are discussed in this chapter.

Chapter 8 discussed a dual function probe for PET and fluorescence imaging. To embrace the increasing interest in dual-modal PET fluorescent tracers, here we disclose for the first time a radiosynthetic strategy that amalgamates a dimeric peptide, a fluorophore, and a facile  $^{18}\text{F}$ -labelling. This construct not only successfully provides fluorescent imaging for a binding affinity assay, but also is labeled in high radiochemical yield and at high specific activity as a “kit”, as well as specifically targeting the tumor in *in vivo* PET imaging and in *ex vivo* optical imaging.

In a final concluding thought, I believe that within the scope of only 4 years, I have addressed four important challenges for using  $^{18}\text{F}$ -prosthetics in clinical studies: these are 1) demonstrating record high specific activities in record-short labeling times; 2) developing an isotope exchange reaction that would enable use of clinical-grade quantities of fluoride in an HPLC-free labeling method; 3) identification of 2 new radioprosthetics along with a relationship that now teaches others how to prepare such prosthetics; and 4) assembling all of these discoveries around TATE in a preclinical study that sets the stage for first-in-man studies. These are currently underway and should bring this work to completion for the using boron as a radiotracer in clinic for the first time.

## References

- (1) Zhu, L.; Ploessl, K.; Kung, H. F. *Science* **2013**, *342*, 429.
- (2) Price, E. W.; Orvig, C. *Chem. Soc. Rev.* **2014**, *43*, 260.
- (3) Aina, O. H.; Liu, R. W.; Sutcliffe, J. L.; Marik, J.; Pan, C. X.; Lam, K. S. *Mol. Pharm.* **2007**, *4*, 631.
- (4) Gagnon, M. K. J.; Hausner, S. H.; Marik, J.; Abbey, C. K.; Marshall, J. F.; Sutcliffe, J. L. *Proc. Natl. Acad. Sci.* **2009**, *106*, 17904.
- (5) Lee, S.; Xie, J.; Chen, X. Y. *Biochemistry* **2009**, *49*, 1364.
- (6) Lee, S.; Xie, J.; Chen, X. Y. *Chem. Rev.* **2010**, *110*, 3087.
- (7) Liu, S. *Bioconjug. Chem.* **2009**, *20*, 2199.
- (8) Serdons, K.; Verbruggen, A.; Bormans, G. M. *Methods* **2009**, *48*, 104.
- (9) Azhdarinia, A.; Wilganowski, N.; Robinson, H.; Ghosh, P.; Kwon, S.; Lazard, Z. W.; Davis, A. R.; Olmsted-Davis, E.; Sevic-Muraca, E. M. *Biorg. Med. Chem.* **2011**, *19*, 3769.
- (10) Banerjee, S. R.; Pullambhatla, M.; Byun, Y.; Nimmagadda, S.; Foss, C. A.; Green, G.; Fox, J. J.; Lupold, S. E.; Mease, R. C.; Pomper, M. G. *Angew. Chem. Int. Ed.* **2011**, *50*, 9167.
- (11) Cheng, Z.; Wu, Y.; Xiong, Z. M.; Gambhir, S. S.; Chen, X. Y. *Bioconjug. Chem.* **2005**, *16*, 1433.
- (12) Qin, Z. T.; Hall, D. J.; Liss, M. A.; Hoh, C. K.; Kane, C. J.; Wallace, A. M.; Vera, D. R. *J. Biomed. Opt.* **2013**, *18*.
- (13) Nahrendorf, M.; Keliher, E.; Marinelli, B.; Waterman, P.; Feruglio, P. F.; Fexon, L.; Pivovarov, M.; Swirski, F. K.; Pittet, M. J.; Vinegoni, C.; Weissleder, R. *Proc. Natl. Acad. Sci.* **2010**, *107*, 7910.
- (14) Contag, C. H.; Bachmann, M. H. *Annu. Rev. Biomed. Eng.* **2002**, *4*, 235.
- (15) Mather, S. J. *Mol. Biosyst.* **2007**, *3*, 30.
- (16) Czernin, J.; Phelps, M. E. *Annu. Rev. Med.* **2002**, *53*, 89.
- (17) Alberini, J. L.; Edeline, V.; Giraudet, A. L.; Champion, L.; Paulmier, B.; Madar, O.; Poinignon, A.; Bellet, D.; Pecking, A. P. *J. Surg. Oncol.* **2011**, *103*, 602.

- (18) Worsley, D. F.; Wilson, D. C.; Powe, J. E.; Benard, F. *Canadian Association of Radiologists Journal-Journal De L Association Canadienne Des Radiologistes* **2010**, *61*, 13.
- (19) Liu, S. L.; Lin, T. P.; Li, D.; Leamer, L.; Shan, H.; Li, Z. B.; Gabbai, F. P.; Conti, P. S. *Theranostics* **2013**, *3*, 181.
- (20) Lee, J.; Zylka, M. J.; Anderson, D. J.; Burdette, J. E.; Woodruff, T. K.; Meade, T. J. *J. Am. Chem. Soc.* **2005**, *127*, 13164.
- (21) Louie, A. Y.; Huber, M. M.; Ahrens, E. T.; Rothbacher, U.; Moats, R.; Jacobs, R. E.; Fraser, S. E.; Meade, T. J. *Nat. Biotechnol.* **2000**, *18*, 321.
- (22) Yu, M. K.; Kim, D.; Lee, I. H.; So, J. S.; Jeong, Y. Y.; Jon, S. *Small* **2011**, *7*, 2241.
- (23) Price, E. W.; Zeglis, B. M.; Cawthray, J. F.; Ramogida, C. F.; Ramos, N.; Lewis, J. S.; Adam, M. J.; Orvig, C. *J. Am. Chem. Soc.* **2013**, *135*, 12707.
- (24) Hicks, R. J.; Hofman, M. S. *Nature Reviews Clinical Oncology* **2012**, *9*, 712.
- (25) Pauwels, E. K. J.; Bergstrom, K.; Mariani, G.; Kairemo, K. *Curr. Pharm. Des.* **2009**, *15*, 928.
- (26) Kung, M.-P.; Kung, H. F. *Nucl. Med. Biol.* **2005**, *32*, 673.
- (27) Rahmim, A.; Zaidi, H. *Nucl. Med. Commun.* **2008**, *29*, 193.
- (28) Rosenthal, M. S.; Cullom, J.; Hawkins, W.; Moore, S. C.; Tsui, B. M.; Yester, M. *J. Nucl. Med.* **1995**, *36*, 1489.
- (29) Newswire, P. *MarketsandMarkets:* **2011**, <http://www.prnewswire.com/news>.
- (30) Huebner, R. H.; Park, K. C.; Shepherd, J. E.; Schwimmer, J.; Czernin, J.; Phelps, M. E.; Gambhir, S. S. *J. Nucl. Med.* **2000**, *41*, 1177.
- (31) Schwimmer, J.; Essner, R.; Patel, A.; Jahan, S. A.; Shepherd, J. E.; Park, K.; Phelps, M. E.; Czernin, J.; Gambhir, S. S. *Q. J. Nucl. Med.* **2000**, *44*, 153.
- (32) Ametamey, S. A.; Honer, M.; Schubiger, P. A. *Chem. Rev.* **2008**, *108*, 1501.
- (33) Carlucci, G.; Ananias, H. J. K.; Yu, Z.; Hoving, H. D.; Helfrich, W.; Dierckx, R.; Liu, S.; de Jong, I. J.; Elsinga, P. H. *Mol. Pharm.* **2013**, *10*, 1716.
- (34) Anderson, C. J.; Welch, M. J. *Chemical Reviews* **1999**, *99*, 2219.

- (35) Hooker, J. M. *Curr. Opin. Chem. Biol.* **2010**, *14*, 105.
- (36) Cai, L. S.; Lu, S. Y.; Pike, V. W. *European J. Org. Chem.* **2008**, 2853.
- (37) Okarvi, S. M. *Eur. J. Nucl. Med.* **2001**, *28*, 929.
- (38) Day, K. E.; Sweeny, L.; Kulbersh, B.; Zinn, K. R.; Rosenthal, E. L. *Mol. Imaging Biol.* **2013**, *15*, 722.
- (39) Selvaraj, R.; Fox, J. M. *Curr. Opin. Chem. Biol.* **2013**, *17*, 753.
- (40) Zheng, Q. H.; Fei, X.; DeGrado, T. R.; Wang, J. Q.; Stone, K. L.; Martinez, T. D.; Gay, D. J.; Baity, W. L.; Mock, B. H.; Glick-Wilson, B. E.; Sullivan, M. L.; Miller, K. D.; Sledge, G. W.; Hutchins, G. D. *Nucl. Med. Biol.* **2003**, *30*, 753.
- (41) Zheng, Q. H.; Fei, X.; Liu, X.; Wang, J. Q.; Bin Sun, H.; Mock, B. H.; Lee Stone, K.; Martinez, T. D.; Miller, K. D.; Sledge, G. W.; Hutchins, G. D. *Nucl. Med. Biol.* **2002**, *29*, 761.
- (42) Zheng, Q. H.; Fei, X.; Liu, X.; Wang, J. Q.; Stone, K. L.; Martinez, T. D.; Gay, D. J.; Baity, W. L.; Miller, K. D.; Sledge, G. W.; Hutchins, G. D. *Nucl. Med. Biol.* **2004**, *31*, 77.
- (43) Boros, E.; Ferreira, C. L.; Cawthray, J. F.; Price, E. W.; Patrick, B. O.; Wester, D. W.; Adam, M. J.; Orvig, C. *J. Am. Chem. Soc.* **2010**, *132*, 15726.
- (44) Ramogida, C. F.; Orvig, C. *Chem. Commun.* **2013**, *49*, 4720.
- (45) Zhan, C. G.; Dixon, D. A. *J. Phys. Chem. A* **2004**, *108*, 2020.
- (46) Olberg, D. E.; Cuthbertson, A.; Solbakken, M.; Arukwe, J. M.; Qu, H.; Kristian, A.; Bruheim, S.; Hjelstuen, O. K. *Bioconjug. Chem.* **2010**, *21*, 2297.
- (47) Olberg, D. E.; Hjelstuen, O. K.; Solbakken, M.; Arukwe, J.; Karlsen, H.; Cuthbertson, A. *Bioconjug. Chem.* **2008**, *19*, 1301.
- (48) Bergman, J.; Eskola, O.; Lehtikoinen, P.; Solin, O. *Appl. Radiat. Isot.* **2001**, *54*, 927±933.
- (49) Breyholz, H. J.; Wagner, S.; Levkau, B.; Schober, O.; Schafers, M.; Kopka, K. *Q. J. Nucl. Med. Mol. Imaging.* **2007**, *51*, 24.
- (50) Glaser, M.; Karlsen, H.; Solbakken, M.; Arukwe, J.; Brady, F.; Luthra, S. K.; Cuthbertson, A. *Bioconjug. Chem.* **2004**, *15*, 1447.
- (51) Guo, N.; Lang, L. X.; Li, W. H.; Kiesewetter, D. O.; Gao, H. K.; Niu, G.; Xie, Q. G.; Chen, X. Y. *PLoS One* **2012**, *7*.

- (52) Jeon, J.; Shen, B.; Xiong, L.; Miao, Z.; Lee, K. H.; Rao, J.; Chin, F. T. *Bioconjug. Chem.* **2012**, *23*, 1902.
- (53) Lasne, M. C.; Perrio, C.; Rouden, J.; Barre, L.; Roeda, D.; Dolle, F.; Crouzel, C. *Contrast Agents II Topics in Current Chemistry* **2002**, *222*, 201.
- (54) Lee, E.; Hooker, J. M.; Ritter, T. *Journal of the American Chemical Society* **2012**, *134*, 17456.
- (55) Huiban, M.; Tredwell, M.; Mizuta, S.; Wan, Z.; Zhang, X.; Collier, T. L.; Gouverneur, V.; Passchier, J. *Nat. Chem.* **2013**, *5*, 941.
- (56) Becaud, J.; Mu, L. J.; Karamkam, M.; Schubiger, P. A.; Ametamey, S. M.; Graham, K.; Stellfeld, T.; Lehmann, L.; Borkowski, S.; Berndorff, D.; Dinkelborg, L.; Srinivasan, A.; Smits, R.; Kokschi, B. *Bioconjug. Chem.* **2009**, *20*, 2254.
- (57) Hoehne, A.; Mu, L.; Honer, M.; Schubiger, P. A.; Ametamey, S. M.; Graham, K.; Stellfeld, T.; Borkowski, S.; Berndorff, D.; Klar, U.; Voigtmann, U.; Cyr, J. E.; Friebe, M.; Dinkelborg, L.; Srinivasan, A. *Bioconjug. Chem.* **2008**, *19*, 1871.
- (58) Hohne, A.; Yu, L.; Mu, L. J.; Reiher, M.; Voigtmann, U.; Klar, U.; Graham, K.; Schubiger, P. A.; Ametamey, S. M. *Chem. Eur. J.* **2009**, *15*, 3736.
- (59) Mu, L. J.; Hohne, A.; Schubiger, R. A.; Ametamey, S. M.; Graham, K.; Cyr, J. E.; Dinkelborg, L.; Stellfeld, T.; Srinivasan, A.; Voigtmann, U.; Klar, U. *Angewandte Chemie International English Edition* **2008**, *47*, 4922.
- (60) Mu, L. J.; Hohne, A.; Schubiger, R. A.; Ametamey, S. M.; Graham, K.; Cyr, J. E.; Dinkelborg, L.; Stellfeld, T.; Srinivasan, A.; Voigtmann, U.; Klar, U. *Angew. Chem. Int. Ed.* **2008**, *47*, 4922.
- (61) Ross, T. L.; Honer, M.; Muller, C.; Groehn, V.; Schibli, R.; Ametamey, S. M. *J. Nucl. Med.* **2010**, *51*, 1756.
- (62) Gao, Z.; Gouverneur, V.; Davis, B. G. *Journal of the American Chemical Society* **2013**, *135*, 13612.
- (63) Carroll, L.; Boldon, S.; Bejot, R.; Moore, J. E.; Declerck, J.; Gouverneur, V. *Org. Biomol. Chem.* **2011**, *9*, 136.
- (64) Schirmacher, R.; Wangler, C.; Schirmacher, E. *Mini Rev. Org. Chem.* **2007**, *4*, 317.
- (65) Huang, H. F.; Liang, K.; Liu, Y. P.; Huang, S. T.; Chu, T. W. *Progress in Chemistry* **2011**, *23*, 1501.
- (66) Smith, G. E.; Sladen, H. L.; Biagini, S. C. G.; Blower, P. J. *Dalton Transactions* **2011**, *40*, 6196.

- (67) Wangler, B.; Schirmacher, R.; Bartenstein, P.; Wangler, C. *Mini-Rev. Med. Chem.* **2011**, *11*, 968.
- (68) Dijkgraaf, I.; Franssen, G. M.; McBride, W. J.; D'Souza, C. A.; Laverman, P.; Smith, C. J.; Goldenberg, D. M.; Oyen, W. J. G.; Boerman, O. C. *J. Nucl. Med.* **2012**, *53*, 947.
- (69) Kostikov, A. P.; Chin, J.; Orchowski, K.; Niedermoser, S.; Kovacevic, M. M.; Aliaga, A.; Jurkschat, K.; Wangler, B.; Wangler, C.; Wester, H. J.; Schirmacher, R. *Bioconjug. Chem.* **2012**, *23*, 106.
- (70) Wangler, C.; Niedermoser, S.; Chin, J. S.; Orchowski, K.; Schirmacher, E.; Jurkschat, K.; Iovkova-Berends, L.; Kostikov, A. P.; Schirmacher, R.; Wangler, B. *Nat. Protoc.* **2012**, *7*, 1946.
- (71) McBride, W. J.; D'Souza, C. A.; Sharkey, R. M.; Karacay, H.; Rossi, E. A.; Chang, C. H.; Goldenberg, D. M. *Bioconjug. Chem.* **2010**, *21*, 1331.
- (72) D'Souza, C. A.; McBride, W. J.; Sharkey, R. M.; Todaro, L. J.; Goldenberg, D. M. *Bioconjug. Chem.* **2011**, *22*, 1793.
- (73) McBride, W. J.; D'Souza, C. A.; Karacay, H.; Sharkey, R. M.; Goldenberg, D. M. *Bioconjug. Chem.* **2012**, *23*, 538.
- (74) Bergman, J.; Eskola, O.; Lehtikoinen, P.; Solin, O. *Appl. Radiat. Isot.* **2001**, *54*, 927.
- (75) Eckelman, W. C.; Bonardi, M.; Volkert, W. A. *Nucl. Med. Biol.* **2008**, *35*, 523.
- (76) Berridge, M. S.; Apana, S. M.; Hersh, J. M. *J. Labelled Comp. Radiopharm.* **2009**, *52*, 543.
- (77) Zhang, X. Z.; Cai, W. B.; Cao, F.; Schreiber, E.; Wu, Y.; Wu, J. C.; Xing, L.; Chen, X. Y. *J. Nucl. Med.* **2006**, *47*, 492.
- (78) Breeman, W. A. P.; Kwekkeboom, D. J.; Kooij, P. P. M.; Bakker, W. H.; Hofland, L. J.; Visser, T. J.; Ensing, G. J.; Lamberts, S. W. J.; Krenning, E. P. *J. Nucl. Med.* **1995**, *36*, 623.
- (79) de Goeij, J. J. M.; Bonardi, M. L. *J. Radioanal. Nucl. Chem.* **2005**, *263*, 13.
- (80) Ding, Y. S.; Fowler, J. S.; Gately, S. J.; Dewey, S. L.; Wolf, A. P.; Schlyer, D. J. *J. Med. Chem.* **1991**, *34*, 861.
- (81) Lapi, S. E.; Welch, M. J. *Nucl. Med. Biol.* **2012**, *39*, 601.

- (82) Liu, Z.; Li, Y.; Lozada, J.; Lin, K.-S.; Schaffer, P.; Perrin, D. M. *J. Labeled Compounds and Radiopharmaceuticals* **2012**, *14*, 491.
- (83) Liu, Z.; Li, Y.; Lozada, J.; Wong, M. Q.; Greene, J.; Lin, K.-S.; Yapp, D.; Perrin, D. M. *Nucl. Med. Biol.* **2013**, *40*, 841.
- (84) Macgregor, R. R.; Schlyer, D. J.; Fowler, J. S.; Wolf, A. P.; Shiue, C. Y. *J. Nucl. Med.* **1987**, *28*, 60.
- (85) Warashina, M.; Kuwabara, T.; Nakamatsu, Y.; Taira, K. *Chem. Biol.* **1999**, *6*, 237.
- (86) Li, Y.; Ting, R.; Harwig, C. W.; Keller, U. A. D.; Bellac, C. L.; Lange, P. F.; Inkster, J. A. H.; Schaffer, P.; Adam, M. J.; Ruth, T. J.; Overall, C. M.; Perrin, D. M. *Medchemcomm* **2011**, *2*, 942.
- (87) Wan, W.; Guo, N.; Pan, D.; Yu, C.; Weng, Y.; Luo, S.; Ding, H.; Xu, Y.; Wang, L.; Lang, L.; Xie, Q.; Yang, M.; Chen, X. *J. Nuclear Medicine* **2013**, *54*, 691.
- (88) Wan, W.; Guo, N.; Pan, D.; Yu, C.; Weng, Y.; Luo, S.; Ding, H.; Xu, Y.; Wang, L.; Lang, L.; Xie, Q.; Yang, M.; Chen, X. *J. Nucl. Med.* **2013**, *54*, 691.
- (89) Chin, F. T.; Shen, B.; Liu, S. L.; Berganos, R. A.; Chang, E.; Mittra, E.; Chen, X. Y.; Gambhir, S. S. *Mol. Imaging Biol.* **2012**, *14*, 88.
- (90) Poethko, T.; Schottelius, M.; Thumshim, G.; Hersel, U.; Herz, M.; Henriksen, G.; Kessler, H.; Schwaiger, M.; Wester, H. J. *J. Nucl. Med.* **2004**, *45*, 892.
- (91) Marik, J.; Sutcliffe, J. L. *Tetrahedron Lett.* **2006**, *47*, 6681.
- (92) Li, Z. B.; Wu, Z.; Chen, K.; Chin, F. T.; Chen, X. *Bioconjug. Chem.* **2007**, *18*, 1987.
- (93) Moses, J. E.; Moorhouse, A. D. *Chem. Soc. Rev.* **2007**, *36*, 1249.
- (94) Glaser, M.; Arstad, E. *Bioconjug. Chem.* **2007**, *18*, 989.
- (95) Thonon, D.; Kech, C.; Paris, J.; Lemaire, C.; Luxen, A. *Bioconjug. Chem.* **2009**, *20*, 817.
- (96) Mercier, F.; Paris, J.; Kaisin, G.; Thonon, D.; Flagothier, J.; Teller, N.; Lemaire, C.; Luxen, A. *Bioconjug. Chem.* **2011**, *22*, 108.
- (97) Carberry, P.; Lieberman, B. P.; Ploessl, K.; Choi, S. R.; Haase, D. N.; Kung, H. F. *Bioconjug. Chem.* **2011**, *22*, 642.
- (98) Shiraishi, T.; Kitamura, Y.; Ueno, Y.; Kitade, Y. *Chem. Commun.* **2011**, *47*, 2691.

- (99) Carpenter, R. D.; Hausner, S. H.; Sutcliffe, J. L. *ACS Med. Chem. Lett.* **2011**, *2*, 885.
- (100) Priem, T.; Bouteiller, C.; Camporese, D.; Romieu, A.; Renard, P. Y. *Org. Biomol. Chem.* **2012**, *10*, 1068.
- (101) Wangler, C.; Schirmacher, R.; Bartenstein, P.; Wangler, B. *Curr. Med. Chem.* **2010**, *17*, 1092.
- (102) Ting, R.; Adam, M. J.; Ruth, T. J.; Perrin, D. M. *J. Am. Chem. Soc.* **2005**, *127*, 13094.
- (103) Ting, R.; Harwig, C.; Lo, J.; Li, Y.; Adam, M. J.; Ruth, T. J.; Perrin, D. M. *J. Org. Chem.* **2008**, *73*, 4662.
- (104) Ting, R.; Harwig, C. W.; auf dem Keller, U.; McCormick, S.; Austin, P.; Overall, C. M.; Adam, M. J.; Ruth, T. J.; Perrin, D. M. *J. Am. Chem. Soc.* **2008**, *130*, 12045.
- (105) Ting, R.; Lermer, L.; Perrin, D. M. *J. Am. Chem. Soc.* **2004**, *126*, 12720.
- (106) Ting, R.; Lo, J.; Adam, M. J.; Ruth, T. J.; Perrin, D. M. *J. Fluorine Chemistry* **2008**, *129* 349.
- (107) Ting, R.; Lo, J.; Adam, M. J.; Ruth, T. J.; Perrin, D. M. *J. Fluorine Chem.* **2008**, *129*, 349.
- (108) Ting, R.; Thomas, J. M.; Lermer, L.; Perrin, D. M. *Nucleic Acids Res.* **2004**, *32*, 6660.
- (109) Ting, R.; Thomas, J. M.; Perrin, D. M. *Canadian Journal of Chemistry- Revue Canadienne De Chimie* **2007**, *85*, 313.
- (110) Keller, U. A. D.; Bellac, C. L.; Li, Y.; Lou, Y. M.; Lange, P. F.; Ting, R.; Harwig, C.; Kappelhoff, R.; Dedhar, S.; Adam, M. J.; Ruth, T. J.; Benard, F.; Perrin, D. M.; Overall, C. M. *Cancer Res.* **2010**, *70*, 7562.
- (111) Li, Y.; Asadi, A.; Perrin, D. M. *J. Fluorine Chem.* **2009**, *130*, 377.
- (112) Li, Y.; Liu, Z. B.; Lozada, J.; Wong, M. Q.; Lin, K. S.; Yapp, D.; Perrin, D. M. *Nucl. Med. Biol.* **2013**, *40*, 959.
- (113) Li, Y.; Liu, Z.; Pourghiasian, M.; Lin, K.-S.; Schaffer, P.; Benard, F.; Perrin, D. M. *Am. J. Nucl. Med. Mol. Imaging* **2013**, *3*, 57.
- (114) Lau, J.; Pan, J.; Zhang, Z.; Hundal-Jabal, N.; Liu, Z.; Bénard, F.; Lin, K.-S. *Biorg. Med. Chem. Lett.* **2014**, *24*, 3064.
- (115) Cai, H. C.; Conti, P. S. *J. Labelled Comp. Radiopharm.* **2013**, *56*, 264.

- (116) Choi, H.; Phi, J. H.; Paeng, J. C.; Kim, S.-K.; Lee, Y.-S.; Jeong, J. M.; Chung, J.-K.; Lee, D. S.; Wang, K.-C. *Molecular imaging* **2013**, *12*, 213.
- (117) Cutler, C. S.; Hennkens, H. M.; Sisay, N.; Huclier-Markai, S.; Jurisson, S. S. *Chem. Rev.* **2013**, *113*, 858.
- (118) Libert, L. C.; Franci, X.; Plenevaux, A. R.; Ooi, T.; Maruoka, K.; Luxen, A. J.; Lemaire, C. F. *J. Nucl. Med.* **2013**, *54*, 1154.
- (119) Mueller, C. *Molecules* **2013**, *18*, 5005.
- (120) Pfeifer, A.; Knigge, U.; Mortensen, J.; Oturai, P.; Berthelsen, A. K.; Loft, A.; Binderup, T.; Rasmussen, P.; Elema, D.; Klausen, T. L.; Holm, S.; von Benzon, E.; Hojgaard, L.; Kjaer, A. *J. Nucl. Med.* **2012**, *53*, 1207.
- (121) Vedejs, E.; Chapman, R. W.; Fields, S. C.; Lin, S.; Schrimpf, M. R. *J. Org. Chem.* **1995**, *60*, 3020.
- (122) McCusker, P. A.; Kilzer, S. M. L. *J. Am. Chem. Soc.* **1960**, *82*, 372.
- (123) McCusker, P. A.; Makowski, H. S. *J. Am. Chem. Soc.* **1957**, *79*, 5185.
- (124) Li, Y.; Guo, J.; Tang, S.; Lang, L.; Chen, X.; Perrin, D. M. *Am. J. Nucl. Med. Mol. Imaging* **2013**, *3*, 44.
- (125) Liu, Z.; Hundal-Jabal, N.; Wong, M.; Yapp, D.; Lin, K. S.; Benard, F.; Perrin, D. M. *Medchemcomm* **2014**, *5*, 171.
- (126) Pan, J.; Lau, J.; Mesak, F.; Hundal, N.; Pourghiasian, M.; Liu, Z.; Bénard, F.; Dedhar, S.; Supuran, C. T.; Lin, K.-S. *J. Enzyme Inhib. Med. Chem.* **2014**, *29*, 249.
- (127) Baskin, J. M.; Prescher, J. A.; Laughlin, S. T.; Agard, N. J.; Chang, P. V.; Miller, I. A.; Lo, A.; Codelli, J. A.; Bertozzi, C. R. *Proc. Natl. Acad. Sci.* **2007**, *104*, 16793.
- (128) Becer, C. R.; Hoogenboom, R.; Schubert, U. S. *Angew. Chem. Int. Ed.* **2009**, *48*, 4900.
- (129) Campbell-Verduyn, L. S.; Mirfeizi, L.; Schoonen, A. K.; Dierckx, R. A.; Elsinga, P. H.; Feringa, B. L. *Angew. Chem. Int. Ed.* **2011**, *50*, 11117.
- (130) Evans, H. L.; Slade, R. L.; Carroll, L.; Smith, G.; Nguyen, Q. D.; Iddon, L.; Kamaly, N.; Stockmann, H.; Leeper, F. J.; Aboagye, E. O.; Spivey, A. C. *Chem. Commun.* **2012**, *48*, 991.
- (131) Fiore, M.; Lo Conte, M.; Pacifico, S.; Marra, A.; Dondoni, A. *Tetrahedron Lett.* **2011**, *52*, 444.
- (132) Jewett, J. C.; Bertozzi, C. R. *Chem. Soc. Rev.* **2010**, *39*, 1272.

- (133) Jewett, J. C.; Sletten, E. M.; Bertozzi, C. R. *J. Am. Chem. Soc.* **2010**, *132*, 3688.
- (134) Kolb, H. C.; Finn, M. G.; Sharpless, K. B. *Angew. Chem. Int. Ed.* **2001**, *40*, 2004.
- (135) Suzuki, A.; Yamamoto, Y. *Chem. Lett.* **2011**, *40*, 894.
- (136) Tomsho, J. W.; Pal, A.; Hall, D. G.; Benkovic, S. J. *ACS Med. Chem. Lett.* **2012**, *3*, 48.
- (137) Springsteen, G.; Wang, B. H. *Tetrahedron* **2002**, *58*, 5291.
- (138) Gravel, M.; Berube, C. D.; Hall, D. G. *J. Comb. Chem.* **2000**, *2*, 228.
- (139) Bellina, F.; Carpita, A.; Rossi, R. *Synthesis-Stuttgart* **2004**, 2419.
- (140) Lennox, A. J. J.; Lloyd-Jones, G. C. *J. Am. Chem. Soc.* **2012**, *134*, 7431.
- (141) Molander, G. A.; Ellis, N. *Acc. Chem. Res.* **2007**, *40*, 275.
- (142) Butters, M.; Harvey, J. N.; Jover, J.; Lennox, A. J. J.; Lloyd-Jones, G. C.; Murray, P. M. *Angew. Chem. Int. Ed.* **2010**, *49*, 5156.
- (143) Hudnall, T. W.; Lin, T. P.; Gabbai, F. P. *J. Fluorine Chem.* **2010**, *131*, 1182.
- (144) Ishiyama, T.; Murata, M.; Miyaura, N. *J. Org. Chem.* **1995**, *60*, 7508.
- (145) Iwadate, N.; Suginome, M. *J. Organomet. Chem.* **2009**, *694*, 1713.
- (146) Molander, G. A.; Figueroa, R. *Aldrichimica Acta* **2005**, *38*, 49.
- (147) Lennox, A. J. J.; Lloyd-Jones, G. C. *Isr. J. Chem.* **2010**, *50*, 664.
- (148) Lennox, A. J. J.; Lloyd-Jones, G. C. *Angew. Chem. Int. Ed.* **2013**, *52*, 7362.
- (149) Lee, B. C.; Paik, J. Y.; Chi, D. Y.; Lee, K. H.; Choe, Y. S. *Bioconjug. Chem.* **2004**, *15*, 104.
- (150) Briard, E.; Zoghbi, S. S.; Simeon, F. G.; Imaizumi, M.; Gourley, J. P.; Shetty, H. U.; Lu, S. Y.; Fujita, M.; Innis, R. B.; Pike, V. W. *J. Med. Chem.* **2009**, *52*, 688.
- (151) Haubner, R.; Kuhnast, B.; Mang, C.; Weber, W. A.; Kessler, H.; Wester, H. J.; Schwaiger, M. *Bioconjug. Chem.* **2004**, *15*, 61.

- (152) de Bruin, B.; Kuhnast, B.; Hinnen, F.; Yaouancq, L.; Amessou, M.; Johannes, L.; Samson, A.; Boisgard, R.; Tavitian, B.; Dolle, F. *Bioconjug. Chem.* **2005**, *16*, 406.
- (153) Hausner, S. H.; Marik, J.; Gagnon, M. K. J.; Sutcliffe, J. L. *J. Med. Chem.* **2008**, *51*, 5901.
- (154) Olberg, D. E.; Cuthbertson, A.; Solbakken, M.; Arukwe, J. M.; Qu, H.; Kristian, A.; Bruheim, S.; Hjelstuen, O. K. *Bioconjug. Chem.* **2010**, *21*, 2297.
- (155) Jacobson, O.; Zhu, L.; Ma, Y.; Weiss, I. D.; Sun, X.; Niu, G.; Kiesewetter, D. O.; X., C. *Bioconjug. Chem.* **2011**, *22*, 422.
- (156) Wuest, F.; Berndt, M.; Bergmann, R.; van den Hoff, J.; Pietzsch, J. *Bioconjug. Chem.* **2008**, *19*, 1202.
- (157) Lee, E.; Kamlet, A. S.; Powers, D. C.; Neumann, C. N.; Boursalian, G. B.; Furuya, T.; Choi, D. C.; Hooker, J. M.; Ritter, T. *Science* **2011**, *334*, 639.
- (158) Battle, M. R.; Goggi, J. L.; Allen, L.; Barnett, J.; Morrison, M. S. *J. Nucl. Med.* **2011**, *52*, 424.
- (159) Ceccarini, G.; Flavell, R. R.; Butelman, E. R.; Synan, M.; Willnow, T. E.; Bar-Dagan, M.; Goldsmith, S. J.; Kreek, M. J.; Kothari, P.; Vallabhajosula, S.; Muir, T. W.; Friedman, J. M. *Cell Metabolism* **2009**, *10*, 148.
- (160) Haubner, R.; Wester, H. J.; Weber, W. A.; Mang, C.; Ziegler, S. I.; Goodman, S. L.; Senekowitsch-Schmidtke, R.; Kessler, H.; Schwaiger, M. *Cancer Res.* **2001**, *61*, 1781.
- (161) Beer, A. J.; Niemeyer, M.; Carlsen, J.; Sarbia, M.; Nahrig, J.; Watzlowik, P.; Wester, H.-J.; Harbeck, N.; Schwaiger, M. *J. Nucl. Med.* **2008**, *49*, 255.
- (162) Wester, H. J.; Schottelius, M.; Scheidhauer, K.; Meisetschlager, G.; Herz, M.; Rau, F. C.; Reubi, J. C.; Schwaiger, M. *Eur. J. Nucl. Med. Mol. Imaging* **2003**, *30*, 117.
- (163) Anderson, C. J.; Dehdashti, F.; Cutler, P. D.; Schwarz, S. W.; Laforest, R.; Bass, L. A.; Lewis, J. S.; McCarthy, D. W. *J. Nucl. Med.* **2001**, *42*, 213.
- (164) Liu, Z. B.; Li, Y.; Lozada, J.; Schaffer, P.; Adam, M. J.; Ruth, T. J.; Perrin, D. M. *Angew. Chem. Int. Ed.* **2013**, *52*, 2303.
- (165) Li, Z. B.; Cai, H. C.; Hassink, M.; Blackman, M. L.; Brown, R. C. D.; Conti, P. S.; Fox, J. M. *Chem. Commun.* **2010**, *46*, 8043.
- (166) Sun, L. Q.; Cairns, M. J.; Gerlach, W. L.; Witherington, C.; Wang, L.; King, A. *J. Biol. Chem.* **1999**, *274*, 17236.

- (167) Sun, L. Q.; Cairns, M. J.; Saravolac, E. G.; Baker, A.; Gerlach, W. L. *Pharmacol. Rev.* **2000**, *52*, 325.
- (168) Wu, Y.; Cai, W. B.; Chen, X. Y. *Mol. Imaging Biol.* **2006**, *8*, 226.
- (169) Schirmmacher, R.; Bradtmoller, G.; Schirmmacher, E.; Thews, O.; Tillmanns, J.; Siessmeier, T.; Buchholz, H. G.; Bartenstein, P.; Waengler, B.; Niemyer, C. M.; Jurkschat, K. *Angew. Chem. Int. Ed.* **2006**, *45*, 6047.
- (170) Kuhnast, B.; de Bruin, A.; Hinnen, F.; Tavitian, B.; Dolle, F. *Bioconjug. Chem.* **2004**, *15*, 617.
- (171) Kamlet, A. S.; Neumann, C. N.; Lee, E.; Carlin, S. M.; Moseley, C. K.; Stephenson, N.; Hooker, J. M.; Ritter, T. *PLoS One* **2013**, *8*.
- (172) Liu, X. C.; Scouten, W. H. *J. Chromatogr. A* **1994**, *687*, 61.
- (173) Liu, S. L.; Liu, Z. F.; Chen, K.; Yan, Y. J.; Watzlowik, P.; Wester, H. J.; Chin, F. T.; Chen, X. Y. *Mol. Imaging Biol.* **2010**, *12*, 530.
- (174) Liu, Z. F.; Shi, J. Y.; Jia, B.; Yu, Z. L.; Liu, Y.; Zhao, H. Y.; Li, F.; Tian, J.; Chen, X. Y.; Liu, S. A.; Wang, F. *Mol. Pharm.* **2011**, *8*, 591.
- (175) Liu, Z. F.; Yan, Y. J.; Liu, S. L.; Wang, F.; Chen, X. Y. *Bioconjug. Chem.* **2009**, *20*, 1016.
- (176) Yan, Y. J.; Chen, K.; Yang, M.; Sun, X. L.; Liu, S. L.; Chen, X. Y. *Amino Acids* **2011**, *41*, 439.
- (177) Hausner, S. H.; Carpenter, R. D.; Bauer, N.; Sutcliffe, J. L. *Nucl. Med. Biol.* **2013**, *40*.
- (178) Tateishi, U.; Oka, T.; Inoue, T. *Curr. Med. Chem.* **2012**, *19*, 3301.
- (179) Tredwell, M.; Preshlock, S. M.; Taylor, N. J.; Gruber, S.; Huiban, M.; Passchier, J.; Mercier, J.; Genicot, C.; Gouverneur, V. *Angew. Chem. Int. Ed. Engl.* **2014**.
- (180) Chen, X. Y.; Liu, S.; Hou, Y. P.; Tohme, M.; Park, R.; Bading, J. R.; Conti, P. S. *Mol. Imaging Biol.* **2004**, *6*, 350.
- (181) Chen, Y. X.; Triola, G.; Waldmann, H. *Acc. Chem. Res.* **2011**, *44*, 762.
- (182) Chen, Z.; Penet, M. F.; Nimmagadda, S.; Li, C.; Banerjee, S. R.; Winnard, P. T.; Artemov, D.; Glunde, K.; Pomper, M. G.; Bhujwala, Z. M. *Acs Nano* **2012**, *6*, 7752.
- (183) Kimura, R. H.; Miao, Z.; Cheng, Z.; Gambhir, S. S.; Cochran, J. R. *Bioconjug. Chem.* **2010**, *21*, 436.

- (184) Lang, L. X.; Li, W. H.; Guo, N.; Ma, Y.; Zhu, L.; Kiesewetter, D. O.; Shen, B. Z.; Niu, G.; Chen, X. Y. *Bioconjug. Chem.* **2011**, *22*, 2415.
- (185) Campos, M. M.; Leal, P. C.; Yunes, R. A.; Calixto, J. B. *Trends Pharmacol. Sci.* **2006**, *27*, 646.
- (186) Calixto, J. B.; Medeiros, R.; Fernandes, E. S.; Ferreira, J.; Cabrini, D. A.; Campos, M. M. *Br. J. Pharmacol.* **2004**, *143*, 803.
- (187) Supuran, C. T. *Nat. Rev. Drug Discov.* **2008**, *7*, 168.
- (188) Kwekkeboom, D. J.; Kam, B. L.; van Essen, M.; Teunissen, J. J. M.; van Eijck, C. H. J.; Valkema, R.; de Jong, M.; de Herder, W. W.; Krenning, E. P. *Endocr. Relat. Cancer* **2010**, *17*, R53.
- (189) Krausz, Y.; Keidar, Z.; Kogan, I.; Even-Sapir, E.; Bar-Shalom, R.; Engel, A.; Rubinstein, R.; Sachs, J.; Bocher, M.; Agranovicz, S.; Chisin, R.; Israel, O. *Clin. Endocrinol. (Oxf.)* **2003**, *59*, 565.
- (190) Buchmann, I.; Henze, M.; Engelbrecht, S.; Eisenhut, M.; Runz, A.; Schaefer, M.; Schilling, T.; Haufe, S.; Herrmann, T.; Haberkorn, U. *Eur. J. Nucl. Med. Mol. Imaging* **2007**, *34*, 1617.
- (191) Storch, D.; Behe, M.; Walter, M. A.; Chen, J. H.; Powell, P.; Mikolajczak, R.; Macke, H. R. *J. Nucl. Med.* **2005**, *46*, 1561.
- (192) Breeman, W. A. P.; de Jong, M.; Kwekkeboom, D. J.; Valkema, R.; Bakker, W. H.; Kooij, P. P. M.; Visser, T. J.; Krenning, E. P. *Eur. J. Nucl. Med.* **2001**, *28*, 1421.
- (193) Ginj, M.; Schmitt, J. S.; Chen, J. H.; Waser, B.; Reubi, J. C.; de Jong, M.; Schulz, S.; Maecke, H. R. *Chem. Biol.* **2006**, *13*, 1081.
- (194) Antunes, P.; Ginj, M.; Walter, M. A.; Chen, J. H.; Reubi, J. C.; Maecke, H. R. *Bioconjug. Chem.* **2007**, *18*, 84.
- (195) Gabriel, M.; Decristoforo, C.; Donnemiller, E.; Ulmer, H.; Rychlinski, C. W.; Mather, S. J.; Moncayo, R. *J. Nucl. Med.* **2003**, *44*, 708.
- (196) Grierson, J. R.; Yagle, K. J.; Eary, J. F.; Tait, J. F.; Gibson, D. F.; Lewellen, B.; Link, J. M.; Krohn, K. A. *Bioconjug. Chem.* **2004**, *15*, 373.
- (197) Sprague, J. E.; Peng, Y. J.; Sun, X. K.; Weisman, G. R.; Wong, E. H.; Achilefu, S.; Anderson, C. J. *Clin. Cancer Res.* **2004**, *10*, 8674.
- (198) Gabriel, M.; Decristoforo, C.; Kandler, D.; Dobrozemsky, G.; Heute, D.; Uprimny, C.; Kovacs, P.; Von Guggenberg, E.; Bale, R.; Virgolini, I. J. *J. Nucl. Med.* **2007**, *48*, 508.

- (199) Guo, Y. J.; Ferdani, R.; Anderson, C. J. *Bioconjug. Chem.* **2012**, *23*, 1470.
- (200) Guo, Y. Y.; Yuan, H. S.; Rice, W. L.; Kumar, A. T. N.; Goergen, C. J.; Jokivarsi, K.; Josephson, L. *J. Am. Chem. Soc.* **2012**, *134*, 19338.
- (201) Li, W. H.; Lang, L. X.; Niu, G.; Guo, N.; Ma, Y.; Kiesewetter, D. O.; Shen, B. Z.; Chen, X. Y. *Amino Acids* **2012**, *43*, 1349.
- (202) Haubner, R. H.; Wester, H. J.; Weber, W. A.; Schwaiger, M. *Q. J. Nucl. Med.* **2003**, *47*, 189.
- (203) Kuhnast, B.; Bodenstein, C.; Wester, H. E.; Weber, W. *J. Labelled Compd. Radiopharm.* **2003**, *46*, 539.
- (204) Leyton, J.; Iddon, L.; Perumal, M.; Indrevoll, B.; Glaser, M.; Robins, E.; George, A. J. T.; Cuthbertson, A.; Luthra, S. K.; Aboagye, E. O. *J. Nucl. Med.* **2011**, *52*, 1441.
- (205) Henze, M.; Schuhmacher, J.; Hipp, P.; Kowalski, J.; Becker, D. W.; Doll, J.; Macke, H. R.; Hofmann, M.; Debus, J.; Haberkorn, U. *J. Nucl. Med.* **2001**, *42*, 1053.
- (206) Kayani, I.; Conry, B. G.; Groves, A. M.; Win, T.; Dickson, J.; Caplin, M.; Bomanji, J. B. *J. Nucl. Med.* **2009**, *50*, 1927.
- (207) Poeppel, T. D.; Binse, I.; Petersenn, S.; Lahner, H.; Schott, M.; Antoch, G.; Brandau, W.; Bockisch, A.; Boy, C. *J. Nucl. Med.* **2011**, *52*, 1864.
- (208) Banerjee, S. R.; Pomper, M. G. *Appl. Radiat. Isot.* **2013**, *76*, 2.
- (209) Laforest, R.; Liu, X. *Q. J. Nucl. Med. Mol. Imaging* **2008**, *52*, 151.
- (210) Kemerink, G. J.; Visser, M. G. W.; Franssen, R.; Beijer, E.; Zamburlini, M.; Halders, S.; Brans, B.; Mottaghy, F. M.; Teule, G. J. *J. Eur. J. Nucl. Med. Mol. Imaging* **2011**, *38*, 940.
- (211) Zhang, H. W.; Chen, J. H.; Waldherr, C.; Hinni, K.; Waser, B.; Reubi, J. C.; Maecke, H. R. *Cancer Res.* **2004**, *64*, 6707.
- (212) Zhang, Y.; Pavlova, O. A.; Chefer, S. I.; Hall, A. W.; Kurian, V.; Brown, L. L.; Kimes, A. S.; Mukhin, A. G.; Horti, A. G. *J. Med. Chem.* **2004**, *47*, 2453.
- (213) Kostikov, A. P.; Iovkova, L.; Chin, J.; Schirmacher, E.; Wangler, B.; Wangler, C.; Jurkschat, K.; Cosa, G.; Schirmacher, R. *J. Fluorine Chem.* **2011**, *132*, 27.
- (214) Wangler, C.; Waser, B.; Alke, A.; Iovkova, L.; Buchholz, H. G.; Niedermoser, S.; Jurkschat, K.; Fottner, C.; Bartenstein, P.; Schirmacher, R.; Reubi, J. C.; Weste, H. J.; Wangler, B. *Bioconjug. Chem.* **2010**, *21*, 2289.

- (215) Laverman, P.; D'Souza, C. A.; Eek, A.; McBride, W. J.; Sharkey, R. M.; Oyen, W. J. G.; Goldenberg, D. M.; Boerman, O. C. *Tumor Biol.* **2012**, *33*, 427.
- (216) Laverman, P.; McBride, W. J.; Sharkey, R. M.; Eek, A.; Joosten, L.; Oyen, W. J. G.; Goldenberg, D. M.; Boerman, O. C. *J. Nucl. Med.* **2010**, *51*, 454.
- (217) Bass, L. A.; Wang, M.; Welch, M. J.; Anderson, C. J. *Bioconjug. Chem.* **2000**, *11*, 527.
- (218) Forster, G. J.; Engelbach, M.; Brockmann, J.; Reber, H.; Buchholz, H. G.; Macke, H. R.; Rosch, F.; Herzog, H.; Bartenstein, P. *Eur. J. Nucl. Med.* **2001**, *28*, 1743.
- (219) Hanaoka, H.; Tominaga, H.; Yamada, K.; Paudyal, P.; Iida, Y.; Watanabe, S.; Paudyal, B.; Higuchi, T.; Oriuchi, N.; Endo, K. *Ann. Nucl. Med.* **2009**, *23*, 559.
- (220) Lewis, J. S.; Srinivasan, A.; Schmidt, M. A.; Anderson, C. J. *Nucl. Med. Biol.* **1999**, *26*, 267.
- (221) Yim, C. B.; van der Wildt, B.; Dijkgraaf, I.; Joosten, L.; Eek, A.; Versluis, C.; Rijkers, D. T. S.; Boerman, O. C.; Liskamp, R. M. J. *ChemBioChem* **2011**, *12*, 750.
- (222) Fani, M.; Maecke, H. R. *Eur. J. Nucl. Med. Mol. Imaging* **2012**, *39*, 11.
- (223) Fischer, C. R.; Mueller, C.; Reber, J.; Mueller, A.; Kraemer, S. D.; Ametamey, S. M.; Schibli, R. *Bioconjug. Chem.* **2012**, *23*, 805.
- (224) Fischer, C. R.; Muller, C.; Reber, J.; Muller, A.; Kramer, S. D.; Ametamey, S. M.; Schibli, R. *Bioconjug. Chem.* **2012**, *23*, 805.
- (225) Reubi, J. C.; Wenger, S.; Schmuckli-Maurer, J.; Schaer, J. C.; Gugger, M. *Clin. Cancer Res.* **2002**, *8*, 1139.
- (226) Wild, D.; Fani, M.; Behe, M.; Brink, I.; Rivier, J. E. F.; Reubi, J. C.; Maecke, H. R.; Weber, W. A. *J. Nucl. Med.* **2011**, *52*, 1412.
- (227) Schkeryantz, J. M.; Woo, J. C. G.; Siliphaivanh, P.; Depew, K. M.; Danishefsky, S. J. *J. Am. Chem. Soc.* **1999**, *121*, 11964.
- (228) Matteson, D. S.; Majumdar, D. *J. Organomet. Chem.* **1979**, *170*, 259.
- (229) Tsien, R. Y. *Nat. Cell Biol.* **2003**, Ss16.
- (230) Smith, G.; Carroll, L.; Aboagye, E. O. *Mol. Imaging Biol.* **2012**, *14*, 653.
- (231) Culver, J.; Akers, W.; Achilefu, S. *J. Nucl. Med.* **2008**, *49*, 169.
- (232) Kuil, J.; Velders, A. H.; van Leeuwen, F. W. B. *Bioconjug. Chem.* **2010**, *21*, 1709.

(233) van der Poel, H. G.; Buckle, T.; Brouwer, O. R.; Olmos, R. A. V.; van Leeuwen, F. W. B. *Eur. Urol.* **2011**, *60*, 826.

(234) Lee, H.; Akers, W. J.; Cheney, P. P.; Edwards, W. B.; Liang, K.; Culver, J. P.; Achilefu, S. *J. Biomed. Opt.* **2009**, *14*.

(235) Houston, J. P.; Ke, S.; Wang, W.; Li, C.; Sevick-Muraca, E. M. *J. Biomed. Opt.* **2005**, *10*.

(236) Azhdarinia, A.; Ghosh, P.; Ghosh, S.; Wilganowski, N.; Sevick-Muraca, E. M. *Mol. Imaging Biol.* **2012**, *14*, 261.

(237) Hendricks, J. A.; Keliher, E. J.; Wan, D. P.; Hilderbrand, S. A.; Weissleder, R.; Mazitschek, R. *Angew. Chem. Int. Ed.* **2012**, *51*, 4603.

(238) Li, Z. B.; Lin, T. P.; Liu, S. L.; Huang, C. W.; Hudnall, T. W.; Gabbai, F. P.; Conti, P. S. *Chem. Commun.* **2011**, *47*, 9324.

(239) Ting, R.; Aguilera, T. A.; Crisp, J. L.; Hall, D. J.; Eckelman, W. C.; Vera, D. R.; Tsien, R. Y. *Bioconjug. Chem.* **2010**, *21*, 1811.

(240) Li, Z. B.; Chansaenpak, K.; Liu, S. L.; Wade, C. R.; Conti, P. S.; Gabbai, F. P. *Medchemcomm* **2012**, *3*, 1305.

(241) Liu, S. L.; Li, Z. B.; Yap, L. P.; Huang, C. W.; Park, R.; Conti, P. S. *Chem. Eur. J.* **2011**, *17*, 10222.

(242) Rostovtsev, V. V.; Green, L. G.; Fokin, V. V.; Sharpless, K. B. *Angew. Chem. Int. Ed.* **2002**, *41*, 2596.

(243) Wu, P.; Malkoch, M.; Hunt, J. N.; Vestberg, R.; Kaltgrad, E.; Finn, M. G.; Fokin, V. V.; Sharpless, K. B.; Hawker, C. J. *Chem. Commun.* **2005**, 5775.

(244) Wang, Q.; Chan, T. R.; Hilgraf, R.; Fokin, V. V.; Sharpless, K. B.; Finn, M. G. *J. Am. Chem. Soc.* **2003**, *125*, 3192.

(245) Maschauer, S.; Haubner, R.; Kuwert, T.; Prante, O. *Mol. Pharm.* **2014**, *11*, 505.

(246) Cao, J.; Wan, S. N.; Tian, J. M.; Li, S. W.; Deng, D. W.; Qian, Z. Y.; Gu, Y. Q. *Contrast Media Mol.* **2012**, *7*, 390.

(247) Cai, W. B.; Chen, K.; Li, Z. B.; Gambhir, S. S.; Chen, X. Y. *J. Nucl. Med.* **2007**, *48*, 1862.

(248) Wang, W.; Ke, S.; Kwon, S.; Yallampalli, S.; Cameron, A. G.; Adams, K. E.; Mawad, M. E.; Sevick-Muraca, E. M. *Bioconjug. Chem.* **2007**, *18*, 397.

(249) Adams, K. E.; Ke, S.; Kwon, S.; Liang, F.; Fan, Z.; Lu, Y.; Hirschi, K.; Mawad, M. E.; Barry, M. A.; Sevick-Muraca, E. M. *J. Biomed. Opt.* **2007**, *12*.

(250) Huang, R. M.; Vider, J.; Kovar, J. L.; Olive, D. M.; Mellinghoff, I. K.; Mayer-Kuckuk, P.; Kircher, M. F.; Blasberg, R. G. *Clin. Cancer Res.* **2012**, *18*, 5731.

(251) Choi, H. S.; Gibbs, S. L.; Lee, J. H.; Kim, S. H.; Ashitate, Y.; Liu, F. B.; Hyun, H.; Park, G.; Xie, Y.; Bae, S.; Henary, M.; Frangioni, J. V. *Nat. Biotechnol.* **2013**, *31*, 148.

(252) Namavari, M.; Cheng, Z.; Zhang, R.; De, A.; Levi, J.; Hoerner, J. K.; Yaghoubi, S. S.; Syud, F. A.; Gambhir, S. S. *Bioconjug. Chem.* **2009**, *20*, 432.